

TECHNISCHE UNIVERSITÄT MÜNCHEN

Fakultät für Chemie

Fachgebiet Physikalische Chemie

Vanadium-Based Materials as Electrode Materials in Sodium-Ion Batteries

Steffen Uwe Hartung

Vollständiger Abdruck der von der Fakultät für Chemie der Technischen Universität München zur Erlangung des akademischen Grades eines

Doktors der Naturwissenschaften

genehmigten Dissertation.

Vorsitzende(r): Univ.-Prof. Dr. U. K. Heiz

Prüfer der Dissertation:

1. Univ.-Prof. Dr. M.-E. Michel-Beyerle (i.R.)
2. Univ.-Prof. Dr. F. E. Kühn
3. Prof. M. Srinivasan, Ph.D.
Nanyang Technological University Singapore

Die Dissertation wurde am 26.11.2015 bei der Technischen Universität München eingereicht und durch die Fakultät für Chemie am 21.12.2015 angenommen.

Table of Contents

List of Acronyms	5
Abstract	7
1 Introduction.....	8
2 Energy Storage Technologies.....	11
2.1 Fuel Cells	11
2.2 Capacitors	12
2.3 Batteries	13
2.3.1 Overview	13
2.3.2 Charge Storage Mechanisms	14
3 Sodium-Ion Batteries	16
3.1 The Case for Sodium-Ion Batteries.....	16
3.2 Materials for Sodium-Ion Batteries – Current Status	19
3.2.1 Cathode Materials.....	19
3.2.2 Anode Materials.....	21
3.3 Vanadium Oxides in Sodium-Ion Batteries – Motivation and Approaches	23
4 Experimental Methods	25
4.1 Electron Microscopy	25
4.2 Energy Dispersive Spectroscopy and X-Ray Fluorescence	28
4.3 X-Ray Photoelectron Spectroscopy	29
4.4 X-Ray Diffraction	30
4.4.1 Laboratory X-Ray Diffraction.....	30
4.4.2 Synchrotron X-Ray Diffraction	33
4.5 Inductively Coupled Plasma Optical Emission Spectrometry	33
4.6 Electrochemical Measurements.....	34
4.6.1 Electrode Preparation.....	34
4.6.2 Coin Cell Preparation.....	34
4.6.3 Galvanostatic Cycling	35

4.6.4	Galvanostatic Intermittent Titration Technique.....	38
4.6.5	Cyclic and Linear Sweep Voltammetry	39
4.6.6	Electrochemical Impedance Spectroscopy	40
4.7	Thermogravimetric Analysis.....	42
4.8	Rheometry.....	43
5	Vanadium-Based Materials in Sodium-Ion Batteries	44
5.1	Sodium Vanadium Oxide: A New Material for High-Performance Symmetric Sodium-Ion Batteries.....	45
5.2	Electrochemical cell for <i>in operando</i> X-ray diffraction measurements on a conventional X-ray diffractometer.....	59
5.3	Mechanism of Na ⁺ Insertion in Alkali Vanadates and its Influence on Battery Performance.	65
5.4	Vanadium-based polyoxometalate as new material for sodium-ion battery anodes	112
5.5	A novel ionic liquid for Li ion batteries – uniting the advantages of guanidinium and piperidinium cations.....	123
6	Conclusion.....	134
	References	137
	List of Figures	147

List of Acronyms

CE	Counter Electrode
CV	Cyclic Voltammogram/Cyclic Voltammetry
<i>e.g.</i>	<i>exempli gratia</i> (for example)
EDS	Energy-Dispersive Spectroscopy
EIS	Electrochemical Impedance Spectroscopy
<i>etc.</i>	<i>et cetera</i> (and so on)
FWHM	Full Width at Half Maximum
<i>i.e.</i>	<i>id est</i> (that is)
ICP-OES	Inductively Coupled Plasma Optical Emission Spectrometry
IL	Ionic Liquid
KVO	$K_{1.8}V_6O_{16}$
LIB	Lithium-Ion Battery
LSV	Linear Sweep Voltammetry
LVO	$Li_{2.55}V_6O_{16}$
NIB	Sodium-Ion Battery
NMP	N-Methyl-2-Pyrrolidone
NVO	$Na_xV_6O_{16}$
OCV	Open Circuit Voltage
PBA	Prussian Blue Analogue
PipGuan-TFSI	<i>N,N,N',N'</i> -tetramethyl- <i>N''</i> , <i>N''</i> -pentamethyleneguanidinium bis(trifluoromethylsulfonyl)imide
POM	Polyoxometalate
PVDF	Polyvinylidene Difluoride
RE	Reference Electrode
SEI	Solid Electrolyte Interphase

SEM	Scanning Electron Microscopy
TEM	Transmission Electron Microscopy
TFSI	Bis(trifluoromethylsulfonyl)imide
TGA	Thermogravimetric Analysis
vs.	<i>versus</i>
WE	Working Electrode
XPS	X-ray Photoelectron Spectroscopy
XRD	X-ray Diffraction
XRF	X-ray Fluorescence

Abstract

Natrium-Ionen-Batterien haben Vorteile gegenüber Lithium-Ionen-Batterien hinsichtlich Kosten und Kinetik. Jedoch sind die Identifikation neuer Elektrodenmaterialien sowie ein besseres Verständnis der Ladungsspeicherung notwendig, um die Zyklenstabilität zu verbessern. Diese Arbeit beschreibt die Untersuchung Vanadium-basierter Elektrodenmaterialien. Der beobachtete Kapazitätsverlust von Alkali-Vanadaten während des Zyklisierens wird erklärt und erfolgreich umgesetzte Strategien zur Verbesserung der Zyklenstabilität werden beschrieben.

Sodium-ion batteries have advantages over the wide-spread lithium-ion batteries with regard to cost and kinetics. However, low cycling stability is still a common problem for many electrode materials. Thus, identification of suitable materials and understanding of the respective charge-storage mechanisms are necessary. This work presents investigations on vanadium-based electrode materials in sodium-ion batteries. Reasons for the observed decrease in capacity during cycling are identified and successful strategies to improve cycling stability are presented.

This doctoral thesis comprises the scientific publications resulting from my work as a research associate at TUM CREATE. After an introduction to sodium-ion batteries, the main experimental methods employed in this work are described. Subsequently, my four scientific publications, as well as one further publication in which my contribution was crucial, are presented. The thesis is concluded with a discussion of the described results.

1 Introduction

Availability and usability of energy, defined as the capacity of a physical system to perform work, have always had a major impact on societal and economic developments. Various approaches to generate energy in the form of electricity from electrochemical reactions were developed as early as the 19th century. The first device to build on this principle was the Voltaic pile, developed by Alessandro Volta in 1800, which was based on the different electromotive forces of the elements copper and zinc. These metal plates were separated by cloth soaked in brine. This set-up is considered the first battery.^[1-3] In 1836, John Frederic Daniell demonstrated the so-called “Daniell cell”. He separated the two metals and immersed each in an individual electrolyte, which was copper sulphate for the copper side and zinc sulphate for the zinc side, while the two half-cells were separated by a porous diaphragm so that ions could move from one side to the other to maintain charge neutrality. The external circuit, which connected the two metals, provided an electrical current of 1.1.

In 1839, shortly after Christian Friedrich Schönbein described the occurrence of “inverse electrolysis”, Sir William Robert Grove generated electricity based on the reaction of oxygen and hydrogen.^[4,5] The new type of device Grove used became later known as fuel cell. A lot of work that followed in the field of fuel cells was focussed on using coal as energy source. In the 1930’s, important work was done by Francis Thomas Bacon, who employed alkaline electrolytes and nickel electrodes and built on the initial idea of using oxygen and hydrogen as reagents.^[5]

In 1859, Gaston Planté invented the first secondary (*i.e.* rechargeable) battery, exploiting electrochemical reactions of lead and lead oxide, immersed in sulphuric acid. This system became commonly known as the lead-acid battery.^[2] A further breakthrough came only seven years later with the development of the LeClanché cell, which consisted of manganese dioxide with some added carbon as cathode, metallic zinc as anode, and an ammonium chloride solution as electrolyte. Around 1900, Waldemar Jungner devised the nickel-cadmium rechargeable battery, which delivers 1.2 V and whose energy density superseded the lead acid system.^[2]

After these inventions, development of new battery systems stalled for several decades, and only modifications and incremental improvement of these early concepts took place until the late 1960’s.^[2] Work on molten-salt sodium-based batteries led to the development of the ZEBRA battery (zero-emission battery research activities), which is based on the chemistry of Na-NiCl₂, and the Na-S battery in the 1970’s.^[6] Developments in various fields, such as consumer electronics and implantable medical devices, required reliable energy storage systems with better energy densities. Therefore, lithium, which is both the lightest metallic element, and has the highest standard reduction potential, received considerable attention. However, due to the reactivity of lithium with water, aqueous electrolytes needed to be replaced with less reactive, *i.e.* organic electrolytes. Among the first batteries, lithium iodine cells were used in pacemakers, in which they replaced the previously predominant zinc–mercury oxide based systems due to an increase in energy density of almost 400%, higher durability and great reduction

of weight and volume.^[2] These systems were, like subsequently developed lithium-ion batteries using SO_2 , SOCl_2 , or SO_2Cl_2 as cathode material, primary batteries. Naturally, the success of these systems spurred interest in secondary lithium-based systems. The breakthrough for such systems came with the discovery of intercalation or insertion materials, which are based on the reversible incorporation of lithium ions into a lattice structure.^[7] First systems developed by companies like Exxon and Moli Energy focused on materials such as TiS_2 or MoS_2 .^[2] The metallic lithium anode, however, posed an inherent safety risk, which is why alternative anode materials, particularly for the field of consumer electronics, were needed. Thus, the concept of a ‘rocking chair’ type battery was introduced, in which both cathode and anode consist of insertion type electrodes; this concept was commercialized by Sony with graphite as the anode, and lithium cobalt oxide as the cathode material in 1991.^[2]

Initial work on intercalation compounds was not only focussed on lithium, but described intercalation of different alkali ions into a variety of compounds such as $\text{Na}_{0.8}\text{TiS}_2$, $\text{K}_{0.8}\text{TiS}_2$, $\text{Cs}_{0.6}\text{TiS}_2$ and $\text{Na}_{0.95}\text{TiSe}_2$.^[7,8] For example, Rudorff reported initial studies on intercalation compounds as early as 1959.^[9,10] Specifically for Na-based systems, other intercalation materials were reported such as, e.g. Na_xCoO_2 ^[8,11,12], which was the analogue to the LiCoO_2 employed in lithium-ion batteries (LIBs). However, owing to the promising prospects of lithium-based systems, subsequent research focussed on lithium(-ion) batteries as far as intercalation/insertion compounds are concerned, and sodium-based intercalation materials were neglected for a long time.

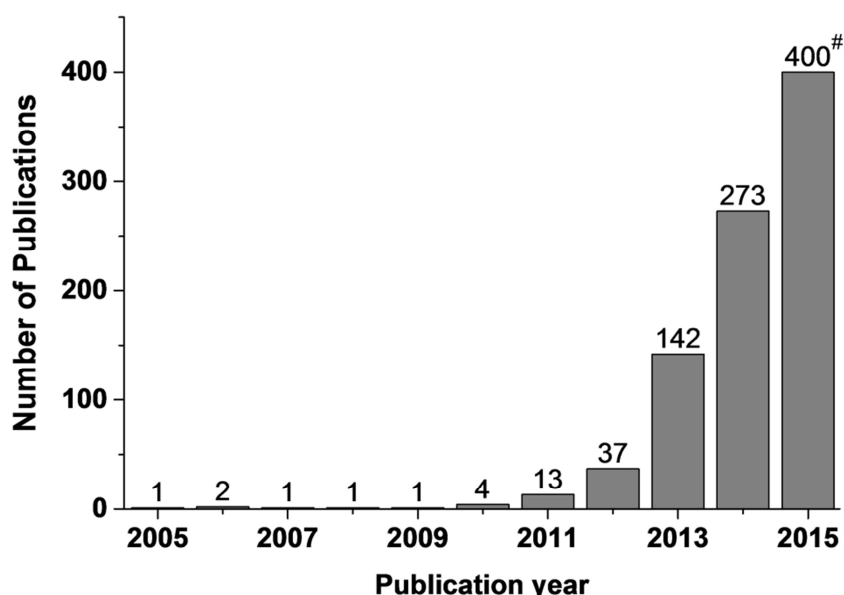


Figure 1. Development of the number of publications on the topic sodium-ion battery as found by Web of Science, search term: "sodium-ion batter*"; #: year to date; date of search Oct 26, 2015.

Only in recent years, with growing concerns about the cost and resource abundance of lithium-ion based battery systems, research in intercalation-based sodium-ion batteries (NIBs) has surged, which is reflected in the immense increase of publications on this topic in recent years (see Figure 1).

2 Energy Storage Technologies

Electrical energy can be stored in various ways, which can be broadly categorized in energy storage in electrical charges (e.g. capacitors), and energy storage via conversion to other forms of energy. These include, *inter alia*, kinetic energy (e.g. flywheel), potential energy (e.g. compressed air), or (electro-)chemical storage (e.g. fuel cell, battery).^[13–15] As this work focusses on sodium-ion batteries, *i.e.* electrochemical energy storage, the functional principles of electrochemical energy storage, as well as the related capacitors, will be briefly explained.

2.1 Fuel Cells

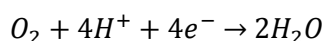
There are several types of fuel cells, however, all work according to the same underlying principles of converting chemical energy to electrical energy during discharge via chemical redox reactions.^[4,16] The fuel cell is divided into two half-cells with their respective electrodes, the cathode and the anode, which are separated internally by an ionically conductive, but electrically insulating electrolyte, and connected externally by an electric circuit. There is a wide range of electrolytes that can be employed, and the respective electrolyte type serves as the basis of the classification of fuel cells. The major types of fuel cells are the acidic and the alkaline fuel cell. The electrolytes obviously differ with regard to their physical properties, but have in common that they enable ion movement and prevent electron movement through the electrolyte. The fuel cell demonstrated by Bacon as mentioned above was later developed further by Pratt & Whitney to be used as the primary source of electrical energy in the Apollo space programme.^[5]

In the half-cells, the chemical reactions providing electrical energy occur, namely the reduction of oxygen at the cathode side, and the oxidation of the fuel, commonly hydrogen, methane, or propane, at the anode side. To illustrate the working principle, the underlying chemical reactions for an acidic hydrogen-based fuel cell are depicted as an example:

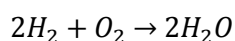
Anode



Cathode



Overall reaction



The electrons generated during the oxidation reactions are fed into the external circuit, where they provide an electric current that can be harnessed, and reduce the oxygen at the cathode side. Positively charged ions, in the case of the acidic fuel cell portrayed here protons, transfer from the anode through the electrolyte to the cathode, where they react with oxygen to form water, which is the reaction product. As these reactions are thermodynamically favoured, but kinetically hindered, catalysts, typically noble metals like platinum are employed in low-temperature fuel cells as additive to the electrodes to enable these reactions. The necessity to employ expensive catalysts in low temperature fuel cells presents a challenge for widespread application of this technology. It is important to note, especially in contrast to the working principle of batteries described below, that the relevant chemical processes, *i.e.* redox reactions, occur at the surface of the electrodes and are not accompanied by physical or chemical alteration of the electrode material (except for undesired side reactions). Consequently, the electrode material is not consumed during use, but only the fuel. Moreover, as the cell is fed with fuel from an external reservoir, continuously ongoing operation is possible, and electrical 'recharging' processes are not necessary. The respective fuel, however, needs to be refilled.

2.2 Capacitors

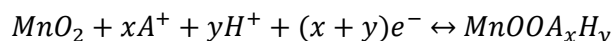
Even though, strictly speaking, capacitors are not subsumed under the (electro-) chemical storage category, this technology is included because one branch, electrochemical capacitors, is related to the working principle of batteries described below. Traditional capacitors consist of a dielectric material that separates two metal plates on which charges are collected when a voltage is applied, so that one metal plate is positively, the other negatively charged.

Electrochemical capacitors can be sub-categorized into electrochemical double-layer capacitors, pseudo-capacitors or redox pseudo-capacitors, and hybrid capacitors.^[17]

In electrochemical double-layer capacitors, the energy is stored at the electrode/electrolyte interface, *i.e.* within the electrochemical double-layer (Helmholtz layer), as cations and anions within the electrolyte accumulate at the electrode surface to compensate the oppositely charged electrodes.^[18] To increase capacitance, typically electrodes with a high surface area are used, most commonly porous carbons.^[17,18] Both aqueous solutions, which provide higher capacitance, and organic solvents, which endure higher voltages, can be used as electrolytes.

In pseudo-capacitors, or redox supercapacitors, fast, reversible redox reactions take place at the electrode surface.^[17,18] Conducting polymers (*e.g.* polyanilines, polypyrroles, polythiophenes) and metal oxides (*e.g.* MnO₂, RuO₂, Fe₃O₄) have been reported as electrode materials.

Electrolyte cations (e.g. alkali metal cations), adsorb on the electrode surface; moreover, H^+ can be incorporated into the electrode structure^[17]:



Hybrid capacitors combine a capacitive or pseudo-capacitive electrode as described above, with a battery electrode, which will be described below. The idea behind this combination is to combine the advantages of the working principles of batteries and supercapacitors.^[17]

In general capacitors have the advantage that they can provide energy fast (*i.e.* power density is high), while the amount of energy that is delivered (*i.e.* energy density) is low, which limits the application of this technology.

2.3 Batteries

2.3.1 Overview

In batteries, energy is stored in the electrode materials, and released during discharge by electrochemical redox reactions of the electrode material. This means that, in contrast to fuel cells and some capacitors, the electrode material actively takes part in the energy conversion process (*i.e.* is reduced and oxidised) and is therefore consumed/replenished during discharge/charge processes. Similar to fuel cells, cathode and anode are separated by an ionically conductive but electrically insulating electrolyte, and connected via an external circuit. By convention, the negative electrode is typically referred to as anode, and the positive electrode as cathode. Ions released during the respective electrochemical reactions migrate through the electrolyte from one electrode to the other. Simultaneously the released electrons migrate through the external circuit, where they can be used to power electronic devices. As the underlying reactions are reactions of the electrode material, the energy that can be provided by a battery is limited by the amount that can be stored in the electrode material. Thus, in secondary batteries, which are defined by their ability to be recharged, the ability to supply energy needs to be regenerated after discharge processes by charging the battery. This is achieved by forcing a current from an external source through the battery in the opposite direction of the current flow during discharge to reverse the chemical reactions. Subsequently, the regenerated electrode material can again be used to provide electrical current. This process of charging/discharging the battery is known as cycling. The chemistry, on which these processes are based, can be very diverse.^[19] In the following, different principles of charge storage mechanisms for insertion-type batteries are outlined.

2.3.2 Charge Storage Mechanisms

In general, the charge carriers (e.g. Li^+ in LIBs or Na^+ in NIBs) move between two electrodes; the direction depends on whether the battery is being charged (cathode to anode) or discharged (anode to cathode). Typically, three different storage mechanisms are identified, based on the structural changes which they entail: insertion, alloying, and conversion reactions.^[20,21]

Insertion-type batteries, which are the basis of this work, have dominated for the past decades in the field of LIBs, and now also play a major part in the research and development (R&D) of rechargeable room temperature NIBs. These systems became known as 'rocking chair' electrodes^[2]. A schematic of the working principle of a NIB, based on some individually investigated materials presented in this work (anode: $\text{Na}_6\text{V}_{10}\text{O}_{28}$ ^[22], cathode: $\text{Na}_{2+x}\text{V}_6\text{O}_{16}$ ^[23]) can be seen in Figure 2.

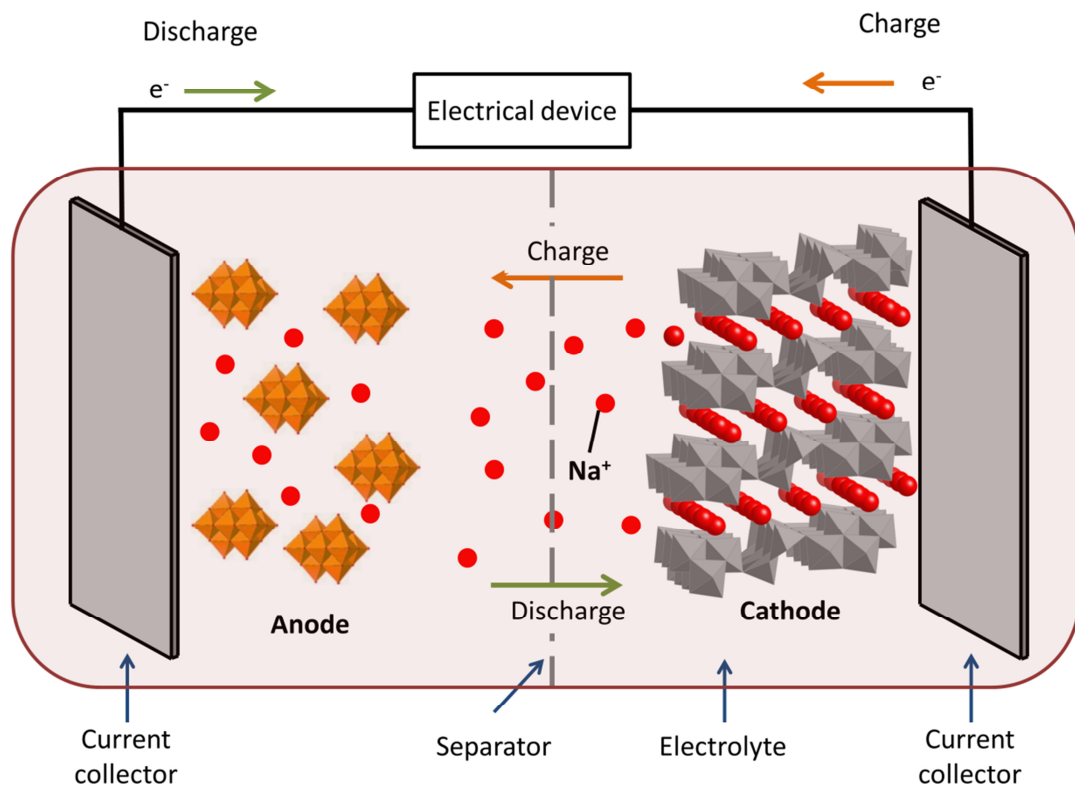


Figure 2. Schematic of a sodium-ion battery (anode: $\text{Na}_6[\text{V}_{10}\text{O}_{28}]$ ^[22], cathode: $\text{Na}_{2.5}\text{V}_6\text{O}_{16}$ ^[23]).

The charge carrier ion Na^+ intercalates into/from a host structure - one electrode acts as a ion sink, the other one as a source. The incorporation of the charge carrier into the host lattice can either be in form of a solid solution, *i.e.* homogeneous inclusion into the host lattice, or lead to phase transitions, *i.e.* heterogeneous inclusion. While in general the advantage of this type of storage mechanism is the absence of major structural changes, the disadvantage is limited capacity. In the discharged state, Na^+ or Li^+ occupies defined lattice sites in the

crystal structure of the cathode material. Upon charging, Na^+ or Li^+ vacate these structural sites on the cathode side, migrate through the electrolyte, and insert into the material on the anode side. Simultaneously, the redox centre in the cathode, which is vanadium for the case depicted in Figure 2, is oxidised, and the released electron moves through the external electrical circuit to create an electrical current, to the anode side, where it induces the corresponding reduction process.

Alloying-type electrode materials, which are typically anodes, react with the charge carrier to form an alloy. Typical materials include tin, silicon, antimony, or their mixtures. Even though they hold immense promises with regard to capacity, their huge disadvantage is the significant volume changes they undergo during the alloying – dealloying reactions, which can lead to a disintegration of the electrode and detachment of the active material from the current collector. Thus, some of the active material is lost for the relevant electrochemical processes, so that capacity considerably decreases during cycling. Strategies to alleviate these problems include limiting the volume expansion, or buffering the volume changes by embedding the active material into a matrix, such as amorphous carbon.^[24]

In conversion-type batteries, the charge carrier reacts with a host compound, typically a transition metal compound (*i.e.* oxide, sulphide, fluoride, *etc.*). A matrix of the respective lithium or sodium compound (oxide, sulphide, *etc.*) is formed, together with the transition metal in its reduced form. These metallic nanoparticles are then embedded in the matrix of the alkali metal compound formed during cycling.

Both batteries with aqueous and organic electrolytes are being researched. Aqueous systems are advantageous with regard to safety and cost, whereas higher potentials can be attained with organic electrolytes. Organic electrolytes typically consist of organic carbonates, *i.e.* propylene carbonate, dimethyl carbonate, diethyl carbonate, ethylene carbonate, or their mixtures. Ethylene carbonate is added to help in the formation of a solid electrolyte interphase (SEI). It decomposes below approximately 0.6 V vs. $\text{Na}|\text{Na}^+$ to form various salts, which deposit on the anode. This SEI, which acts as a protective layer, is crucial for the reversibility of the reaction by preventing unwanted side reactions and co-intercalation, *i.e.* intercalation of solvent molecules, which would lead to detrimental structural changes.

3 Sodium-Ion Batteries

Even though research on the intercalation of Li^+ and Na^+ started out more or less in parallel, lithium-insertion materials were the focus of research for many years, while sodium-insertion materials were largely neglected.^[25] One of the reasons for this was the larger ionic radius of the Na-ion (1.02 Å) as compared to the Li-ion (0.76 Å), as well as its higher atomic mass, which is 23.00 u for Na^+ and 6.94 u for Li^+ . As a consequence, the energy density, both volumetric and gravimetric, is, *ceteris paribus*, lower for Na-based systems than for Li-based systems. The second reason for the lack of interest in sodium-ion systems was that, even though suitable cathode insertion materials were available, suitable anode materials were scarce. Only in 1993, Doeff *et al.* reported on carbon with good insertion properties for Na-ions, and described Na-Pb alloys as a negative electrode material in a NIB full-cell (*i.e.* with a material other than Na metal as the opposite electrode, here: Na_xCoO_2).^[26,27] However, energy density of these systems could not compete with graphite as a LIB anode.^[25] Interest in this field of research rather stagnated until the early 2000's, when several breakthroughs were achieved. In 2000, Stevens and Dahn showed that hard carbon exhibits capacities of up to 300 mA h g⁻¹ and holds promise as a viable anode material for NIBs.^[28,29] On the cathode side, layered transition metal oxides, $\text{Na}_x\text{MeO}_{2+z}$ (Me: transition metal) showed promising results with respect to high-performing, cost-efficient systems. Concurrently, the number of publications in this field significantly increased as well (Figure 1).

3.1 The Case for Sodium-Ion Batteries

As the predominant battery technology is LIBs, it naturally serves as the standard against which competing technologies are compared. Thus, in this chapter, advantages and disadvantages of sodium-ion based systems will be portrayed briefly with the lithium-ion technology as the benchmark.

As mentioned before, NIBs are at a disadvantage with regard to gravimetric and volumetric capacities due to the higher atomic weight and larger ionic radius of sodium vs. lithium. When comparing not only the charge carrier, but the electrode materials, however, this difference is decreased. While Na^+ is 3.3 times greater in mass and 34% larger than Li^+ as per the Shannon ionic radii, LiCoO_2 has a reversible gravimetric capacity which is only 14% higher than that of NaCoO_2 .^[30] As Na^+ is only one constituent in this structure, it accounts for only 20% of its mass, which decreases the negative influence of the mass of the Na-ion. This effect is decreased further when not only the active material, but the complete electrode mass loading, or even the total battery mass is considered. Moreover, while copper is used as anodic current collector in LIBs, in NIBs the lighter and cheaper Al can be used as Na (unlike Li) does not alloy with Al.^[31-35] As far as volumetric capacities are concerned, the trend is similar. Even though the volume difference of the molar volume is significant for the respective metals (39.3 Å³ per Na atom vs. 21.3 Å³ per

Li atom), the difference between the molar volume per formula unit of LiCoO_2 , and NaCoO_2 , respectively, is only 5 \AA^3 (LiCoO_2 : 32.3 \AA^3 , NaCoO_2 : 37.3 \AA^3).^[25] Therefore, even though metallic Na has a significantly higher mass and volume than metallic lithium, these factors carry less weight when the respective crystal structures are considered.

Apart from capacities, the attainable voltage for Na^+ -based system is also considered to be a disadvantage of NIBs when compared to LIBs. The overall voltage of a battery is defined as the difference of the electrochemical potential of the reactions occurring on the cathode side and the anode side, respectively. Consequently, to increase battery voltage, research directed towards finding and establishing high-voltage batteries mainly aims at finding and understanding cathode materials that undergo reactions with Li^+ or Na^+ at high potentials. Naturally, this approach is limited by the electrochemical stability of the other battery components at elevated potentials, particularly the electrolyte. The other possible research direction, *i.e.* finding an anode with a low reaction potential, is limited by the fact that below a potential of 0 V vs. $\text{Li}|\text{Li}^+$ or $\text{Na}|\text{Na}^+$, respectively, (neglecting overpotentials), reduction of the respective alkali ions to metal is favoured over insertion, alloying, or similar reactions. This limit is inherently higher for the redox couple $\text{Na}|\text{Na}^+$ than for $\text{Li}|\text{Li}^+$. The standard electrode potential (*i.e.* for reactions occurring at 298.15 K and an effective concentration of 1 mol L^{-1} for each species in aqueous solution, measured vs. a standard hydrogen electrode) is -3.04 V for the redox couple $\text{Li}|\text{Li}^+$, and -2.71 V for the redox couple $\text{Na}|\text{Na}^+$.^[30] Thus, the reaction of Na to Na^+ occurs at a potential that is 0.33 V higher, which inherently decreases the operating potential of NIBs. The significance of these absolute numbers for battery applications is limited as these numbers are based on standard conditions in an aqueous system. In batteries, however, reactions do not only typically occur in organic solvents, but also the 'reaction site' is usually heterogeneous and ill-defined: apart from the active material which takes part in the reaction, there are several constituents, such as the activated carbon, binder or the SEI layer, which do not actively take part in the relevant electrochemical reactions, but could influence it. However, even though the absolute numbers cannot be quantitatively used to explain and forecast differences between NIBs and LIBs, the qualitative conclusion is that the lower limit for NIB anode materials is higher than for LIBs, which limits the operation voltage of potential batteries.

As a consequence of these two factors, battery capacity and battery voltage, energy density for NIBs is lower than for LIBs for similar chemistries. Energy density is defined as the amount of energy that is stored per mass (gravimetric energy density) or volume (volumetric energy density). As both voltage and capacity provided by a system contribute to its energy density, shortcomings in both factors lead to a decrease in energy density.

The comparisons described above are based on comparing the Li- and Na-analogues of the same chemistries, *i.e.* similar materials whose main difference is that a host structure is filled with either Na-ions or Li-ions. However, for NIB to become a competitive technology, the focus should not only be on materials that are isostructural to LIB materials, but also be extended to different structures. One of the advantages of NIB is that the structural chemistry of Na-compounds is very

diverse, which also means that more structural variations are obtainable for NIB materials than for LIB materials. This is also exploited for LIBs by synthesizing sodium-containing compounds first, and performing an ion-exchange afterwards to obtain LIB insertion materials.^[36–38] This variety is known for polyanionic compounds, but also for metal oxide materials, for which the flexibility for material design is enhanced by the increased gap between the ionic radius of Na^+ on the one hand, and the transition metal ion Me^{3+} on the other hand.^[30]

A further potential advantage of Na-ions as a charge carrier in batteries is that Na^+ -transport in the system can be favourable over Li^+ -transport with regard to kinetic properties. As described in detail above, during the charge/discharge process, the charge carrier ion is transported in the electrolyte, transferred through the electrolyte/electrode interface, and then again transported within the active material. If kinetic limitations from transport in the electrolyte and in the active material are eliminated by optimised set-ups, such as the utilization of thin film electrode materials, optimised particle size and morphology, and electrolytes with high ionic conductivities are used, the transfer at the electrolyte/electrode interface can become the rate determining step for the ion transfer, and therefore for the occurring reactions as a whole.^[39] It was calculated that Na^+ , which is a weaker Lewis acid than Li^+ , has a significantly lower de-solvation energy than Li^+ for a variety of organic solvents, including the carbonates that are typically used for battery electrolytes, such as propylene carbonate, ethylene carbonate, or diethylene carbonate.^[39] As a consequence, the energy that is required for the respective ions to be stripped of their solvation shell is smaller for Na^+ , which can result in enhanced kinetics for this particular step.^[40,41]

Furthermore, it has been shown for propylene carbonate and γ -butyrolactone that the ion transport characteristics of Na-ion based electrolytes are advantageous as compared to Li-ion based electrolytes.^[42] As conductivity is higher and viscosity is lower for Na^+ -based electrolytes, Na-ion transport in Na-based systems is kinetically favoured over Li-ion transport in Li-based systems.

Moreover, rather counter-intuitive considering the larger size of the Na-ions, diffusion of Na^+ within certain active materials can also be faster than for Li^+ in the respective Li-analogue. Ong et al., e.g. showed that the diffusion barrier for Na^+ in layered NaCoO_2 is lower than the diffusion barrier for Li^+ in LiCoO_2 , whereas the diffusion barrier for Na^+ is significantly higher than for Li^+ in olivine-type materials.^[43] Consequently, for certain types of materials, ion transport within the electrode is favourable for NIBs over LIBs materials, which can be an additional advantage with regard to kinetics.

Apart from the scientific arguments presented above, the most-cited arguments for the development of NIBs are rather pragmatic and application-oriented: abundance, availability and cost. Na has a crustal abundance of $\sim 26,000$ ppm, whereas abundance for Li is only ~ 10 .^[44] Numbers slightly vary between different sources, but the crustal abundance of sodium is approximately 25,000 ppm, whereas for lithium it is approximately 17 ppm. Furthermore, global distribution is also an important factor. While lithium resources are highly concentrated in South America, mainly Bolivia, Chile, and Argentina, sodium resources are more widely

distributed. Being highly concentrated in one region of the world means that the price of the resource is intertwined with the political and economic climate of the region. Thus, switching from lithium- to sodium-based systems can generate a more reliable resource base. In addition, as mentioned before, switching from Cu to Al as the anodic current collector constitutes an additional cost advantage.

3.2 Materials for Sodium-Ion Batteries – Current Status

In recent years, activity in the field of NIBs has increased tremendously. A variety of new material (classes) is being reported, and understanding of known systems progresses fast. In the following chapter, a short non-exhaustive overview of the main material classes that are being researched is presented. For a more in-depth reading, several excellent reviews are available.^[25,34,45–49]

3.2.1 Cathode Materials

Oxides. Layered sodium transition-metal oxides are the most extensively investigated materials for NIBs. These materials appear interesting as insertion materials for NIB cathodes due to their relatively high redox potential and energy density.^[34] In addition, as a multitude of transition metals can be incorporated into the structure in various ratios, the advantages of the respective elements can be combined. For example, Mn and Fe are often employed due to their abundance, low cost, and environmental friendliness, whereas Co is incorporated as it increases cycling stability. The structure typically consists of layers of edge-sharing MeO_6 -octahedra (Me: transition metal), with Na^+ located between these layers. These sheets of MeO_6 -octahedra can be stacked along the c-axis in a variety of ways, giving rise to different classes of materials, for which a classification has been proposed by Delmas *et al.*^[50] In P-type materials, Na^+ is coordinated by oxygen prismatically, whereas in O-type materials the coordination is octahedral. The letters are annotated by the number of MeO_6 -layers that need to be depicted in a unit cell to account for the different stacking of the layers. The unit cell of P2-type materials, e.g. consists of two sheets of MeO_6 -octahedra, and Na-ions which are prismatically coordinated by oxygen between these layers. One of the most promising materials is P2- $\text{Na}_{2/3}\text{Mn}_{1/2}\text{Fe}_{1/2}\text{O}_2$.^[32] This cathode material, which is composed of the cheap Mn and Fe, shows a high capacity of 190 mA h g^{-1} at a C-rate of C/20 (C-rate is explained in Chapter 4.6.3) and an average voltage of 2.75 vs. Na metal and an energy density of $\sim 520 \text{ W h kg}^{-1}$. This value is comparable to the 530 W h kg^{-1} delivered by LiFePO_4 in LIBs. In different studies, Mg has been incorporated into the P2-layered oxide structure resulting in promising cyclability.^[34,51–53] For example, Bruce and co-workers reported that P2- $\text{Na}_{0.67}\text{Mn}_{0.8}\text{Mg}_{0.2}\text{O}_2$ provides a capacity of 150 mA h g^{-1} between 1.5 V – 4.0 V with a capacity retention of 96% after 25 cycles.^[52] However, despite its popularity, there are several drawbacks to this material class. Sensitivity to moisture restricts handling of these materials in air and raises concerns with regard to material storage and reproducibility of results. In

addition, many layered oxides are Na^+ -deficient, so that the capacity of full-cells based on this material class is limited if the anodic material does not contribute to the Na content.^[25] Vanadium-based materials will be elaborated on in more detail in Chapter 3.3.

Polyanions. Unlike the olivine-type LiFePO_4 , which is a prominent material in LIBs, the thermodynamically stable structure of the Na-analogue, NaFePO_4 , is the maricite structure^[25,54], which provides insufficient capacities for use as NIB cathode^[55,56]. Even though the electrochemically active olivine-version with a capacity of 125 mA h g^{-1} at an average voltage of $\sim 2.7 \text{ V}$ can be obtained from LiFePO_4 via an ion exchange^[54,57], kinetics are sluggish due to large volumetric changes of the material during cycling.^[25,34,46]

NASICON (Na^+ Super Ionic Conductor) materials, were initially researched as solid electrolytes, but have emerged as a promising material class for insertion electrodes. Thus, a variety of materials with the general formula $\text{A}_x\text{Me}_2(\text{PO}_4)_3$ (A: Li, Na; Me: V, Fe, Mn, Co; X: P, S, W) has been studied as insertion hosts.^[49] They consist of corner-sharing MeO_6 and XO_4 polyhedra, which form tunnels that ensure fast Na^+ -transport.^[34] One promising material is $\text{Na}_3\text{V}_2(\text{PO}_4)_3$, which is based on the $\text{V}^{4+}/\text{V}^{3+}$ and $\text{V}^{3+}/\text{V}^{2+}$ redox couples, respectively.^[34,48] One advantage of this class of materials is cycling stability as recently reported. However, capacities in interesting voltage regions are low. For example, a recent study reported a capacity of 113 mA h g^{-1} at $\sim 3.4 \text{ V}$ at a C-rate of 1.^[58] In addition, electronic conductivity is rather low.^[49] Even though this can be improved by carbon coating, the resulting low coulomb efficiency in conventional electrolytes reported in some studies poses further challenges.^[59,60] Attempts at replacing V by the cheaper Fe have been made, yet both capacity and the potential of the reaction are insufficient for practical applications (45 mA h g^{-1} cell voltage $\sim 2.5 \text{ V}$).^[48,61] Incorporating the electronegative fluoride-ion, F^- , into the polyanionic framework, elevates the potential of the redox reaction in the material.^[34] $\text{Na}_3\text{V}_2(\text{PO}_4)_2\text{F}_3$, for example, has an average Na^+ insertion potential of $\sim 3.95 \text{ V}$ and a capacity of $\sim 110 \text{ mA h g}^{-1}$ (C-rate of C/10).^[62]

Several sulphates have been explored as NIB cathodes as well. One of those materials, $\text{Na}_2\text{Fe}_2(\text{SO}_4)_3$ was reported to have the highest operating potential of all Fe compounds to date, with a redox potential of approximately 3.8 V along with fast kinetics.^[63] However, also in this case capacity is rather low with 100 mA h g^{-1} (C/20).

Prussian Blue Analogues (PBAs). As the insertion of Na^+ is accompanied by a larger volume expansion compared to Li^+ due to the larger ionic radius of the Na-ion, structures that flexibly accommodate Na-ions appear promising. Thus, PBAs, which consist of a relatively open framework have been researched as insertion hosts. Goodenough *et al.* first reported on the hexacyanoferrate class, $\text{KMeFe}(\text{CN})_6$ (Me: Mn, Fe, Co, Ni, Zn), which can be synthesised easily and at low cost. The best capacity ($\sim 100 \text{ mA h g}^{-1}$ with two plateaus at 3.6 V and 2.9 V , respectively) is

achieved with the Fe compound.^[64] Even though capacity could be increased to 134 mA h g⁻¹ in Na_{2-x}MnFe(CN)₆ (C/20, between 2.0 V – 4.2 V, 120 mA h g⁻¹ after 30 cycles)^[65], or 120 mA h g⁻¹ in Fe⁺³Fe⁺³(CN)₆, (C/2, 2.0 V – 4.0 V, 87% retention after 500 cycles)^[66], low capacity remained a disadvantage for these systems until recently. In 2014, however, the Cui group demonstrated a PBA (Na₂Mn^{II}[Mn^{II}(CN)₆]) with a capacity of 209 mA h g⁻¹ (C/5) at an average voltage of 2.65 V, which might be a promising basis for future NIB cathodes.^[67]

Organic Electrode Materials. Organic materials have the advantage that they can be obtained from renewable sources and do not contain environmentally problematic or toxic metals. However, the disadvantage of this material class is the high solubility of the active electrode material in organic liquid electrolytes, sluggish kinetics, poor thermal stability, and poor electronic conductivity.^[48,68] One material class that is researched due to its high redox centre and flexible host matrix is p-type electroactive polymers.^[46] For example, aniline-nitroaniline copolymer with a specific capacity of 180 mA h g⁻¹ (at 50 mA g⁻¹) at an average potential of approximately 3.2 V was reported.^[69] Several strategies are investigated to suppress the dissolution of the active material into the electrolyte, such as the encapsulation of the respective material in mesoporous carbon and optimisation of the electrolyte. Guo *et al.* recently demonstrated this strategy for 9,10-anthraquinone, which showed a capacity retention of 88% after 50 cycles (0.2 C, initial capacity: 214 mA h g⁻¹ between 1.2 V – 2.8 V).^[70] Sakaushi *et al.* reported on a bipolar porous organic electrode, consisting of aromatic benzene and triazine rings in a two-dimensional structure, as a new material platform for the development of NIB cathodes.^[71] This system delivers a discharge capacity of approximately 90 mA h g⁻¹ at 1 mA g⁻¹ (1.3 V – 4.1 V) with a capacity retention of 80% after 7000 cycles. However, the rather low average discharge potential and high self-discharge remain a problem.

3.2.2 Anode Materials

Carbon-Based Materials. Na⁺ unlike Li⁺, does not intercalate, to a substantial extent, reversibly into graphite.^[72] This finding is attributed to thermodynamic reasons.^[73,74] Hard (*i.e.* disordered) carbons, however, have been shown to provide good performance in terms of capacity and stability. Stevens and Dahn reported capacities close to 300 mA h g⁻¹ between 0 V – 2 V (C/80)^[28,29] and Komaba *et al.* later reported ~ 240 mA h g⁻¹ (at 25 mA g⁻¹) with ~ 10% capacity loss after 100 cycles between 0 V – 2 V with an increase of stability and decrease of capacity for higher cut-off voltages^[31]. Thus, hard carbon has become the most-studied anode material for NIBs.^[34] Nevertheless, this material class raises safety concerns due to its low insertion potential, which could lead to Na-plating and the inherent safety hazards of metallic Na.^[34] Various other modifications have been proposed, such as hollow carbon nanospheres (~ 200 mA h g⁻¹ at 50 mA g⁻¹ between 0 V – 3 V)^[31], nanowires (~ 250 mA h g⁻¹ at 50 mA g⁻¹ between 0 V – 1.2 V)^[75], and N-doped porous carbon nanosheets (~ 350 mA h g⁻¹ at 50 mA g⁻¹ between 0 V – 3 V)^[76]

which, however, suffer from low coulombic efficiencies and/or low cyclability. Electrolyte decomposition, and thus cyclability, remains a problem, which requires increased understanding of the formation of a SEI in NIBs.^[25,46,49] In order to enable reversible Na⁺-insertion between graphite layers, various methodologies have been employed. For example, expanded graphite with an increased distance between the graphene layers has been shown to be a promising anode material with capacities of up to 180 mA h g⁻¹ at 100 mA g⁻¹ between 0 V – 2 V and promising capacity retention (70% after 2000 cycles).^[77] The insertion potential for this material is higher than for hard carbons, which constitutes a safety advantage to the detriment of energy density.

Oxides and Phosphates. Various oxide materials have been proposed as NIB anodes owing to their good safety characteristics and high volumetric energy densities.^[34] However, application of many of these materials as anodes seems questionable due to their high insertion potential. NaTi₂(PO₄)₃ (NASICON structure), for example, inserts Na⁺ at 2.1 V and at 0.8 V vs. Na|Na⁺, respectively.^[78] Later, an additional plateau at 0.4 V based on the Ti^{+III}/Ti^{+II} redox couple contributing ~60 mA h g⁻¹ (at C/25) was reported.^[79] Titanates appear more promising. Na⁺-insertion into Na₂Ti₃O₇ was shown to occur at a potential of ~0.3 V vs. Na|Na⁺ with a capacity of ~220 mA h g⁻¹ initially and ~ 180 mA h g⁻¹ after 5 cycles.^[80] However, this was achieved at a slow C-rate of C/25 and required a carbon ratio of 30% due to the poor electronic conductivity of titanates,. In addition, Na⁺-insertion into various polymorphs of TiO₂ has been investigated.^[25,46,48,49] Achieved capacities are as high as 150 mA h g⁻¹ (at 50 mA g⁻¹, 0.01 V – 2.50 V) for anatase TiO₂, but certain problems such as low initial coulombic efficiencies or the lack of a defined plateau during Na⁺-insertion remain.^[81] TiO₂(B) nanotubes deliver a high initial capacity of 240 mA h g⁻¹ (50 mA g⁻¹, 0.75 V – 3.00 V) in the initial cycles, but suffer from low cyclability^[82]. Based on the promising characteristics of P2-type layered oxides for cathode materials, the same structure was also tested as anode. Wang et al. reported on the impressive cyclability of P2-Na_{0.66}[Li_{0.22}Ti_{0.78}]O₂.^[83] At 2C, this material shows a capacity retention of 75% over 1200 cycles at an average voltage of 0.75 V, although the initial capacity was rather low (~75 mA h g⁻¹).

Alloys. High capacities at rather low potentials can be achieved with alloys, which makes them an interesting option for NIB anodes. However, considerable volume changes of several hundred percent and the resulting strain remain a significant problem for long-term cycling. Interestingly, when compared to LIB anodes, for which there is a similar trade-off for alloying materials (*i.e.* capacity vs. cyclability), the volumetric energy density of alloys in NIBs is approximately only half the energy density achieved for LIBs owing to the larger size of the Na-ions.^[84] Strategies to alleviate these volume changes include controlling the microstructure of the electrode or embedding the anode in a matrix (*e.g.* carbon) to buffer volume changes. Even though results are promising, these approaches significantly add to the complexity and therefore cost of material design.^[34] The most extensively researched alloying materials are probably Sn and Sb.^[25,85–88] For example, for Sn,

a reversible capacity of 500 mA h g^{-1} over 20 cycles (50 mA g^{-1} , $0.0 \text{ V} - 0.8 \text{ V}$) was obtained^[89], and for micrometric Sb a reversible capacity of $\sim 580 \text{ mA h g}^{-1}$ ($C/2$, $0.02 \text{ V} - 1.50 \text{ V}$) over 160 cycles was observed^[88].

3.3 Vanadium Oxides in Sodium-Ion Batteries – Motivation and Approaches

One material class that has been studied extensively in LIBs is vanadium oxides owing to their promising capacities. Hence, as the underlying processes are similar for LIBs and NIBs, vanadium oxides are materials that seem worthwhile exploring as NIB electrodes as well. The interest in vanadium oxides stems from several advantages.

The underlying basis of insertion-type NIB materials is the reversible insertion of Na-ions into the structure of an electrode material during discharge and the de-insertion during the charge process. Thus, open structures that facilitate this migration are desired. Moreover, as the insertion of Na^+ into the crystal structure is accompanied by a concurrent reduction of a redox centre in the crystal structure, the number of electrons the redox centre can take up determines the capacity of the material. Vanadium is known for its variety of oxidation states, which makes it a promising redox centre in electrochemical reactions. One prominent representative of this material class is vanadium pentoxide, V_2O_5 . From a structural point of view, orthorhombic V_2O_5 consists of layer-forming VO_5 square pyramids; charge carrier ions, such as Li^+ or Na^+ can (de-)insert into (from) this layers. First studies on V_2O_5 as an insertion host for Na^+ were published by Skaarup and co-workers in the 1980's.^[90,91] In the following years, probably because of the focus on research in Li-insertion materials as described in Chapter 1, interest in Na^+ -insertion subsided. Recently, however, V_2O_5 has been revisited as an intercalation host for Na-ions, and promising performance has been reported.^[92] Therefore, further investigations on vanadium oxides as insertion hosts for Na^+ seem promising. A related structure is monoclinic AV_3O_8 , or the respective supercell $\text{A}_2\text{V}_6\text{O}_{16}$, (A: Li^+ , Na^+ , K^+ , NH_4^+). Due to high attainable capacities, it has been considered as an insertion host for a variety of cations, including Li^+ , Na^+ , or Mg^{2+} . These structures also consist of layer-forming VO_x -polyhedra. However, the space between the layers can be occupied by different ions (denoted A), which can help in keeping the structure open and receptive for the insertion of charge carriers.

As already mentioned (Chapter 1), interest in Na^+ -insertion hosts in general was very limited for a long time, and vanadium oxides were no exception. Thus, apart from very few initial studies^[90–94], Na^+ -insertion into (alkali) vanadium oxides and related structures did not receive much attention until very recently, when some studies on this material class were reported.^[95–98] As this material class was neglected for a long time the suitability of many materials as NIB electrode has not been tested. Particularly, the class of vanadate materials $\text{A}_2\text{V}_6\text{O}_{16}$ (A: alkali ion), has not been thoroughly studied. Consequently, concomitant with the lack of knowledge about suitable materials, an in-depth understanding of Na^+ -insertion into V-based

materials is also lacking. In particular, the mechanism of Na⁺-insertion into these materials is of interest so that processes that are detrimental to electrochemical performance such as cycling stability can be identified and, ideally, mitigated.

In order to close this gap in literature, several V-based materials were investigated in NIBs and the results are presented in Chapter 5. Their performances as electrode materials are demonstrated and the mechanism of Na⁺-insertion is investigated. Specifically, in Chapter 5.1, Na_{2.55}V₆O₁₆ (NVO) is shown to deliver high capacities in Na-ion half-cells. Cycling stability, however, is low. Therefore, subsequent work focussed on identifying the causes of this capacity decrease. As structural changes are a common cause of decrease in capacity, structural processes were monitored during cycling using *in operando* X-ray diffraction (XRD). For this purpose, a novel electrochemical cell was constructed for *in operando* XRD in reflection mode. The main advantage of this cell, which is described in detail in Chapter 5.2, is excellent signal quality due to the use of thin (6 μm) Al foil. In addition, employing Al instead of the often-used beryllium decreases cost and toxicity problems with regard to toxicity. In further studies, in addition to NVO, the isostructural Li_{2.55}V₆O₁₆ (LVO) and K_{1.8}V₆O₁₆ (KVO), were investigated to elucidate effects of the alkali ion (Chapter 5.3). *In operando* synchrotron XRD in transmission mode and laboratory scale *in operando* XRD with the developed cell were combined to garner a detailed understanding of structural processes during the insertion and extraction of Na⁺ into/from the vanadate structure. A strong link was found between electrochemical and structural reversibility. Interestingly, while the performance of KVO fell short of NVO, capacity retention over the course of 100 cycles was increased for LVO even though Li⁺ in the structure was mostly replaced by Na⁺. As found by testing a novel ionic liquid (IL) based electrolyte, the electrolyte decomposition does not seem to play a major role for capacity fading (Chapter 5.5). In order to circumvent the insertion of Na-ions into the long-range crystal structure of the vanadate materials, a representative of a different material class, polyoxometalates (POMs), was investigated for the first time in a NIB. The POM Na₆[V₁₀O₂₈] consists of discrete [V₁₀O₂₈]⁶⁻ polyanions with voids between the individual anionic clusters. Thus, Na⁺ can insert between these polyanions without disrupting the crystal structure. Due to their unique structural properties, the insertion of Na⁺ does not result in structural deterioration. The potential range of Na⁺-insertion is in line with anode materials, and cycling stability of Na₆[V₁₀O₂₈] is significantly improved over the A₂V₆O₁₆ material class.

The results of these investigations are presented in Chapter 5 after a description of the methods employed in this work.

4 Experimental Methods

The results presented in this thesis range from material characterisation, to electrochemical testing and investigation of structural processes during cycling. Thus, various techniques were employed. The most important methods are briefly outlined in this chapter. In accordance with the typical workstream, methods employed for physico-chemical characterisation are portrayed first, followed by electrochemical methods.

4.1 Electron Microscopy^[99–103]

Microscopes are used to image and characterise materials at very small scales. The most common type are optical microscopes, which use a series of lenses and mirrors to influence the path of light to generate a magnified image. The resolution of these light microscopes is, however, limited by the wavelength of the light they use. This limit can be alleviated by changing from light to charged particles, *i.e.* ions or electrons. In electron microscopes, the sample is exposed to a beam of electrons, whose pathway is controlled by the use of magnetic lenses. As the wavelength of electrons (e^- with an energy of 2 eV: 0.87 nm) is significantly smaller than the wavelength of light in the UV-VIS spectrum (~200 – 700 nm), the resolution of electron microscopes can be significantly enhanced as compared to optical microscopes. The information that can be obtained is based on the interaction (or the lack thereof) of the incident electron beam and the sample matter. When the sample is irradiated with an electron beam, there are two ways in which the electrons can interact with the sample:

- i) **Elastic interaction:** Electrons interact with matter without the transfer of energy, *i.e.* the energy of the electron upon leaving the sample is the same as the energy of the electron upon entering the sample. Elastic scattering occurs when the interaction is based on Coulomb interaction, *i.e.* the electron is deflected from its path due to the interaction with the positive potential of the nuclei in the sample. Naturally, if the electrons do not interact with the sample, no energy is transferred either.
- ii) **Inelastic interaction:** Energy is transferred from the electrons to the sample, leading to a reduction of the energy of the electrons. The transferred energy can lead to an emission of various forms of energy, such as secondary electrons, Auger electrons, and X-rays. These can be detected and are employed for certain types of microscopy.

Scanning Electron Microscopy (SEM) is mainly based on the inelastic interaction of electrons and matter, whereas for Transmission Electron Microscopy (TEM) elastic interaction is most significant.

Scanning Electron Microscopy

SEM is mainly based on the detection of secondary electrons, *i.e.* electrons which have been ejected from the sample (Figure 3a). For SEM, the relevant electrons are slow secondary electrons, *i.e.* electrons that occupy the valence or conduction band of the element to be measured. Upon irradiation with the electron beam, energy is transferred from the incident electron to the electron in the element's shell. This results in an ejection of this electron, which can be detected and provides the signal for the SEM image.

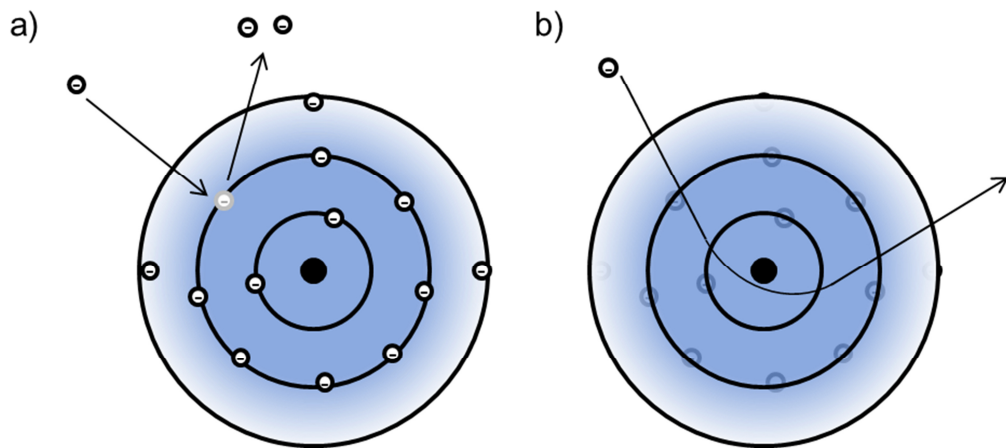


Figure 3. a) Secondary electrons, b) backscattered electrons.

Another information source for SEM is backscattered electrons (Figure 3b). These are the results of elastic scattering between electrons and matter – due to strong interaction, mainly with elements with high atomic numbers, incident electrons are deflected from their path such that they are scattered backwards. Measuring SEM in this mode can mainly be used to enhance the contrast between different elements, particularly between elements with a significant difference in their respective atomic numbers.

Transmission Electron Microscopy

TEM is based on the penetration of a sample with electrons. As the electrons are detected after passing through the sample, thin (usually 10 nm – 1 μm) samples are required. When a sample is irradiated with electrons, elastic scattering can result in a deflection of the electrons from their initial path due to the Coulomb interaction with the positive charges of the nuclei of the sample. Consequently, the chances for this interaction to occur increases with the number of positive charges of the nuclei, *i.e.* the atomic number, and the number of nuclei in the way of the electron, *i.e.* the sample thickness. The electrons which are not deflected are called the 'direct beam'. The number of electrons incident on a detector placed behind the sample varies as a consequence of the effect of the i)

mass of the respective element(s) and ii) sample thickness. Due to this effect, which is called mass-thickness contrast, heavier elements and thicker samples appear darker in a transmission electron microscope (Figure 4). In Bright Field Transmission Electron Microscopy (BF-TEM) an aperture is used to block scattered electrons, and only the direct beam is used for imaging.

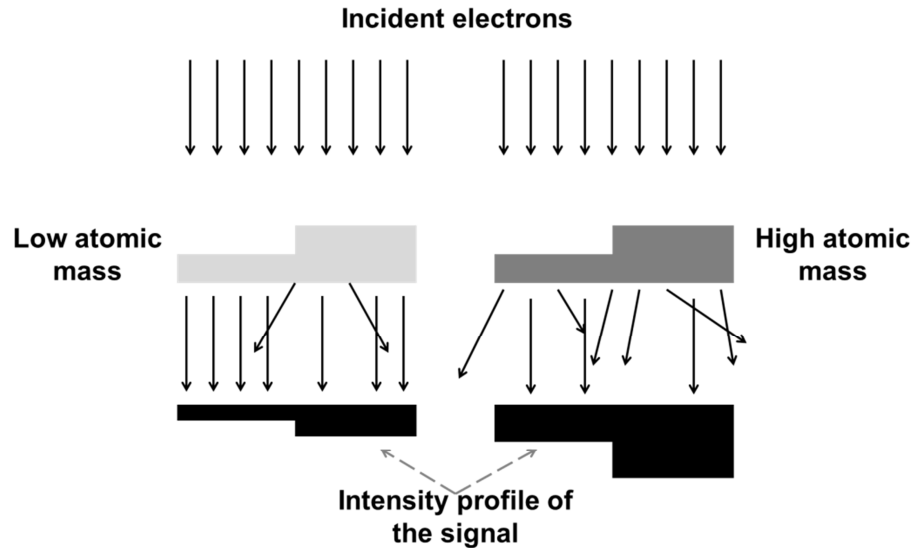


Figure 4. Generation of contrast due to differences in thickness and atomic masses.

In addition to the information that can be obtained from the direct beam, insight into the structure and crystallinity can be obtained for crystalline materials by analysing electron diffraction. For crystalline samples, similarly to XRD measurements, diffraction of the electrons occur when the atomic plane spacings satisfy the Bragg condition. From this diffraction, information on the crystal planes, and thus lattice vectors of the unit cell, can be deduced. The physical basics of this will be briefly explained in Chapter 4.4. Moreover, as the transmitted electrons can be focussed using magnetic lenses, they can provide spatial information. The result is a two-dimensional image, which is recorded by detecting the transmitted electrons using a photographic plate, fluorescent screen, or light sensitive sensor.

In this work, Scanning Electron Microscopy (SEM) was used for imaging to obtain information on the morphology of samples. Transmission Electron Microscopy (TEM) was employed for imaging and obtaining diffraction patterns.

4.2 Energy Dispersive Spectroscopy and X-Ray Fluorescence^[103–106]

Energy dispersive spectroscopy (EDS) and X-ray fluorescence (XRF) measurements are techniques that can be used to determine the chemical composition of samples. The underlying physical principle is the interaction of electrons with matter for EDS, and the interaction of X-ray radiation with matter for XRF.

EDS measurements are often done concurrently with electron microscopy, as they both use electron beams. The incident electron ejects an electron from the inner shell of the sample, as shown in Figure 3a. EDS measurements are based on the subsequent process (Figure 5). An electron from an outer shell fills the void in the electronic shell. As the energy of this new orbital is lower, in accordance with the law of energy conservation, the electron releases energy in the form of X-rays, or photons; this process is called X-ray fluorescence. The energies of these X-rays are specific for the energetic differences of the respective electron shells. These differences are specific for each chemical element. Moreover, the number of photons detected is proportional to the amount of material that emits photons with this exact wavelength in the sample. Therefore, detecting the emitted radiation caused by irradiation with electrons provides information on which elements are present in the sample, and on the respective ratio of these elements.

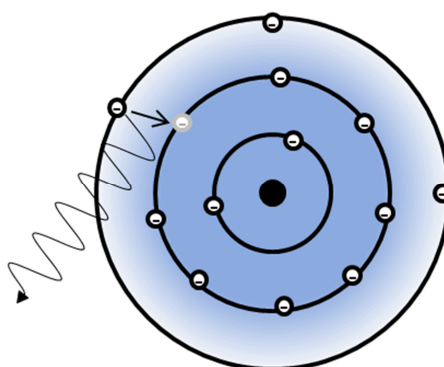


Figure 5. X-ray fluorescence.

In XRF measurements, the same effect is employed to detect the identity of the elements in the sample and the respective ratios. However, the initial ejection of the electrons from the inner shells of the sample elements is not induced by an electron beam, but by irradiating the sample with X-rays. The subsequent steps are the same as for EDS.

Both EDS and XRF were employed in this work to identify chemical elements in synthesised samples and determine the respective elemental ratios.

4.3 X-Ray Photoelectron Spectroscopy^[107]

X-ray Photoelectron Spectroscopy (XPS) is a surface sensitive technique that is used to elucidate information on the elemental composition of samples, the oxidation state of the respective elements, and their chemical environment. Typically, several nanometres close to the surface of a material can be probed. The underlying principle of XPS measurements is based on the photoelectric effect (Figure 6). The material surface is exposed to X-rays, which, provided the X-ray energy is sufficient, leads to an ejection of core electrons of the elements present in the sample to the surface.

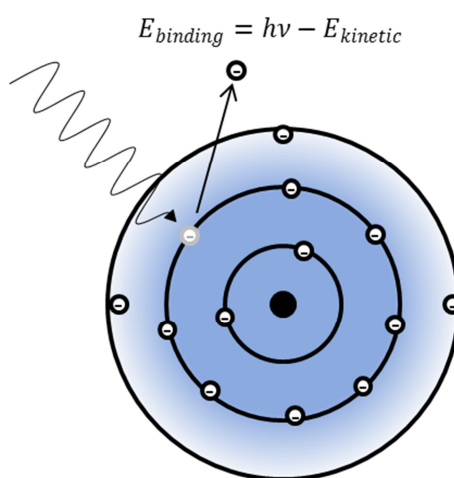


Figure 6. Photoelectric effect employed in X-ray photoelectron spectroscopy.

These electrons, which are called photoelectrons, have binding energies which are described by the following equation:

$$E_{binding} = h\nu - E_{kinetic}$$

Equation 1. Binding energies of ejected electrons.

$h\nu$:	energy of incident X-rays
$E_{binding}$:	binding energy of the photoelectrons
$E_{kinetic}$:	kinetic energy of the photoelectrons

A work function induced by the analyser, which is sometimes included as part of this relationship, can be compensated and is not crucial for understanding the underlying principle. Therefore, it is neglected for this description.

Both the number of electrons and their kinetic energy are measured, which gives a spectrum that correlates the number of detected electrons with their respective binding energies. As the binding energy is highly characteristic for specific elements, as well as their respective oxidation states and chemical environments, XPS can be employed to provide quantitative information on the aforementioned material characteristics.

In this work, XPS measurements were used to observe changes of the oxidation states of electrode materials after discharging battery half-cells. During discharging these half-cells, the expectation was that Na ions are inserted into the respective structures. For Faradaic reactions, this would need to be accompanied by an equivalent electrochemical reduction of the elements present in the electrode to ensure charge neutrality. These changes in the oxidation state were determined to make conclusive statements as to whether Na⁺ insertion into the Na₆[V₁₀O₂₈] polyoxometalate were based on Faradaic reactions, and to quantify the change of oxidation states of Na_{2.55}V₆O₁₆ during Na⁺ (de-)insertion.

4.4 X-Ray Diffraction^[108–115]

4.4.1 Laboratory X-Ray Diffraction

The underlying principle of insertion-type batteries is the (de-)insertion of charge carriers, mostly Li⁺ or Na⁺, into (from) crystal structures. Thus, information on the crystal structure of the host material is crucial. Typically, this information is acquired by XRD measurements. X-rays are generated by an X-ray source, such as a Cu-anode, which is irradiated with electrons. Upon interaction of the electrons with the electron shell of the source material, electrons get slowed down, and X-rays of a continuous energy range are emitted. These emissions are called 'Bremsstrahlung'. Moreover, incident electrons with sufficient energy eject electrons from the inner shell of the anode material leaving a 'hole'. As a consequence, an electron from the outer shell fills this energetically favourable position, and at the same time emits X-rays to account for the conservation of energy (Figure 7). Emitted X-rays based on transitions from the L to the K shell are referred to as K_α X-rays, emission based on the transition from the M to the K shell as K_β X-rays. K_α radiation is used for XRD measurements. This continuum of X-rays ('Bremsstrahlung'), as well as K_β radiation, is filtered out by a monochromator. The X-rays are then directed towards the material that is to be examined. In reflection mode, reflected X-rays are detected, whereas in transmission mode, transmitted X-rays are detected.

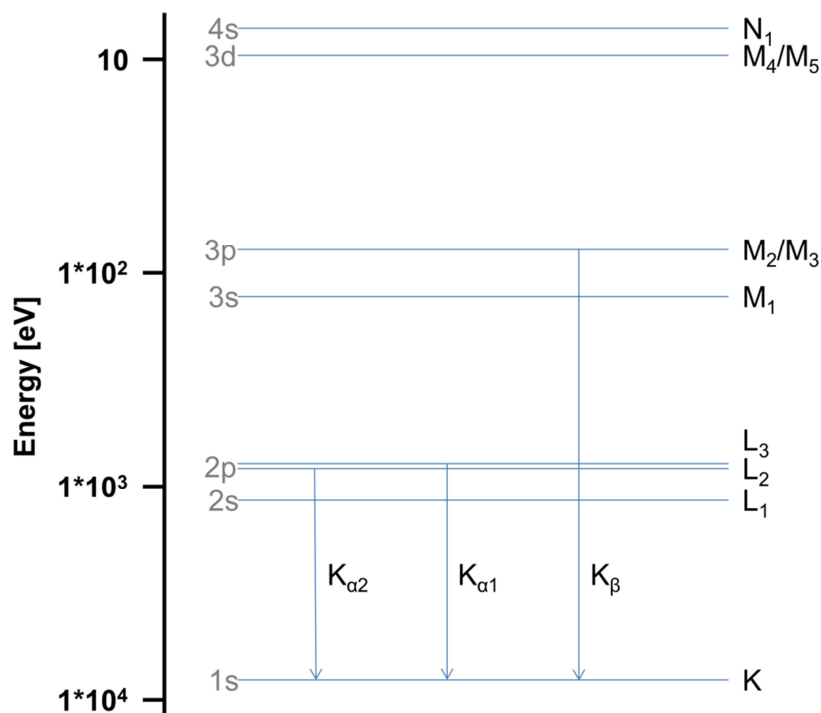


Figure 7. Electronic transitions during X-ray generation.

Active materials in batteries are typically crystalline materials with periodic crystallographic planes. When incident X-rays are directed toward the material, they interfere with the electron shell of elements present in the respective crystallographic plane. The electric field of an X-ray induces an oscillation of the electrons in the sample materials. This acceleration and deceleration results in the emission of an X-ray of the same wavelength as the incident beam. The basis of X-ray diffraction measurements is constructive interference of X-rays after diffraction from a periodic crystallographic plane in the respective crystal lattice. A schematic representation of this process can be seen in Figure 8. This interference occurs when Bragg's law is satisfied.

$$n \cdot \lambda = 2d \cdot \sin\theta$$

Equation 2. Bragg's Law.

- n : positive integer
- λ : wavelength of incident X-rays
- d : interlayer spacing
- θ : scattering angle

Depending on the incident angle θ of the X-rays, this interaction, *i.e.* constructive interference, occurs for different crystallographic planes. The detector,

which captures the reflected X-rays in reflection mode, detects distinct radiation (held at an angle 2θ), caused by constructive interference, at very specific angles, each representing one distinct crystallographic plane of the material. As the angle is gradually varied, different crystallographic planes of the material can be probed. The entirety of these reflections gives a XRD pattern. Thus, the pattern is indicative of a specific arrangement of the crystallographic planes in a material, and thus of a specific crystal structure. This technique is non-destructive.

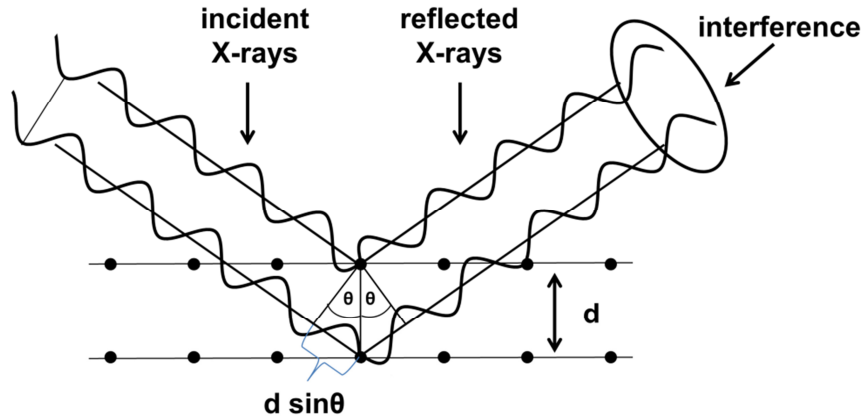


Figure 8. Geometry of the interaction of incident X-rays with crystallographic planes.

The information that can be retrieved from an XRD pattern includes the type of the unit cell and information on lattice parameters. Moreover, the intensity ratios provide information on elements and their position in the structure. Furthermore, the shape of the reflection provides information on crystallite size and strain. The relation between crystallite size and the shape of the reflection, or more specifically, its Full Width at Half Maximum (FWHM), is described by the Scherrer equation:

$$L = \frac{K\lambda}{\beta \cos \theta}$$

Equation 3. Scherrer Equation.

- L : average crystallite size
- K : constant of proportionality/Scherrer constant (typically close to 1)
- β : width of the reflection
- θ : Bragg angle

4.4.2 Synchrotron X-Ray Diffraction

Synchrotron XRD, similarly to the laboratory scale XRD described above, is used to elucidate information on the structural characteristics of materials. One major advantage of synchrotron radiation over laboratory scale X-ray radiation, however, is that high brightness can be achieved. This results in higher signal intensities and a better signal-to-noise ratio. Moreover, synchrotron radiation is coherent, which also results in better signal quality. In contrast to laboratory measurements in reflection mode, synchrotron X-ray diffraction is conducted in transmission mode: X-rays penetrate the sample and diffracted radiation is detected behind the sample. Thus, observed phenomena can be attributed to the bulk of the material, which gives more accurate information than measuring in reflection mode, in which less of the material (few μm close to the surface) is probed.

A synchrotron is based on the acceleration of charge particles, *i.e.* electrons, to relativistic speeds on a closed path using magnetic fields. These electrons are injected into a so-called storage ring using a linear accelerator. As the electron beam path is typically circular, constant acceleration is needed, and electromagnetic radiation is emitted according to Maxwell's equations. This radiation can be focused and directed towards the measurement site, where it is used for the necessary application, such as XRD in the measurement described in Chapter 5.3.

In this work, XRD measurements were employed to identify the crystal structure of synthesised materials. In addition, both laboratory and synchrotron radiation were employed for electrochemical *in operando* measurements (Chapter 5.2 and 5.3). Specifically, structural changes of alkali vanadates were monitored during electrochemical cycling in order to better understand Na^+ insertion into and extraction from these structure.

4.5 Inductively Coupled Plasma Optical Emission Spectrometry^[116,117]

Inductively Coupled Plasma Optical Emission Spectrometry (ICP-OES) is a method to determine the elemental composition of materials. As the sample must be in liquid form, powder samples need to be digested, *i.e.* dissolved in suitable solvents. For the measurements described in this work, a mixture of concentrated nitric acid and hydrochloric acid (volume ratio 1:3, *aqua regia*) was used. The dissolved sample is inserted into a nebulizer, where it is converted into an aerosol with the help of argon gas. Using a spray chamber, the fine aerosol is separated from the larger droplets and transferred into the ICP torch. A plasma is generated by exposing the gas to a copper coil; a strong magnetic field is induced by radio frequency. In this plasma, which has a temperature of several thousand degrees Kelvin, the sample elements are converted to a gaseous state and potentially ionized. Through collisions, an excitation of the atoms and ions is induced. Upon relaxation to the ground state, photons of an element-specific wavelength are

emitted. The characteristic energy of the photons is used to identify the elements that are present in the sample. The number of photons with a specific wavelength is directly proportional to the number of atoms and ions in the sample. Thus, a quantitative compositional analysis and the elucidation of the respective ratio of the elements within a sample is possible. In this work, ICP-OES was employed to verify the elemental composition of synthesised electrode materials.

4.6 Electrochemical Measurements^[118–121]

4.6.1 Electrode Preparation

To ensure consistency and comparability of different measurements and materials, electrodes were always prepared in the same way for all the presented materials. The binding agent, polyvinylidene difluoride (PVDF) polymer, was dissolved in N-methyl pyrrolidone (NMP); the mass ratio PVDF/NMP was typically 6%. The active material, *i.e.* the electrode material to be studied, was mixed with activated carbon to improve conductivity. The PVDF binding agent was added, and everything was thoroughly mixed into a homogeneous slurry. This slurry was applied onto an Al-foil, and evenly distributed using a doctor blade. NMP was evaporated on a heating plate, and circular pieces, *i.e.* electrodes, were punched from the coating. Finally, the electrodes were dried at 110 °C under vacuum for at least four hours.

4.6.2 Coin Cell Preparation

The coin cells employed in this work were 2016 (diameter: 20 mm, height: 1.6 mm) coin cells with a stainless steel casing (1 & 7 in Figure 9). The active material electrode (6) described above was placed into the lower part of the casing (7 in Figure 9), and covered with a glass fibre separator with a diameter of 19 mm. Then, electrolyte (typically 150 μ L) was added to the system. In NIBs, metallic Na was rolled, and circular pieces with a diameter of 16 mm were cut with a hole puncher. The Na-piece (4) was placed onto the separator and covered with a stainless steel spacer (3). Next, a stainless corrugated stainless steel plate (2) was added, which serves as a spring to ensure uniform pressure within the coin cell. For lithium-ion cells that were built for the work described in Chapter 5.5, the same set-up was used, except that Li metal was used instead of Na metal.

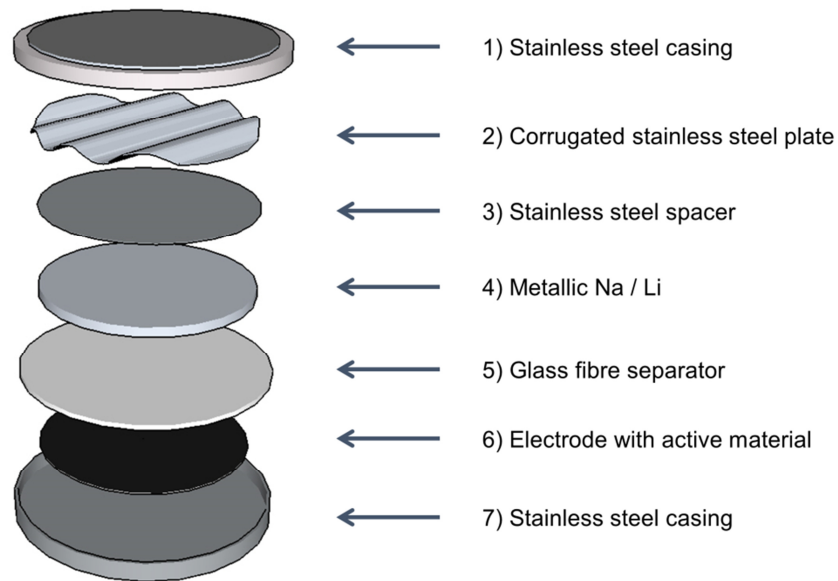


Figure 9. Set-up for coin cell measurements (adapted from ^[122]).

4.6.3 Galvanostatic Cycling^[118,120]

Galvanostatic cycling is typically used to determine the capacity and potential that new materials can provide. For this method, the battery cell is exposed to a current which is controlled, while the voltage is recorded as a function of the overall current flow. Alternatively, the overall current can be multiplied with the time during which the current was flowing to give the capacity. As the amount of transferred charge obviously depends on the amount of active material present in the cell, capacity is typically normalised to the mass of the active material and expressed as mA h g^{-1} . These measurements can be employed for half-cells, in which one electrode is metallic Na (for NIBs), and full-cells, in which both electrodes consist of electrochemically active materials (*i.e.* not metallic Na).

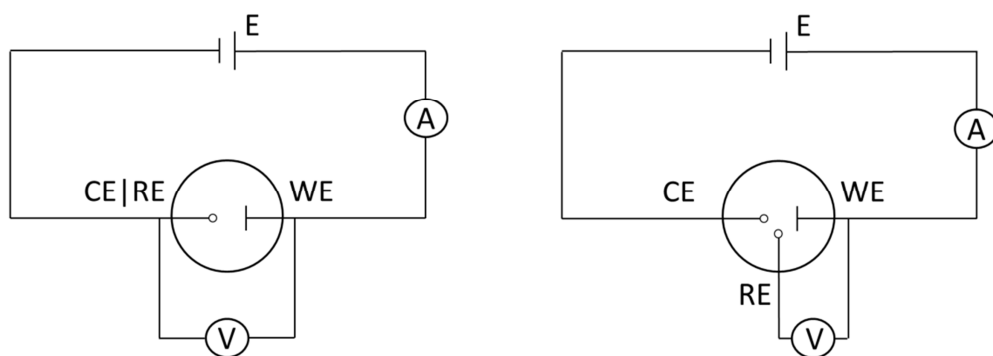


Figure 10. Schematic circuit of a a) 2-electrode and b) 3-electrode set-up (CE: Counter Electrode, WE: Working Electrode, RE: Reference Electrode).

To elucidate basic performance metrics like capacities or voltages, two-electrode coin cell set-ups were used, in which current was transferred between the working electrode (active material + binder + carbon) and the reference/counter electrode. A basic circuit for this can be seen in Figure 10a. A three electrode set-up was employed for cyclic voltammetry measurements described in Chapter 4.6.5.

Typically, the information provided by this type of experiment is plotted as a voltage vs. capacity graph, whose shape can reveal important information. For example, a plateau is typically assigned to a reaction involving a phase transformation during the insertion and extraction of the respective ion. If the voltage is linearly proportional to the capacity during a measurement, which would result in a completely linear slope for the charge or discharge curve, the underlying process is often based on non-Faradaic processes, *i.e.* the storage process is capacitive charge storage. Here, no charges are transferred through the electrode|electrolyte interface, but only a Helmholtz-layer is formed at the electrode surface. However, purely capacitive processes cannot be automatically assumed for all reactions lacking a defined plateau during charge/discharge processes, as the example of Chapter 5.4 shows.

The obtained capacity can be correlated with the number of exchanged electrons via *Faraday's law*:

$$Q = \frac{z * F * m}{M}$$

Equation 4. Faraday's law.

Q:	total charge transferred (i.e. capacity) of a material
z:	number of electrons exchanged per formula unit
F:	Faraday constant – 96,485.3365 s A mol ⁻¹
m:	mass of the active electrode material
M:	molar mass of the active electrode material

Knowledge of *z*, *i.e.* the number of electrons transferred during (dis-)charge of the electrochemically active material can provide important first insights regarding the electrochemical reactions. In case one element is reduced, *e.g.* *z* can give a first idea of the oxidation state changes of this element, whereas for materials that incorporate several potentially active elements, a hypothesis about which elements are electrochemically active in the specific structure that is measured can be deduced.

Apart from the shape and the capacity provided during discharge, another important feature is the capacity ratio between charge and discharge. This reveals information on the reversibility of the reaction. In other words, it shows what percentage of the applied current during charge can be retrieved again during the

subsequent discharge process. This ratio is called *coulombic efficiency*, and is expressed by the following equation:

$$\eta = \frac{Q_{discharge}}{Q_{charge}} * 100\%$$

Equation 5. Coulombic Efficiency.

η : coulombic efficiency

Q_{charge} : capacity obtain upon charge (extraction of the charge carrier)

$Q_{discharge}$: capacity obtained upon discharge (insertion of the charge carrier)

Another important characteristic of a battery material, next to its absolute capacity and the available voltage, is cycling stability, which can be obtained by following the development of capacity over time. Cycling stability is calculated as follows:

$$cycling\ stability = \sqrt[n]{\frac{Q_n}{Q_0}} * 100\%$$

Equation 6. Cycling Stability.

n : number of cycles

Q_n : discharge capacity after n cycles

Q_0 : initial discharge capacity

Typically, a cycling stability of 100% is targeted, which means that the exact number of charge carrier ions (and thus energy) that are (de-)inserted during the charge process can subsequently be extracted (inserted) during discharge. Commercial active materials for secondary insertion type batteries have a cycling stability that is close to 100%.

Reasons for capacity fading, *i.e.* a decrease of capacity over time, can be limited reversibility of the charge storage mechanism (*e.g.* due to structural changes of the material), parasitic side reactions (*e.g.* electrolyte decomposition), or engineering problems (*e.g.* loss of contact between the active material and the conducting carbon or current collector). For some materials, initial cycling stabilities of above 100% can occur, which typically hints at some sort of activation process for the material.

In general, there are two different ways of stating the current that is applied during galvanostatic cycling. For novel materials, for which the theoretical capacity

is unknown, an absolute specific current (*i.e.* applied current normalised to the mass of the active materials) is often used, *e.g.* a value of 100 mA g⁻¹, as this can be calculated and applied regardless of the characteristics of the respective material. Alternatively, and more common especially for well-researched materials, the C-rate terminology is used. Here, the focus is on expressing for how many hours a battery is discharged (or charged) to allow for a full exploitation of the theoretical capacity. A C-rate of 1C, for example, means that a battery is charged with the full theoretical capacity in one hour, whereas a C-rate of 2C describes a full charge within 30 minutes. Accordingly, at a C-rate of 0.5C a charge process takes two hours. For this approach, it is obviously necessary to know how much charge a material can theoretically (reversibly) store. Based on that, the current that is needed to (dis-)charge the battery with a specific C-rate can be calculated.

4.6.4 Galvanostatic Intermittent Titration Technique^[123–127]

Galvanostatic intermittent titration technique (GITT) was used in this work to study the diffusion properties of Na⁺ in a host structure (Chapter 5.3). Measurements were conducted in coin cells (see Chapter 4.6.2). The system is exposed to current pulses of defined durations; in the work reported in Chapter 5.3, it was 200 s. Typically, due to the current pulses, the material is deflected from its thermodynamic equilibrium, and the observed potential during a GITT discharge is lower than the equilibrium potential. During the subsequent relaxation period, the material moves towards its equilibrium state, for example by uniform distribution of the inserted Na-ions in the structure. The relaxation period ends either after a pre-set time, or when a termination criterion with regard to the change of potential is reached (*e.g.*, $\frac{dU}{dt} < 2\text{mV h}^{-1}$). The time the material needs to reach its equilibrium state during the relaxation process, *i.e.* until the potential does not change any more, is indicative of the ionic conductivity of the Na-ion in the electrode.

The diffusion coefficient can be obtained by the following formula:

$$D_{Na} = \frac{4}{\pi} \left(\frac{V_M}{SFz_i} \right)^2 \left[I_0 \frac{\left(\frac{dE}{d\delta} \right)}{\left(\frac{dE}{d\sqrt{t}} \right)} \right]^2$$

Equation 7. Diffusion coefficient as calculated from GITT measurements.

D_{Na} :	diffusion constant of Na ⁺
V_M :	molar volume of the material
S :	electrode/electrolyte contact area
F :	Faraday's constant
z_i :	charge number
$\frac{dE}{d\delta}$:	slope of the coulometric titration curve

$$\frac{dE}{d\sqrt{t}}$$

slope of the linearized plot of the potential E (V) during the current pulse

V_M typically changes during Na^+ -insertion as shown in Chapter 5.3. However, as this change is very small for the materials presented in this work when compared to the change of the diffusion constant, it can be neglected. Moreover, 'S' was approximated by the geometric surface area of the electrode.

4.6.5 Cyclic and Linear Sweep Voltammetry^[118,120,127,128]

Voltammometric measurements belong to the class of potentiostatic techniques. In both cyclic and linear sweep voltammetry, the potential, which constitutes the independent variable, is systematically varied, and the current response is measured.

Cyclic voltammetry (CV) was employed to determine the potential at which redox reactions occur. Typically, a two-electrode coin cell set-up was used for this technique. For the determination of the electrochemical window of the IL described in Chapter 5.5 a three electrode set-up (Figure 10) was employed. A three electrode set-up has the advantage that the RE is 'current free' as the occurring currents flow between the WE and the RE. Thus, polarisation of the RE is reduced, which increases the precision of the electrochemical measurements.

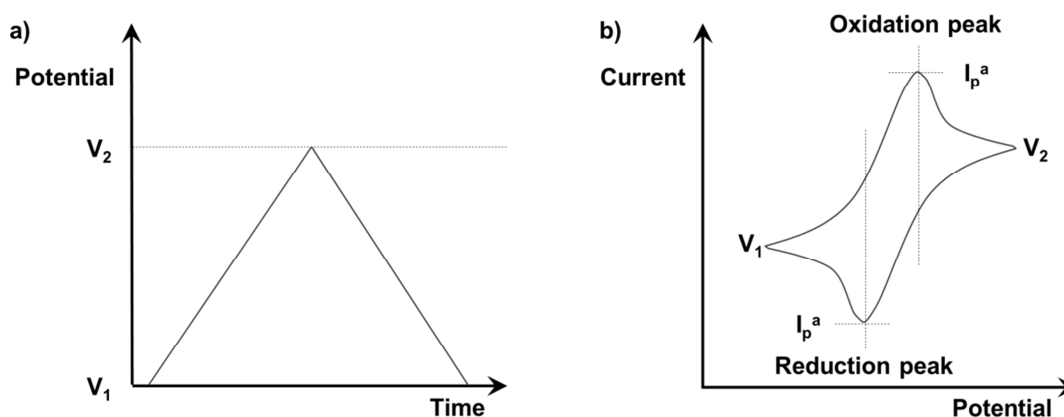


Figure 11. Schematic profile of CV measurements: a) Potential vs. time; b) current vs. potential.

The electrochemical (coin) cell is scanned between an upper and a lower potential limit, and the potential is varied with a distinct scan rate (e.g. 0.1 mV s^{-1}). When a potential limit is reached, the direction of the scan is reversed. Figure 11a shows the typical profile (potential vs. time) of one cycle of a CV curve. A potential increase (anodic sweep) induces oxidation of the electrode material in case it contains a redox-active centre with a redox potential within the scanned potential

region, whereas a decrease of the potential (cathodic sweep) induces reduction. For the investigated materials, an increase in potential resulted in a de-insertion of Na^+ from the crystal structure; a decrease in potential resulted in an insertion of Na^+ into the same. The resulting current response is positive for oxidations, and negative for reductions (Figure 11b).

The area of the peaks in the CV represent the current flow during the investigated redox reactions, and therefore the capacity of the respective material. Thus, the reversibility of the charge-storage process can be assessed by comparing the area of the integrated reduction and oxidation peak. It should be noted here that while in a battery, the term reversibility denotes the ratio of the currents during the discharge and the charge process, reversibility in general electrochemistry relates to the potential difference between the two peaks. A redox reaction that occurs in a very narrow potential range (*i.e.* the peak is sharp) typically indicates a very crystalline material, whereas broad peaks are more indicative of amorphous materials. Moreover, information on the kinetics of the redox reactions can be obtained by varying the scan rate and investigating the change of the current response.

Linear sweep voltammetry is based on the same principle, *i.e.* variation of the potential and measurement of the current response. The difference to CV measurements, however, is that during a LSV, the potential is not repeatedly varied between a lower and an upper limit, but it is only either increased or decreased – the scan rate is not reversed.

4.6.6 Electrochemical Impedance Spectroscopy^[120,129]

Electrochemical impedance spectroscopy (EIS) was employed in this work to obtain information on the SEI of novel ionic liquids (ILs, Chapter 5.5). EIS can be used to measure the impedance of a system, which can be seen as the barrier of a system to permit the flow of an electrical current. The system is exposed to an alternating potential and thus perturbed from its equilibrium state, and the resulting current is measured. The applied potential is typically rather small ($\sim 5 - 10$ mV), so that the response of the system can be linearly approximated. The electrical circuit in Figure 12 gives a schematic model for an interfacial transfer reaction. Electron transfer through the electrolyte|electrode interface is expressed by the charge transfer resistance R_{CT} , which is combined in series with the sum of the resistances of all cell components (Ohmic resistance R_{Ω}) and in parallel with a capacitive element (C) for the double layer capacitance.

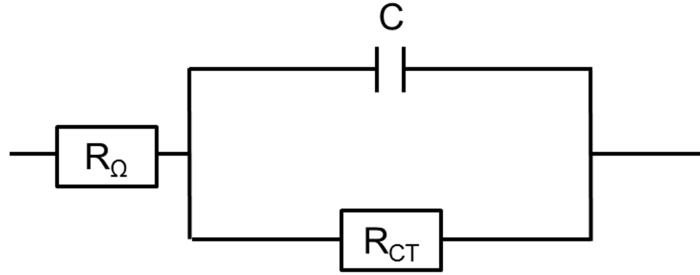


Figure 12. Electrical circuit scheme equivalent for interfacial electrochemical reactions.

In such a system, the current response to a sinusoidal potential perturbation is sinusoidal as well, but shifted in phase (ϕ). This phase shift depends on the frequency of the system. Mathematically, the expression for impedance (Z) can be segmented into a real and an imaginary part:

$$Z = \frac{E}{I} = Z_0 e^{i\phi} = Z_0 (\cos \phi + i \sin \phi) = R_\Omega + \frac{R_{CT}}{1 + i 2\pi \omega R_{CT} C}$$

Equation 8. Impedance of a system.

Z :	impedance
E :	voltage
I :	current
i :	$\sqrt{-1}$
ϕ :	phase angle
R_Ω :	Ohmic resistance
R_{CT} :	charge-transfer resistance
ω :	frequency
C :	capacitance

Using those components, a Nyquist plot with a real x-axis and an imaginary y-axis can be plotted when the frequency (ω) is varied; typically, with this kind of application, the obtained data gives one or several semicircles, which correspond to different processes. For one semicircle at low frequencies, Equation 8 can be simplified to:

$$Z = R_\Omega + R_{CT}$$

Equation 9. Approximation of the impedance at low frequencies.

Z:	impedance
R_{Ω} :	Ohmic resistance
R_{CT} :	charge-transfer resistance

Z in this case corresponds to the intersection of the semicircle with the x-axis at high values. At high frequencies, the equation can be simplified as follows:

$$Z = R_{\Omega}$$

Equation 10. Approximation of the impedance at high frequencies.

Z:	impedance
R_{Ω} :	Ohmic resistance
R_{CT} :	charge-transfer resistance

Here, Z corresponds to the intersection of the semicircle with the x-axis at low values. Thus, the charge-transfer resistance R_{CT} can be obtained by calculating the difference between the x-values of the intersections of the semicircle with the x-axis.

This difference corresponds to the electron transfer at the electrode|electrolyte interface. For the measurement described in Chapter 5.5, R_{CT} was monitored. The major contributor to R_{CT} is the SEI. Thus, a stable value for R_{CT} indicates that the SEI has reached stable state and that the electrolyte has stopped decomposing.

4.7 Thermogravimetric Analysis^[130,131]

In a Thermogravimetric Analysis (TGA) measurement, the sample is heated up, and the change of the sample mass over time is monitored. Changes in mass can be attributed to several factors, such as evaporation of volatile constituents, thermal decomposition or reaction with gases in the measurement chamber (e.g. oxidations). In order to avoid reactions during the measurement process, an inert atmosphere, e.g. N_2 or Ar, is typically used. The sample mass is normalised to percent (initial mass = 100%). For materials for which no reactions occur in the chosen temperature range mass losses are typically attributed to moisture and crystal water. Physically adsorbed water results in a mass loss below 100 °C. For the evaporation of crystal water higher temperatures are necessary. The amount of crystal water molecules per formula unit can then be calculated via the percentage mass change. Other materials, such as organic compounds, decompose at certain temperatures, which typically leads to mass loss for the sample, and evaporation of

the decomposition products. In order to determine the mass of the evaporated components, a TGA measurement can be coupled with a mass spectrometer (TGA-MS). The evolving gases are ionized and transferred into a mass spectrometer, where magnetic and electrostatic fields are employed to separate the respective ions based on their charge-to-mass ratios. As the masses of the molecular fragments that are detected typically differ with regard to temperature, the masses of the fragments can indicate in what order the respective compound decomposes.

In this work, TGA measurements were employed to determine the amount of crystal water of electrode materials. In addition, TGA-MS was employed to monitor the decomposition process of an IL upon heating.

4.8 Rheometry^[132]

An important characteristic of liquid electrolytes is viscosity. Typically, low viscosities are targeted to improve ionic conductivity of the charge carrier ion (*i.e.* Li^+ or Na^+). Viscosities of liquids can be measured with a variety of methods. For the ionic liquid discussed in this work, a shear rheometer was used. This measurement principle is based on the principle that force needs to be used in order to turn an object in a liquid. The sample, in this case presented in Chapter 5.5 an IL, is applied onto a plate, and a cone or plate is lowered from above until it is immersed in the sample. Then, the cone is rotated at a certain speed, and the torque that is required to induce the rotation at the pre-set frequency is measured. From this torque, the viscosity of the sample is deduced.

For applications for which temperature is important, the effect of temperature on viscosity is measured as well. For this, the plate with the sample is heated, and the required torque at various temperatures is measured. This is particularly interesting for the IL investigated in this work, as ionic liquids typically suffer from high viscosities, which is detrimental for applications as battery electrolytes. One possibility to overcome this is to operate the battery at elevated temperatures. Thus, the temperature dependence of the viscosity can provide valuable information with regard to the optimal working temperature of batteries.

5 Vanadium-Based Materials in Sodium-Ion Batteries

As outlined in Chapter 3.3, vanadium-based materials possess interesting characteristics with regard to their application as electrode materials in NIBs. In this chapter, my scientific publications on this topic are presented. These publications describe extended work on the material class $A_2V_6O_{16}$, ($M=Li, Na, K$). Evaluation of its electrochemical properties showed a significant decrease in capacity over cycling (Chapter 5.1). In order to understand this better, and potentially develop strategies to mitigate this capacity fading, an electrochemical *in operando* cell was developed (Chapter 5.2). In addition, synchrotron *in operando* XRD measurements were performed and concomitant structural and electrochemical processes in different potential regions were described (Chapter 5.3). Moreover, polyoxometalates are suggested as a new electrode material in NIBs (Chapter 5.4). Due to their unique structural properties, the insertion of Na^+ does not result in structural deterioration. As the electrolyte can also have a significant effect on cycling stability, a novel ionic liquid was developed and first tested as LIB electrolyte (Chapter 5.5).

5.1 Sodium Vanadium Oxide: A New Material for High-Performance Symmetric Sodium-Ion Batteries

In this chapter, the publication “Sodium Vanadium Oxide: A New Material for High-Performance Symmetric Sodium-Ion Batteries” (ChemPhysChem **2014**, *15*, 2121-2128) is presented. It describes the first results obtained by our group on the application of alkali metal vanadates in sodium-ion batteries. S. Hartung was leading the work that is presented in this publication.

$\text{Na}_{2.55}\text{V}_6\text{O}_{16}$ (NVO) was synthesised via a hydrothermal method. The obtained product crystallises in a monoclinic unit cell ($P12_1/m1$) with a belt-like morphology. Subsequently, NVO was investigated with regard to its behaviour as cathode material in NIBs.

Cyclic voltammetry measurements of Na-ion half-cells vs. $\text{Na}|\text{Na}^+$ show several distinct peaks in the first cycle, indicating different electrochemical processes. In subsequent cycles, the peaks decrease in intensity or disappear completely, indicating (partially) irreversible processes. This behaviour is confirmed by galvanostatic charge/discharge tests. In initial cycles, the material delivers a high capacity of around 200 mA h g^{-1} between $4.0 \text{ V} - 1.3 \text{ V}$, as well as good rate capability. The discharge curves show very distinct plateaus in the first discharge at 2.4 V and 1.5 V which smoothen out in subsequent cycles. Moreover, capacity decreases significantly, which indicates irreversible processes. These different plateaus could indicate different structural processes or different oxidation states of the redox centre, particularly for materials containing vanadium which is known to exist in several oxidation states. As the long plateau at 1.5 V was thought to indicate irreversible processes, a better understanding of the underlying processes was required. XPS measurements were performed at various states of charge to observe the development of the oxidation state of V during cycling. V, which has an average oxidation state of $+4.75$ at OCV, increases its average oxidation to $+4.87$ in the charged state. During discharge, it is gradually decreased until the end of the major plateau at 1.3 V , where only V with an oxidation state of $+4.00$ was detected. These changes are in line with the observed capacities during the galvanostatic processes. Thus, even though the CV and galvanostatic tests indicate different processes during Na-insertion, the oxidation state of vanadium only changes between $+4$ and $+5$. Therefore, factors other than the oxidation state of vanadium are the cause of the different plateaus and the low cycling stability. These factors were investigated in subsequent studies.

In addition, as the composition of NVO varies from $\sim \text{Na}_{1.5}\text{V}_6\text{O}_{16}$ to $\sim \text{Na}_{6.x}\text{V}_6\text{O}_{16}$ during cycling ($4.0 \text{ V} - 1.3 \text{ V}$), it can both insert and de-insert Na^+ starting from a composition of $\text{Na}_{2.55}\text{V}_6\text{O}_{16}$ at OCV. Thus, as a proof of concept, a symmetric full-cell was built with NVO as both cathode and anode. Even though it was shown to work, it is, however, not interesting from a commercial point of view due to the high amount of material needed on the cathode side.

The results in this publication demonstrate that NVO can provide high capacities in NIBs, albeit with significant capacity fading. This observation

encouraged further work on this material to identify the causes of the decrease in capacity during cycling.

Sodium Vanadium Oxide: A New Material for High-Performance Symmetric Sodium-Ion Batteries

Steffen Hartung, Nicolas Bucher, Vivek Sahadevan Nair, Cheah Yan Ling, Yuxi Wang, Harry E. Hoster, Madhavi Srinivasan

S. Hartung, N. Bucher, V. S. Nair, C. Y. Ling, Y. Wang, H. E. Hoster, M. Srinivasan: Sodium Vanadium Oxide: A New Material for High-Performance Symmetric Sodium-Ion Batteries. ChemPhysChem. 2014. Volume 15. Pages 2121-2128. Copyright Wiley-VCH Verlag GmbH & Co. KGaA. Reproduced with permission.

The publication can be found under the following weblink:

<http://dx.doi.org/10.1002/cphc.201402020>

DOI: 10.1002/cphc.201402020

Sodium Vanadium Oxide: A New Material for High-Performance Symmetric Sodium-Ion Batteries

Steffen Hartung,^[a, b] Nicolas Bucher,^[a, b] Vivek Sahadevan Nair,^[c] Cheah Yan Ling,^[c] Yuxi Wang,^[a] Harry E. Hoster,^[a, b] and Madhavi Srinivasan^{*[a, c]}

Room-temperature sodium-ion batteries have the potential to become the technology of choice for large-scale electrochemical energy storage because of the high sodium abundance and low costs. However, not many materials meet the performance requirements for practical applications. Here, we report a novel sodium-ion battery electrode material, $\text{Na}_{2.55}\text{V}_6\text{O}_{16}\cdot 0.6\text{H}_2\text{O}$, that shows significant capacities and stabilities at high current rates up to 800 mA g^{-1} . X-ray photoelec-

tron spectroscopy measurements are carried out to better understand the underlying reactions. Moreover, due to the different oxidation states of vanadium, this material can also be employed in a symmetric full cell, which would decrease production costs even further. For these full cells, capacity and stability tests are conducted using various cathode:anode mass ratios.

1. Introduction

The last years have seen a great increase in the demand for high-performance, environmentally friendly, and affordable energy-storage systems for small-scale electronic devices, electrical vehicles, as well as the electrical grid. The currently dominating lithium-ion battery (LIB) has fulfilled most performance requirements for these applications. However, one inherent problem is costs.^[1] One promising approach to remedy this concern is sodium-ion batteries (NIBs). Its cost advantage is based on two pillars: First, due to the worldwide abundance of sodium and higher production volumes (see Figure 1 a), its compounds are cheaper than its lithium counterparts (e.g. the cost of Na_2CO_3 is only 10% the cost of Li_2CO_3).^[1–3] Second, LIBs require copper as a current collector for the anode, as lithium alloys with the cheaper and lighter aluminum. This is not the case for NIBs.^[4–6] Thus, the current collector costs can be greatly decreased (Figure 1 b). Furthermore, as opposed to lithium resources, which are rather centralized (Figure 1 c), sodium compounds can be found worldwide, both as minerals and dissolved sodium salts in seawater. As the composition of cathode materials for NIBs usually differs from its LIB counterpart,

NIBs offer the potential to avoid common expensive LIB materials such as lithium cobalt oxide. However, NIBs pose the inherent challenges that they often have lower voltages as compared to LIBs, and that the (de)intercalation of the larger sodium puts more strain on the crystal structures than it is the case with lithium ions.^[7]


Several structures have been tested to resolve these problems, and especially layered structures have shown promising results.^[6,8–10] Among those, manganese oxides have received considerable attention,^[11–16] and successful attempts have been made to improve key features such as their cycling stability.^[17] One class of materials that has been extensively studied in LIBs is vanadium oxides, giving initial capacities above 300 mA h g^{-1} .^[18–21] Recently, first approaches have also been made to employ this class of materials in sodium-ion batteries, showing significant capacities of 160 mA h g^{-1} for the orthorhombic and 250 mA h g^{-1} for the bilayered structure.^[22] Sodium vanadium oxides have also attracted considerable attention. For example, Delmas et al. recently examined the structural characteristics of layered NaVO_2 ,^[23] and other compositions have been shown to provide promising capacities as well (e.g. $\text{NaV}_6\text{O}_{15}$: 142 mA h g^{-1} , NaV_3O_8 : 200 mA h g^{-1}).^[24–28] Sodium iron phosphate, NaFePO_4 , has been synthesized from LiFePO_4 , and combines satisfactory capacities (120 mA h g^{-1}) and high cycle stability.^[29] Apart from these half-cells measurements, several NIB full cells have been investigated.^[30–32] One direction that is particularly interesting is symmetric full cells, as they require the same material for cathode and anode, which makes production easier and cheaper. Moreover, as there is no difference in potential between anode and cathode in the discharged state, a potential safety risk is eliminated. This symmetric full cell approach has been performed for NASICON [$\text{Na}_x\text{V}_2(\text{PO}_4)_3$] type materials, providing initial discharge capacities of up to 68 mA h g^{-1} , with significant subsequent

[a] S. Hartung,⁺ N. Bucher,⁺ Dr. Y. Wang, Prof. Dr. H. E. Hoster, Prof. Dr. M. Srinivasan
TUM CREATE
Singapore 138602 (Singapore)
E-mail: Madhavi@ntu.edu.sg

[b] S. Hartung,⁺ N. Bucher,⁺ Prof. Dr. H. E. Hoster
Technische Universität München
85748 Garching (Germany)

[c] V. S. Nair, Dr. C. Y. Ling, Prof. Dr. M. Srinivasan
School of Materials Science and Engineering
Nanyang Technological University
Singapore 639798 (Singapore)

[⁺] These authors contributed equally to this work

 Supporting Information for this article is available on the WWW under <http://dx.doi.org/10.1002/cphc.201402020>.

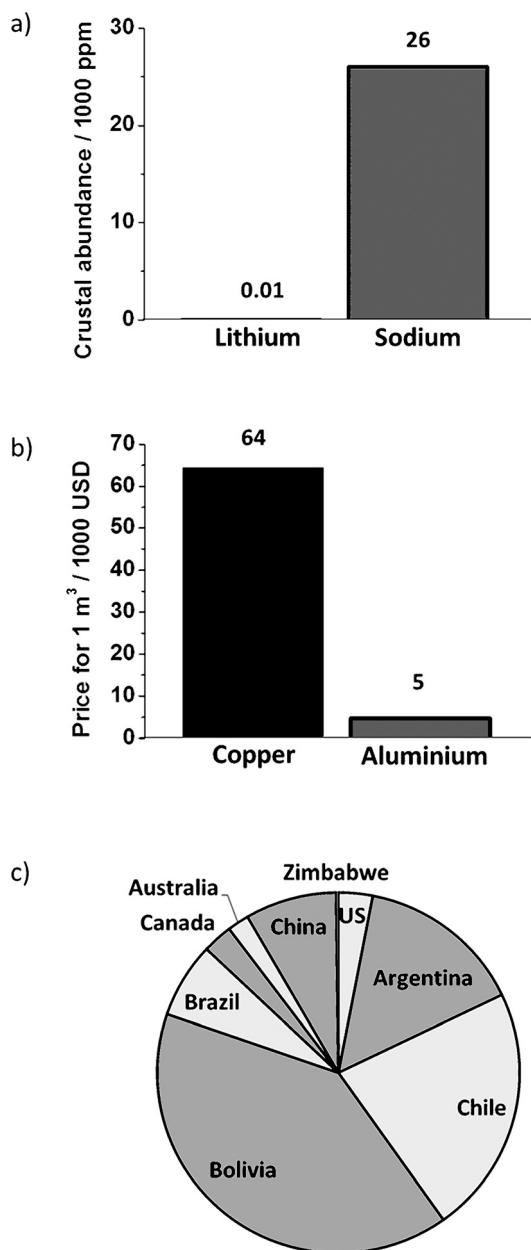


Figure 1. a) Crustal abundance of lithium and sodium (Springer Materials—The Landolt Boernstein Database). b) Cost comparison for copper and aluminium as current collectors for lithium- and sodium-ion batteries (metal prices: London Metal Exchange, 9 September 2013). c) Geographical distribution of lithium reserves (Meridian International Research, 2005).

fading.^[33–35] $\text{Na}_{2+x}\text{V}_6\text{O}_{16}\cdot x\text{H}_2\text{O}$ (NVO),^[36–38] which has shown good performance for lithium-ion batteries, both for aqueous^[39] and organic systems,^[40] has not yet been tested in sodium-ion batteries.

In this paper, we will show that $\text{Na}_{2.55}\text{V}_6\text{O}_{16}\cdot 0.6\text{H}_2\text{O}$ is a promising electrode material for sodium-ion battery half and full cells. After a description of the synthesis procedure, we will first describe the morphology using field-emission scanning electron microscopy (FESEM) and transition electron microscopy (TEM), and the crystal structure by using X-ray diffraction (XRD). Then, we will discuss the electrochemical characteristics

as elucidated through cyclic voltammetry and galvanostatic charge/discharge tests. We will show that NVO is able to deliver remarkable capacities even at high currents, and we will demonstrate that NVO can act as both cathode and anode by constructing a symmetric battery with this material.

2. Results and Discussion

2.1. Morphology and Structure

FESEM images show nanowires with an average diameter of 100–150 nm and a length that varies from several hundred nanometers to a few micrometers, resulting in diverse aspect ratios of > 10 (Figure 2a,b). This has been confirmed by bright-field TEM (Figure 2c,d). Selected-area electron diffraction (SAED) results show the appearance of diffraction rings, indicating the polycrystallinity of NVO. Both selected indexing of the diffraction rings and d-spacing calculations are found to be in good agreement with the XRD data.

The crystal structure is depicted in Figure 3a (space group $P12_1/m1$). The structure consists of V_3O_8 layers that are composed of VO_6 corner-sharing octahedra and edge-sharing units of V_2O_8 pyramids, with the Na ions being located in both tetrahedral and octahedral cavities in between these layers (Figure 3b). Tetrahedrally coordinated Na ions are edge sharing with the VO_6 octahedra, while the octahedrally coordinated Na ions are edge sharing among themselves and corner sharing with the VO_6 structures. The lattice parameters as calculated by the Topas software using a Rietveld refinement (Figure 3c) are $a = 0.73012$ (13) nm, $b = 0.360863$ (32) nm, and $c = 1.21631$ (13) nm, with a cell volume of 0.305210 (96) nm^3 and $\beta = 107.75^\circ$. The stoichiometry of the product, as determined by X-ray fluorescence (XRF) measurements, is $\text{Na}_{2.55}\text{V}_6\text{O}_{16}$. Crystal water, as measured by thermal gravimetric analysis (TGA), was found to be $0.6\text{H}_2\text{O}$ per formula unit, which gives the formula unit $\text{Na}_{2.55}\text{V}_6\text{O}_{16}\cdot 0.6\text{H}_2\text{O}$. The chemical states of vanadium in as-synthesized NVO were determined by X-ray photoelectron spectroscopy (XPS) by collecting $\text{V}2\text{p}_{3/2}$ and $\text{V}2\text{p}_{1/2}$ spin orbit-split peak. Peak fitting of the $\text{V}2\text{p}_{3/2}$ peak resulted in two components: in the plain material, 76% and 24% of the vanadium has an oxidation state of $5+$ and $4+$, respectively (Figure 5, 6). Thus, the average oxidation state of vanadium is < 5 . As expected, sodium (Na1s) only gives one peak as the sodium ions in the structure are equivalent.

2.2. Electrochemical Behavior and ex Situ XPS Studies

After assembling the coin cells, the half cells showed an initial open-circuit voltage of approximately 3 V (vs. sodium metal). Cyclic voltammetry and charge/discharge experiments were performed. At various points of the galvanostatic charge/discharge tests, as indicated in Figure 6, the coin cells were opened and high-resolution XPS scans of the $\text{V}2\text{p}_{3/2}$ peak were collected to deduce the oxidation states of vanadium. As expected, the vanadium $5+/4+$ ratio did not change within the cell before cycling, as measured by XPS of a blind cell (Figure 5, 6); for the blind cell test, a coin cell was built, rested

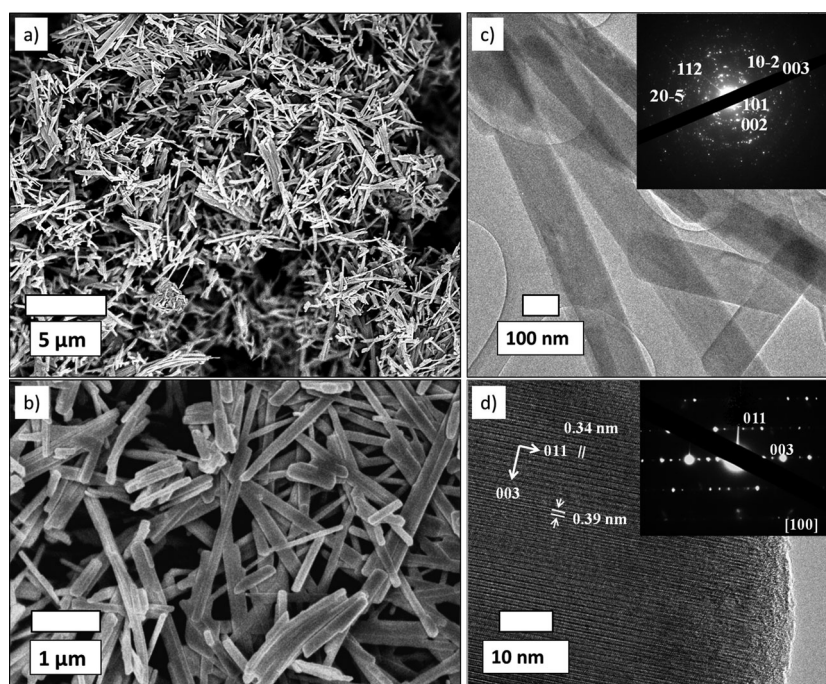


Figure 2. a,b) SEM images showing disordered nanowires. c) Bright-field TEM images showing the presence of 100–150 nm-wide NVO nanowires; the SAED image shows diffraction rings that indicate polycrystallinity. d) High-resolution image and SAED of a single crystallite of NVO showing the orientation along the [100] zone axis.

overnight without applying any current or voltage, and then opened to do the measurement. The cyclic voltammogram (Figure 4) is dominated by the oxidation peak at 2.6 V, and the resulting reduction peak at 2.2 V. Furthermore, oxidation peaks occur at 1.9, 2.2, and 2.3 V with the corresponding reduction peak starting at 1.5 V, and at 3.4 V with the corresponding reduction peak at 3.3 V. Based on the stoichiometry $\text{Na}_{2.55}\text{V}_6\text{O}_{16}$, vanadium has an oxidation state of $<5+$, meaning that it can be further oxidized. The oxidation peak in the CV at 3.4 V indicates that further oxidation is possible. This is confirmed by XPS measurements: after charging the cell to 4.0 V, the content of V^{5+} increases to 87%, while sodium is being removed from the structure. The multiple peak separation can be attributed to the fact that the sodium ions occupy different positions within the lattice structure, which results in different oxidation/reduction potentials of the respective vanadium ions when sodium ions are (de-)inserted.^[39] When the material is again discharged until the first major discharge plateau at 2.4 V (Figure 6), the expected reduction in the average oxidation state of vanadium was confirmed (Figure 6). After discharging the cell completely to 1.3 V, all vanadium is reduced to V^{4+} . As can be seen in Figure 4, the reduction peak starting at 1.5 V in the second cycle is not as pronounced as the one in the first cycle, indicating that less charge is being transferred. This means that part of the charge transfer is irreversible.

2.3. Half-Cell Performance

The initial galvanostatic charge/discharge curves show capacities of 41 and 217 mAhg^{-1} , respectively, for a current rate of 20 mA g^{-1} (0.5C with respect to the insertion of one Na^+)

(Figure 6). This means that sodium can be removed from this structure. For reasons of charge neutrality, vanadium would need to be oxidized. According to the XPS measurements, the content of V^{5+} increases from 75% to 87%, which corresponds to a capacity of 31 mAhg^{-1} . The difference to the observed 41 mAhg^{-1} can come either from a developing oxygen deficiency in the structure or from a minor discharge of the cell during the time it took to disconnect it from the potentiostat, bring it into the glovebox, and open it to conduct the XPS measurement.

When charging and then discharging the cell to 1.3 V, the V^{5+} content decreases from 75% to 0%. This corresponds to a reduction of 4.5 V^{5+} to V^{4+} , and thus an insertion of 4.5 Na ions.

Assuming a capacity per Na ion of 43 mAhg^{-1} (on the basis of $\text{Na}_{2.55}\text{V}_6\text{O}_{16}$), this gives a discharge capacity of 194 mAhg^{-1} , which is based on reversible vanadium oxidation/reduction. For this comparison the capacity of the removed Na^+ during the initial charge (41 mAhg^{-1}) has to be added to the expected discharge capacity to account for the Na^+ deinsertion upon the first charge. This sum gives 235 mAhg^{-1} ($194 + 41 \text{ mAhg}^{-1}$); this value can (almost exactly) be observed in the first discharge. In subsequent cycles, the discharge capacities decrease. The reasons for this irreversible capacity loss are not yet fully understood. Further investigations using in situ X-ray diffraction measurements are underway to clarify this.

A pronounced plateau can be seen in the first discharge at 2.4 V, presumably due to partial reduction of V^{5+} to V^{4+} , corresponding well with the reduction peak in the cyclic voltammogram. Consequently, the plateau at 1.5 V, which is in accordance with the peak in the CV, could correspond to the reduction of the remaining V^{5+} to V^{4+} . As can be seen in Figure 6, the plateau becomes less pronounced over time. The energy density for the first discharge at 0.5C is 431 $\text{Wh}^{-1}\text{kg}^{-1}$. This is easily one of the highest values for NIBs ever reported^[6]. One of the highest energy densities reported is probably for the P2-type $\text{Na}_x[\text{Fe}_{1/2}\text{Mn}_{1/2}]\text{O}_2$ with 520 Whg^{-1} for 1/20C; however, for 0.5C, the energy density decreases to approximately 360 Whg^{-1} .^[6] Recently, Kang and co-workers claimed the highest energy density in NIBs by showing that $\text{Na}_{1.5}\text{VPO}_{4.8}\text{F}_{0.7}$ can provide energy densities of approximately 500 $\text{Wh}^{-1}\text{kg}^{-1}$ at 1/10C, while it seems comparable to NVO at comparable C-rates. For sodium vanadium oxides, the material with the best energy density reported, $\text{NaV}_6\text{O}_{15}$, has an approximate energy density of 300 $\text{Wh}^{-1}\text{kg}^{-1}$ for 20 mA g^{-1} .^[24] Moreover, the

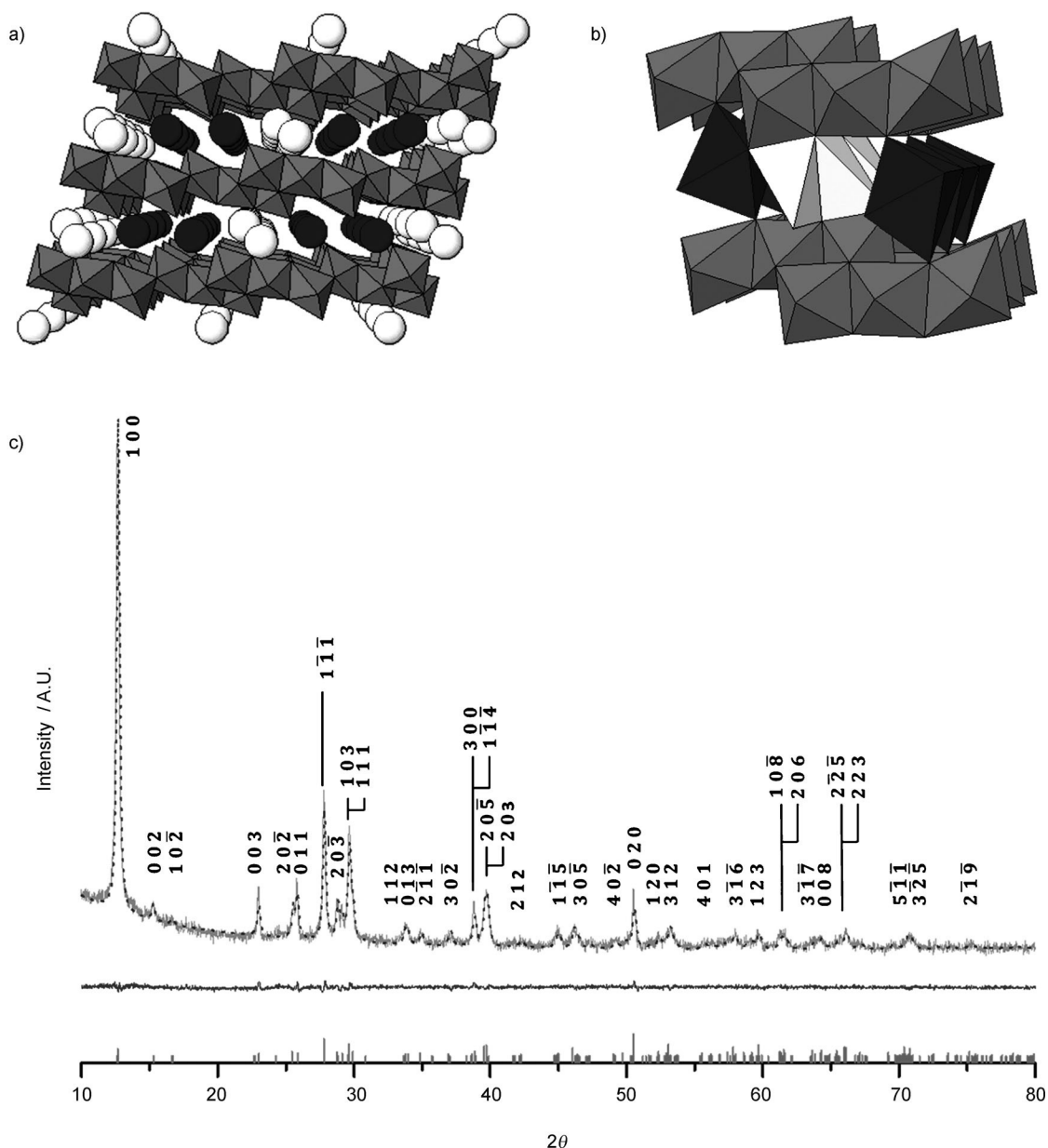


Figure 3. Structure of $\text{Na}_{2.55}\text{V}_6\text{O}_{16} \cdot 0.6\text{H}_2\text{O}$: $\text{Na}_{\text{octahedral}}$: black, $\text{Na}_{\text{tetrahedral}}$: white, O: grey, V: not visible, placed in the center of the grey octahedron: a) structure overview, b) close-up and depiction of the octahedral/tetrahedral surrounding of Na. c) X-ray diffraction measurement on NVO.

energy density for NVO is as much as 80% of the energy density of the commercially available lithium iron phosphate ($530 \text{ Wh}^{-1}\text{kg}^{-1}$), and close to the energy density of LiMn_2O_4 ($450 \text{ Wh}^{-1}\text{kg}^{-1}$) for lithium-ion batteries, as calculated for a half-cell. We believe that by further engineering our NVO system, similar energy densities as for current lithium iron phosphate systems in LIBs can be achieved.

For 100 mA g^{-1} , which corresponds to a C-rate of 2.3 with respect to the (de-)insertion of one sodium ion per formula unit and approximately 0.5C based on a discharge capacity of $217 \text{ mAh}^{-1}\text{g}^{-1}$ (Figure 6), an initial discharge capacity of $194 \text{ mAh}^{-1}\text{g}^{-1}$ is reached; this corresponds to the insertion of 4.5 Na^+ per formula unit. The discharge capacity declines to $178 \text{ mAh}^{-1}\text{g}^{-1}$ for the second discharge. For the 50th cycle,

the provided capacity was $103 \text{ mAh}^{-1}\text{g}^{-1}$, and after 100 cycles, the capacity was still $79 \text{ mAh}^{-1}\text{g}^{-1}$. This results in a cycle stability of 99.1% after 100 cycles. At higher current rates, the capacities slightly decrease, but the cycle stability increases (see Supporting Information, SI).

For practical applications such as, for example, hand-held devices, laptops or mobile phones, the charging time is distinctly more important than the discharging time. Thus, high current rates for charging are desirable, even if the energy provided by discharge is given off at lower currents. Therefore, the material's behavior at fast charge (200 and $400 \text{ mAh}^{-1}\text{g}^{-1}$) and slow discharge ($50 \text{ mAh}^{-1}\text{g}^{-1}$) was tested (SI). For both tests, a better initial discharge capacity could be achieved when compared to cells that were charged and discharged at

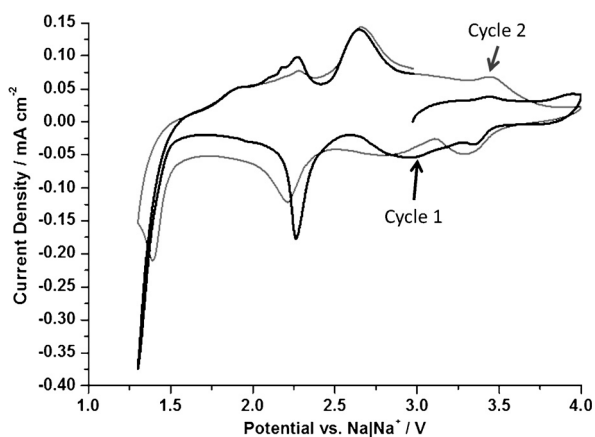


Figure 4. Cyclic voltammogram of NVO in a half-cell versus Na; electrolyte: 1 M NaClO₄ ethylene carbonate/propylene carbonate (1:1 wt%); scan rate 0.1 mV s⁻¹.

the respective high current rates. The capacities after 100 cycles are comparable (i.e. 72 and 64 mA h⁻¹ g⁻¹ respectively).

When compared to the work carried out on this material by Wang et al.^[40] in the field of LIBs, the capacity obtained for NIBs is slightly lower. The cycle stability, however, is significant-

ly lower for the case of NIBs. This could be due to the higher reactivity of the Na metal in the NIB system, leading to an increased decomposition of electrolyte, or decomposition of the conducting salt NaClO₄ at voltages of up to 4 V, as opposed to the more stable LiPF₆. Another possibility, namely an increased strain on the crystal structure of Na⁺, as opposed to Li⁺ (de-)insertion, and a resulting structural deterioration, seems to be implausible due to the data for symmetric full-cell measurements discussed below.

2.4. Symmetric Full Cell

As sodium can be removed from the structure on the first charging process, this material can be employed in symmetric full cells. The optimum voltage range has been found to be between 0–2.8 V. Charge/discharge curves can be seen in Figure 7, showing an initial discharge capacity of 140 mA h⁻¹ g⁻¹ with respect to the anode. Thus, integrating the first discharge curve shows an energy density of 140 Wh⁻¹ kg⁻¹; both capacity and energy density exceed other symmetric sodium-ion batteries reported in the literature. Among the most prominent systems are NASICON symmetric cells, which exhibit an energy density of approximately 70–80 Wh⁻¹ kg⁻¹ at room temperature.^[33–35] For LIBs, not many symmetric systems are known; there are a few reports, however, on the use of lithium vanadium phosphates. Their energy density could recently be improved to approximately the same value that is reported here for NVO.^[41]

As the anode in this symmetric cell takes up more sodium than the same mass of cathodic NVO provides, the capacity of the symmetric cells obviously depends on the cathode:anode weight ratio. Theoretically, the capacity should increase up to a maximum. This maximum is reached when the amount of sodium that the cathode provides equals the amount of sodium that the anode can take in upon charge. This has been confirmed by experiments (SI). When comparing the discharge capacities of the 15th cycle, that is, after stabilization of the system, an increase could be observed up to a mass ratio of approximately 8:1. From here, saturation could be observed and the capacities did not increase further with an increase in the mass ratio.

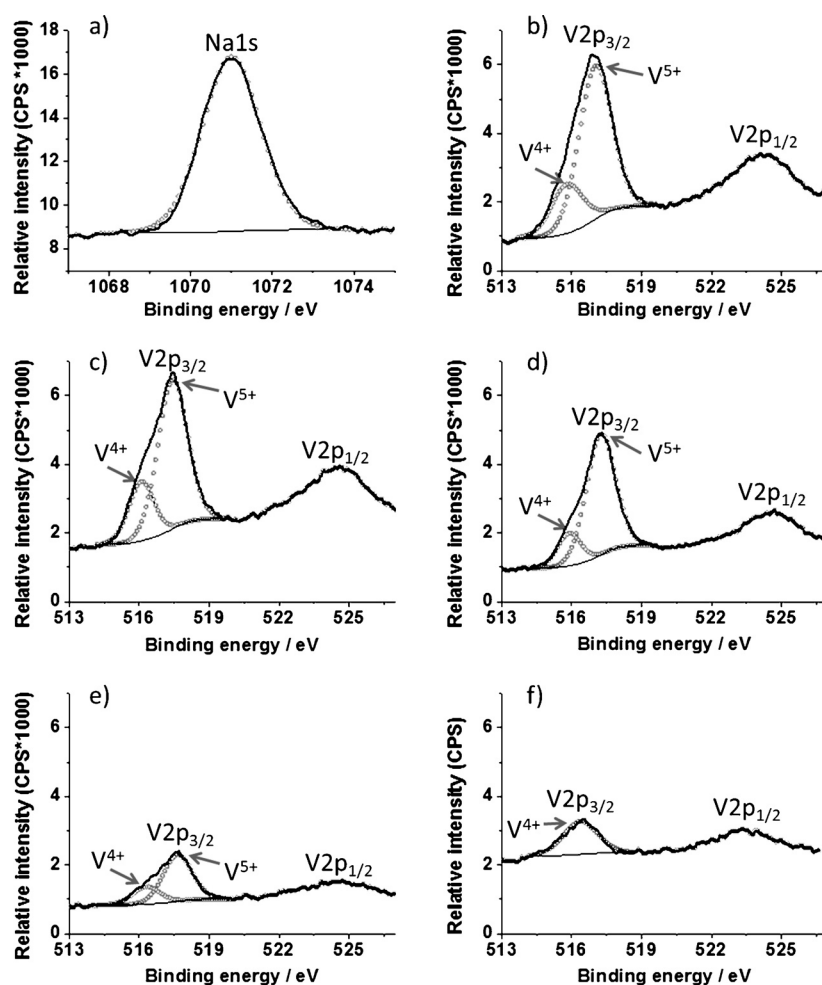


Figure 5. XPS data for NVO at different stages: a) Na 1s peak of the blind cell, b) V 2p peaks of NVO powder, c) blind cell, d) charged cell, e) a cell that was discharged until the first plateau, and f) a discharged cell.

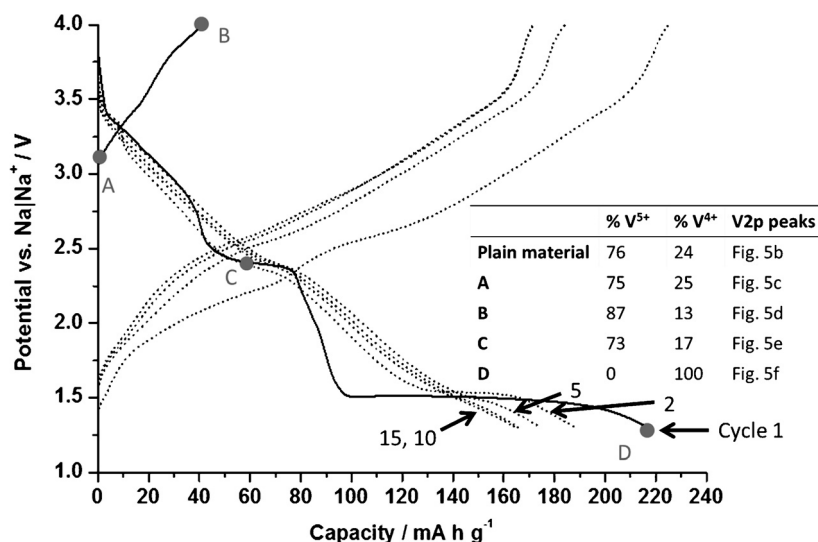


Figure 6. Charge/discharge profile of NVO at 20 mA g⁻¹; electrolyte: 1 M NaClO₄ ethylene carbonate/propylene carbonate (1:1 wt %). Inset: Percentages of V⁵⁺ and V⁴⁺ in NVO at different stages.

and shows significant capacities, even at current rates as high as 800 mA g⁻¹. Thus, NVO belongs to the best materials reported with regard to half-cell performance. Moreover, as sodium ions can be removed from the initial structure, NVO can be used for symmetric sodium-ion full cells. The capacity increases with increasing cathode:anode weight ratio. A maximum is reached for a ratio of 8:1, with an initial capacity of 140 mA h⁻¹ g⁻¹ and an energy density of 140 Wh⁻¹ kg⁻¹, with respect to the anode, that is, the lighter electrode. The easy synthesis and good performance make NVO a promising material for sodium-ion batteries.

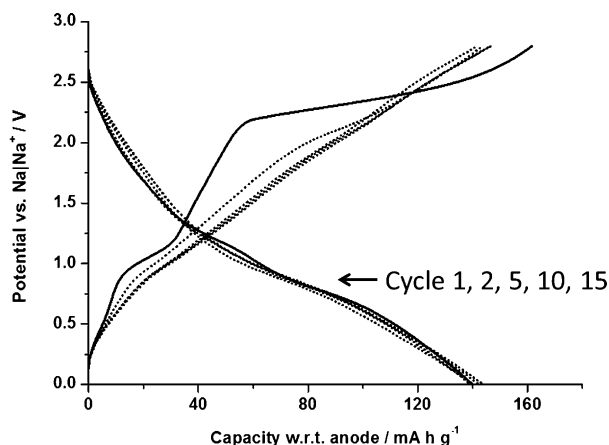


Figure 7. Charge/discharge profile for a symmetric cell with an active mass ratio of 8:1 (NVO | electrolyte | NVO) at 50 mA g⁻¹; electrolyte: 1 M NaClO₄ ethylene carbonate/propylene carbonate (1:1 wt %).

After 100 cycles, the capacity of the symmetric full cell was still 118 mA h⁻¹ g⁻¹, which corresponds to a cycle stability of 99.8% (Figure 8). Compared to the lower cycle stability of the Na-metal | electrolyte | NVO half cells, the high cycle stability of the symmetric full cell indicates that the main reason for capacity loss in half cells is attributable to side reactions involving metallic sodium, or to decomposition reactions at the higher voltages in the half-cells. Further investigations to clarify this matter are underway.

3. Conclusions

Sodium vanadium oxide for sodium-ion batteries can be synthesized using an easily scalable hydrothermal method, yielding multi-crystalline nanowires. In half cells versus Na metal, NVO provides initial capacities of 217 mA h⁻¹ g⁻¹ for 20 mA g⁻¹

Experimental Section

Synthesis

NVO was synthesized by mixing 20 mL of a 0.01 M solution of vanadium pentoxide (Sigma Aldrich, 98%) in deionized (DI) water with 20 mL of a 0.01 M solution of sodium hydroxide (Sigma Aldrich, 98%) and stirring it overnight so that an orange-brownish solution was obtained. Then, the 40 mL solution was transferred to a 50 mL Teflon lined stainless steel autoclave, which was sealed and heated to 180 °C for 48 h. The precipitate was filtered, washed thoroughly with DI water, and dried at 80 °C for 4 h to obtain the NVO powder. Finally, the product was annealed in air for 2 h at 400 °C.

Characterizations

The synthesis product's crystal structure was analysed by powder XRD using a Bruker X-ray diffractometer with Cu_{Kα} radiation. A step size of 0.0196° was used within a range 10–80° for 2 Theta with

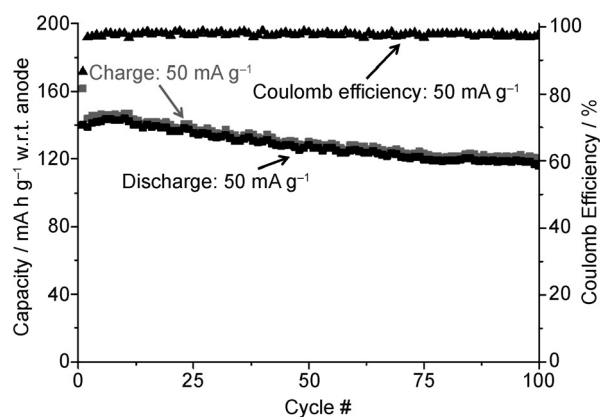


Figure 8. Cycle stability of a symmetric cell (NVO | electrolyte | NVO) with a weight ratio of 8:1 at 50 mA g⁻¹; electrolyte: 1 M NaClO₄ ethylene carbonate/propylene carbonate (1:1 wt %).

0.3 s per step. The XRD patterns obtained were analyzed by Rietveld phase analysis using the Topas version 3 software. The product's morphology was elucidated by FESEM (JEOL JSM-7600F, 5 kV) and TEM (JEOL 2100F, 200 kV). Elemental compositions were determined by micro-XRF analysis (Bruker/M4 Tornado), using Rh as the X-ray source (50 kV, 200 μm). The water content was determined by TGA (MettlerToledo STARe TGA/DSC1). XPS measurements on the samples were carried out with a Kratos Axis Ultra-spectrometer using a focused monochromatized $\text{Al}_{K\alpha}$ radiation ($h\nu = 1486.6$ eV, 15 kV/10 mA). The spectrometer was calibrated using the photoemission line Ag $3d_{5/2}$ [binding energy (BE) 368.26 eV]. For the Ag $3d_{5/2}$ line, the full width at half maximum (FWHM) was 0.61 eV under the recording conditions. The analyzed area of the samples was $300 \times 700 \mu\text{m}^2$. The XPS analysis was performed at room temperature at a take-off angle relative to the surface holder of 90° . All the measurements were performed under charge neutralization. The pressure in the analysis chamber was about 3×10^{-7} Pa. The BE scale was calibrated from the carbon contamination using the C1s peak at 284.5 eV. The spectra were analyzed using a peak synthesis program (CasaXPS version 2.3.15), fitting with distribution of Gaussian (80%), Lorentzian (20%), and Shirley background.

Electrochemistry

Composite electrodes were prepared by mixing NVO with acetylene black (Alfa Aesar, >99%) and polyvinylidene fluoride (PVDF, Arkema, Kynar HSV 900) binder at a weight ratio of 60:20:20 with *N*-methyl-2-pyrrolidone (NMP) to form a homogeneous slurry. This mixture was coated on an Al foil using a doctor blade; the coating was dried in air at 80°C to remove the NMP. The coating was punched into pieces with a diameter of 16 mm, which were then roll-pressed and dried at 110°C under vacuum. For half cells, these electrodes were then assembled in 2016 coin cells using circular sodium pieces (16 mm) as anodes. For full cells, the punched electrodes were used as both cathode and anode. In both cases, the electrodes were separated by a glass fiber (Whatman) swollen with an electrolyte consisting of 1 M NaClO_4 (Sigma Aldrich, >98%) in propylene carbonate (PC)/ethylene carbonate (EC), 1:1 weight% (PC: Sigma Aldrich, $\geq 99.7\%$, EC: Sigma Aldrich 99%). Cyclic voltammetry studies were carried out using a Biologic VMP3 potentiostat; for galvanostatic testing a Neware battery tester system was used. Capacities are reported in milliampere hour per gram ($\text{mAh}^{-1}\text{g}^{-1}$) with respect to the mass of the active material. For the symmetric cells, the capacity is reported with respect to the anode. For C-rate calculations, the first discharge capacity at 20 mA g^{-1} , that is, $217 \text{ mAh}^{-1}\text{g}^{-1}$, can be used as the basis. Due to the significant capacity decrease in the first cycles and lower initial discharge capacities for other current rates, this may seem a bit arbitrary. Alternatively, the C-rate could be calculated on the basis of the (de-)insertion of one Na^+ per formula unit, that is, $43 \text{ mAh}^{-1}\text{g}^{-1}$. In this work, both alternatives are reported.

Acknowledgements

The authors thank Jochen Friedl for insightful discussions and Jan Geder for his help in conducting the TGA measurements. This work was financially supported by the Singapore National Research Foundation under its Campus for Research Excellence and Technological Enterprise (CREATE) program.

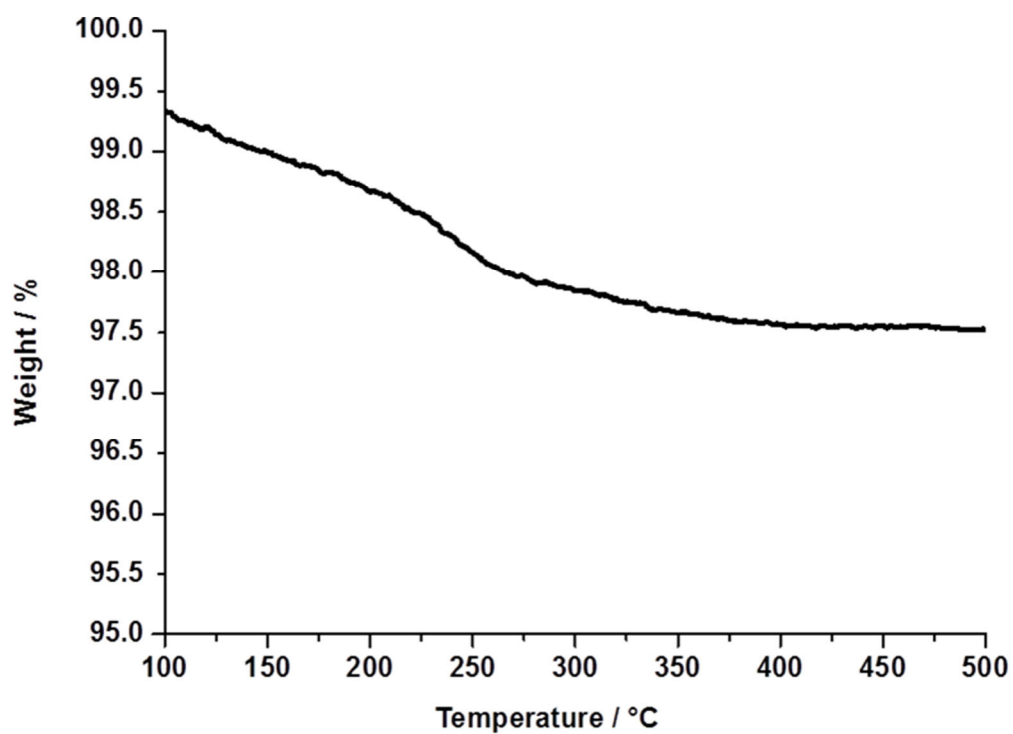
Keywords: cathode materials · energy storage · sodium-ion batteries · sodium vanadium oxide · symmetric batteries

- [1] V. Palomares, P. Serras, I. Villaluenga, K. B. Hueso, J. Carretero-González, T. Rojo, *Energy Environ. Sci.* **2012**, *5*, 5884–5901.
- [2] Jackson, I.: 2.4.3 The crust. (Ed.: K. Fuchs, H. Soffel). *SpringerMaterials—The Landolt-Börnstein Database* (<http://www.springermaterials.com>). DOI: 10.1007/10201917_63.
- [3] Y. Wang, X. Yu, S. Xu, J. Bai, R. Xiao, Y.-S. Hu, H. Li, X.-Q. Yang, L. Chen, X. Huang, *Nat. Commun.* **2013**, *4*, 2365.
- [4] S. Komaba, W. Murata, T. Ishikawa, N. Yabuuchi, T. Ozeki, T. Nakayama, A. Ogata, K. Gotoh, K. Fujiwara, *Adv. Funct. Mater.* **2011**, *21*, 3859–3867.
- [5] S. Komaba, T. Ishikawa, N. Yabuuchi, W. Murata, A. Ito, Y. Ohsawa, *ACS Appl. Mater. Interfaces* **2011**, *3*, 4165–4168.
- [6] N. Yabuuchi, M. Kajiyama, J. Iwatate, H. Nishikawa, S. Hitomi, R. Okuyama, R. Usui, Y. Yamada, S. Komaba, *Nat. Mater.* **2012**, *11*, 512–517.
- [7] V. L. Chevrier, G. Ceder, *J. Electrochem. Soc.* **2011**, *158*, A1011–A1014.
- [8] H. Pan, Y.-S. Hu, L. Chen, *Energy Environ. Sci.* **2013**, *6*, 2338–2360.
- [9] V. Palomares, M. Casas-Cabanas, E. Castillo-Martínez, M. H. Han, T. Rojo, *Energy Environ. Sci.* **2013**, *6*, 2312–2337.
- [10] R. Berthelot, D. Carlier, C. Delmas, *Nat. Mater.* **2011**, *10*, 74–80.
- [11] A. Mendiboure, C. Delmas, P. Hagenmuller, *J. Solid State Chem.* **1985**, *57*, 323–331.
- [12] A. Caballero, L. Hernán, J. Morales, L. Sánchez, J. Santos, *J. Solid State Chem.* **2003**, *174*, 365–371.
- [13] X. Ma, H. Chen, G. Ceder, *J. Electrochem. Soc.* **2011**, *158*, A1307–A1312.
- [14] H. Kim, D. J. Kim, D.-H. Seo, M. S. Yeom, K. Kang, D. K. Kim, Y. Jung, *Chem. Mater.* **2012**, *24*, 1205–1211.
- [15] F. Sauvage, L. Laffont, J.-M. Tarascon, E. Baudrin, *Inorg. Chem.* **2007**, *46*, 3289–3294.
- [16] N. Bucher, S. Hartung, A. Nagasubramanian, Y. L. Cheah, H. E. Hoster, S. Madhavi, *ACS Appl. Mater. Interfaces* **2014**, *6*, 8059–8065.
- [17] N. Bucher, S. Hartung, I. Gocheva, Y. L. Cheah, M. Srinivasan, H. E. Hoster, *J. Solid State Electrochem.* **2013**, *17*, 1923–1929.
- [18] Y. L. Cheah, V. Aravindan, S. Madhavi, *J. Electrochem. Soc.* **2012**, *159*, A273–A280.
- [19] Y. L. Cheah, V. Aravindan, S. Madhavi, *J. Electrochem. Soc.* **2013**, *160*, A1016–A1024.
- [20] N. A. Chernova, M. Roppolo, A. C. Dillon, M. S. Whittingham, *J. Mater. Chem.* **2009**, *19*, 2526–2552.
- [21] C. Ban, N. A. Chernova, M. S. Whittingham, *Electrochem. Commun.* **2009**, *11*, 522–525.
- [22] S. Tepavcevic, H. Xiong, V. R. Stamenkovic, X. Zuo, M. Balasubramanian, V. B. Prakapenka, C. S. Johnson, T. Rajh, *ACS Nano* **2012**, *6*, 530–538.
- [23] M. Guignard, C. Didier, J. Darriet, P. Bordet, E. Elkaim, C. Delmas, *Nat. Mater.* **2012**, *11*, 1–7.
- [24] H. Liu, H. Zhou, L. Chen, Z. Tang, W. Yang, *J. Power Sources* **2011**, *196*, 814–819.
- [25] P. Novák, W. Scheifele, O. Haas, *J. Power Sources* **1995**, *54*, 479–482.
- [26] K. West, B. Zachau-Christiansen, T. Jacobsen, *Solid State Ionics* **1988**, *28*, 1128–1131.
- [27] G. Wang, G. Pistoia, *J. Electroanal. Chem.* **1991**, *302*, 275–278.
- [28] H. He, G. Jin, H. Wang, X. Huang, Z. Chen, D. Sun, Y. Tang, *J. Mater. Chem. A* **2014**, *2*, 3563–3570.
- [29] S.-M. Oh, S.-T. Myung, J. Hassoun, B. Scrosati, Y.-K. Sun, *Electrochem. Commun.* **2012**, *22*, 149–152.
- [30] D. Kim, E. Lee, M. Slater, W. Lu, S. Rood, C. S. Johnson, *Electrochem. Commun.* **2012**, *18*, 66–69.
- [31] A. Abouimrane, W. Weng, H. Eltayeb, Y. Cui, J. Niklas, O. Poluektov, K. Amine, *Energy Environ. Sci.* **2012**, *5*, 9632–9638.
- [32] S.-M. Oh, S.-T. Myung, M.-W. Jang, B. Scrosati, J. Hassoun, Y.-K. Sun, *Phys. Chem. Chem. Phys.* **2013**, *15*, 3827–3833.
- [33] K. Saravanan, C. W. Mason, A. Rudola, K. H. Wong, P. Balaya, *Adv. Energy Mater.* **2013**, *3*, 444–450.
- [34] L. S. Plashnitsa, E. Kobayashi, Y. Noguchi, S. Okada, J. Yamaki, *J. Electrochem. Soc.* **2010**, *157*, A536–A543.
- [35] Y. Noguchi, E. Kobayashi, L. S. Plashnitsa, S. Okada, J. Yamaki, *Electrochim. Acta* **2013**, *101*, 59–65.

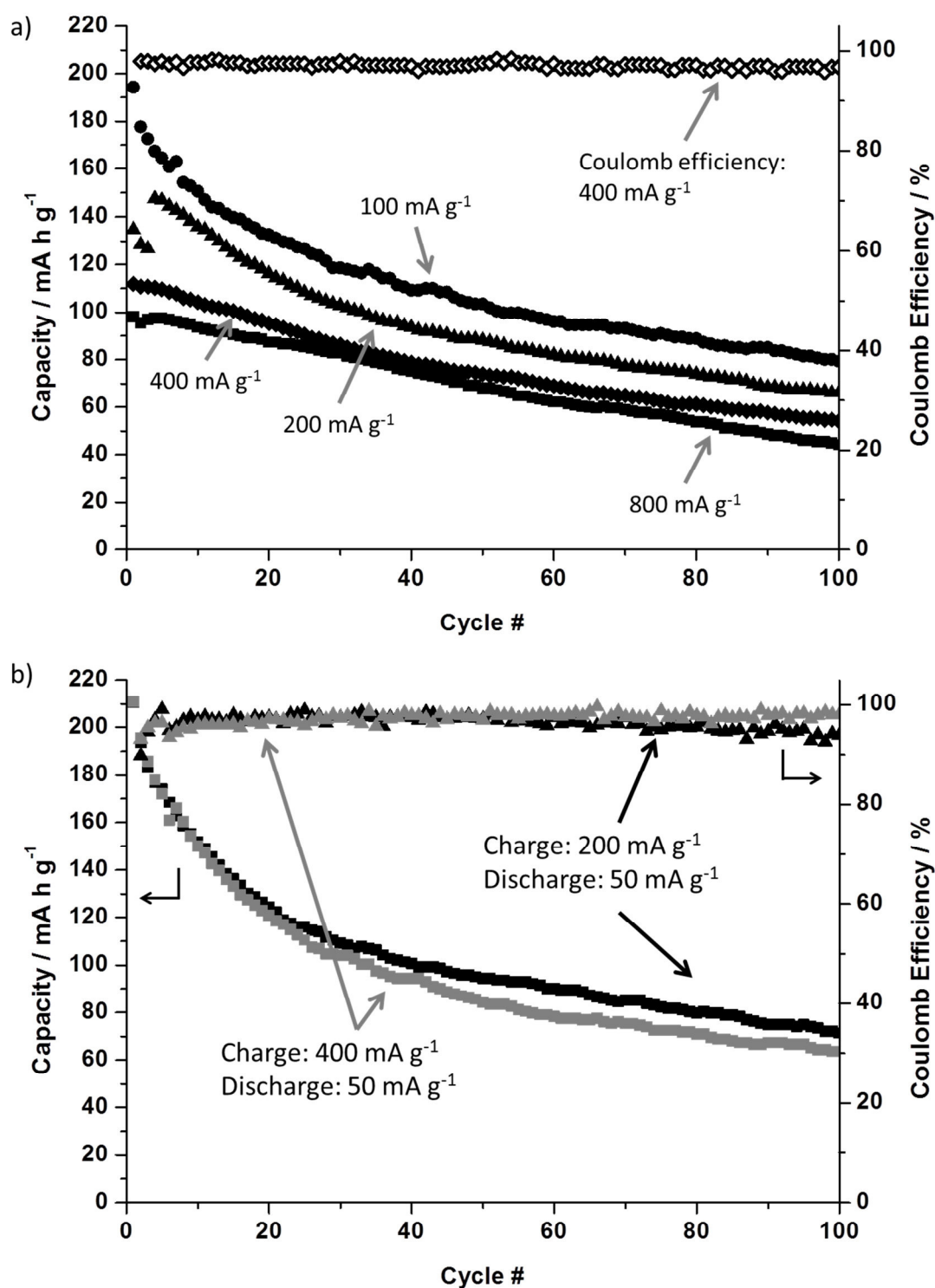
- [36] W. Avansi, Jr., C. Ribeiro, E. R. Leite, V. R. Mastelaro, *Mater. Chem. Phys.* **2011**, *127*, 56–61.
- [37] J. Yu, J. C. Yu, W. Ho, L. Wu, X. Wang, *J. Am. Chem. Soc.* **2004**, *126*, 3422–3423.
- [38] G.-T. Zhou, X. Wang, J. C. Yu, *Cryst. Growth Des.* **2005**, *5*, 969–974.
- [39] D. Zhou, S. Liu, H. Wang, G. Yan, *J. Power Sources* **2013**, *227*, 111–117.
- [40] H. Wang, W. Wang, Y. Ren, K. Huang, S. Liu, *J. Power Sources* **2012**, *199*, 263–269.
- [41] E. Kobayashi, A. Kitajou, S. Okada, J. Yamaki, *J. Power Sources* **2013**, *244*, 312–317.

Received: February 8, 2014

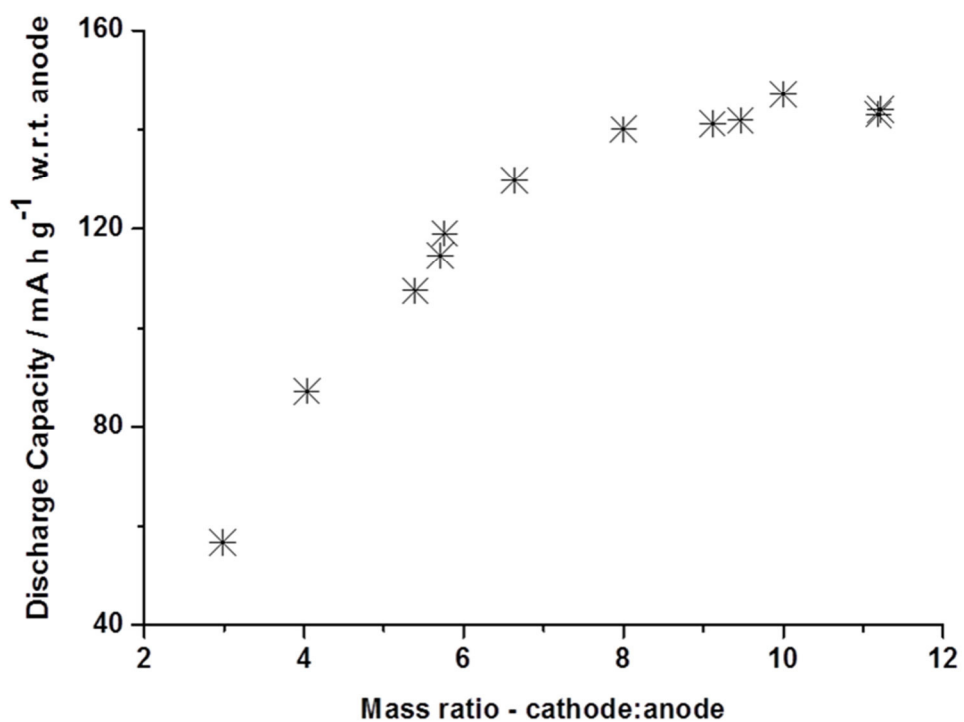
Revised: June 2, 2014



Supplementary information; Figure 1. Thermogravimetric analysis of Na_{2.55}V₆O₁₆·0.6H₂O; heating rate: 5 °C / min in argon atmosphere



Supplementary information; Figure 2. a) Cycle stability of NVO at 100, 200, 400 and 800 mA g⁻¹ in half-cells vs. Na; electrolyte: 1 M NaClO₄ in ethylene carbonate / propylene carbonate (1:1 wt %); Coulomb efficiency is defined as discharge capacity / charge capacity; efficiency of the first cycle is 627%, b) Cycle stability of NVO with fast charge / slow discharge in half-cells vs. Na; electrolyte: 1 M NaClO₄ in ethylene carbonate / propylene carbonate (1:1 wt %)



Supplementary information; Figure 3. Discharge capacity of symmetric cells (NVO | electrolyte | NVO) with different weight ratios at cycle 15; electrolyte: 1 M NaClO₄ in ethylene carbonate / propylene carbonate (1:1 wt %)

5.2 Electrochemical cell for *in operando* X-ray diffraction measurements on a conventional X-ray diffractometer

In this chapter, the note “Electrochemical cell for *in operando* X-ray diffraction measurements on a conventional X-ray diffractometer” (Rev. Sci. Instrum. 2014, 86, 086102) is presented. The construction of this electrochemical cell for *in operando* XRD measurements enabled our group, as the first group in Singapore, to perform XRD measurements of lithium- and sodium-ion battery materials during cycling. This work was jointly performed by S. Hartung and N. Bucher. S. Hartung focussed on the verification and testing of the cell and drafted the manuscript. N. Bucher focussed on the development and construction of the cell.

As described in the previous chapter, structural changes are a potential cause of low cycling stability of battery materials. In order to learn more about the structural changes of the above-mentioned material ($\text{Na}_{2.55}\text{V}_6\text{O}_{16}$), XRD is the method of choice. *Ex situ* XRD measurements of battery materials, *i.e.* measurements of the active material at various states of (dis-)charge, are possible, but not only practically limit the number of data points, but could also entail problems with regard to comparability. Moreover, some materials are not air-stable at various states of charge, so that special precautions need to be taken. *In operando* measurements eliminate these problems, as they continuously probe the same material during (dis-)charge.

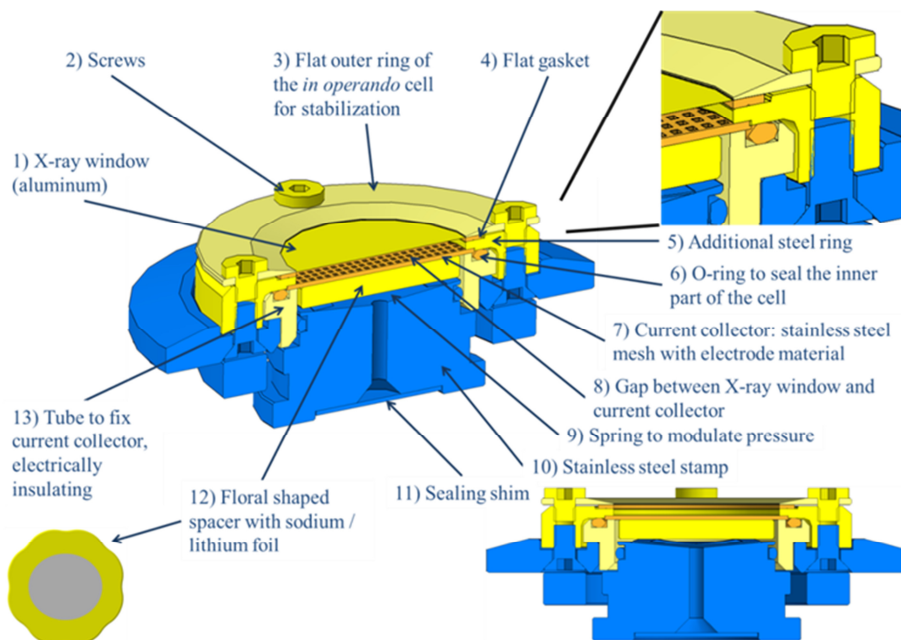


Figure 13. (Figure 1 in the publication). Setup of the electrochemical *in operando* XRD cell.

Various factors need to be considered in the construction of such a cell. It needs to be airtight, as otherwise the ‘content’ of the cell, *i.e.* active material and

alkali metal in half-cells, would react with H_2O , O_2 or N_2 in the air. Thus, the cell needs to be sealed from the outer atmosphere. As the X-rays of the diffractometer need to penetrate the cell through an X-ray window, the window material should ideally not interfere with the electrochemical reactions in the battery, absorb as little radiation as possible, and give rise to limited X-ray reflections which could overlap with the reflections of the material that is being probed. In the cell presented here very thin ($6\ \mu\text{m}$) aluminium foil can be employed as X-ray window. A schematic of the cell can be seen in Figure 13. As the X-ray window and the current collector are separated by a gap, electrical current is not dissipated via the X-ray window, which reduces corrosion. Mechanical pressure induced while assembling the cell and during cycling is accommodated by the current collector, so that requirements in terms of mechanical stability can be greatly reduced for the X-ray window. The spacer that is placed onto the Li/Na foil was constructed in a floral shape, so that its outer edges touch the casing wall to prevent lateral movements, and excess electrolyte can 'leave' the inner part of the cell through these indentations when the cell is closed, which further reduces pressure on the Al foil. Due to the low thickness of the Al foil, both the signal intensity and the signal-to-noise ratio are excellent. First measurements of $\text{Na}_{2.55}\text{V}_6\text{O}_{16}$, which was introduced in the previous chapter, were demonstrated. The results indicate reversibility of structural processes when this material is cycled between $4.0\ \text{V} - 1.6\ \text{V}$.

The construction of this XRD cell enables *in operando* measurements during electrochemical cycling and thus allows monitoring structural processes during the insertion and extraction of Na^+ into (from) the respective host structure.

Note: Electrochemical cell for in operando X-ray diffraction measurements on a conventional X-ray diffractometer

Steffen Hartung, Nicolas Bucher, Ramona Bucher, Madhavi Srinivasan

Reproduced with permission from Review of Scientific Instruments, 2015, Volume 86, Issue 8, 086102. Copyright 2015, AIP Publishing LLC.

The publication can be found under the following weblink:

<http://dx.doi.org/10.1063/1.4926465>

Note: Electrochemical cell for *in operando* X-ray diffraction measurements on a conventional X-ray diffractometer

Steffen Hartung,^{1,2,3,a)} Nicolas Bucher,^{1,2,3,a)} Ramona Bucher,¹ and Madhavi Srinivasan^{1,3}

¹TUM CREATE, Singapore 138602, Singapore

²Technical University of Munich, Garching 85748, Germany

³School of Materials Science and Engineering, Nanyang Technological University, Singapore 639798, Singapore

(Received 29 April 2015; accepted 28 June 2015; published online 10 August 2015)

Electrochemical *in operando* X-ray diffraction (XRD) is a powerful method to analyze structural changes of energy storage materials while inserting/de-inserting charge carriers, such as Li- or Na-ions, into/from a host structure. The design of an XRD *in operando* cell is presented, which enables the use of thin (6 μm) aluminum foil as X-ray window as a non-toxic alternative to conventional beryllium windows. Owing to the reduced thickness, diffraction patterns and their changes during cycling can be observed with excellent quality, which was demonstrated for two cathode materials for sodium-ion batteries in a half-cell set-up, $\text{P2-Na}_{0.7}\text{MnO}_2$ and $\text{Na}_{2.55}\text{V}_6\text{O}_{16}\cdot 0.6\text{H}_2\text{O}$. © 2015 AIP Publishing LLC. [<http://dx.doi.org/10.1063/1.4926465>]

As electrochemical energy storage devices are being intensely researched for a variety of applications, approaches to optimize their performance are of high commercial interest. The underlying mechanism of energy storage for many systems is the intercalation of ions, e.g., Li^+ and Na^+ , into a given crystal structure.^{1–3} Thus, elucidating potential structural changes during (de-)insertion might go a long way in explaining observed electrochemical phenomena like capacity fading, and therefore deliver important information for better energy storage devices. Consequently, experimental setups have been developed to study these changes *in operando*.^{4–6} For the observation of crystal structure changes, the method of choice is X-ray diffraction.

For electrochemical *in operando* XRD measurements, a setup needs to fulfill several requirements. An airtight system is crucial to prevent a reaction of air with the components of the electrochemical cell, particularly for half-cell setups that contain metallic lithium or sodium. The window, shielding the electrochemically active components from the outer atmosphere, should be as thin as possible and needs to have a low X-ray absorption coefficient to minimize X-ray absorption, and thus a decrease in signal intensity. Ideally, of course, non-toxic materials are preferred.

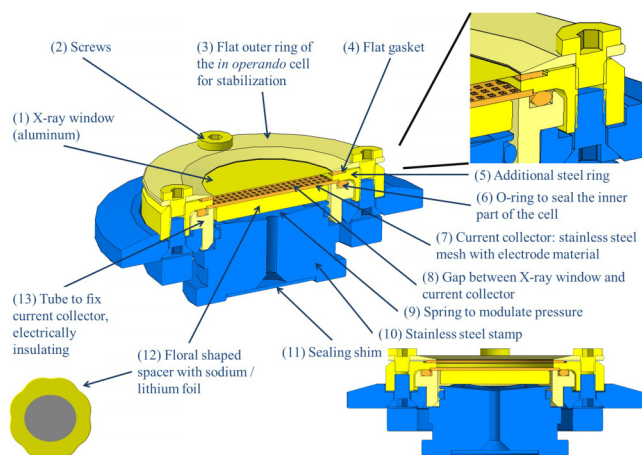
Even though commercial cell setups are available, they have some shortcomings. In a typical setup, the active material, which is to be measured during cycling in a half-cell setup with lithium or sodium as the negative electrode, is pressed onto the X-ray window. This is typically aluminum-coated beryllium, which serves both as current collector and as X-ray window due to its low X-ray absorption coefficient. Moreover, as the active material is mechanically pressed against the X-ray window, mechanical stability is desired to prevent fissures in the window. This can be achieved by using a rigid beryllium window with a typical thickness of around 125 μm . The main

drawbacks of beryllium, however, are its toxicity and high cost. Furthermore, dissipating the current via the beryllium as it is the case in this setup makes the window more susceptible to electrochemically induced corrosion, as beryllium dissolves at voltages above 3 V.⁷ After early studies by Chianelli *et al.* in 1978,⁸ several approaches to tailor *in operando* XRD cells to specific needs have been proposed.^{5,7,9–12}

This work presents a new cell setup developed by our group to address the obstacles for *in operando* diffraction measurements mentioned above. In this cell, the X-ray window and current collector are separated by a gap (see Figure 1 (8)). This setup has two main advantages. First, as the current is no longer dissipated via the X-ray window, corrosion is decreased and lifetime of the window, and thus possible *in operando* measurement time, can be extended. Second, mechanical pressure during cell assembly and subsequent cycling is no longer exerted on the X-ray window, but on the current collector. Thus, requirements in terms of mechanical stability can be greatly reduced for the X-ray window. As a consequence, beryllium can be replaced by the cheaper, non-toxic aluminum. Moreover, the thickness of the X-ray window can be reduced, so that X-ray reflection of the window material is minimized, and signal quality of the battery material is enhanced.

For the approach presented here, an aluminum foil with a thickness of 6 μm was used. The active material, together with teflonized acetylene black as binder, and activated carbon as conducting agent, was pressed into a stainless steel grid, which acted as the current collector (component (7) in Figure 1). After mounting the window (i.e., assembling parts (1)–(5)), the cell is turned around so that the inner part faces upward, and component (7) is placed onto (5), and then held in place by (13). A separator and lithium/sodium disc are placed onto (7), followed by a stainless steel spacer (12) in a floral shape—the outer edges touch the walls (component (13)), which inhibits lateral movement and prevents the electrodes from slipping out of position. The indentations ensure that the electrolyte, which is added after (12) is in place, can penetrate past the spacer and

^{a)}S. Hartung and N. Bucher contributed equally to this work.

FIG. 1. Setup of the new *in operando* cell.

soak the separator and active material. These components are pressed together when closing the cell. Excess electrolyte can “leave” the inner part of the cell due to the indentations, which avoids pressure on the aluminum foil. Moreover, due to the steel ring (5), onto which the current collector is pressed, this pressure is accommodated without effect for the aluminum foil. For the lower part (blue (color code refers to online version) components in Figure 1), a setup rebuilt from a conventional commercial setup was used.¹³ X-ray diffraction is measured in reflection mode from above, as the active material to be measured is exposed to X-rays due to the use of a stainless steel mesh. As the active material is slightly below the X-ray window, the outer stainless steel ring (3) needs to be flat to avoid reflection of incoming X-rays by the ring at small angles.

This *in operando* cell setup has been tested for various materials on a conventional Rigaku SmartLab X-ray diffractometer (200 mA, 45 kV) in reflection mode, with copper as X-ray source. One example is P2- $\text{Na}_{0.7}\text{MnO}_2$ (NMO), a promising material for sodium-ion batteries.^{14,15} Figure 2 shows the X-ray diffraction patterns of NMO in powder form, and of a pellet, which was prepared in the way described above

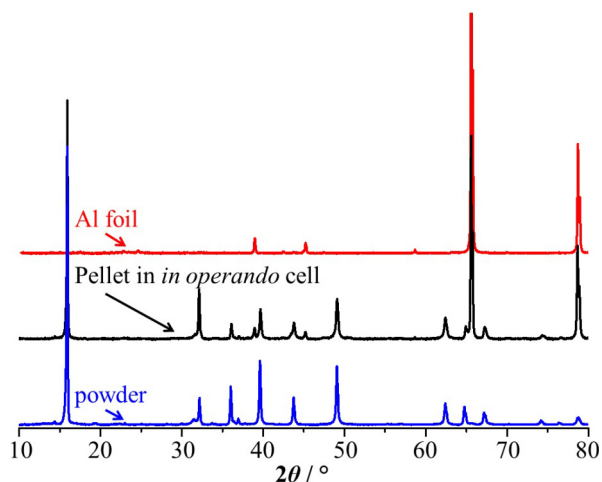


FIG. 2. X-ray diffraction pattern of P2- $\text{Na}_{0.7}\text{MnO}_2$ powder (bottom), a pellet with P2- $\text{Na}_{0.7}\text{MnO}_2$, teflonized acetylene black, and activated carbon (8:1:1 weight) on a stainless steel grid in the *in operando* cell (middle), the aluminum window (top).

and built into the *in operando* XRD cell; the pattern of the aluminum used as X-ray window is added as reference. As can be seen, the pattern is well visible. The high signal intensity and excellent signal-to-noise ratio allow the monitoring of shifts of the observed reflections, or phase transformations, during cycling. The X-ray window does not reduce signal intensity detrimentally, and the well-defined reflections of the aluminum only hinder analysis in the rare case when a material has reflections in the same narrow angle range.

A good example for the easily observable shifts of the observed reflections is $\text{Na}_{2.55}\text{V}_6\text{O}_{16}\cdot 0.6\text{H}_2\text{O}$,¹⁶ which was cycled vs. Na in the presented setup with 1M NaClO_4 (Sigma Aldrich, >98%) in ethylene carbonate: propylene carbonate (1:1 % wt) as the electrolyte (PC: Sigma Aldrich, 99.7%, EC: Sigma Aldrich, 99%).

Figure 3(a) shows the XRD pattern of a $\text{Na}_{2.55}\text{V}_6\text{O}_{16}\cdot 0.6\text{H}_2\text{O}$ pellet in the *in operando* cell. Figure 3(b) shows reversible shifts during electrochemical cycling for selected reflections in the range of $2\theta = 26.5^\circ\text{--}31^\circ$, which comprises reflections of diverse intensities. The color code represents the height profile, with blue (color code refers to online version) being the “noise,” i.e., only background reflection.

As can be seen, reversible shifts of the observed reflections are clearly observable, which can give new insights into changes of the lattice parameters, and thus enhance the understanding of the expanding and shrinking unit cell

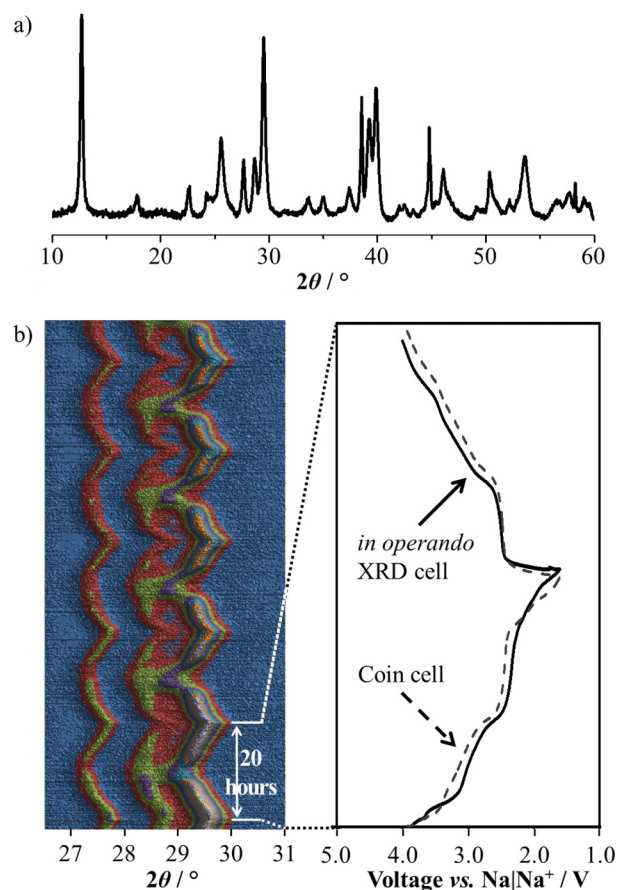


FIG. 3. (a) XRD pattern of $\text{Na}_{2.55}\text{V}_6\text{O}_{16}\cdot 0.6\text{H}_2\text{O}$ in the *in operando* cell; (b) *in operando* XRD measurement for 5 cycles at 10 mA g^{-1} ; left: reversible shifts of the observed reflections, right: representative charge/discharge curve in the *in operando* cell (solid line) and in a coin cell (dashed line).

during Na-ion insertion and de-insertion. This can be nicely correlated to the electrochemical charge/discharge data as presented on the right side of Figure 3(b), which also corresponds well with similar measurements in an established coin cell setup (solid line: *in operando* cell, dashed line: coin cell). Quantitative analyses to study this from a scientific, not instrument-focused point of view will be concluded shortly.

In summary, we have designed, constructed, and verified a new setup for electrochemical *in operando* X-ray diffraction measurements using a conventional X-ray diffractometer. The setup is based on a separation of X-ray window and current collector, which enables the use of non-toxic and cheap ultrathin aluminum foil, and thus ensures excellent signal quality. This facilitates the examination of structural changes while electrochemically inserting/deinserting Li- and Na-ions into/from a host material. Consequently, a deeper understanding for structural processes during charging/discharging battery materials can be obtained. These insights can be used to develop strategies to mitigate capacity fading in energy storage materials.

This work was financially supported by the Singapore National Research Foundation under its Campus for Research Excellence and Technological Enterprise (CREATE)

programme. The authors thank Steffen Schlueter and Patrick Osswald for initial discussions.

- ¹D. Kundu, E. Talaie, V. Duffort, and L. F. Nazar, *Angew. Chem., Int. Ed.* **54**, 3431 (2015).
- ²N. Yabuuchi, K. Kubota, M. Dahbi, and S. Komaba, *Chem. Rev.* **114**, 11636 (2014).
- ³L. Croguennec and M. R. Palacin, *J. Am. Chem. Soc.* **137**, 3140 (2015).
- ⁴J. N. Weker and M. F. Toney, *Adv. Funct. Mater.* **25**, 1622 (2015).
- ⁵Y. Shen, E. E. Pedersen, M. Christensen, and B. B. Iversen, *Rev. Sci. Instrum.* **85**, 104103 (2014).
- ⁶C. J. Pelliccione, E. V. Timofeeva, J. P. Katsoudas, and C. U. Segre, *Rev. Sci. Instrum.* **85**, 126108 (2014).
- ⁷M. N. Richard, I. Koetschau, and J. R. Dahn, *J. Electrochem. Soc.* **144**, 554 (1997).
- ⁸R. R. Chianelli, J. C. Scanlon, and B. M. L. Rao, *J. Electrochem. Soc.* **125**, 1563 (1978).
- ⁹M. Morcrette, Y. Chabre, G. Vaughan, G. Amatucci, J. Leriche, S. Patoux, C. Masquelier, and J.-M. Tarascon, *Electrochim. Acta* **47**, 3137 (2002).
- ¹⁰N. A. Cañas, S. Wolf, N. Wagner, and K. A. J. Friedrich, *J. Power Sources* **226**, 313 (2013).
- ¹¹G. A. Roberts and K. D. Stewart, *Rev. Sci. Instrum.* **75**, 1251 (2004).
- ¹²K. Rhodes, M. Kirkham, R. Meisner, C. M. Parish, N. Dudney, and C. Daniel, *Rev. Sci. Instrum.* **82**, 075107 (2011).
- ¹³Rigaku, *Rigaku J.* **27**, 32 (2011).
- ¹⁴N. Bucher, S. Hartung, I. Gocheva, Y. L. Cheah, M. Srinivasan, and H. E. Hoster, *J. Solid State Electrochem.* **17**, 1923 (2013).
- ¹⁵N. Bucher, S. Hartung, A. Nagasubramanian, Y. L. Cheah, H. E. Hoster, and S. Madhavi, *ACS Appl. Mater. Interfaces* **6**, 8059 (2014).
- ¹⁶S. Hartung, N. Bucher, V. S. Nair, C. Y. Ling, Y. Wang, H. E. Hoster, and M. Srinivasan, *Chemphyschem* **15**, 2121 (2014).

5.3 Mechanism of Na⁺ Insertion in Alkali Vanadates and its Influence on Battery Performance.

The study presented in this chapter, “Mechanism of Na⁺ Insertion in Alkali Vanadates and its Influence on Battery Performance.” (submitted to *Advanced Energy Materials*) is a continuation of the work on vanadates presented in Chapters 5.1 and 5.2. It proposes a mechanism that describes the observed behaviour. Synchrotron XRD data presented here was performed at the Stanford Linear Accelerator Centre (SLAC), and laboratory scale XRD data was measured with the *in operando* cell described in the previous chapter. S. Hartung was leading the work that is presented in this publication.

Na_{2.46}V₆O₁₆ (NVO) was examined using synchrotron radiation in a voltage range in which the material exhibits high cycling stability (4.0 V – 1.6 V) and in a wider range in which significant capacity fading occurs (4.0 V – 1.0 V). Moreover, as it was assumed that the radius of the ion between the layers of VO_x polyhedra has an influence on electrochemical properties, Li_{2.55}V₆O₁₆ (LVO) and K_{1.8}V₆O₁₆ were also investigated with the intention of deducing a trend based on ionic radii. All three materials exhibit very stable cycling behaviour when cycled vs. Na|Na⁺ between 4.0 V – 1.6 V, with LVO delivering the highest capacity (LVO: 97 mA h g⁻¹ in the 10th/81 mA h g⁻¹ in the 100th cycle; NVO: 71 mA h g⁻¹/70 mA h g⁻¹, KVO: 70 mA h g⁻¹/60 mA h g⁻¹). When cycled in the wider potential region between 4.0 V – 1.0 V, capacities are significantly higher, but all material exhibit significant fading with a decrease in capacity retention from LVO to NVO to KVO (LVO: 231 mA h g⁻¹ in the 1st/100 mA h g⁻¹ in the 100th cycle; NVO: 196 mA h g⁻¹/58 mA h g⁻¹, KVO: 144 mA h g⁻¹/50 mA h g⁻¹).

In the voltage range in which cycling stability is high (4.0 V – 1.6 V), *i.e.* electrochemical processes are reversible, structural processes are shown to be reversible as well based on the development of the unit cell lattice parameters and the area of the reflections. Two different crystallographic sites, α and β, are reversibly occupied during charge/discharge in this potential range. Upon further decreasing the voltage to 1.0 V, additional Na-ions are inserted into the structure. The development of the lattice parameters indicates that interstices in the plane of the VO_x-polyhedra are gradually occupied. When comparing the 2nd and the 5th discharge in the wide voltage region, it could be observed that the changes of the unit cell are not fully reversible. Moreover, a decrease of the areas of the investigated reflections indicates a loss of long range order during cycling. These results show irreversible structural change concomitant with a decrease in capacity.

In the LVO structure, Li⁺ is exchanged by Na⁺ to a large extent during cycling of LVO vs. Na metal. A minority of Li-ions (~10%), however, remains and stabilises the structure. This stabilisation diminishes irreversible structural changes and results in improved capacity retention compared to NVO.

The presented results shed light on the strong correlation between structural and electrochemical reversibility with regard to Na⁺ insertion into and extraction from vanadates. The superior capacity retention of LVO over NVO shows the positive

influence of smaller ions in the host structure on cycling performance and suggests further exploitation of this effect in future studies.

Mechanism of Na⁺ Insertion in Alkali Vanadates and its Influence on Battery Performance.

Steffen Hartung, Nicolas Bucher, Joseph B. Franklin, Anna M. Wise, Linda Y. Lim, Han-Yi Chen, Johanna Nelson Weker, Maria-E. Michel-Beyerle, Michael F. Toney, Madhavi Srinivasan

Manuscript submitted to *Advanced Energy Materials* (manuscript number aenm.201502336)

After the review process, a revised version of this manuscript was accepted:

S. Hartung, N. Bucher, J. B. Franklin, A. M. Wise, L. Y. Lim, H.-Y. Chen, J. N. Weker, M.-E. Michel-Beyerle, M. F. Toney, M. Srinivasan: Mechanism of Na⁺ Insertion in Alkali Vanadates and Its Influence on Battery Performance. *Advanced Energy Materials*. 2016. 1502336. doi:10.1002/aenm.201502336. Copyright Wiley-VCH Verlag GmbH & Co. KGaA. Reproduced with permission.

The publication can be found under the following weblink:

<http://dx.doi.org/10.1002/aenm.201502336>

DOI: 10.1002/ ((please add manuscript number))

Article type: **Full Paper**

Mechanism of Na⁺ Insertion in Alkali Vanadates and its Influence on Battery Performance.

*Steffen Hartung, Nicolas Bucher, Joseph B. Franklin, Anna M. Wise, Linda Y. Lim, Han-Yi Chen, Johanna Nelson Weker, Maria-E. Michel-Beyerle, Michael F. Toney, Madhavi Srinivasan**

Steffen Hartung, Nicolas Bucher, Han-Yi Chen, Maria-E. Michel-Beyerle, Madhavi Srinivasan
TUM CREATE, 1 CREATE Way, Singapore 138602
E-mail: Madhavi@ntu.edu.sg

Steffen Hartung, Nicolas Bucher, Han-Yi Chen, Maria-E. Michel-Beyerle
Department of Chemistry, Technische Universität München, Lichtenbergstr. 4, Garching 85748, Germany

Steffen Hartung, Nicolas Bucher, Madhavi Srinivasan
School of Materials Science and Engineering, 50 Nanyang Avenue, Nanyang Technological University, Singapore 639798

Joseph B. Franklin
Energy Research Institute at NTU (ERI@N), Nanyang Technological University, 1 CleanTech Loop, Singapore 637141

Anna M. Wise, Linda Y. Lim, Johanna Nelson Weker, Michael F. Toney
Stanford Synchrotron Radiation Lightsource, SLAC National Accelerator Laboratory, 2575 Sand Hill Rd., Menlo Park, CA, USA

Linda Y. Lim
Department of Materials Science and Engineering, Stanford University, 496 Lomita Mall, Stanford, CA, USA

Maria-E. Michel-Beyerle
School of Physical and Mathematical Sciences, Nanyang Technological University, 21 Nanyang Link, Singapore 637371

Keywords: sodium-ion batteries, vanadates, in operando, X-ray diffraction, irreversible Na⁺-insertion

Sodium-ion batteries can become an alternative to the widespread lithium-ion technology due to cost and kinetic advantages provided that cyclability is improved. For this purpose, the interplay between electrochemical and structural processes is key and is demonstrated in this

work for $\text{Na}_{2.46}\text{V}_6\text{O}_{16}$ and $\text{Li}_{2.55}\text{V}_6\text{O}_{16}$ employing *operando* synchrotron X-ray diffraction. When NVO is cycled between 4.0 V – 1.6 V, Na-ions reversibly occupy two crystallographic sites, which results in remarkable cyclability. Upon discharge to 1.0 V, however, Na-ions occupy also interstitial sites, inducing irreversible structural change with some loss of crystallinity concomitant with a decrease in capacity. Capacity fading increases with the ionic radius of the alkali ions ($\text{K}^+ > \text{Na}^+ > \text{Li}^+$), suggesting that smaller ions stabilize the structure due to stronger attraction to the vanadate layers. This correlation of structural variation and electrochemical performance suggests a route towards improving cycling stability based on minor Li^+ -retention in an $\text{A}_{2+x}\text{V}_6\text{O}_{16}$ structure. Even though exchange of the majority of Li^+ by the abundant Na^+ occurs, the remaining Li-ions (~10%) are sufficient to stabilize the layered structure, diminishing the irreversible structural damage. These results pave the way for further exploitation of the role of small ions in lattice stabilization that increases cycling performance.

1. Introduction

Sodium-ion batteries (NIBs) have recently become the subject of increasing research efforts, and are considered a viable future electrochemical energy storage technology for a variety of applications such as stationary energy storage. As of now, lithium-ion batteries (LIBs) dominate the market, owing to their excellent performance, which is also the result of decades of research and optimization. Sodium-ion batteries (NIBs), however, could play a similar role in the future, provided that suitable electrode materials are found and fundamental understanding of the respective systems is enhanced.^[1-8] Na-ion-based systems have an advantage in terms of cost, availability, and abundance. Moreover, recent studies^[9-12] relate the larger ionic radius of Na^+ to some benefits emerging from the lower desolvation energy which may facilitate insertion of Na^+ into the active electrode material. Moreover, faster diffusion of Na^+ ions within the active electrode material is also favoured in certain

structures.^[13] In addition, in the search of commercially viable materials the immense structural variety of Na-compounds can be exploited once basic principles are understood.^[2]

In a previous publication^[14], we reported on $\text{Na}_{2+x}\text{V}_6\text{O}_{16}$ (NVO) as a NIB cathode. As in the case of $\text{Li}_{2+x}\text{V}_6\text{O}_{16}$ (LVO), NVO consists of V-O layers, with Na-ions located between these layers (International Crystal Structure Database, ICSD-67844 and -164514). Even though the initial capacity was promising, the cycling stability was low. Therefore, in this paper this material serves as an exemplary system for studies of the origin of strong capacity fading. We note in passing that various studies have investigated similar systems with different foci^[15-25], however, without detailed structural analysis.

In this report, we present in-depth structural characterization of the insertion process of Na^+ into (from) $\text{Na}_{2+x}\text{V}_6\text{O}_{16}$ (NVO) employing electrochemical *operando* synchrotron X-ray diffraction (XRD). Our data indicate that for NVO the structural and electrochemical reversibility of Na^+ -insertion depends on the potential. In a narrow potential region, Na^+ reversibly occupies two distinct lattice sites, while in a wider potential range, *i.e.*, at lower potentials, additional Na-ions insert into interstices. This effect induces irreversible structural changes causing a decrease in discharge capacity. Interestingly, when the isostructural LVO is cycled in a Na-ion half cell, Li^+ is not entirely replaced by Na^+ . Approximately 10% of Li^+ ions are retained and this is the origin of small, although defined structural changes as compared to “native” NVO. Specifically, this small Li^+ -retention is responsible for the improved cycling performance of the capacity.

2. Results and Discussion

2.1. Physical characterization

The crystal structures of the alkali vanadates NVO, LVO, and KVO ($\text{K}_{1.8}\text{V}_6\text{O}_{16}$) were determined using XRD as shown in Figure S1. Their synthesis is described in the Experimental Section. For all three systems, the unit cell was found to be monoclinic with the $P12_1/m1$ space group. VO_x -polyhedra form layers and the respective alkali ion, Na^+ , Li^+ , or K^+ , is located between these layers. The unit cell increases with the radius of the alkali ion as detailed in the Experimental Section. All three materials have a belt-like morphology (Figure S2a-c). The individual belts differ in length (typically several hundred nanometers to a few micrometers) and aspect ratio.

2.2. Electrochemistry

The electrochemistry of NVO, LVO, and KVO depends significantly on the potential range in which the materials are cycled (**Figure 1a,b**).

Potential range 4.0 V – 1.0: NVO shows a rather high capacity of 201 mA h g^{-1} in the first discharge when cycled vs. $\text{Na}|\text{Na}^+$ at a current rate of 20 mA g^{-1} ($\approx C/10$). This initial capacity corresponds to the insertion of 4.7 Na-ions into the lattice of NVO and therefore to a formal unit $\text{Na}_{6.3}\text{V}_6\text{O}_{16}$ at the end of the discharge. The insertion of one Na-ion, based on the initial formula unit for NVO, corresponds to 43 mA h g^{-1} . The most striking feature in Figure 1a is the steep decrease of capacity over the course of 100 cycles. It is this prominent trait that prompted us to study and relate electrochemical information to structural processes (Section 2.3). For LVO the initial discharge capacity at 20 mA g^{-1} is higher (279 mA h g^{-1}) than for NVO and somewhat stable for the first ~ 20 cycles before fading in subsequent cycles (Figure 1a). For KVO the initial discharge capacity is lower (168 mA h g^{-1}) for NVO while its capacity retention resembles the curve for NVO.

Moreover, not only does the capacity of all three materials decrease, but also the shape of the galvanostatic charge/discharge curves change, *i.e.*, they lose structure during cycling (Figure S3). While in the first discharge the shape is quite structured with a plateau at ~ 2.4 V (for KVO at 2.0 V) and a long plateau around 1.3 V, in subsequent cycles these plateaus are washed out. Thus, during cycling the Na-ions appear to occupy lattice sites with a wider range of electrochemical potentials as opposed to the occupation of distinct lattice sites in a well-defined structure. The similar shape of the discharge curves for all three isostructural materials (Figure S3) suggests a similar structural insertion process (for a more detailed description of the discharge curves, see Supporting Information).

Potential range 4.0 V – 1.6 V: When the potential range is limited to 4.0 V – 1.6 V, the second, long plateau is not reached (Figure 1b). All capacities increase ($< 10\%$ for NVO and KVO, 30% for LVO) over the first ten cycles due to ongoing Na^+ insertion into the oxide lattices, so that the discharge capacity in the 10th cycle is 70 mA h g⁻¹ for NVO (consistent with a recent report by Dong *et al.*^[25]), 97 mA h g⁻¹ for LVO, and 70 mA h g⁻¹ for KVO (50 mA g⁻¹).

This difference in stability dependant on the potential range cycled suggests that potential-dependent material characteristics are the origin of the observed capacity fading rather than failing of the Na-electrode as proposed elsewhere.^[21] Such interpretation would be consistent with Na-ions which reversibly occupy specific lattice sites when cycled in the smaller potential range between 4.0 V – 1.6 V, whereas the process causing the extended plateau in the discharge curve starting at 1.5 V involves irreversible capacity fading. In the following section we test whether and how these electrochemical observations are correlated with structural developments.

2.3. Electrochemistry and Structure. *Operando* X-ray diffraction

2.3.1. $\text{Na}_{2.46}\text{V}_6\text{O}_{16}$ in Sodium-Ion Batteries

Narrow potential range 4.0 V – 1.6 V: Upon limiting the potential to this range, the development of the XRD pattern is reversible (**Figure 2**). As these measurements were performed with synchrotron radiation in transmission mode, all the observed processes can be attributed to bulk processes. The Na content, x , in $\text{Na}_x\text{V}_6\text{O}_{16}$ is calculated based on the assumption that the cells at 3.0 V, the typical open-circuit potential (OCP), contain the amount of Na^+ that was determined for the powder by Inductively-Coupled Plasma Optical Emission Spectrometry (ICP-OES) and that all the current goes into Na^+ -insertion or extraction (no side reactions).

For a better understanding of the structural processes which are occurring, individual reflections representing the different planes were analysed. The crystal structure of this material is depicted in **Figure 3**. The a -lattice parameter is perpendicular to the plane of VO_x -polyhedra and thus is the interlayer spacing, while the b - and c -lattice parameters span this plane. In this work, the (100), (020), and (001) reflections are used to calculate the a -, b - and c -lattice parameters, respectively. During discharge, the a -lattice parameter increases up to a Na^+ -content of 2.5 and then stays constant, whereas the b - lattice parameter continuously expands from 4.0 V to 1.6 V (**Figure 4a**). The c -lattice parameter remains constant until a Na content of $x \sim 2.8$ and then increases. At Open Circuit Potential (OCP), Na-ions are located at two different sites in the crystal lattice, α and β , one of which (β) is only partially occupied. During charge, these positions are partially vacated such that the Na^+ -content of the formula unit is decreased by one, and the resulting formula unit is $\approx \text{Na}_{1.6}\text{V}_6\text{O}_{16}$. Upon discharge, *i.e.*, the insertion of Na-ions, these sites are gradually occupied, which leads to an increased number of Na-ions between the VO_x -layers. Complete occupation of the α and β sites would

result in a discharge capacity of 103 mA h g^{-1} , 70% of which is achieved in a coin cell set up tested at 50 mA g^{-1} (see Electrochemistry section). Initial contraction of the unit cell, coming from electrostatic interaction between Na^+ and O^{2-} in the layers, is overcompensated by the electrostatic repulsion between the cations and / or the space requirement of the ‘new’ Na-ions. This results in an increase of the unit cell volume (Figure S4), and an increase of the a -lattice parameter up to a Na^+ -content of $x = 2.5$ (Figure 4a). Interestingly, this corresponds to the Na^+ -content of the pristine material, in which the α -positions are fully occupied. Hence, as the a -lattice parameter stays constant after the α positions are fully occupied, it is suggested that the length of the a -lattice parameter, and thus the interlayer spacing between the VO_x -layers is predominantly influenced by the Na^+ on the α -position. The b -lattice parameter expands continuously with increasing Na^+ -content, which is consistent with a repulsion of the inserted Na-ions. The c -lattice parameters does not increase up to Na^+ -content of $x = 2.8$ while the α positions are occupied. Once the α positions are fully occupied, Na^+ inserts onto the β positions. Initially, this has no effect on the c -lattice parameter. Starting from a Na^+ -content of ~ 2.8 , which corresponds to an occupation of $\sim 40\%$ of the β positions, c expands due to repulsive interaction between the Na-ions. This coincides with a decrease of conductivity in the structure as determined by Galvanostatic Intermittent Titration Technique (GITT, Supporting Information).

The integrated areas of the (100), (001) and (020) reflections change reversibly (Figure 4b), which corresponds well with the reversibility of the electrochemistry. While the area of (100) reflection shows a minor decrease during discharge, which is reversed during the subsequent charge, the area of the (001) reflection shows an increase during discharge and a decrease during charge; the area of the (020) reflection increases slightly during discharge and decreases during charge. Simulations of diffraction patterns using the Mercury software, based on gradually filling up the two lattice sites α and β , were conducted. Qualitative

comparison of the development of the reflection area to the measurement data substantiates the hypothesis that during Na-insertion the α -position is occupied first, followed by the β -position.

Wide potential range 4.0 V – 1.0 V: In the subsequent cycle (after one cycle within the narrow range), when discharging now from 4.0 to 1.0 V, *i.e.*, increasing the Na⁺-content in the crystal structure from 1.5 to 6.2, the a -lattice parameter, again, expands up to a Na⁺-content of 2.5, after which it remains constant (**Figure 5**). The b -lattice parameter increases steadily until the onset of the large plateau in the discharge curve. Then, the driving force to expand along the b -lattice parameter weakens and the gradient of the curve depicting the change of the b -lattice parameter decreases. Moreover, an increase in the c -lattice parameter is observed. Over the course of several cycles in this wide potential range, this lattice expansion/contraction is observed to be irreversible (**Figure 6**). To be more specific, the lattice vectors at both the onset and the end of the 5th discharge to 1.0 V are larger as compared to the respective values for the 2nd discharge in the same potential range. This increase is most pronounced for the a - and c -lattice parameter, while the change for the b -lattice parameter is insignificant. In addition, in the 5th discharge the c -lattice parameter starts increasing at a higher Na⁺ content than in the 2nd discharge to 1.0 V. The increase of the b -lattice parameter in the second discharge at wide potential range, (Figure 5), changes its slope at a Na⁺-content of $x = 3.25$. Together with the slope and subsequent plateau of the a -lattice parameter, this change in the slope indicates that the α - and β -sites are initially filled followed by occupation of the interstices for $x > 3.25$. These Na-ions are located on distorted trigonal bipyramidal interstices (Figure 3b) in the plane of the VO_x polyhedra, which forces the c -planes apart. We speculate that the occupancy of these interstices results in the irreversible deterioration of the structural integrity of NVO during deep cycling to 4.0 V - 1.0 V. This is also substantiated by GITT measurements (Supporting Information) as the Na⁺-diffusion coefficient decreases starting

from a Na⁺-content of $x = 3.25$, which suggests structural changes. This effect is also reflected in the irreversible change of the unit cell volume (Figure S4). At both the onset and the end of the 5th deep discharge, the unit cell volume is larger than at the onset and end of the 2nd deep discharge, which is showing irreversible expansion of the unit cell during cycling. This irreversible expansion is attributed to an increasing amount of Na-ions which, over the course of cycling get increasingly trapped in the structure. A correlation between structural changes and electrochemistry has been reported previously^[26,27], although for a different system (Ge as LIB anode) and different parameters (C-rate).

To confirm the insertion of Na⁺ into crystal structure interstices, the diffraction pattern of a hypothetical NVO structure with a Na⁺-content of 6 was simulated in **Figure 7**. The pattern at OCP (Na_{2.5}V₆O₁₆) was simulated using the unmodified $P12_1/m1$ unit cell. For the simulation of Na₆V₆O₁₆, all α and β positions are fully occupied, and additional Na⁺ is inserted into the four interstices (0.5 Na⁺ each) of the initial unit cell (Figure 3b). These simulations for Na₆V₆O₁₆ and Na_{2.5}V₆O₁₆ are qualitatively similar. The simulated pattern of Na₆V₆O₁₆ shows an anticipated shift to lower angles as compared to the simulated OCP pattern, as well as some new low intensity reflections (Figure 7). The NVO pattern measured at the end of the 5th discharge shows features from both simulations, including the new reflections (Figure S5). This indicates a coexistence of regions with and regions without Na⁺ in the interstices, *i.e.*, a two-phase region, which corresponds well with the long plateau observed for the galvanostatic discharge tests. Thus, four Na-sites ($2x\alpha$, $2x\beta$) in the unit cell can potentially be occupied reversibly without detrimental structural effects, resulting in a high stability for the narrow potential region. For a Na⁺-content > 3.25 , *i.e.*, fully occupied α and partially occupied β positions, it is concluded that interstices are filled and Na-rich regions form (interstices are occupied). This latter process is irreversible. It should be noted that this new structure is different from the one which was shown to form upon Li⁺-insertion into LVO.^[28] Thus,

although isostructural initially, NVO forms a different phase upon Na^+ -insertion than LVO does upon Li^+ -insertion.

Structural irreversibility is confirmed by the development of the integrated areas of the (100), (001) and (020) reflections. Between the beginning of the second deep discharge and the fifth deep discharge (Figure 6a) the areas of several reflections irreversibly decrease by 20 – 30%. One potential reason for this is a distortion of the regular arrangement of the crystal structure upon Na^+ -insertion, leading to a loss of the long-range order, and thus a decrease of reflection intensity. As Na^+ -insertion could be more detrimental to the structure than Li^+ -insertion, due to its larger ionic radius, this effect is potentially amplified compared to Li^+ -insertion. Loss of crystallinity also explains the fading of the capacity accompanied by the lack of distinct plateaus in the discharge curves after several cycles.

Overall, our data show parallel development of structural and electrochemical reversibility. Between 4.0 V – 1.6 V, the lattice parameters show reversible changes as Na^+ is inserted into and extracted from the distinct lattice sites α and β , with a concomitant stable electrochemical behaviour for > 100 charge / discharge cycles. Insertion of higher Na-amounts into interstices results in a higher capacity, but has a detrimental effect on the reversibility of both structural changes and electrochemical behaviour. Irreversible changes of the lattice parameters result in some loss of long range order, and a concomitant irreversible capacity fading.

2.3.2. Advantage of $\text{Li}_{2.55}\text{V}_6\text{O}_{16}$ in a Sodium-Ion Battery

LVO was cycled vs. $\text{Na}|\text{Na}^+$ in order to test whether the Li-ions have an effect on the performance. If *operando* ion exchange resulted in a complete replacement of Li^+ by Na^+ , cycling stability is expected to be similar.

In contrast to the pattern development of NVO, some significant changes become apparent when cycling LVO between 4.0 V – 1.6 V (Figure S7). Particularly, during discharge, the reflection at approximately $2\theta = 8.9^\circ$ appears to broaden, and eventually a new reflection can be resolved at a lower angle ($2\theta \sim 8.2^\circ$), indicating the co-existence of two phases. This (100) reflection is indicative of the interlayer spacing between the VO_x -layers, between which Na^+ inserts during discharge. During cycling, the new low angle reflection becomes more pronounced (Figure S8), while the intensity of the original reflection continuously decreases. The patterns in **Figure 8a** show the gradual change from LVO (lowest pattern) to a Li^+ -modified NVO (3rd pattern). These patterns were measured at 4.0 V in consecutive cycles. As reference, the diffraction pattern of NVO in the 3rd cycle at the same potential is shown at the top. As can be seen in Figure 8a, the initial (100) peak for LVO eventually disappears, and only the reflection at a lower angle remains. The XRD pattern of LVO after several cycles shows a strong resemblance to the NVO pattern at the same potential. In the charged state after three cycles, for both NVO and LVO the (100) reflections occur at $2\theta = 8.13^\circ$. While, during charge, both Li^+ and Na^+ are extracted during discharge, the insertion of Na^+ is favored owing to the large amount of Na^+ in the system.

Thus, based on the similarity of the NVO and LVO patterns after the 3rd charge, our data show that an *operando* ion-exchange occurred, and LVO partially transforms into NVO. One explanation for the difference between NVO and LVO regarding both capacity and cycling performance is that, despite structural conversion, some Li^+ remains in the original sites stabilizing the structure.

This interpretation has been substantiated by electrochemical *operando* laboratory scale XRD measurements.^[29] Figure 8b-e show the development of the *a*-lattice parameter of the original

LVO and the mixed phase in consecutive cycles. As can be seen in Figure 8b, the a -lattice parameter does not increase for LVO during the first discharge in the narrow potential range. The NVO phase already emerges during the first discharge (Figure S8). At the start of the second discharge (until 1.6 V, Figure 8c), the NVO phase is present from the beginning, and both phases coexist, while neither shows a remarkable increase of the a -lattice parameter. In the subsequent discharge steps (to 1.0 V, Figure 8d-e), reflections indicating the LVO phase gradually disappear. Rather broad reflections of LVO after several cycles, as well as not quite full accordance of every reflection with NVO (Figure 8a), suggest that some Li^+ still remains and stabilizes the structure. This is substantiated by the slightly smaller value ($\sim 0.1 \text{ \AA}$) for the a -lattice parameter of the converted structure as compared to the ‘pristine’ NVO phase (Figure 8 b-e). Upon applying Vegard’s law^[30] to this Li^+/Na^+ -vanadate system we find that the contribution from the LVO-phase is of the order of 10%. Thus, it can be concluded that the majority of Li^+ is replaced by Na^+ during cycling. The effect of this Li^+ -remnant is an increase of cycling performance.

3. Conclusions

In parallel to the electrochemical measurements in NIB half cells, we monitor the structure by employing *operando* synchrotron X-ray diffraction for studying “native” NVO ($\text{Na}_{2.46}\text{V}_6\text{O}_{16}$) and “native” LVO ($\text{Li}_{2.55}\text{V}_6\text{O}_{16}$) cathodes. When NVO is cycled between 4.0 V – 1.6 V, Na-ions reversibly occupy two different crystallographic sites, α and β , which results in remarkable cycling stability. Upon discharge to 1.0 V, however, Na-ions additionally occupy interstitial sites in the crystal structure. This occupation of interstices induces irreversible structural change with some loss of crystallinity concomitant with a decrease in capacity. Capacity fading increases with an increase of the ionic radius of the alkali ions ($\text{K}^+ > \text{Na}^+ > \text{Li}^+$), suggesting that smaller ions stabilize the structure due to the formation of stronger bonds with the vanadate layers. This correlation of structural variation and electrochemical

performance also suggests a route towards improvement of cycling stability. Key is a minor Li^+ -retention in an $\text{A}_{2+x}\text{V}_6\text{O}_{16}$ structure, where A in the “native” structure is Li. Even though an *operando* exchange of the majority of Li^+ -ions by the vast abundance of Na-ions takes place, the remaining Li^+ -ions (~10%) are sufficient to stabilize the layered structure, thus diminishing the irreversible structural damage. The nature of this damage has been identified in this paper. These experimental results pave the way for further exploitation of the role of small ions in lattice stabilization that increases cycling performance.

4. Experimental Section

Synthesis and Electrode Preparation: NVO was synthesized as described previously.^[14] 20 mL of a vanadium pentoxide solution (0.01 M, Sigma Aldrich, 98%) in deionized water was mixed with a sodium hydroxide solution (0.01 M, Sigma Aldrich, 98%) and stirred overnight to obtain a brownish-orange solution. It was transferred to a 50 mL Teflon-lined stainless steel autoclave and then heated to 180°C for 48 h. The resulting precipitate was filtered and washed using deionized water, and dried at 80°C for 4 h. The resulting powder was annealed in air at 400°C for 2 h. The chemical composition $\text{Na}_{2.46}\text{V}_6\text{O}_{16}$ was determined by ICP-OES.

To synthesize LVO^[31], a solution of CH_3COOLi in DI water was prepared. Then V_2O_5 was added (molar ratio V:Li = 1:1.2) and dispersed, followed by the stepwise addition of 8.5 mL H_2O_2 (32%). Afterwards, the orange-brownish solution was stirred for 3 h, and subsequently heated at 110°C for 24 h. The resulting powder was heated at 400°C for 2 h. The chemical composition $\text{Li}_{2.55}\text{V}_6\text{O}_{16}$ was determined by ICP-OES. KVO was synthesized using a hydrothermal process.^[32] 2 mmol of K_3VO_4 were dissolved in 30 mL DI water and vigorously stirred. 2 M HCl was added until the pH was 3.0 and the solution turned orange. This step was followed by 5 min of gentle stirring. Then, the solution was heated to 200°C for 24 h in an autoclave. The product was centrifuged, washed with DI water and ethanol, and subsequently dried at 50°C. Unlike for NVO and LVO, a final calcination step was omitted, as it leads to

irreversible phase transformation. The chemical composition $K_{1.8}V_6O_{16}$ was determined by energy dispersive X-ray spectroscopy.

Composite electrodes were prepared by mixing the active material, acetylene black (Alfa Aesar, >99%), and polyvinylidene fluoride (PVDF, Arkema, Kynar HSV 900) at a weight ratio 6:2:2 with *N*-methyl-2-pyrrolidone (NMP) to form a homogeneous slurry. This slurry was then coated onto Al foil using a doctor blade. The dried coating was punched into circular electrodes ($\varnothing = 16$ mm). Crystallographic water was found previously in NVO with 0.6 molecules of water per formula unit at room temperature using thermogravimetric analysis.^[14] In order to maximally reduce the water content, all electrodes studied were exposed to long-term (17 hours) drastic drying at 110°C in vacuum (10^{-6} bar) and then assembled in 2016 type coin cells with sodium metal as the anode (half cell). Glass fibre (Whatman) was used as separator, and the electrolyte for all measurements was a 1 M solution of $NaClO_4$ in a mixture of propylene carbonate (PC) and ethylene carbonate (EC) (wt % 1:1).

Structure and Morphology: Powder X-ray diffraction of the synthesized materials was performed on a Rigaku SmartLab X-ray diffractometer (200 mA, 45 kV) in reflection mode with $Cu-K_\alpha$ radiation, *i.e.*, with a wavelength of 1.54 Å. For NVO, a Rietveld refinement was employed in the PDXL2 software (.cif file: Inorganic Crystal Structure Database 164514). Based on this, the lattice parameters are $a = 7.207(4)$ Å, $b = 3.596(2)$ Å, and $c = 12.124(7)$ Å. The angle β between the *a*- and *c*-lattice parameters is $107.80(2)^\circ$ ($R_{WP} = 9.63$, $S = 4.8299$). For LVO, using the same approach, the lattice parameters were found to be $a = 6.648(1)$ Å, $b = 3.592(1)$ Å, and $c = 11.988(1)$ Å, and $\beta = 107.758(2)^\circ$ ($R_{WP} = 11.22$, $S = 5.3687$). For KVO, according to a Pawley fit, the lattice parameters are $a = 16.325$ Å, $b = 3.595$ Å, and $c = 12.171$ Å, with an angle $\beta = 106.63^\circ$. As this fit was performed with the supercell, the *a*-lattice parameter is ~ twice as large as for LVO and NVO. The crystal structure in Figure 3 was

drawn from the NVO .cif file using the CrystalMaker software (version 8.76). Diffraction patterns (Figure 7) were simulated using the Mercury software (version 3.6). For field emission scanning electron microscopy (FESEM), a Zeiss Supra 55 FESEM was used.

Electrochemical Measurements: Galvanostatic cycling was carried out using a Neware battery tester system. Galvanostatic intermittent titration technique was measured using a Biologic VMP3 potentiostat. The constant current pulse was 50 mA for 200 seconds, with a subsequent OCP relaxation period of 5 h. If the potential relaxation stabilized below a change of $dE/dt = 2 \text{ mV h}^{-1}$ the next current pulse was inserted. The diffusion coefficient was calculated according to the following formula:

$$D = \frac{4}{\pi} \left(\frac{i V_m}{z_A F S} \right)^2 \left[\frac{\left(\frac{dE}{d\delta} \right)}{\left(\frac{dE}{d\sqrt{t}} \right)} \right]^2$$

In this equation, V_m is the molar volume of the unit cell, i is the applied current, z_A is the charge number, F is Faraday's constant, S is the electrode/electrolyte contact area which was assumed to be the geometric surface of the electrode, $\frac{dE}{d\delta}$ is the slope of the Coulometric titration curve, $\frac{dE}{d\sqrt{t}}$ is the slope of the linearized plot of the potential $E(\text{V})$ during the current pulse. The calculation for the diffusion coefficients is based on the volume of the initial unit cell; even though its volume changes slightly, this can be neglected in light of the significant changes of D_{Na} .

Synchrotron in operando diffraction measurements: A small hole (3 mm in diameter) was drilled into commercial 2016 coin cells and subsequently sealed using Kapton film (25 μm) and epoxy resin. The active material was prepared as a pellet by mixing it with acetylene black and teflonized acetylene black (6:2:2) and pressing it onto aluminum foil. Synchrotron X-ray diffraction was performed at the Stanford Synchrotron Radiation Lightsource at

beamline 11-3. The beam energy was 12.7 keV, and a MAR345 area detector was used. The scattering vector range measured was $0.45 - 5.0 \text{ \AA}^{-1}$. The sample-detector distance was 166.9 mm and the GSAS 2 software³² was used to convert the diffraction data from 2D to 1D and concurrently from Q to 2θ for better comparability with previous studies. The sample was rocked by 0.3 mm in one direction to improve the powder averaging.

Laboratory scale in operando X-ray diffraction: Measurements were performed using a set-up without Kapton described previously using a Rigaku SmartLab X-ray diffractometer (200 mA, 45 kV)^[29]. This was done to avoid the Kapton reflections in the pattern. The position of both the original and the newly emerging (100) reflection were determined based on maximum reflection intensity, and employed to monitor the development of the a -lattice parameter of the unit cell.

[Further details of the crystal structure investigation(s) may be obtained from the Fachinformationszentrum Karlsruhe, 76344 Eggenstein-Leopoldshafen (Germany), on quoting the depository numbers CSD-164514 and - 67844]

Supporting Information

Supporting Information is available from the Wiley Online Library.

Acknowledgements

Steffen Hartung and Nicolas Bucher contributed equally to this manuscript. This work was financially supported by the Singapore National Research Foundation within the programme TUM CREATE (Campus for Research Excellence and Technological Enterprise). Anna M. Wise was fully supported and Johanna Nelson Weker was partially supported by the Department of Energy, Laboratory Direct Research and Development funding, under contract DE-AC02-76SF00515. Use of the Stanford Synchrotron Radiation Lightsource, SLAC

National Accelerator Laboratory, is supported by the U.S. Department of Energy, Office of Science, Office of Basic Energy Sciences under Contract No. DE-AC02-76SF00515.

Received: ((will be filled in by the editorial staff))
Revised: ((will be filled in by the editorial staff))
Published online: ((will be filled in by the editorial staff))

References

- [1] D. Kundu, E. Talaie, V. Duffort, L. F. Nazar, *Angew. Chemie Int. Ed.* **2015**, *54*, 3431.
- [2] N. Yabuuchi, K. Kubota, M. Dahbi, S. Komaba, *Chem. Rev.* **2014**, *114*, 11636.
- [3] V. Palomares, P. Serras, I. Villaluenga, K. B. Hueso, J. Carretero-González, T. Rojo, *Energy Environ. Sci.* **2012**, *5*, 5884.
- [4] V. Palomares, M. Casas-Cabanas, E. Castillo-Martínez, M. H. Han, T. Rojo, *Energy Environ. Sci.* **2013**, *6*, 2312.
- [5] H. Pan, Y.-S. Hu, L. Chen, *Energy Environ. Sci.* **2013**, *6*, 2338.
- [6] B. L. Ellis, L. F. Nazar, *Curr. Opin. Solid State Mater. Sci.* **2012**, *16*, 168.
- [7] M. D. Slater, D. Kim, E. Lee, C. S. Johnson, *Adv. Funct. Mater.* **2013**, *23*, 947.
- [8] S.-W. Kim, D.-H. Seo, X. Ma, G. Ceder, K. Kang, *Adv. Energy Mater.* **2012**, *2*, 710.
- [9] M. Okoshi, Y. Yamada, A. Yamada, H. Nakai, *J. Electrochem. Soc.* **2013**, *160*, A2160.
- [10] Y. Yamada, Y. Iriyama, T. Abe, Z. Ogumi, *Langmuir* **2009**, *25*, 12766.
- [11] Y. Yamada, Y. Koyama, T. Abe, Z. Ogumi, *J. Phys. Chem. C* **2009**, *113*, 8948.
- [12] K. Kuratani, N. Uemura, H. Senoh, H. T. Takeshita, T. Kiyobayashi, *J. Power Sources* **2013**, *223*, 175.

- [13] S. P. Ong, V. L. Chevrier, G. Hautier, A. Jain, C. Moore, S. Kim, X. Ma, G. Ceder, *Energy Environ. Sci.* **2011**, *4*, 3680.
- [14] S. Hartung, N. Bucher, V. S. Nair, Y. L. Cheah, Y. Wang, H. E. Hoster, M. Srinivasan, *Chemphyschem* **2014**, *15*, 2121.
- [15] S. Tepavcevic, H. Xiong, V. R. Stamenkovic, X. Zuo, M. Balasubramanian, V. B. Prakapenka, C. S. Johnson, T. Rajh, *ACS Nano* **2012**, *6*, 530.
- [16] H. He, G. Jin, H. Wang, X. Huang, Z. Chen, D. Sun, Y. Tang, *J. Mater. Chem. A* **2014**, *2*, 3563.
- [17] H. Liu, H. Zhou, L. Chen, Z. Tang, W. Yang, *J. Power Sources* **2011**, *196*, 814.
- [18] S. Hartung, N. Bucher, H.-Y. Chen, R. Al-Oweini, S. Sreejith, P. Borah, Z. Yanli, U. Kortz, U. Stimming, H. E. Hoster, M. Srinivasan, *J. Power Sources* **2015**, *288*, 270.
- [19] G. Wang, G. Pistoia, *J. Electroanal. Chem.* **1991**, *302*, 275.
- [20] K. West, B. Zachau-Christiansen, T. Jacobsen, *Solid State Ionics* **1988**, *28-30*, 1128.
- [21] K. West, B. Zachau-Christiansen, T. Jacobsen, S. Skaarup, *J. Power Sources* **1989**, *26*, 341.
- [22] K. West, B. Zachau-Christiansen, T. Jacobsen, S. Skaarup, *Solid State Ionics* **1990**, *40/41*, 585.
- [23] D. Nguyen, J. Gim, V. Mathew, J. Song, S. Kim, D. Ahn, J. Kim, *ECS Electrochem. Lett.* **2014**, *3*, A69.
- [24] H. Kang, Y. Liu, M. Shang, T. Lu, Y. Wang, L. Jiao, *Nanoscale* **2015**, *7*, 9261.
- [25] Y. Dong, S. Li, K. Zhao, C. Han, W. Chen, B. Wang, L. Wang, B. Xu, Q. Wei, L. Zhang, X. Xu, L. Mai, *Energy Environ. Sci.* **2015**, *8*, 1267.
- [26] L. Y. Lim, S. Fan, H. H. Hng, M. F. Toney, *Adv. Energy Mater.* **2015**, *5*, 1500599.
- [27] L. Y. Lim, S. Fan, H. H. Hng, M. F. Toney, *J. Phys. Chem. C* **2015**, *119*, 22772.
- [28] L. A. de Picciotto, K. T. Adendorff, D. C. Liles, M. M. Thackeray, *Solid State Ionics*

1993, 62, 297.

- [29] S. Hartung, N. Bucher, R. Bucher, M. Srinivasan, *Rev. Sci. Instrum.* **2015**, 86, 086102.
- [30] L. Vegard, *Zeitschrift fuer Physik.* **1921**, 5, 17.
- [31] M.-X. Zhang, Y.-X. Zhang, *Chinese J. Inorg. Chem.* **2012**, 28, 2065.
- [32] L. Bai, Y. Xue, J. Zhang, B. Pan, C. Wu, *Eur. J. Inorg. Chem.* **2013**, 2013, 3497.

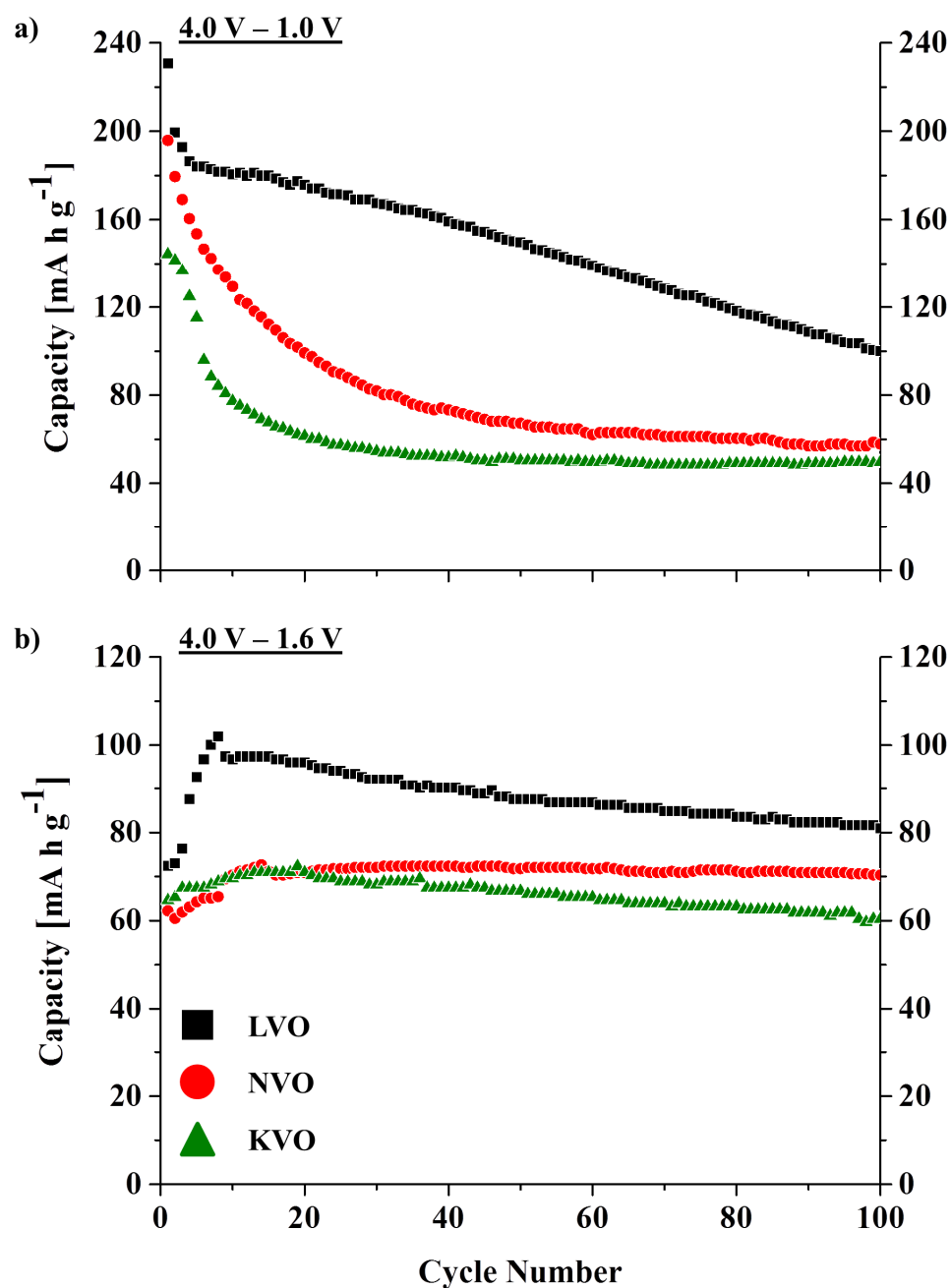


Figure 1. Cycling performance of LVO, NVO, and KVO in the potential regions a) $4.0 \text{ V} - 1.0 \text{ V}$ and b) $4.0 \text{ V} - 1.6 \text{ V}$.

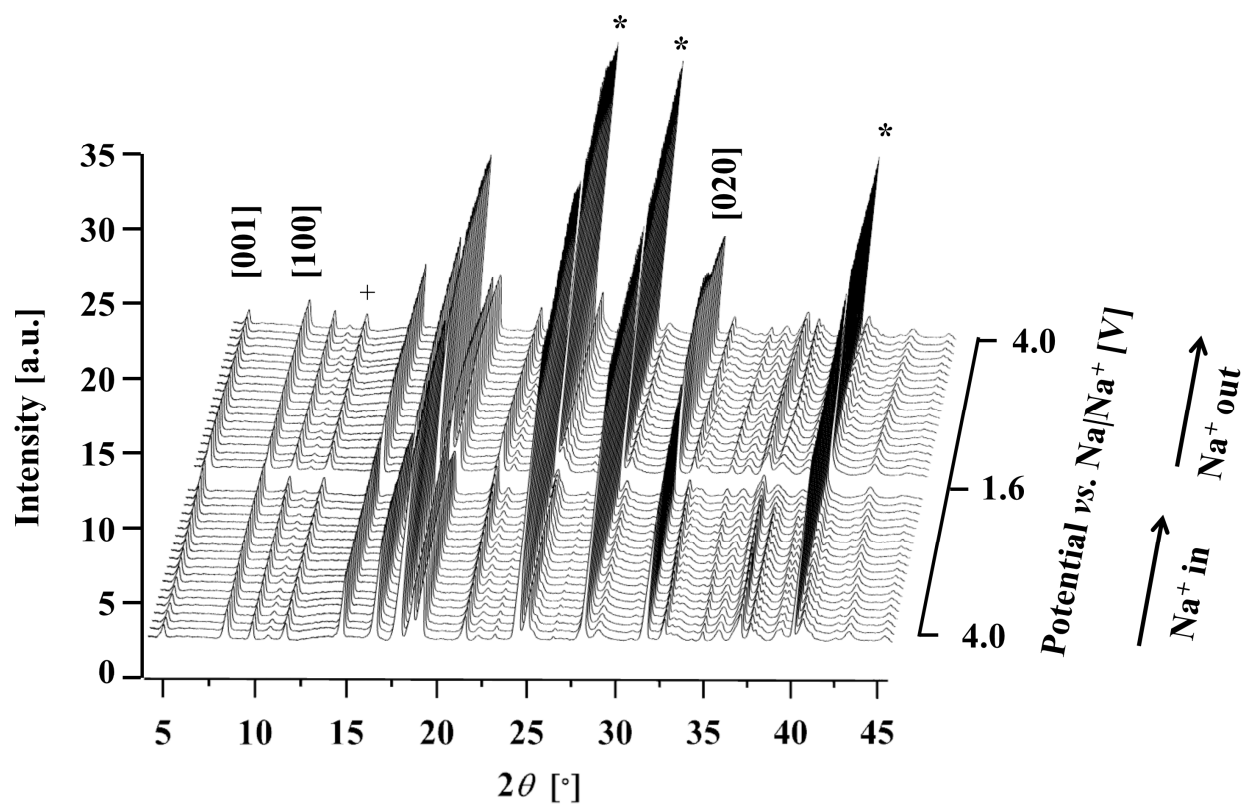


Figure 2. NVO, Narrow Range. Development of the X-ray diffraction pattern (synchrotron radiation, $\lambda = 0.974 \text{ \AA}$) during charge/discharge (* denotes aluminium reflections, + denotes teflonized acetylene black).

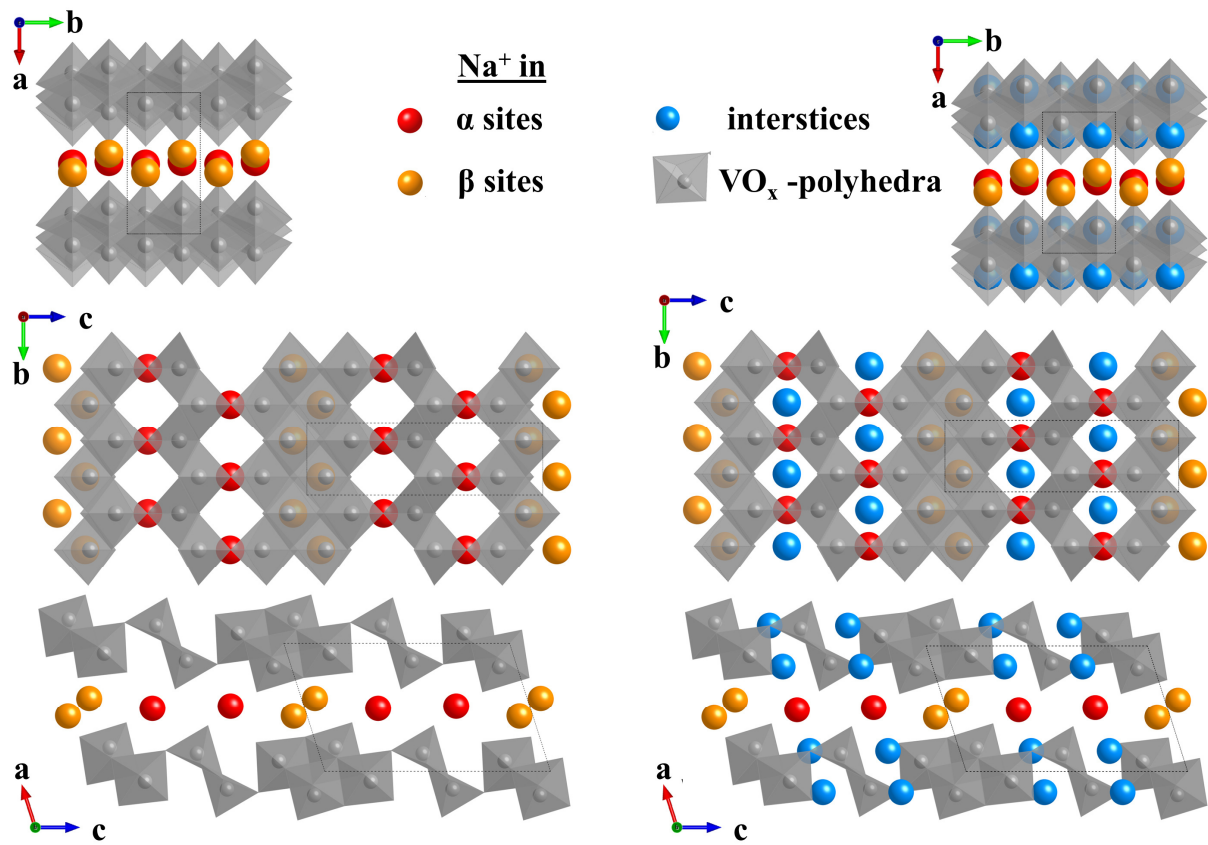


Figure 3. NVO crystal structure without (left) and with interstices marked (right).

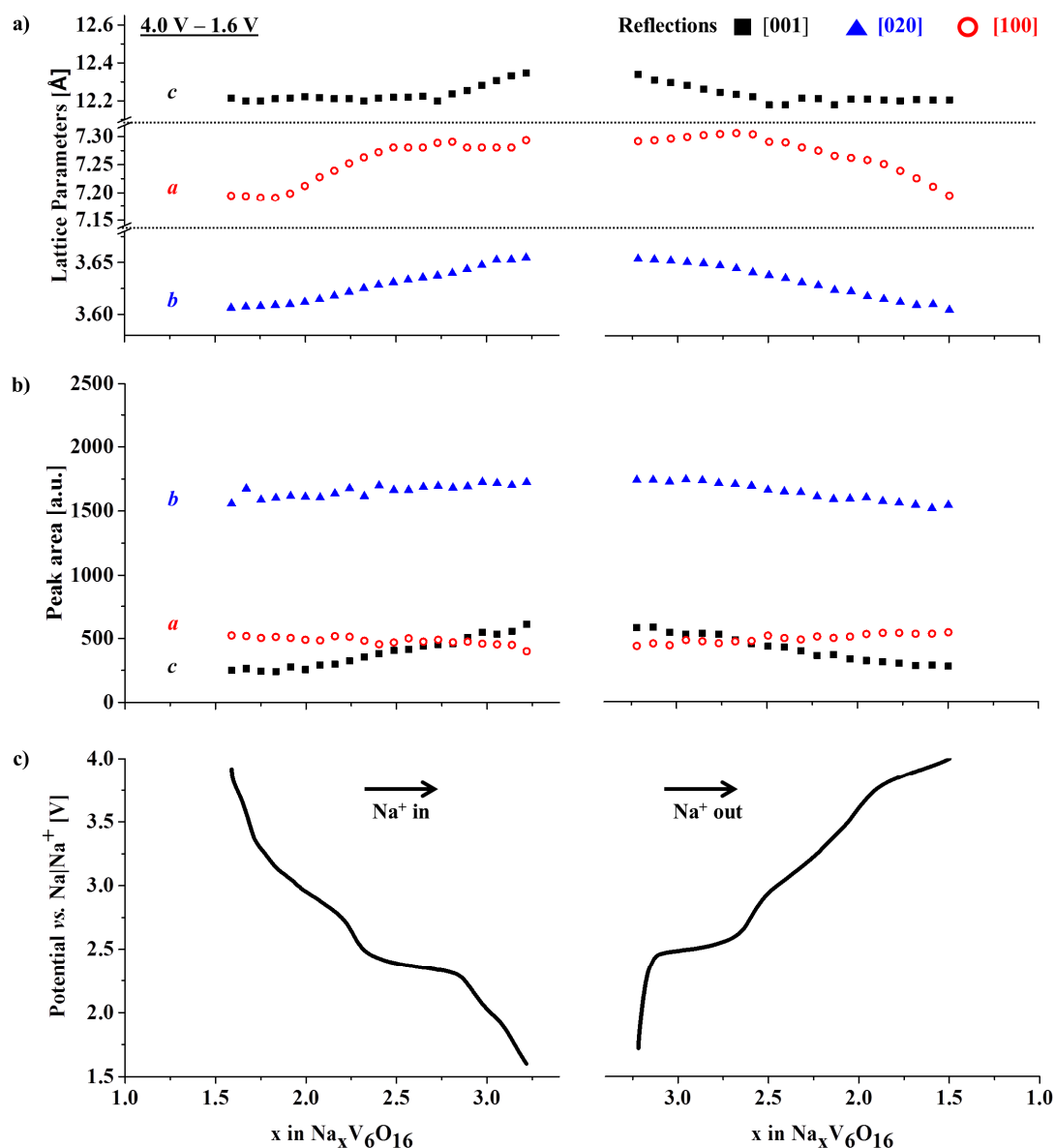


Figure 4. NVO, Narrow Potential Range. a) Changes of the lattice parameters (top/black: c -lattice parameter, middle/red: a -lattice parameter, bottom/blue: b -lattice parameter). Note: y-axis: different spacing for lattice parameters a , b , c (same spacing: Figure S11), b) Changes of the integrated areas of the (001), (020) & (100) reflections in the first cycle, c) galvanostatic charge / discharge profile.

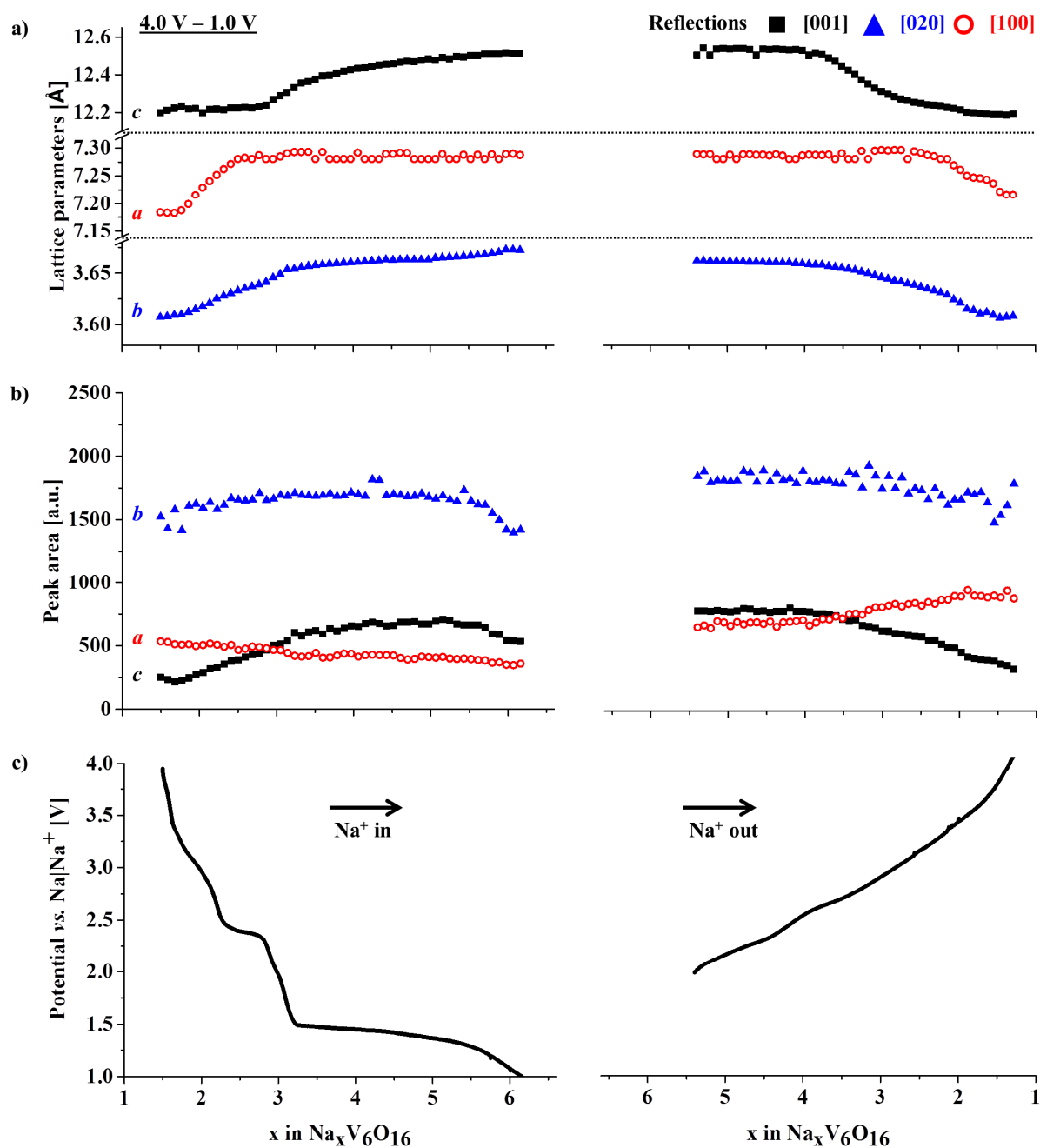


Figure 5. NVO, Potential Range. a) Changes of the lattice parameters in the 1st cycle from 4.0 V – 1.0 V (top/black: c -lattice parameter, middle/red: a -lattice parameter, bottom/blue: b -lattice parameter). Note: y-axis: different spacing for lattice parameters a , b , c (same spacing: Figure S11), b) Changes of the integrated areas of the (001), (020) & (100) reflections in the first cycle (the difference between the endpoint of the discharge and the starting point of the charge is due to cell change after the discharge), c) galvanostatic charge / discharge profile.

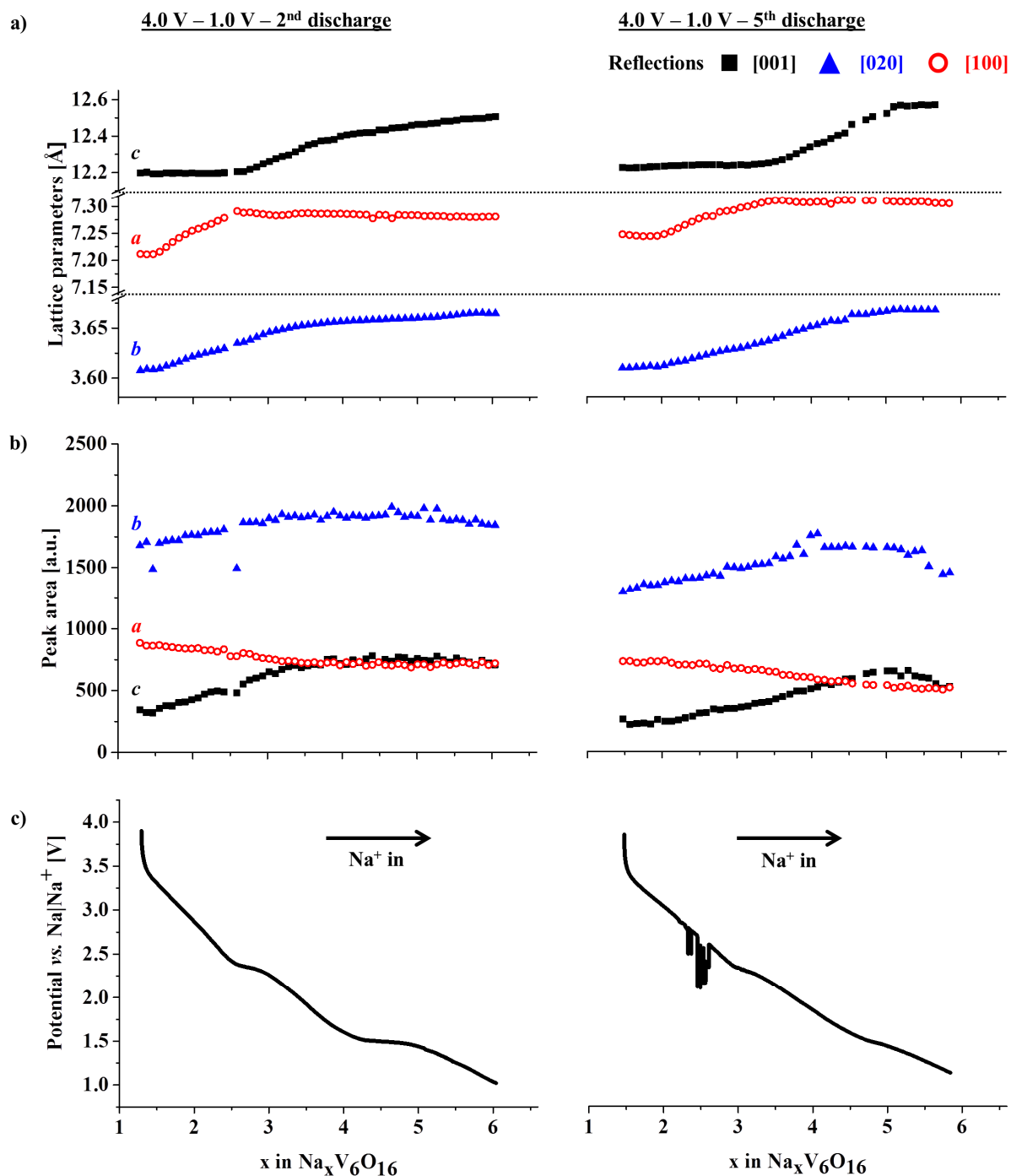


Figure 6. NVO, Wide Potential Range. a) Changes of the lattice parameters (top/black: c -lattice parameter, middle/red: a -lattice parameter, bottom/blue: b -lattice parameter) in the 2nd and 5th cycle from 4.0 V – 1.0 V (development 2nd discharge: $a = 7.21 \text{ \AA} - 7.28 \text{ \AA}$, $b = 3.61 \text{ \AA} - 3.67 \text{ \AA}$, $c = 12.20 \text{ \AA} - 12.51 \text{ \AA}$, development 5th discharge: $a = 7.25 \text{ \AA} - 7.31 \text{ \AA}$, $b = 3.61 \text{ \AA} - 3.67 \text{ \AA}$, $c = 12.22 \text{ \AA} - 12.56 \text{ \AA}$.) Note: y-axis: different spacing for lattice parameters a , b , c (same spacing: Figure S11), b) Changes of the integrated areas of the (001), (020) & (100)

reflections for the 2nd and 5th discharge from 4.0 V to 1.0 V, c) galvanostatic charge / discharge profile (the glitches in the 5th discharge were due to problems with the coin cell holder; this did not influence the typically observed characteristics in the 5th discharge for this material); the measurements presented in this figure were conducted with the same cell.

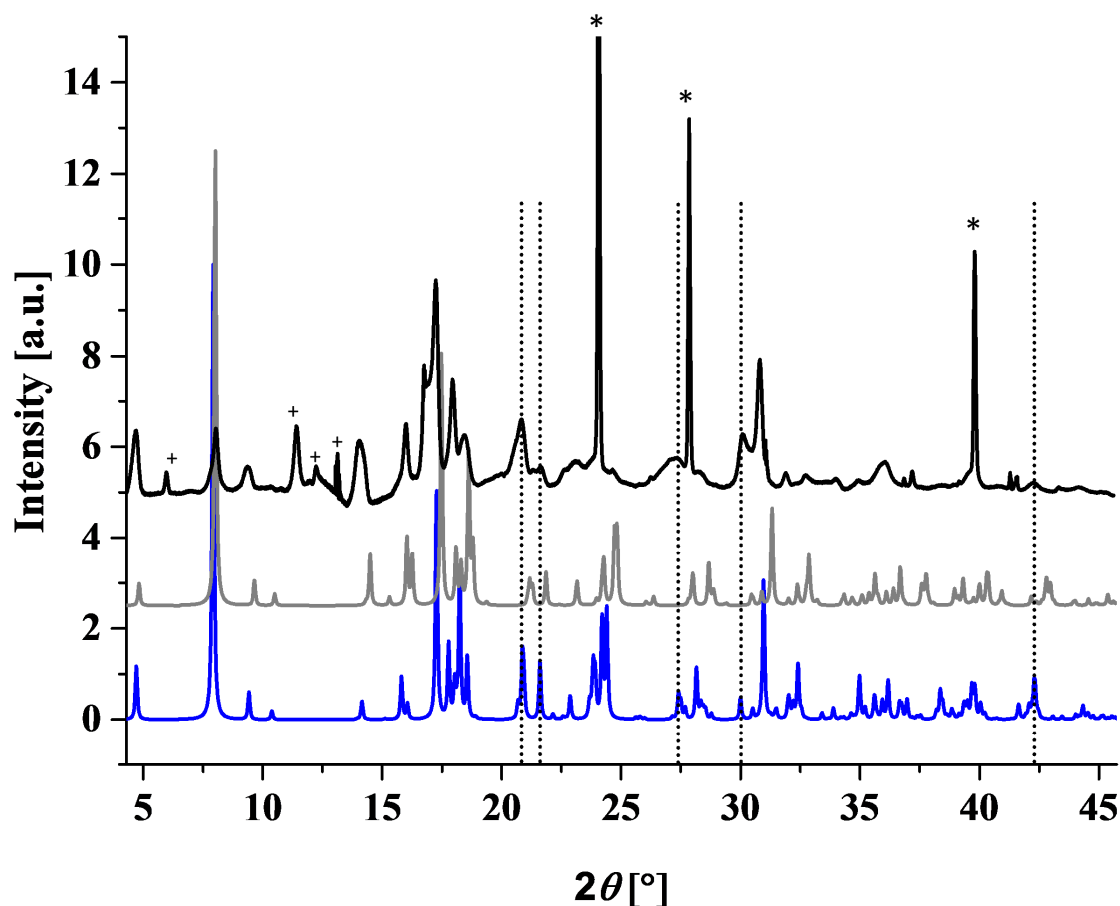


Figure 7. Top/Black: XRD pattern (synchrotron radiation, $\lambda = 0.974 \text{ \AA}$) of NVO at the end of the 5th discharge (+: reflections attributed to teflonized acetylene black used for making the pellets and from the epoxy resin used for sealing the coin cells; *: aluminum reflections); Middle/Grey: Simulated pattern based on the original structure, Bottom/Blue: Simulated pattern of the NVO structure with fully occupied lattice sites and interstices (Na₆V₆O₁₆); dotted lines denote significant new reflections.

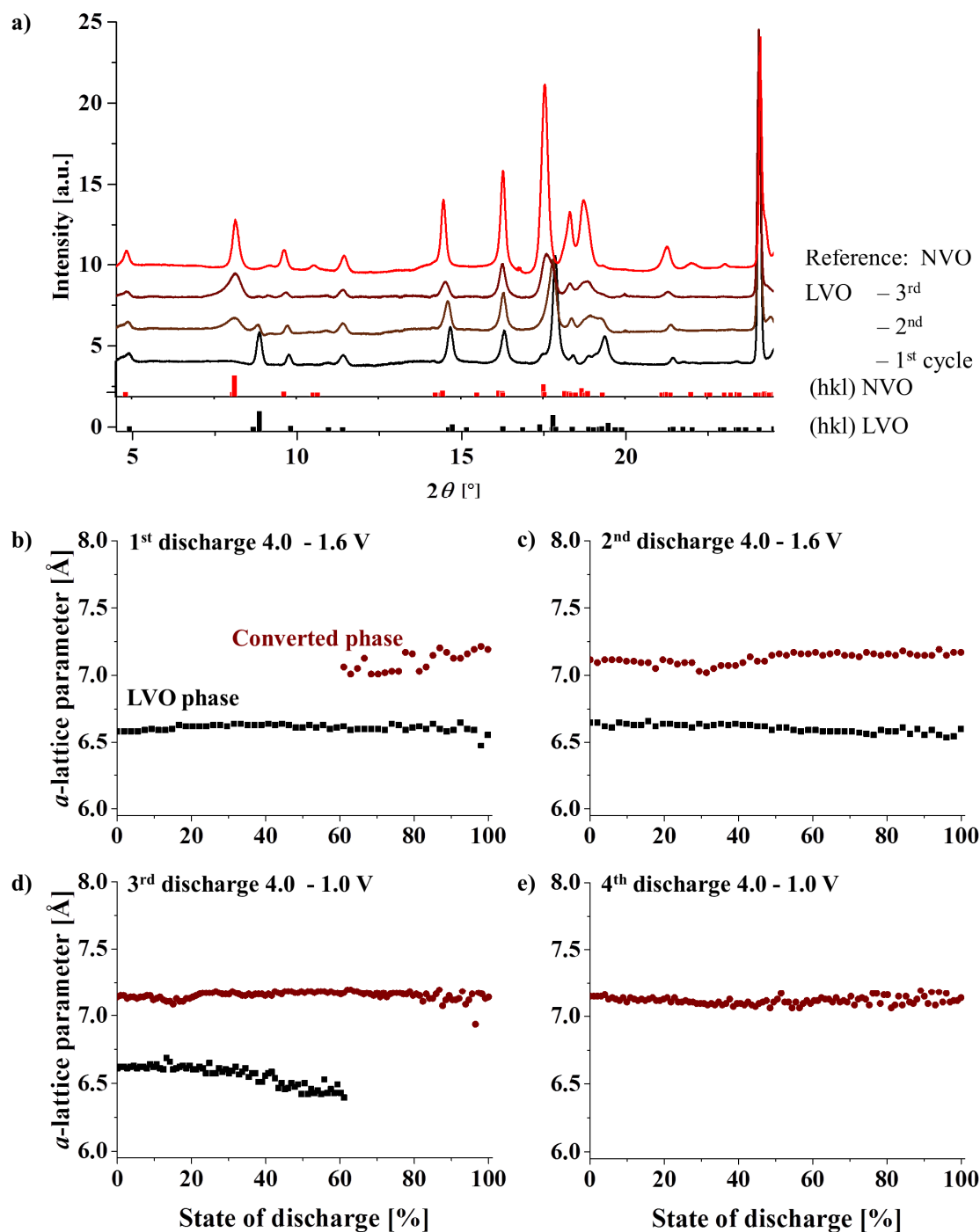


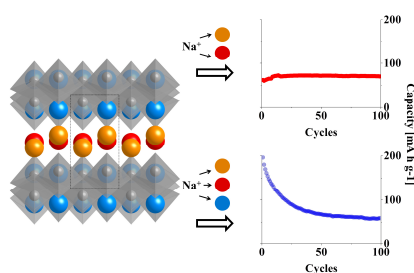
Figure 8. a): XRD pattern (synchrotron radiation, $\lambda = 0.974 \text{ \AA}$) of LVO at 4.0 V in the 1st, 2nd, and 3rd cycle, and XRD of NVO at 4.0 V in the 3rd cycle, (hkl) of LVO and NVO at OCP (*: aluminum reflections; +: teflonized acetylene black); b) – e): change in the a -lattice parameter for LVO (pristine) and NVO (newly emerging) during cycling (data based on Figure S8).

Na⁺-insertion into Na_{2.46}V₆O₁₆ (NVO) and Li_{2.55}V₆O₁₆ (LVO) were investigated using *in operando* synchrotron X-ray diffraction. Two crystallographic sites (orange, red) are reversibly occupied upon Na⁺-insertion into NVO between 4.0 V – 1.6 V. In contrast, at lower potentials Na⁺ occupies interstices (blue) resulting in irreversible structural changes concomitantly with capacity fading. For LVO, cycling performance is enhanced due to minor Li⁺-retention.

Sodium-ion battery

*Steffen Hartung, Nicolas Bucher, Joseph B. Franklin, Anna M. Wise, Linda Y. Lim, Han-Yi Chen, Johanna Nelson Weker, Maria-E. Michel-Beyerle, Michael F. Toney, Madhavi Srinivasan**

Mechanism of Na⁺ Insertion in Alkali Vanadates and its Influence on Battery Performance.



Supporting Information

Mechanism of Na⁺ Insertion in Alkali Vanadates. and its Influence on Battery Performance.

*Steffen Hartung, Nicolas Bucher, Joseph B. Franklin, Anna M. Wise, Linda Y. Lim, Han-Yi Chen, Johanna N. Weker, Maria-E. Michel-Beyerle, Michael F. Toney, Madhavi Srinivasan**

The Supporting Information comprises:

Figure S1) Powder XRD data for Li_{2.55}V₆O₁₆ (LVO), Na_{2.46}V₆O₁₆ (NVO), and K_{1.8}V₆O₁₆ (KVO).

Figure S2) FESEM pictures of LVO, NVO, and KVO.

Figure S3) Galvanostatic discharge profile of LVO, NVO, and KVO (20 mA g⁻¹) in the 1st and 5th cycle

Figure S4) Changes in the NVO unit cell volume for all cycles.

Figure S5) Depiction of the new reflections in the NVO pattern at the end of the 5th discharge to 4.0 V.

Figure S6) Synchrotron *operando* measurement of LVO in the first cycle between 4.0 V – 1.6 V.

Figure S7) Development of the (100) reflection of LVO during *operando* cycling using a laboratory X-ray diffraction set-up.

Figure S8) Relaxation behavior of NVO and LVO in the galvanostatic intermittent titration technique (GITT) measurement at various potentials.

Figure S9) Development of the diffusion coefficient of NVO and LVO as measured by GITT during one discharge to 1.0 V

Figure S10) Development of the NVO lattice parameters during cycling with uniform spacing on the y-axis.

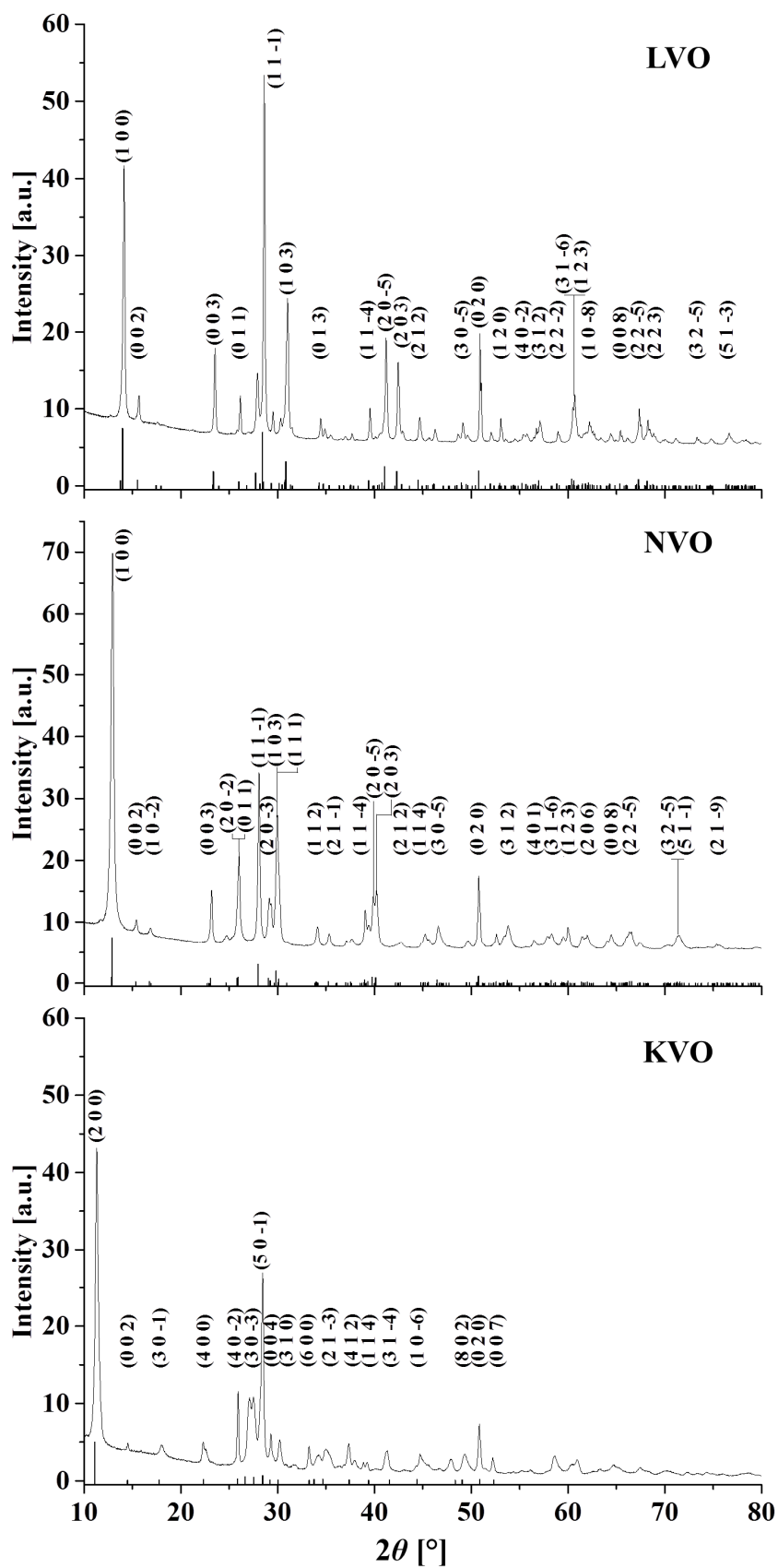


Figure S1. XRD patterns ($\text{Cu}_{K\alpha}$ -radiation, $\lambda = 1.54 \text{ \AA}$) of $\text{Li}_{2.55}\text{V}_6\text{O}_{16}$ (LVO), $\text{Na}_{2.46}\text{V}_6\text{O}_{16}$ (NVO) and $\text{K}_{1.8}\text{V}_6\text{O}_{16}$ (KVO).

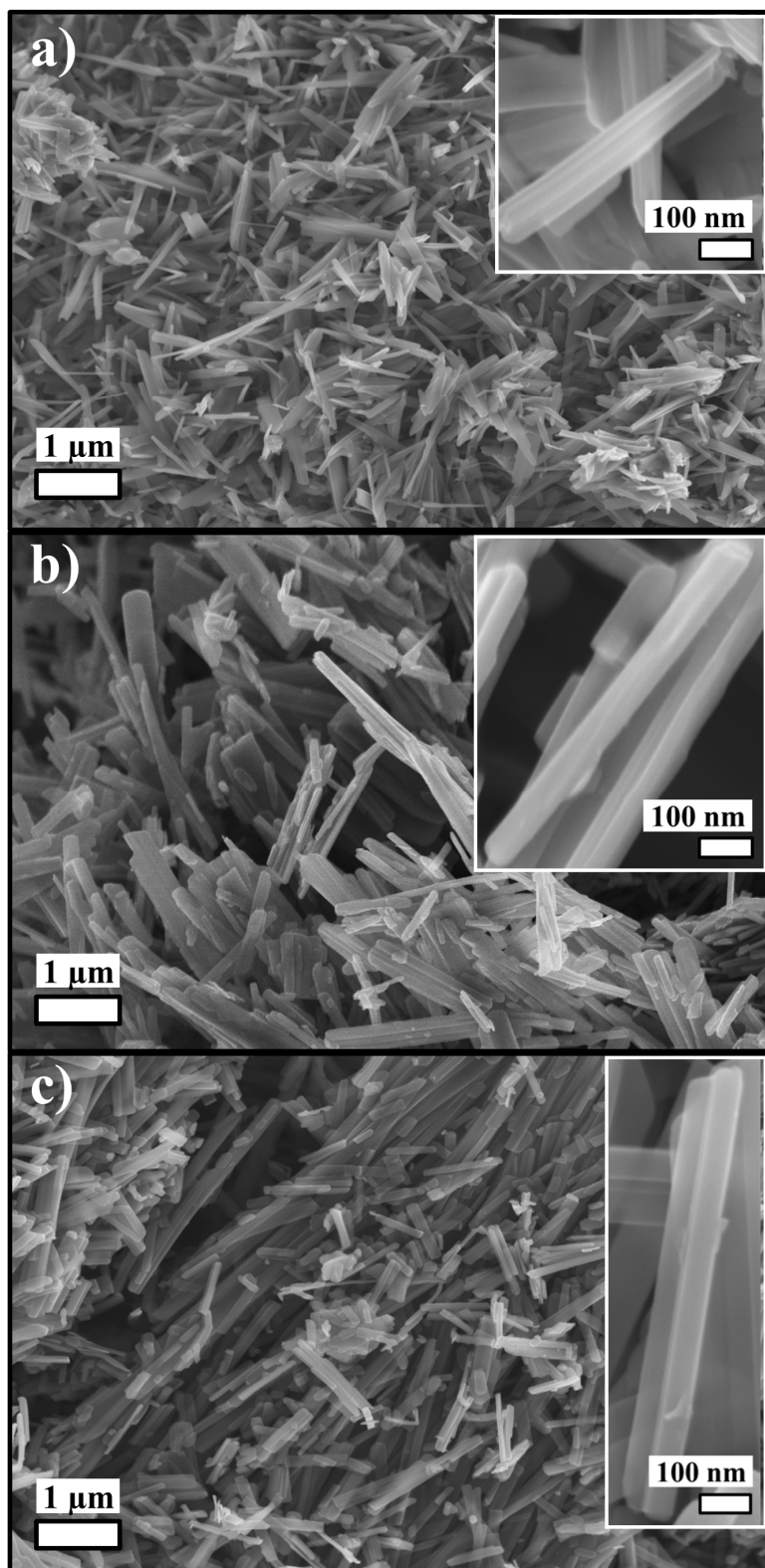


Figure S2. SEM image of a) $\text{Li}_{2.55}\text{V}_6\text{O}_{16}$ (LVO), b) $\text{Na}_{2.46}\text{V}_6\text{O}_{16}$ (NVO), and c) $\text{K}_{1.8}\text{V}_6\text{O}_{16}$ (KVO).

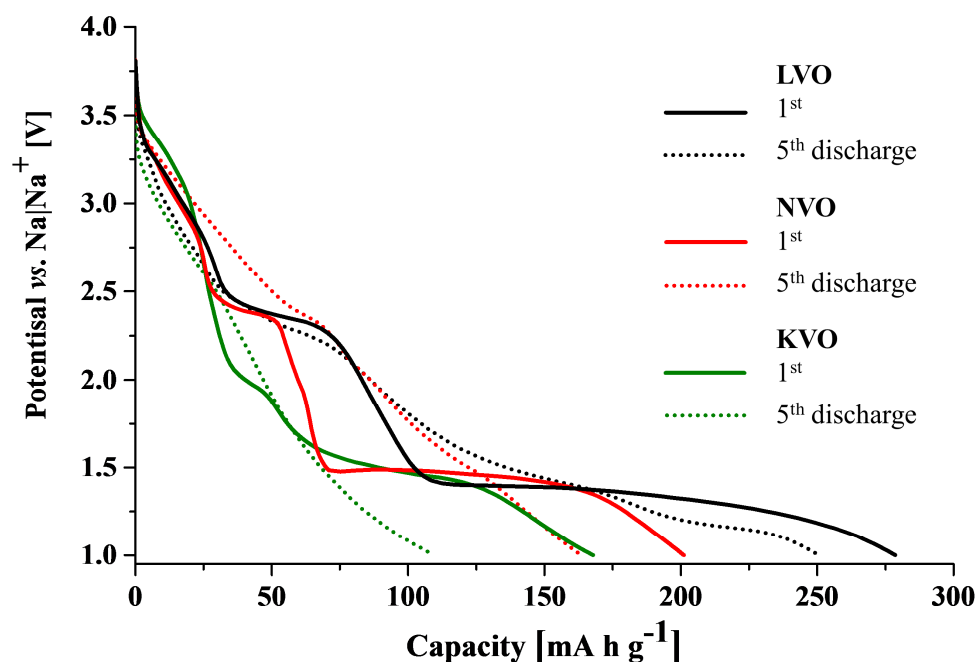


Figure S3. Galvanostatic discharge profile of LVO, NVO and KVO between 4.0 V – 1.0 V, 1st & 5th discharge (20 mA g⁻¹). The onset of the long plateau is at a deeper potential for LVO as compared to NVO and KVO. The radius of Li⁺ is smaller compared to Na⁺ and Li-O-bonds are typically stronger than Na-O bonds.^[1,2] This difference potentially results in an increased electrostatic attraction of the surrounding VO_x-polyhedra, and thus in a smaller unit cell for LVO than for NVO. Thus, the electrochemical force to insert Na⁺ into the LVO structure needs to be higher, which would explain the plateau at a lower potential as compared to the Na- and K-analogue.

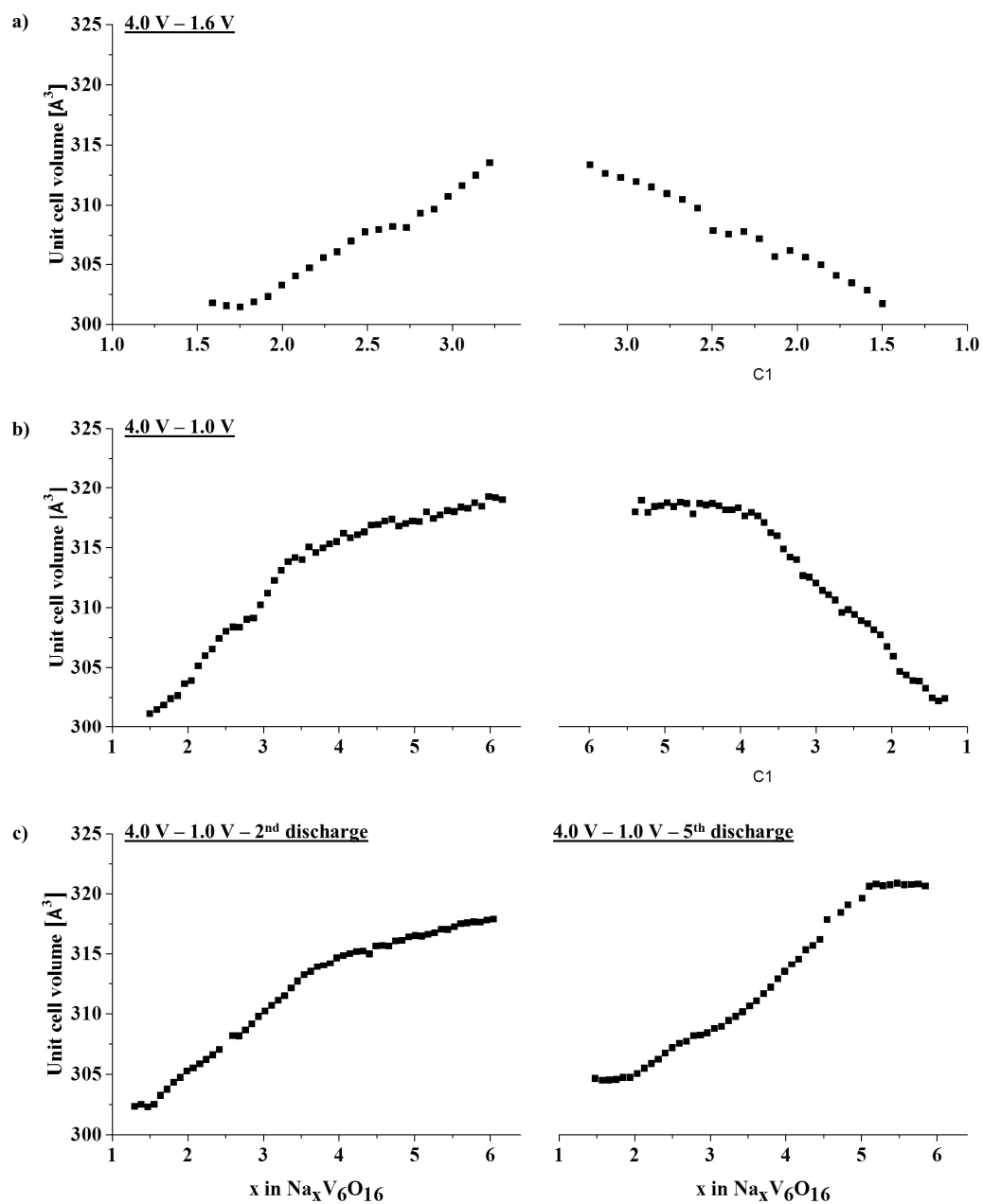


Figure S4. Change of the unit cell volume during a) discharge / charge between 4.0 V – 1.6 V, b) discharge / charge between 4.0 V – 1.0 V, c) 2nd and 5th discharge to 1.0 V.

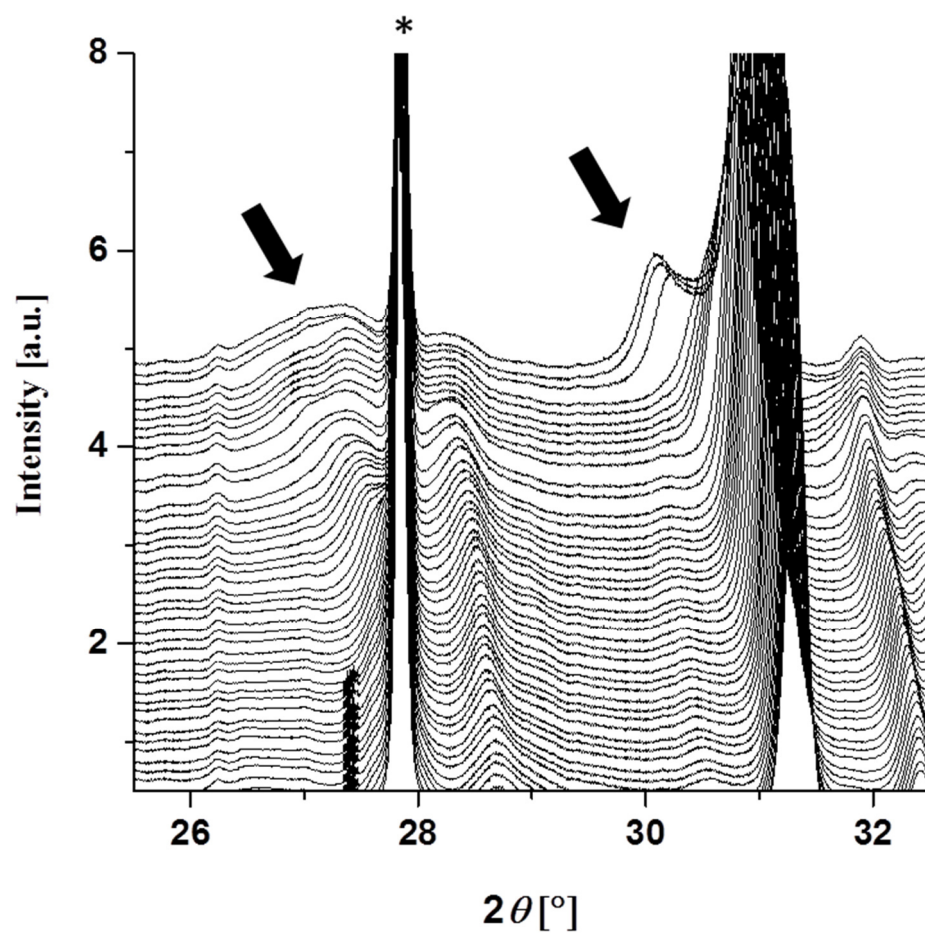


Figure S5. XRD pattern development (synchrotron radiation, $\lambda = 0.974 \text{ \AA}$) of NVO at the end of the 5th discharge.

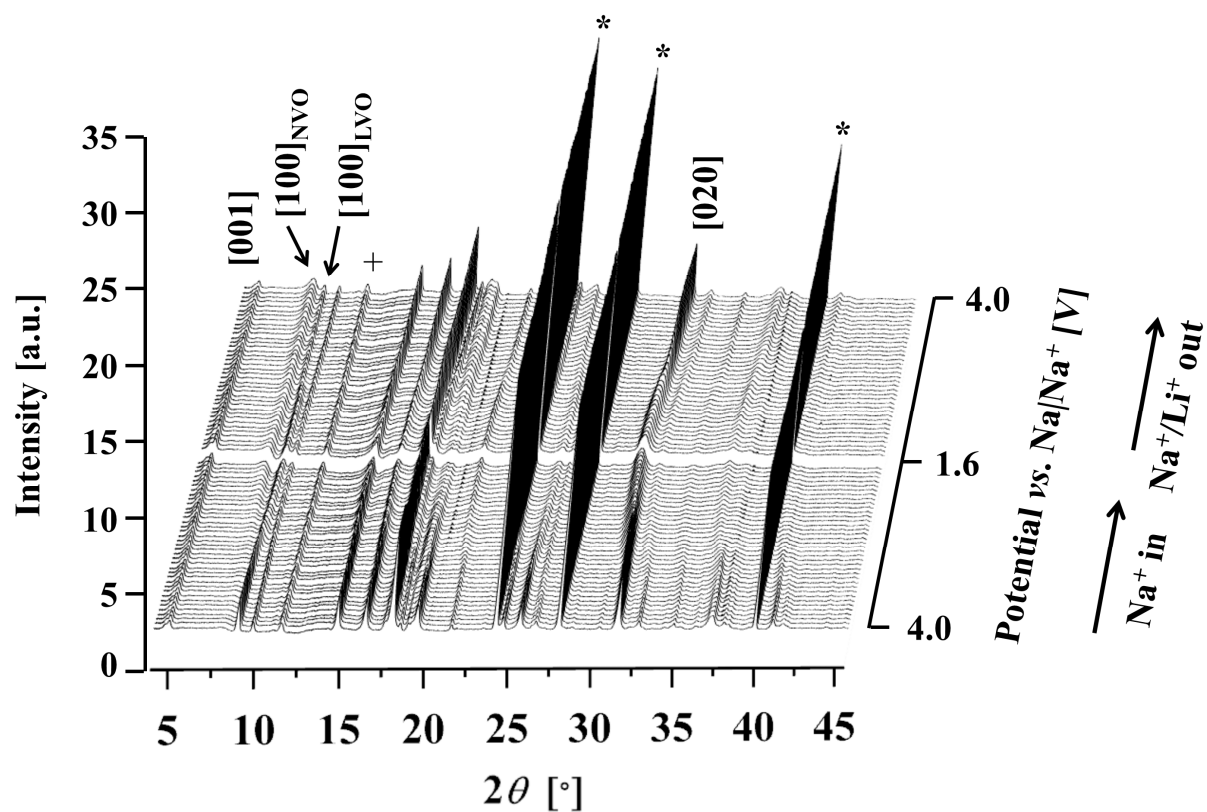


Figure S6. Development of the X-ray pattern (synchrotron radiation, $\lambda = 0.974 \text{ \AA}$) of LVO in the narrow potential region between 4.0 V – 1.6 V (*: aluminum reflections; +: teflonized acetylene black).

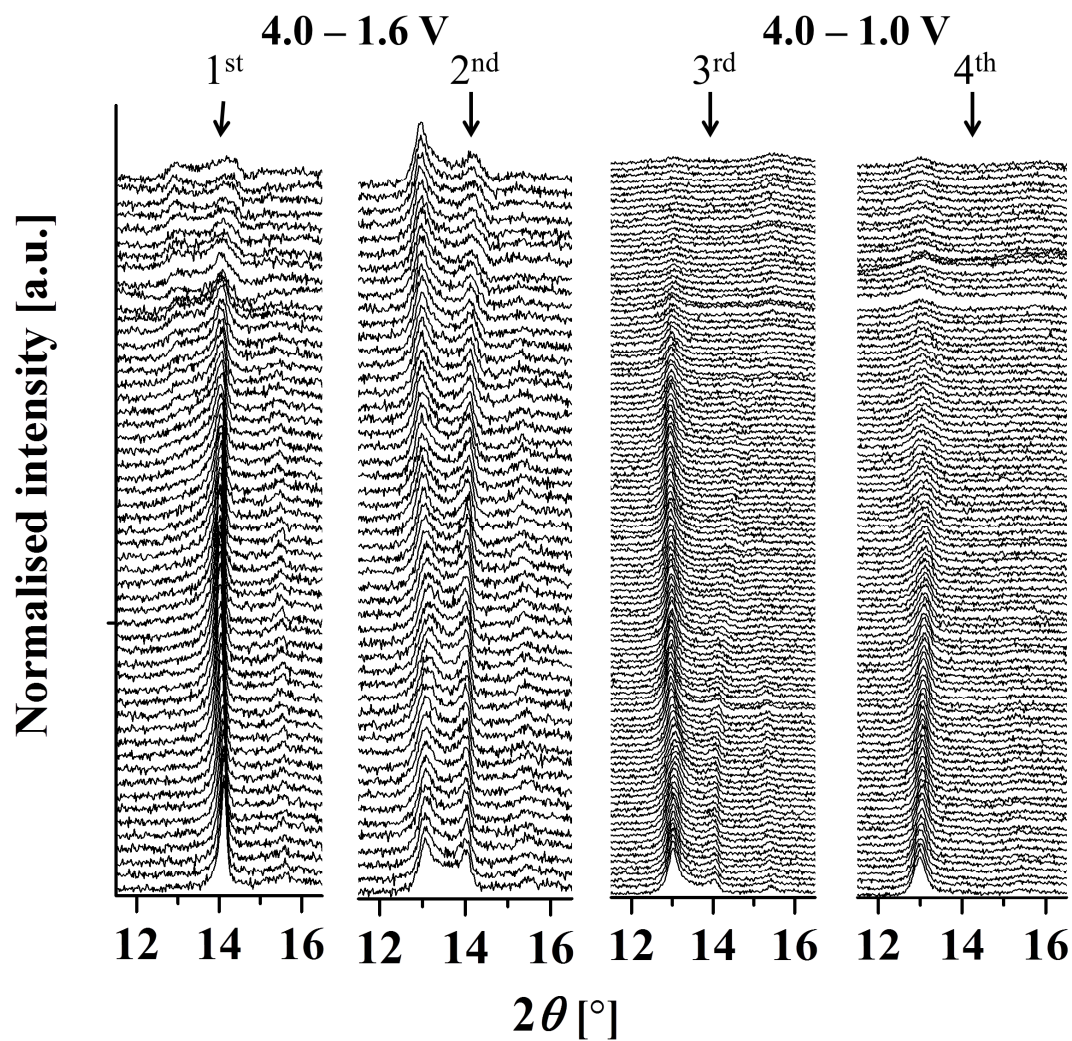


Figure S7. Development of the (100)_{LVO} and the (100)_{NVO} reflection as measured with a laboratory scale diffractometer (Cu_{K α} -radiation, $\lambda = 1.54 \text{ \AA}$) in reflection mode.

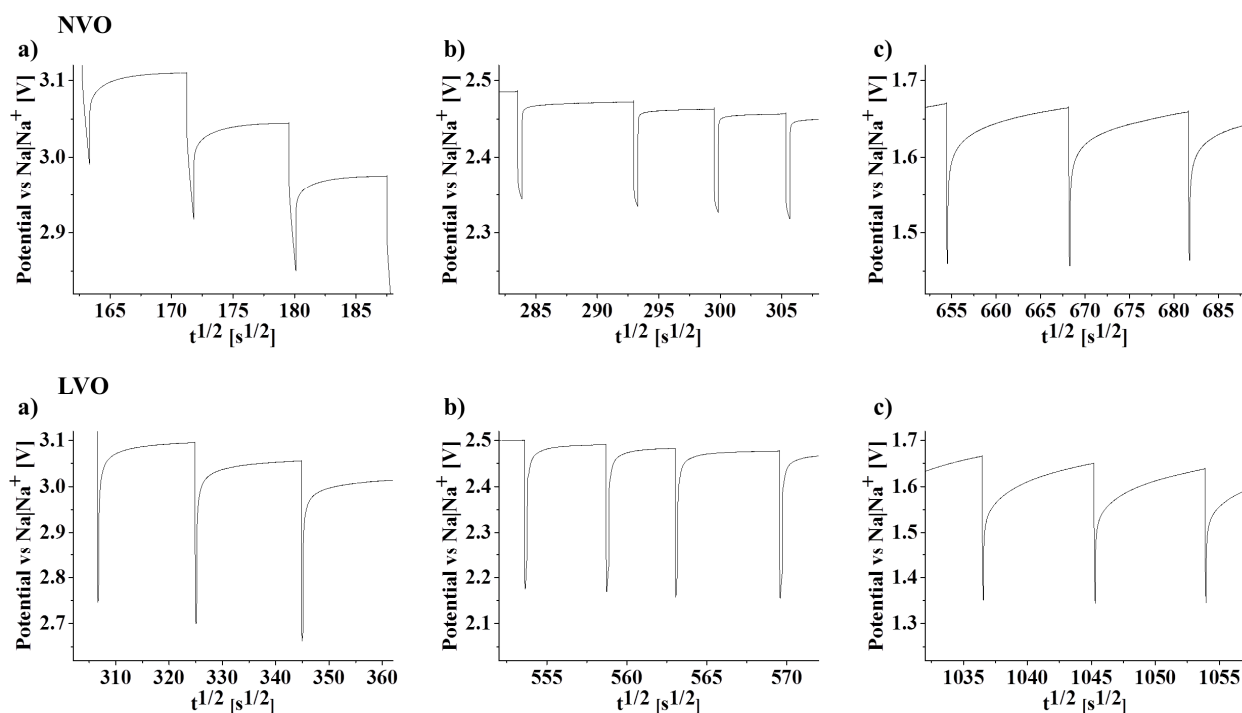


Figure S8. Time-dependent variation of the GITT curve of NVO and LVO: a) before the 1st plateau, b) during the first plateau, c) during the 2nd plateau.

Relaxation times vary during cycling. For NVO, up to a Na⁺-content of approximately 2.8, *i.e.*, until the end of the first plateau, the system relaxes after one current pulse (a) and b)). At higher Na⁺-contents, in the second plateau, the material is clearly not in equilibrium after 5 hours of relaxation time (c). As relaxation criteria were the same throughout the measurement (5 hours, or a potential change of $< 2 \text{ mV h}^{-1}$), this behavior is attributed to a decrease of electric and/or ionic conductivity. For LVO, relaxation times are comparable to NVO. While the system appears to be in equilibrium after a relaxation time of 5 hours or less until the end of the first plateau, *i.e.*, a Na⁺-content of ~ 3.1 (a), b)), it does not fully relax anymore in the long plateau at 1.3 V. Thus, similar to NVO, electronic and/or ionic conductivity decreases upon insertion of high Na⁺-contents.

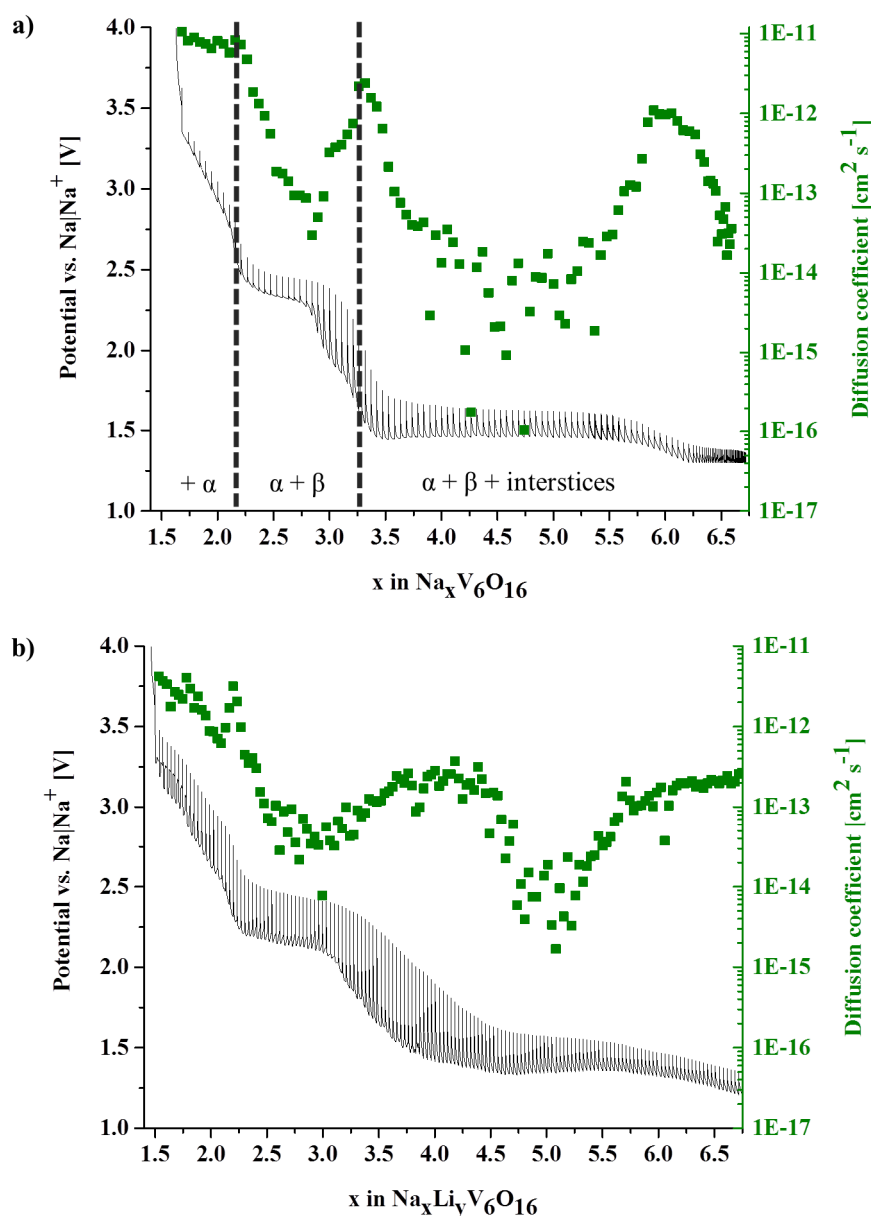


Figure S9. Development of the diffusion coefficient for Na^+ during the discharge of a) NVO (dotted lines indicate which site is being filled up in the respective range of Na-occupancy) and b) LVO, as measured by galvanostatic intermittent titration technique (GITT).

Na⁺-diffusion in NVO and (initial) LVO: In section 3.2, we correlated structural and electrochemical reversibility and suggested that different sites in the crystal structure are occupied successively. In this section, we investigate if this is also reflected in the diffusion behaviour of Na^+ within the active electrode material using galvanostatic intermittent titration technique (GITT).^[3,4] Changes in the occupation of lattice sites or phase changes often result

in a change of the diffusion behavior of the respective ions in the crystal structure.^[5] Therefore, GITT was employed to monitor the change of the diffusion properties of NVO and LVO and to relate this to the structural changes described above.

The GITT for NVO is in good qualitative agreement with the galvanostatic discharge curve. In general, the long relaxation times are indicative of rather slow kinetics. The effective diffusion coefficient (Figure S10), for Na⁺ in the NVO structure is relatively constant at the beginning of the discharge up to a Na⁺-content of approximately 2.2. At the same Na⁺-content at which the discharge curve reaches a plateau, Na⁺-diffusion in the structure also decreases, followed by an increase at the end of the electrochemical plateau. At approximately $x = 3.25$, Na⁺-diffusion drops again; this coincides with the onset of the plateau at 1.3 V in the discharge curve. Minor differences regarding Na⁺-content between the galvanostatic measurements described above, and GITT measurements, are attributed to diffusion processes during relaxation times.^[3] For oxide cathodes, a minimum of the diffusion constant in combination with a plateau in the galvanostatic profile is typical for structural changes^[5]. This suggests, as also argued above based on structural data, that until the diffusion minimum Na⁺ occupies the pre-defined lattice sites, the α and β sites, in the given crystal structure. However, the XRD data shows no phase transition for the region around the diffusion coefficient minimum. It can be hypothesized that the minimum corresponds to a rearrangement of the Na-ions between the different sites, but ultimately the reason for the observed minimum remains unknown. The second minimum coincides with the plateau around 1.3 V. In this region, the XRD data shows structural changes, *i.e.*, insertion of Na⁺ into the interstices of the NVO structure. Thus, the GITT measurements support the hypothesis that for the initial insertion of Na-ions, the structure does not change, whereas subsequent structural changes occur based on the insertion of Na⁺ into the interstices (Figure 7, S7).

For LVO (Figure S10), the Na⁺-diffusion coefficient is slightly lower in the beginning than for NVO. This is attributed to the smaller interlayer spacing of LVO, which makes it harder for the Na-ions to move in the structure. This trend of higher ionic conductivity for NVO as compared to LVO was reported for the case of Li⁺-conductivity before.^[6] During discharge, the underlying trend is comparable, albeit the curve is more stretched out. However, the minimum of the diffusion coefficient which coincides with the plateau at 1.3 V starts at a higher Na⁺-content for LVO. Thus, structural changes seem to occur at higher Na⁺-contents as compared to NVO. This is in line with the initial hypothesis that Li⁺ has a stabilizing effect on the structure, and can therefore increase cycling stability.

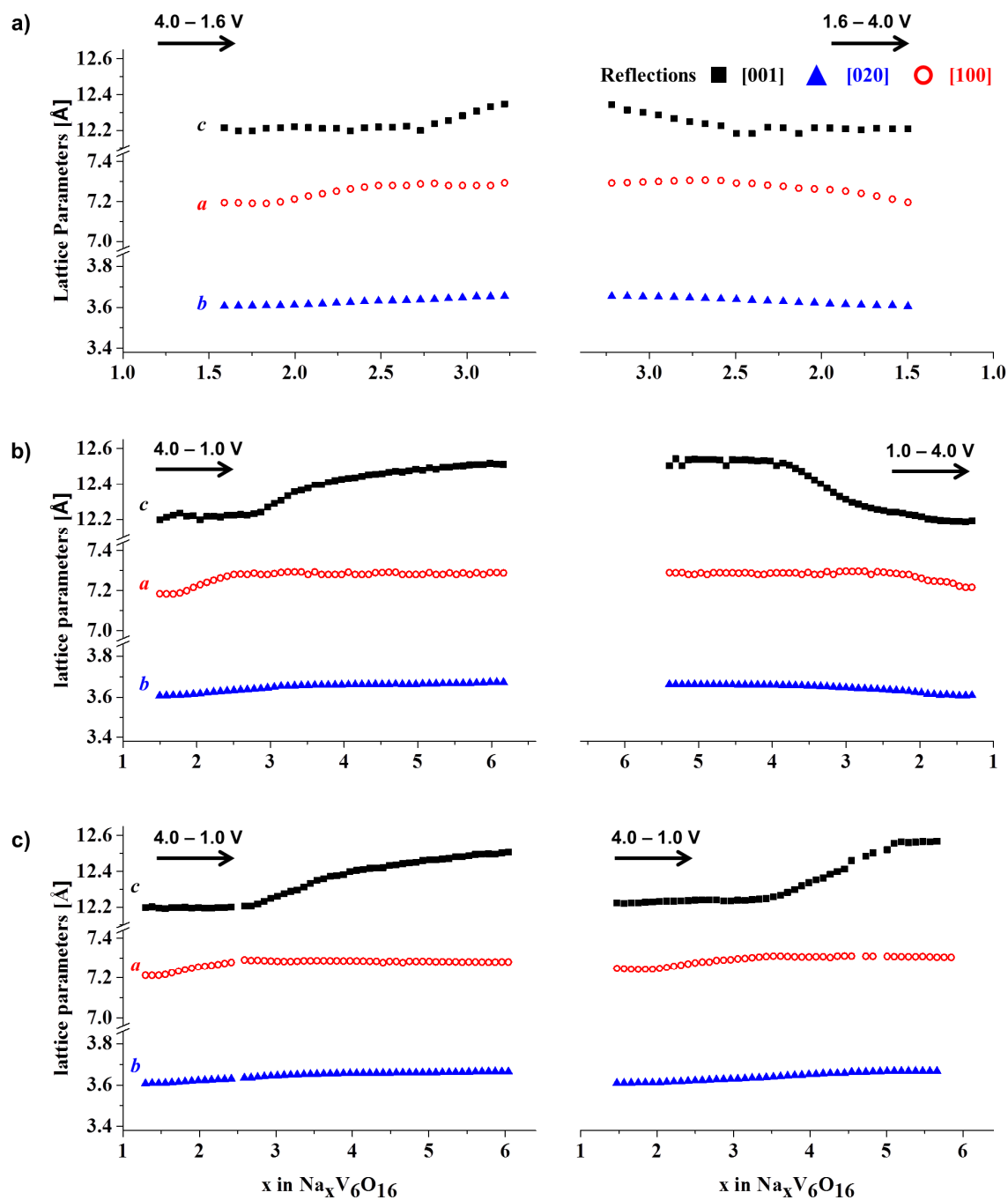


Figure S10. Development of the lattice parameters with uniform spacing on the y-axis during cycling between a) 4.0 V – 1.6 V, b) subsequent cycle between 4.0 V – 1.0 V, c), 2nd and 5th discharge to 1.0 V, respectively.

References

- [1] S. P. Ong, V. L. Chevrier, G. Hautier, A. Jain, C. Moore, S. Kim, X. Ma, G. Ceder, *Energy Environ. Sci.* **2011**, *4*, 3680.
- [2] J. Malcolm W. Chase, *NIST-JANAF Thermochemical Tables.*, American Chemical Society ; American Institute Of Physics For The National Institute Of Standards And Technology, Washington, DC : New York, **1998**.
- [3] E. Markevich, M. D. Levi, D. Aurbach, *J. Electroanal. Chem.* **2005**, *580*, 231.
- [4] D. W. Dees, S. Kawauchi, D. P. Abraham, J. Prakash, *J. Power Sources* **2009**, *189*, 263.
- [5] K. M. Shaju, G. V. Subba Rao, B. V. R. Chowdari, *Electrochim. Acta* **2004**, *49*, 1565.
- [6] M. Pasquali, G. Pistoia, *Electrochim. Acta* **1991**, *36*, 1549.

5.4 Vanadium-based polyoxometalate as new material for sodium-ion battery anodes

In this chapter, the publication “Vanadium-based polyoxometalate as new material for sodium-ion battery anodes” (J. Power Sources, **2015**, 288, 270 – 277) is presented. It describes for the first time the application of a new class of materials, POMs, as NIB anodes. S. Hartung was leading the work on electrochemical investigations that are presented in this publication. Synthesis and most of the physical characterization of the POM was performed by Rami Al-Oweini.

As described in previous chapters, the investigated vanadates exhibit significant capacity loss during cycling, potentially due to irreversible insertion of Na^+ into the crystal structure. One route to alleviate structural degradation is to use materials with an alternative structural constitution. POMs consist of anionic metal-oxo clusters of (early) transition metal oxides. They do not have extended crystal structures, but, also as a solid, consist of isolated polyanions with cavities between the individual clusters. These cavities can take up cations, such as Li^+ or Na^+ . Thus, to circumvent the insertion of Na^+ into vanadates with a long-range crystal structure that could be broken up in the process, the POM $\text{Na}_6[\text{V}_{10}\text{O}_{28}]$ was tested. Interestingly, as opposed to the materials described in previous chapters, $\text{Na}_6[\text{V}_{10}\text{O}_{28}]$ shows considerable electrochemical activity in the anodic region; the average discharge potential was 0.4 V. No pronounced peaks are observed in the cyclic voltammogram (except for peaks corresponding to SEI formation in the first discharge), which indicates a continuous insertion of Na^+ between the $[\text{V}_{10}\text{O}_{28}]^{6-}$ -polyanions. This is substantiated by galvanostatic tests, which show a continuous distribution of insertion voltages. As the shape of the CV resembles that of supercapacitor, XPS measurements were conducted to exclude pure physical adsorption processes, and showed that during insertion, the vanadium in the $[\text{V}_{10}\text{O}_{28}]^{6-}$ -clusters is (at least partially) reduced from V^{+5} to V^{+4} . The underlying mechanism of the Na-insertion is reasoned to be a surface-induced capacitive redox process, as opposed to the insertion-mechanism described in Chapter 2.3.2.

The cycling stability of $\text{Na}_6[\text{V}_{10}\text{O}_{28}]$ as NIB anode well exceeded the cyclability of the materials described in previous chapters. Discharge capacity in cycle 15 is 221 mA h g^{-1} (at 50 mA g^{-1}), and after 50 cycles 200 mA h g^{-1} are maintained. Moreover, to confirm that $\text{Na}_6[\text{V}_{10}\text{O}_{28}]$ works in Na-ion full-cells, a proof-of-concept study was conducted and the POM was tested in a full-cell as the anode, with spherical $\text{Na}_x\text{MnO}_2^{[44]}$ as the cathode material. Although the focus here was not on optimising the anode:cathode weight ratio, and therefore performance, it was shown that $\text{Na}_6[\text{V}_{10}\text{O}_{28}]$ works in a NIB full-cell and can thus be considered a viable, new NIB anode material.

Even though, in contrast to the vanadates presented in previous chapters, this POM is a NIB anode material, the target of increasing cycling stability has been achieved. This improvement is attributed to the structural features of the POM. Na-ions are believed to insert into the cavities between the polyanionic $[\text{V}_{10}\text{O}_{28}]^{6-}$

clusters, which minimizes structural strain and thus eliminates a major cause for capacity fading.

Vanadium-based polyoxometalate as new material for sodium-ion battery anodes

Steffen Hartung, Nicolas Bucher, Han-Yi Chen, Rami Al-Oweini, Sivaramapanicker Sreejith, Parijat Borah, Zhao Yanli, Ulrich Kortz, Ulrich Stimming, Harry E. Hoster, Madhavi Srinivasan

Reproduced from Journal of Power Sources, 2015, Volume 288, 270-277 with permission from Elsevier.

The publication can be found under the following weblink:

<http://dx.doi.org/10.1016/j.jpowsour.2015.04.009>



Vanadium-based polyoxometalate as new material for sodium-ion battery anodes



Steffen Hartung^{a, b, 1}, Nicolas Bucher^{a, b, 1}, Han-Yi Chen^{a, b}, Rami Al-Oweini^{d, g}, Sivaramapanicker Sreejith^f, Parijat Borah^f, Zhao Yanli^f, Ulrich Körtz^d, Ulrich Stimming^a, Harry E. Hoster^{a, b, e}, Madhavi Srinivasan^{a, c, e, *}

^a TUM CREATE, 1 CREATE Way, #10-02 CREATE Tower, Singapore 138602, Singapore

^b Technische Universität München, 85748 Garching, Germany

^c School of Materials Science and Engineering, Nanyang Technological University, Singapore 639798, Singapore

^d School of Engineering and Science, Jacobs University, P.O. Box 750561, 28725 Bremen, Germany

^e Energy Research Institute @ NTU (ERI@N), Research Techno Plaza, 50 Nanyang Drive, Singapore 637553, Singapore

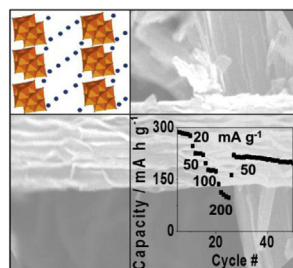
^f Division of Chemistry and Biological Chemistry, School of Physical and Mathematical Sciences, Nanyang Technological University, 21 Nanyang Link, Singapore 637371, Singapore

^g Department of Chemistry, Faculty of Science, Beirut Arab University, P.O. Box 11 50 20, Riad El Solh 1107 2809, Beirut, Lebanon

HIGHLIGHTS

- $\text{Na}_6[\text{V}_{10}\text{O}_{28}] \cdot 16\text{H}_2\text{O}$, a polyoxometalate, was synthesized in a rod-like morphology.
- The POM was thoroughly characterized by ^{51}V -NMR, IR, TGA and TEM.
- $\text{Na}_6[\text{V}_{10}\text{O}_{28}]$ shows high capacities and stabilities as anode material in sodium-ion batteries.
- Reduced strain on crystal structures is proposed as the reason for high stability.
- Na^+ is reasoned to insert between $[\text{V}_{10}\text{O}_{28}]^{6-}$ polyanions, not into a continuous lattice.

GRAPHICAL ABSTRACT



ARTICLE INFO

Article history:

Received 6 January 2015

Received in revised form

13 March 2015

Accepted 3 April 2015

Available online 9 April 2015

Keywords:

Sodium-ion batteries

Polyoxometalates

Cluster electrodes

ABSTRACT

Affordable energy storage is crucial for a variety of technologies. One option is sodium-ion batteries (NIBs) for which, however, suitable anode materials are still a problem. We report on the application of a promising new class of materials, polyoxometalates (POMs), as an anode in NIBs. Specifically, $\text{Na}_6[\text{V}_{10}\text{O}_{28}] \cdot 16\text{H}_2\text{O}$ is being synthesized and characterized. Galvanostatic tests reveal a reversible capacity of approximately 276 mA h g^{-1} with an average discharge potential of 0.4 V vs. Na/Na^+ , as well as a high cycling stability. The underlying mechanism is rationalized to be an insertion of Na^+ in between the $[\text{V}_{10}\text{O}_{28}]^{6-}$ anions rather than an intercalation into a crystal structure; the accompanying reduction of V^{+V} to V^{+IV} is confirmed by X-ray Photoelectron Spectroscopy. Finally, a working full-cell set-up is

* Corresponding author. Energy Research Institute @ NTU (ERI@N), Research Techno Plaza, 50 Nanyang Drive, Singapore 637553, Singapore.

E-mail address: Madhavi@ntu.edu.sg (M. Srinivasan).

¹ Steffen Hartung and Nicolas Bucher contributed equally.

1. Introduction

In recent years, research in the field of electrochemical energy storage has intensified as the need to reliably and economically store electricity has been identified as a crucial factor in a broad variety of fields. This includes portable electronic devices and electrically powered vehicles, which require high power and energy densities. Another area in which energy storage will play a key role is the stabilization of the electricity grid. As green ways to harvest electricity from renewable sources like wind or solar power become increasingly popular, economical solutions to smoothen electricity peaks are paramount for these green technologies to play a major role in the energy mix. However, for such large-scale applications, the crucial factor is neither energy nor power density, but cost. Thus, novel battery technologies that reduce the storage cost are being researched. One promising candidate is sodium-ion batteries, due to the relative abundance of sodium in the earth's crust and, consequently, its lower cost [1–3]. Furthermore, sodium, in contrast to lithium, does not alloy with aluminum. Thus, copper current collectors can be replaced with the cheaper aluminum in sodium-ion batteries [4–6].

However, for sodium-ion batteries to become a viable alternative to lithium-ion batteries, novel materials need to be developed that can compete with lithium-ion battery materials with regard to capacity and cycling behavior. At the cathode end, layered oxides seem to be the material of choice, with a variety of sodium metal oxides (metal: vanadium, manganese, iron, cobalt) being researched, including different compositions/doping with various metals [6–11]. So far, anode materials seem to be a big challenge, as graphite anodes commercially employed in lithium-ion batteries are not suitable for sodium-ion batteries, owing to the graphite interlayer spacing that is not sufficient to intercalate sodium ions [12]. Thus, several prospective anode materials are being researched which fulfill the requirements for commercial applications of sodium-ion batteries [13], a selection of which is presented in Fig. 1.

Current research foci are on different storage mechanisms for Na^+ -ions within the active material. Recent works on intercalation materials include studies on amorphous TiO_2 , and layered $\text{P2-Na}_{0.66}[\text{Li}_{0.22}\text{Ti}_{0.78}\text{O}_2]$ [14,15]. The former forms Na_xTiO_2 in-situ with an approximate capacity of 140 mA h g^{-1} at potentials between 0.9 and 2.5 V, while the latter provides 130 mAh g^{-1} (at 10.6 mA g^{-1}) between 0.4 and 1.25 V. Phase change materials are mainly metal oxides; titanium-based materials seem promising with capacities of approximately 200 mA h g^{-1} for $\text{Na}_2\text{Ti}_3\text{O}_7$ [16]; however, only five cycles are shown. Rudola *et al.* reported 180 mA h g^{-1} for this material, with 120 mA h g^{-1} after 50 cycles [17]. $\text{Li}_4\text{Ti}_5\text{O}_{12}$ was found to provide 155 mA h g^{-1} at an average potential of 0.75 V [18]. Furthermore, phosphate-based NASICON materials have also been explored recently [19]. Metal-based anodes react with Na^+ -ions to form alloys. Although alloy materials are considered to be safe anodes with high capacities, cycling stability is usually poor due to the large volume changes during (de-)insertion of Na^+ , which is often alleviated by introducing a carbon matrix [20,21]. Oh *et al.*, for example, described the application of tin-carbon in a sodium-ion full cell [22]. Qian *et al.* showed that Sb/C composites can deliver around 600 mA h g^{-1} (at 100 mA g^{-1}) [23].

Work in the field of carbon-based materials focuses on hard-carbon, which consists of partially graphitized areas and irregular regions with cavities. Stevens *et al.* found that, for graphitic regions, an intercalation mechanism takes place up to a capacity of around 100 mA h g^{-1} , followed by an insertion of Na^+ into the cavities, which contributes an additional 150 mA h g^{-1} (at $33 \mu\text{A cm}^{-2}$) [24]. While hard-carbons combine reasonable capacities with high stabilities, safety problems arise due to the low insertion voltage which facilitates Na-plating. Another class of materials that has received some attention recently is organic materials. Zhao *et al.* and Park *et al.*, for example, recently reported 225 and 300 mA h g^{-1} , respectively, for $\text{Na}_2\text{C}_8\text{H}_4\text{O}_4$ at 0.4 V [25,26]; here, disodium terephthalate reacts to tetrasodium terephthalate via a radical intermediate.

Polyoxometalates (POMs) are anionic metal-oxo clusters of early transition metal ions in high oxidation states, and they exhibit unique structural and compositional properties, leading to potential applications in various areas such as catalysis, magnetism, electro- and photochemistry, as well as in materials science [27–32]. It has been shown that POMs can also be used as electrode material in lithium-ion batteries, and that their multi-electron redox properties could provide good capacities for lithium-based systems, especially the Keggin-based POM structures [33–38]. A unique characteristic of POMs as electrode material in batteries is that they do not consist of extended crystal structures, but rather of isolated, discrete polyanions, making them an intermediate between intercalation electrodes and organic radical electrodes [33,35,37]. Thus, POMs tap into the same advantageous mechanism like sodium terephthalate and hard-carbons, i.e., Na^+ -insertion in intercluster cavities. Therefore, strain on crystal structures and resulting structural deterioration can be excluded as potential reasons for capacity fading. Moreover, safety features can be enhanced when this insertion occurs at a higher potential than the one at which Na-plating occurs.

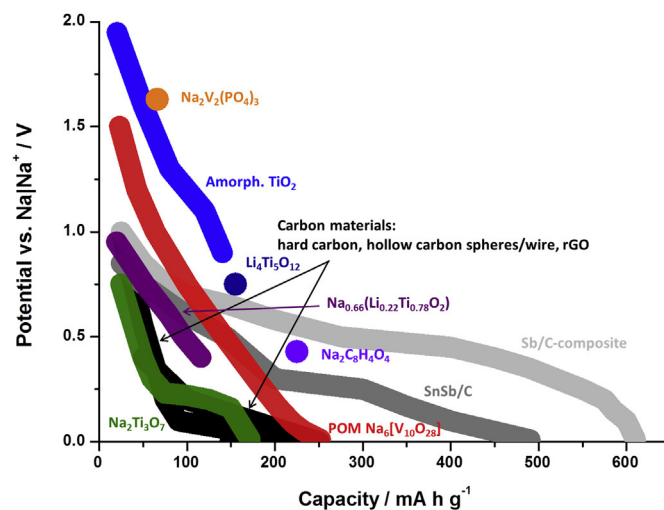


Fig. 1. Voltage profiles of different sodium-ion battery anode materials. The circles represent potentials at which the respective materials have a plateau; for the other materials, the voltage profile is indicated. The capacities shown here represent approximate values after initial stabilization, i.e., after irreversible reactions in the first cycles.

Even though POMs have been tested for lithium-ion batteries, no reports of POM-based electrodes for sodium-ion batteries have been published. In this work, we report on the properties of the decavanadate ion in the $\text{Na}_6[\text{V}_{10}\text{O}_{28}] \cdot 16\text{H}_2\text{O}$ POM, and show its suitability as anode material in sodium-ion batteries. We first describe its physical properties, and then discuss the electrochemical data, including cyclic voltammetry and charge/discharge performance.

2. Experimental

2.1. Synthesis of $\text{Na}_6[\text{V}_{10}\text{O}_{28}] \cdot 16\text{H}_2\text{O}$

Sodium decavanadate, $\text{Na}_6[\text{V}_{10}\text{O}_{28}] \cdot 16\text{H}_2\text{O}$, was synthesized according to Domaille et al. [39]. Typically, NaVO_3 (3 g) is dissolved in de-ionized water (100 mL); then, 4 M HCl is added to acidify the solution until a pH of 4.8 is reached. The solution is filtered and additional HCl is added to maintain a pH of around 4.5. Subsequently, ethanol (95%, 200 mL) was added to precipitate $\text{Na}_6[\text{V}_{10}\text{O}_{28}] \cdot 16\text{H}_2\text{O}$ as an orange bulk product, which is then filtered and air-dried.

2.2. Material characterization of $\text{Na}_6[\text{V}_{10}\text{O}_{28}] \cdot 16\text{H}_2\text{O}$

The product was characterized by Vanadium Nuclear Magnetic Resonance Spectroscopy (^{51}V -NMR) and Fourier Transform Infrared Spectroscopy (FTIR). NMR measurements were performed on a 400-MHz JEOL-ECX instrument in 5 mm tubes. ^{51}V -NMR (105.4 MHz, D_2O), δ : -514 ppm (s, 4 V, terminal O–V=O), -500 ppm (s, 4 V, terminal O–V=O), -424 ppm (s, 2 V, O–V–O).

FTIR was measured with a PerkinElmer Frontier FT-IR Spectrometer using KBr pellets. FTIR (KBr): $\nu = 847$ and 746 cm^{-1} ($\nu_{\text{as}}(\text{V–O–V})$), 521 cm^{-1} ($\nu_{\text{s}}(\text{V–O–V})$), 956 cm^{-1} (terminal $\text{V} = \text{O}_{\text{stretch}}$ bond).

Inductively Coupled Plasma Spectroscopy (ICP) measurements were performed using a Dual-view Optima 5300 DV ICP-OES system.

Field Emission Scanning Electron Microscopy (FESEM, JEOL JSM 7600F) and High Resolution Transmission Electron Microscopy (HRTEM, JOEL-JSM 2100F) were used to elucidate information on the morphology of $\text{Na}_6[\text{V}_{10}\text{O}_{28}] \cdot 16\text{H}_2\text{O}$.

Thermogravimetric Analysis (TGA) was performed on a TA Instruments SDT Q600 thermobalance to test the thermal stability of the product. The flow rate of nitrogen was 100 mL min^{-1} , and the temperature range was 20–800 °C with a heating rate of $5 \text{ }^\circ\text{C min}^{-1}$.

N_2 adsorption–desorption isotherms were carried out to determine the Brunau–Emmet–Teller (BET) surface area and Barrett–Joyner–Halenda (BJH) pore size distribution, using a Nova 3200e surface area and porosity analyzer. For X-ray photoelectron spectroscopy, a monochromatic X-ray source at 1486.7 eV (Al K_{α}) (XR50M, SPECS) was used, and electron detection was done by a hemispherical analyzer (EA125, Omicron).

2.3. Electrochemistry

The composite electrodes were prepared by mixing the POM with acetylene black (Alfa Aesar, > 99%) and polyvinylidene fluoride (PVDF, Arkema, Kynar HSV 900) binder in the weight ratio 60:20:20 with N-methyl-2-pyrrolidone (NMP) to form a homogeneous slurry. This mixture was coated on an Al foil using a doctor blade; the coating was dried in air at 80 °C to remove the NMP. The coating was punched into pieces with a diameter of 16 mm, which were then roll-pressed. Subsequently, they were dried at 110 °C under vacuum. These electrodes were then assembled in 2016 coin cells with

circular metallic sodium pieces with a diameter of 16 mm as the anode, and glass fiber (Whatman) as the separator. A 1 M solution of NaClO_4 (Sigma Aldrich, $\geq 98\%$) in a mixture of ethylene carbonate and propylene carbonate (1:1 weight %, EC: 99%, PC: $\geq 99.7\%$, Sigma Aldrich) was employed as electrolyte. Cyclic voltammetry was measured using a BioLogic potentiostat, and a Neware battery tester was used for galvanostatic charge/discharge tests.

3. Results and discussion

3.1. Material characterization of $\text{Na}_6[\text{V}_{10}\text{O}_{28}] \cdot 16\text{H}_2\text{O}$

Polyoxometalate (POM) synthesis is based solely on self-assembly. As the product consists of singular polyanionic compounds with Na^+ -ions between the $[\text{V}_{10}\text{O}_{28}]^{6-}$ polyanions, there is no well-defined long-range order but only the formation of a non-continuous structure, with differences for example in the amount of embedded water molecules. Thus, powders of this class of material lack an unequivocal crystal structure. Therefore, powder XRD is not considered to be an appropriate method to determine the identity and purity of the POM. A suitable method to identify the compound – and its purity – is single crystal-XRD, or ^{51}V -NMR for powders. Since the polyoxovanadate for this material was synthesized as powder, as is typical for battery materials, ^{51}V -NMR was chosen to determine the identity of the compound.

^{51}V -NMR measurements revealed the characteristic signals of the decavanadate, $[\text{V}_{10}\text{O}_{28}]^{6-}$ (δ : -514, -500 and -424 ppm), indicating the successful synthesis of the targeted structure (Fig. 2a) [39,40]. This was confirmed by the FTIR spectrum, which showed the typical absorption bands of $[\text{V}_{10}\text{O}_{28}]^{6-}$, with the asymmetric stretchings at $\nu = 847$ and 746 cm^{-1} and the symmetric stretching at 521 cm^{-1} being attributable to the V–O–V bridging, while the mode at 956 cm^{-1} is attributed to the terminal $\text{V} = \text{O}_{\text{stretch}}$ bond (Fig. 2b) [41,42]. ICP analysis revealed a Na–V ratio of 0.59, confirming the expected stoichiometry within the POM.

TGA of the POM shows a weight loss starting already at temperatures slightly above room temperature, which continues until 220 °C (Fig. 2c). The total weight loss of 21% is consistent with the removal of 16 water molecules from the structure, indicating the presence of 16 molecules of crystal water per formula unit. Thus, the overall chemical formula is $\text{Na}_6[\text{V}_{10}\text{O}_{28}] \cdot 16\text{H}_2\text{O}$. As the coated electrodes were dried at 110 °C under vacuum for several hours, it can safely be assumed that no crystal water is present after the drying process, and the chemical composition of the POM on the electrode is hence $\text{Na}_6[\text{V}_{10}\text{O}_{28}]$.

Surface area of the material, as measured by BET, was $21 \text{ m}^2 \text{ g}^{-1}$; the corresponding adsorption–desorption isotherms can be seen in Fig. 3a. Pore-size distribution, as elucidated by BJH, ranges from ~3 to 5 nm, indicating mesoporosity, for the majority of pores; for the remainder, pore size varies between ~5 and 160 nm (Fig. 3b).

According to FESEM and HRTEM measurements (Fig. 4), the $\text{Na}_6[\text{V}_{10}\text{O}_{28}] \cdot 16\text{H}_2\text{O}$ POM shows a rod-like morphology in the solid state; the micro-rods have a diameter of 0.5–1 μm and a typical length of several micrometers, resulting in a typical aspect ratio of 5–10. According to TEM, the POM microrods are polycrystalline, and show a random orientation with d-spacings of 0.769 and 0.333 nm. These findings are consistent with the ICSD data file 66807. As discussed above, one characteristic of discrete POMs is that they do not consist of extended crystal structures, but rather consist of individual, well-separated polyanions.

In the case of decavanadate, as examined in this work, the clusters consist of $[\text{V}_{10}\text{O}_{28}]^{6-}$ units, comprising ten edge-shared VO_6 octahedra. As discussed in previous publications about the

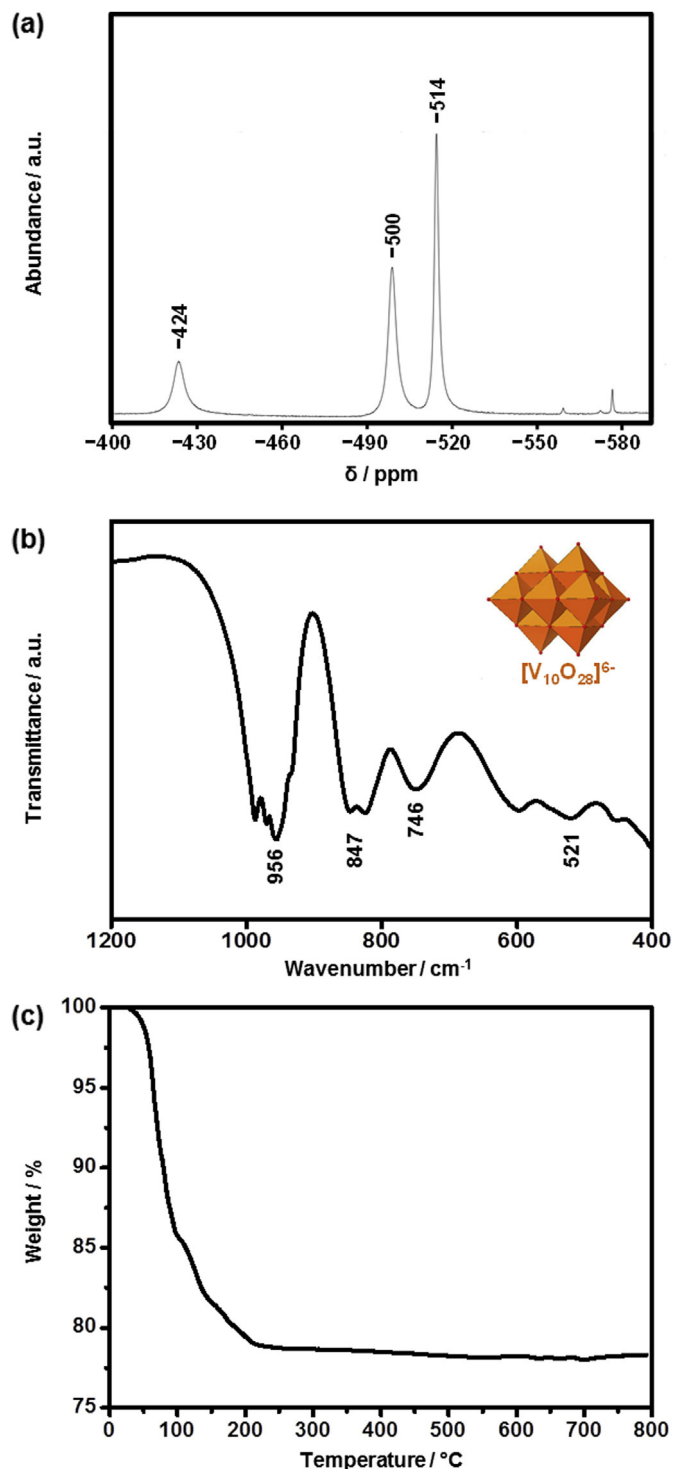


Fig. 2. (a) ^{51}V -NMR spectrum, (b) FTIR spectrum, and (c) TGA graph of $\text{Na}_6[\text{V}_{10}\text{O}_{28}] \cdot 16\text{H}_2\text{O}$. Inset in (b) is the polyhedral representation of $[\text{V}_{10}\text{O}_{28}]^{6-}$.

lithium salt, $\text{Li}_6[\text{V}_{10}\text{O}_{28}]$, crystal water molecules and counter cations separate the individual $[\text{V}_{10}\text{O}_{28}]^{6-}$ ions [36]. Upon heating, the crystal water can be removed so that the material consists of individual $[\text{V}_{10}\text{O}_{28}]^{6-}$ clusters separated only by the alkali ions. As the same $[\text{V}_{10}\text{O}_{28}]^{6-}$ units make up the structure of $\text{Na}_6[\text{V}_{10}\text{O}_{28}] \cdot 16\text{H}_2\text{O}$, and TGA shows that crystal water molecules can be removed from the structure, the same overall behavior is assumed. The lattice would then consist only of sodium ions separating the individual $[\text{V}_{10}\text{O}_{28}]^{6-}$ clusters. Thus, sodium is not incorporated into the

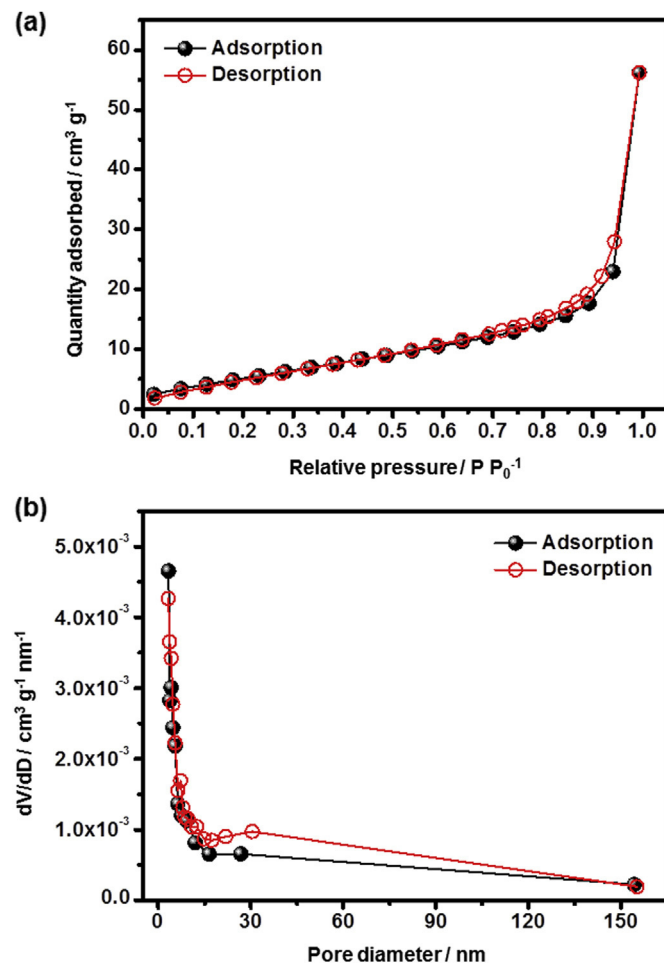


Fig. 3. (a) BET dinitrogen sorption/desorption graph, and (b) the corresponding BJH pore size distribution curve for $\text{Na}_6[\text{V}_{10}\text{O}_{28}] \cdot 16\text{H}_2\text{O}$.

crystal structure of the $[\text{V}_{10}\text{O}_{28}]^{6-}$ clusters, but rather inserted into the space between different polyanions.

3.2. Electrochemical measurements

In the cyclic voltammogram the half-cell is first discharged, and subsequently cycled between 0.01 V and 3 V (solid and dashed black line in Fig. 5a). In the first discharge, i.e., in the first process of inserting Na^+ ions into the POM structure, various distinct reduction peaks can be seen at 1.9, 1.3, 0.6, and 0.4 V in Fig. 5a. This indicates distinct reduction processes. However, as the corresponding oxidation peaks are, if existent, significantly less pronounced, these processes are largely irreversible. Similar peaks can be observed when cycling a battery half-cell with sodium as anode, and a cathode of pure activated carbon and PVDF binder coated on aluminum, i.e., for the same set-up without active material (see dotted red line in Fig. 5a). This indicates that the observed processes and the current coming from reduction processes in the first discharge are (at least partly) not due to redox reactions involving the active material. Thus, it seems as if reactions of the active material are not responsible for this irreversible capacity. Instead, the data indicates that these processes show partial decomposition of the electrolyte, and concurrent formation of a solid electrolyte interphase as described in literature [43–47]. In subsequent cycles, no distinct peaks are visible, and the electrochemical processes do not occur at specific voltages. Hence, the cyclic voltammogram resembles that of a supercapacitor rather than that of a typical

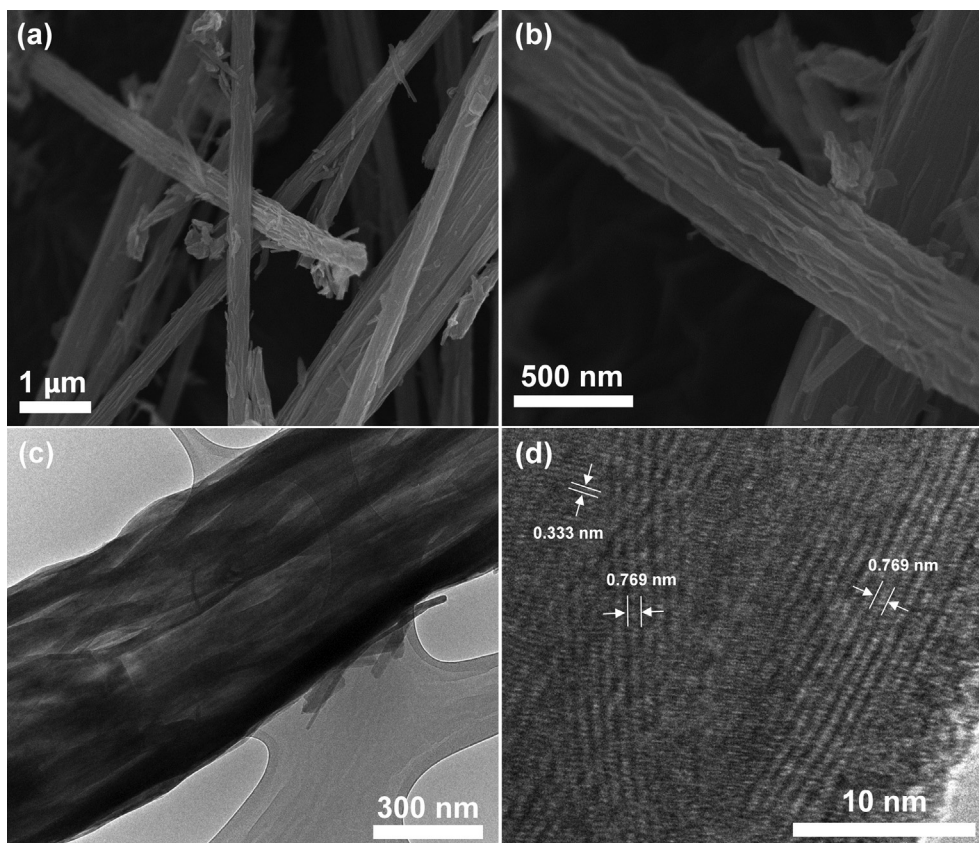


Fig. 4. (a) and (b) SEM image of $\text{Na}_6[\text{V}_{10}\text{O}_{28}] \cdot 16\text{H}_2\text{O}$ powder, (c) bright-field TEM image of a $\text{Na}_6[\text{V}_{10}\text{O}_{28}]$ rod, and (d) high-resolution TEM image.

intercalation process for the major part of the voltage range. However, two minor peaks become visible at a potential of 0.01 V for the reduction and 0.09 V for the oxidation, indicating a defined electrochemical process. This can potentially be attributed to the acetylene black in the electrode as can be seen from Fig. 3a.

The capacitive behavior can be explained by the special structural and morphological characteristics of POMs as discussed above. It has been shown before for lithium-ion batteries that POMs do not act as an intercalation material. In fact, the ions move between the polyanionic clusters and seem to get adsorbed at the surface [36,37]. Thus, the capacitive process for $\text{Na}_6[\text{V}_{10}\text{O}_{28}]$ is based on a continuous insertion of Na^+ -ions into the cavities between the $[\text{V}_{10}\text{O}_{28}]^{6-}$ clusters. X-ray Photoelectron Spectroscopy was employed to examine whether the behavior is only physical adsorption, or accompanied by electrochemical redox reactions. As Fig. 6 indicates, in the pristine POM material only vanadium with an oxidation state of +V is present. When discharged, however, vanadium with an oxidation state of +IV can be observed as well. Thus, it can be said that during the insertion of Na^+ -ions between the $[\text{V}_{10}\text{O}_{28}]^{6-}$ clusters, reduction from V^{+V} to V^{+IV} is induced. Therefore, these polyanions seem to act as redox centers in the sense that Na^+ -ions accumulate between them while vanadium ions are reduced to maintain the charge balance.

The hypothesis of a continuous insertion of Na^+ -ions is substantiated by the charge/discharge profile, in which the lack of plateaus indicates a steady insertion of Na^+ (Fig. 5b). Unlike phase change materials, in which Na^+ continuously occupies a defined lattice space and thus triggers a structural change at a specified voltage, POMs do not exhibit these defined insertion processes at a distinct voltage. This variety of insertion sites results in a variety of chemical potentials of the Na^+ -ions in the material, which in turn

results in a virtually continuous distribution of insertion voltages [24]. This would explain the absence of peaks in the CV and the slopy charge/discharge curves, rather than a distinct plateau. It should be emphasized that the observed data does not indicate an intercalation-based mechanism but rather a behavior comparable to the insertion of Na^+ into hard carbon as described above. Li *et al.* recently described two possible storage mechanisms for the insertion of Na^+ -ions into carbonaceous materials: a diffusion-controlled intercalation process and surface-induced capacitive processes. The slopy discharge curve of $\text{Na}_6[\text{V}_{10}\text{O}_{28}]$ corresponds well with the observed behavior for surface-induced capacitive processes, which includes adsorption processes onto the material surface and into voids [13,48]. The voids in carbon materials are comparable to the voids between $[\text{V}_{10}\text{O}_{28}]^{6-}$ polyanions in the POM salt $\text{Na}_6[\text{V}_{10}\text{O}_{28}]$, which suggests a similar mechanism that explains the similarly-shaped discharge curve. Additional measurements, such as X-ray Absorption Spectroscopy, are planned to substantiate this hypothesis with more experimental data. In previous works, similar-looking curves for LIBs have been fitted using the Redlich–Kister relation [49,50]. However, as we do not yet have a full understanding of the Na^+ -insertion mechanism into our POM and have doubts if the theoretical background of the Redlich–Kister derivation (thermodynamics of solutions) justifies its application in this case, we refrain from performing this fit [49]. The average discharge potential, as measured by the potential at which the area under the 10th discharge curve was cut in half, was found to be 0.4 V.

In the first discharge cycles at 20 mA g^{-1} , the capacities exceed 300 mA h g^{-1} ; these high values are not achieved in subsequent cycles and can probably be attributed to the formation of a solid-electrolyte interphase, based on the partial decomposition of electrolyte as explained for the cyclic

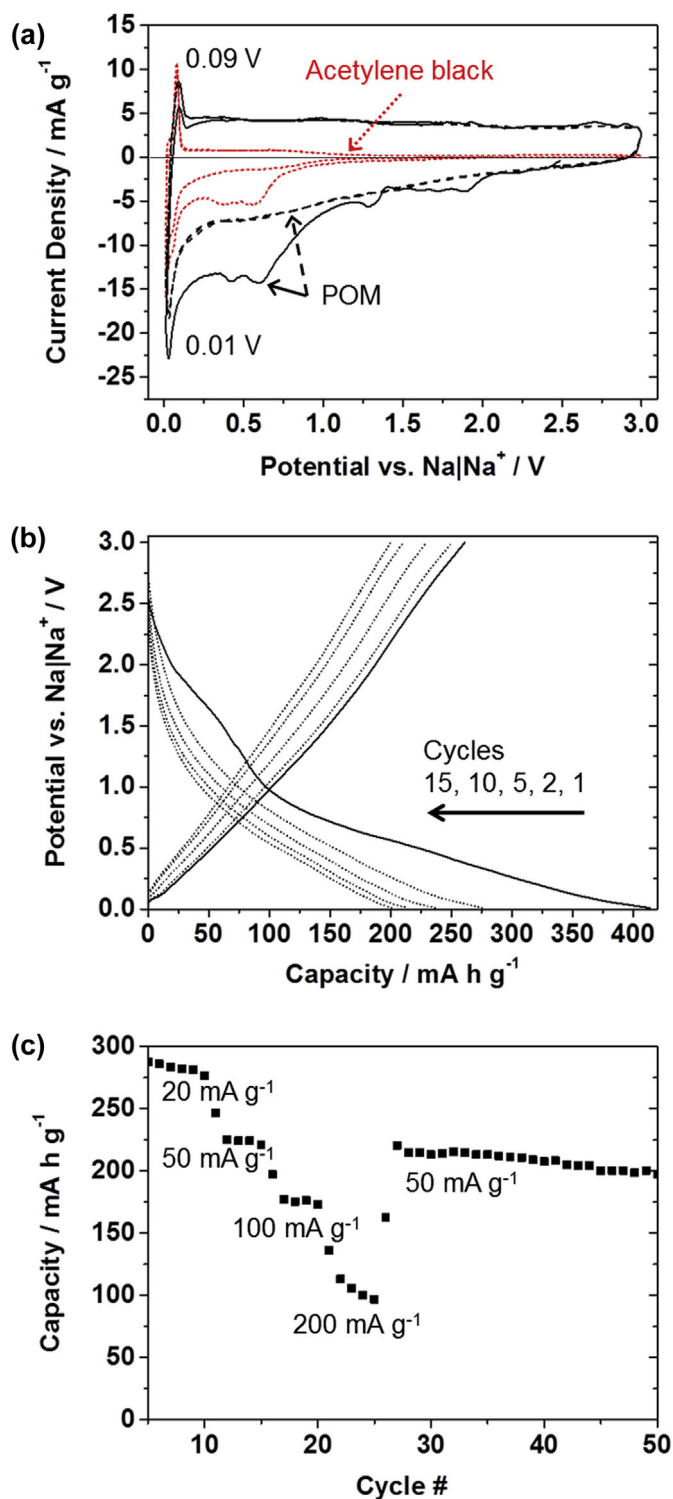


Fig. 5. (a) Cyclic voltammogram (cycles 1–5) of Na₆[V₁₀O₂₈] in a half-cell set-up with 1 M NaClO₄ in EC:PC (1:1% weight) as electrolyte at a scan rate of 0.01 mV s⁻¹ (solid and dashed black line); the dotted red line shows the first two cycles of an acetylene black electrode in the same set-up at 0.01 mV s⁻¹ normalized to the carbon mass-ratio in the active-material cell (b) Galvanostatic charge/discharge profile in a half-cell set-up with 1 M NaClO₄ in EC:PC (1:1% weight) as electrolyte at 50 mA g⁻¹. (c) Rate capability and stability of Na₆[V₁₀O₂₈] in a half-cell set-up with 1 M NaClO₄ in EC:PC (1:1% weight) as electrolyte. (For interpretation of the references to color in this figure legend, the reader is referred to the web version of this article.)

voltammogram above. This is a known phenomenon and is also substantiated by the charges transferred during cyclic voltammetry as found by integration. While for the first cycle the charge transferred during reduction is approximately 150% of the charge transferred during oxidation, this number decreases for subsequent cycles. For the following cycles, discharge capacities stabilize and for the tenth cycle reach approximately 276 mA h g⁻¹ for a current rate of 20 mA g⁻¹. As the rate test in Fig. 5c shows, discharge capacities decrease for higher current rates, giving 221 mA h g⁻¹ for 50 mA g⁻¹ (cycle 15), 173 mA h g⁻¹ for 100 mA g⁻¹ (cycle 20) and 97 mA h g⁻¹ for 200 mA g⁻¹ (cycle 25). When changing the current rate again back to 50 mA g⁻¹, discharge capacity is rather stable on a high level, with 220 mA h g⁻¹ for cycle 27, compared to 221 mA h g⁻¹ for cycle 15. This indicates that the fading, even though capacities are lower at higher current rates, is not exacerbated when increasing the current. The reason for this remarkable cycle stability is probably the unique structural and morphological features of POMs. As the Na⁺-ions (de-)insert into/from cavities between the [V₁₀O₂₈]⁶⁻ clusters and are not built into a defined crystal lattice, structural strain is minimized. Consequently, a major cause for capacity fading is omitted, and stability is increased. The observable capacity fading is possibly due to electrolyte decomposition; as reported in literature, this can be remedied by adding fluorinated ethylene carbonate to the electrolyte [5]. Tests to examine the effect of this additive on the POM system are under way.

The achieved capacities are in the same region as the values reported for hard carbon (Fig. 1). However, as the insertion process takes place at higher voltages, the risk of Na-plating is eliminated, which leads to an increase in safety. When compared to phase-change materials like Li₄Ti₅O₁₂ and Na₂Ti₃O₇, Na₆[V₁₀O₂₈] reaches higher capacities in a voltage region that lies between the two aforementioned materials. The same classification can be made for intercalation materials, i.e., the POM lies between TiO₂ and P2-Na_{0.66}[Li_{0.22}Ti_{0.78}]O₂ with respect to voltage, and exceeds both materials regarding capacity [14,15]. Alloy materials exceed Na₆[V₁₀O₂₈] with regard to capacity; however, they typically have the disadvantage of low cycle stabilities. Even though this can be improved by embedding the active material into a matrix (e.g., carbon nanotubes), this often requires complex synthesis methods, which is a barrier to commercial applications. Sodium terephthalates match Na₆[V₁₀O₂₈] with regard to capacity, while their plateau during discharge matches the average discharge voltage of the POM [25,26].

As discussed above, the chemical formula of the electrode material can be assumed to be Na₆[V₁₀O₂₈]. With respect to this composition, the capacity of 1 Na⁺ ion is 24.5 mA h g⁻¹. Reduction of all vanadium +V to +IV would be accompanied by an insertion of 10 Na⁺-ions per formula unit Na₆[V₁₀O₂₈], i.e., a capacity of 245 mA h g⁻¹. As discussed, in the first discharge cycles the current coming from the formation of an SEI adds to the reversible capacity of the insertion of sodium ions, which expresses itself as a rather high fading during the initial cycles. Furthermore, this is also substantiated by a coulomb efficiency of >100% in the first cycles. This would explain that, in case 10 Na⁺ are inserted, the measured capacity exceeds theoretical capacity in the beginning. Another potential reason could be minor electrochemical activity of the acetylene black in the electrode (Fig. 3a). When increasing the current rate to 50 mA g⁻¹, discharge capacities drop to values around 221 mA h g⁻¹. The insertion of Na⁺ would have to be accompanied by a reduction of V^{+V} to V^{+IV}. According to XPS measurements, as discussed before, this reduction indeed takes place. However, V^{+V} is still present in the discharged sample. This can either be attributed to an incomplete reduction of vanadium or to a re-oxidation during ex-situ sample handling. As the

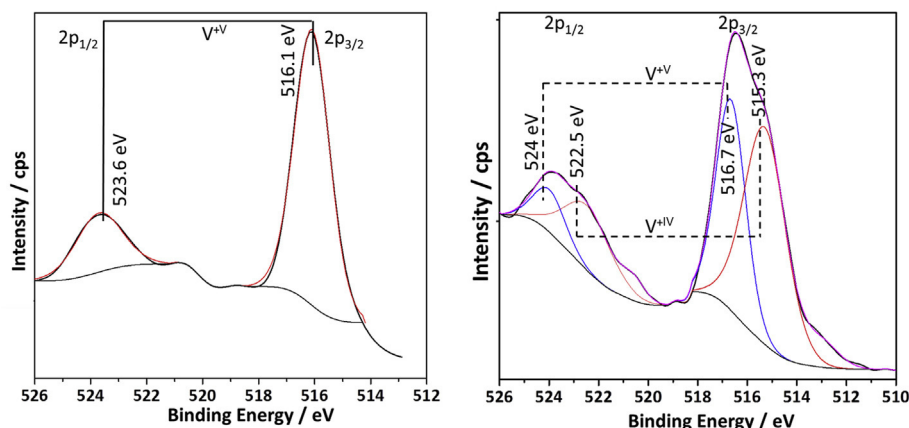
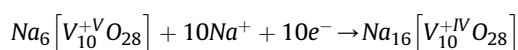


Fig. 6. XPS measurement of (left) pristine $\text{Na}_6[\text{V}_{10}\text{O}_{28}]$ electrode and (right) discharged $\text{Na}_6[\text{V}_{10}\text{O}_{28}]$ electrode.

measured discharged sample was briefly exposed to air during the measurement, the oxygen in the air might have re-oxidized some vanadium from V^{+IV} to V^{+V} . However, based on the achieved capacity we assume, from a mechanistic point of view, that ten additional Na^+ -ions are inserted per cluster, resulting in the following reaction:



As an additional substantiation to the hypothesis of reversible redox reactions, a sodium full cell with $\text{Na}_6[\text{V}_{10}\text{O}_{28}]$ as anode and spherical sodium manganese oxide as cathode was built [51]. It is important to note that for this full cell the target was not to optimize performance, but rather to conduct a proof-of-concept study to show that $\text{Na}_6[\text{V}_{10}\text{O}_{28}]$ can be used for full-cells and undergoes reversible redox reactions. As can be seen in the cyclic voltammogram in Fig. 7a, this is the case.

The system exhibits several reversible electrochemical processes, even though at this point the variety of peaks cannot be unequivocally identified, as the resulting CV is a superposition of anodic and cathodic reactions as well as complex sodium ordering processes [51]. However, the peaks clearly indicate reversible redox processes, which substantiate the assumption that the POM undergoes electrochemical reactions. Moreover, as batteries with metallic sodium electrodes pose significant safety risks, full cells without metallic sodium are essential for practical applications. With this full-cell set-up demonstrated here, a capacity of 140 mA h g^{-1} (with regard to the mass of $\text{Na}_6[\text{V}_{10}\text{O}_{28}]$) was achieved for a voltage range of 0–3.8 V (Fig. 7b). As the sodium manganese oxide was the limiting factor in this set-up, a higher mass of this material had to be used, so that the capacity with regard to the mass of sodium manganese oxide would be inherently lower (as it would obviously be for the total mass of active material, i.e., anode + cathode, in the cell). However, this proves that $\text{Na}_6[\text{V}_{10}\text{O}_{28}] \cdot 16\text{H}_2\text{O}$ not only shows promising half-cell data, but is also an interesting option for sodium-ion full cells.

4. Conclusions

We have introduced POMs as a new class of materials for sodium-ion batteries and demonstrated their capability as anode material with good cycling stability. $\text{Na}_6[\text{V}_{10}\text{O}_{28}] \cdot 16\text{H}_2\text{O}$ was synthesized via a known procedure and characterized by ^{51}V -NMR and FTIR. Cyclic voltammetry and charge/discharge profiles showed no distinct peaks or plateaux, respectively, but continuous slopes. This can be attributed to the insertion of Na^+ -ions between the $[\text{V}_{10}\text{O}_{28}]^{6-}$ anions instead of into defined crystal interstices. We suggest that this working principle of vanadium-based POM electrodes is also responsible for the good cycling stability and the negligible “damage” caused by cycling at higher current rates. Finally, we demonstrated that vanadium POM electrodes function as anodes in sodium-ion full cells, using sodium manganese oxide as cathode material.

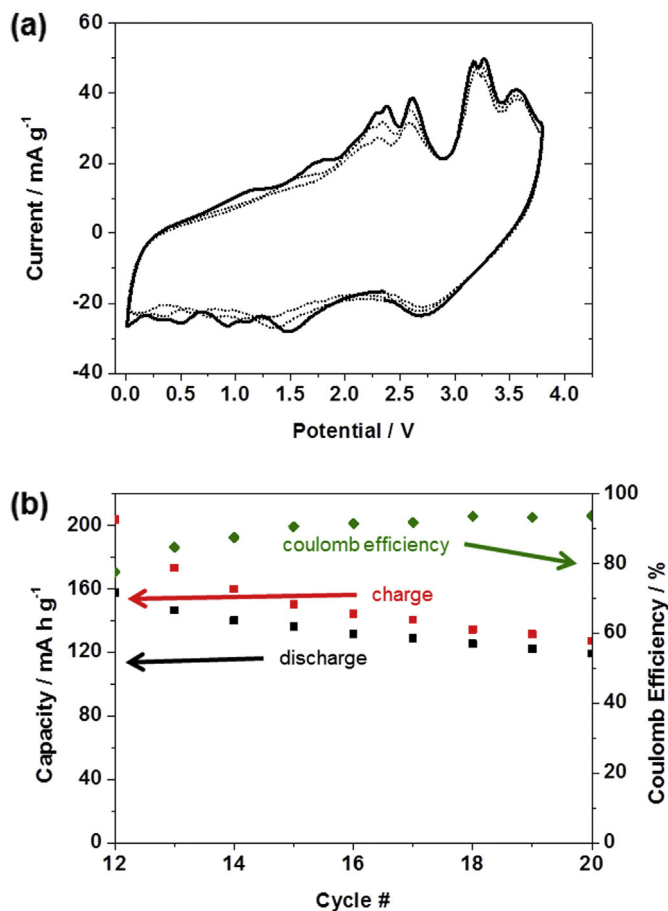


Fig. 7. (a) Cyclic voltammogram of the full cell at 0.2 mV s^{-1} . Anode: POM, Cathode: Spherical $\text{Na}_x\text{MnO}_{2+y}$ (not weight balanced). Cycles 7–9 after cycling six times in narrower voltage ranges. (b) Full cell charge/discharge capacities with respect to the POM as well as the corresponding coulomb efficiencies. Anode: POM, Cathode: Spherical $\text{Na}_x\text{MnO}_{2+y}$ (not weight balanced). Potential range: 0–3.8 V; previous cycles were cycled in narrower voltage ranges.

Funding sources

This work was financially supported by the Singapore National Research Foundation (NRF) under its Campus for Research Excellence and Technological Enterprise (CREATE) programme. NRF had no involvement in the study design; in the collection, analysis and interpretation of data; in the writing of the report; and in the decision to submit the article for publication.

References

- [1] V. Palomares, P. Serras, I. Villaluenga, K.B. Hueso, J. Carretero-González, T. Rojo, *Energy Environ. Sci.* 5 (2012) 5884.
- [2] V. Palomares, M. Casas-Cabanas, E. Castillo-Martínez, M.H. Han, T. Rojo, *Energy Environ. Sci.* 6 (2013) 2312.
- [3] H. Pan, Y.-S. Hu, L. Chen, *Energy Environ. Sci.* 6 (2013) 2338.
- [4] S. Komaba, W. Murata, T. Ishikawa, N. Yabuuchi, T. Ozeki, T. Nakayama, A. Ogata, K. Gotoh, K. Fujiwara, *Adv. Funct. Mater.* 21 (2011) 3859.
- [5] S. Komaba, T. Ishikawa, N. Yabuuchi, W. Murata, A. Ito, Y. Ohsawa, *ACS Appl. Mater. Interfaces* 3 (2011) 4165.
- [6] N. Yabuuchi, M. Kajiyama, J. Iwatate, H. Nishikawa, S. Hitomi, R. Okuyama, R. Usui, Y. Yamada, S. Komaba, *Nat. Mater.* 11 (2012) 512.
- [7] N. Bucher, S. Hartung, I. Gocheva, Y.L. Cheah, M. Srinivasan, H.E. Hoster, *J. Solid State Electrochem.* 17 (2013) 1923.
- [8] D. Kim, E. Lee, M. Slater, W. Lu, S. Rood, C.S. Johnson, *Electrochem. Commun.* 18 (2012) 66.
- [9] M. D'Arienzo, R. Ruffo, R. Scotti, F. Morazzoni, C.M. Mari, S. Polizzi, *Phys. Chem. Chem. Phys.* 14 (2012) 5945.
- [10] M. Guignard, C. Didier, J. Darriet, P. Bordet, E. Elkaïm, C. Delmas, *Nat. Mater.* 11 (2012) 1.
- [11] S. Hartung, N. Bucher, V.S. Nair, C.Y. Ling, Y. Wang, H.E. Hoster, M. Srinivasan, *ChemPhysChem.* 15 (2014) 2121.
- [12] Y. Cao, L. Xiao, M.L. Sushko, W. Wang, B. Schwenzer, J. Xiao, Z. Nie, L.V. Saraf, Z. Yang, J. Liu, *Nano Lett.* 12 (2012) 3783.
- [13] V.L. Chevrier, G. Ceder, *J. Electrochem. Soc.* 158 (2011) A1011.
- [14] H. Xiong, M.D. Slater, M. Balasubramanian, C.S. Johnson, T. Rajh, *J. Phys. Chem. Lett.* 2 (2011) 2560.
- [15] Y. Wang, X. Yu, S. Xu, J. Bai, R. Xiao, Y.-S. Hu, H. Li, X.-Q. Yang, L. Chen, X. Huang, *Nat. Commun.* 4 (2013) 2365.
- [16] P. Senguttuvan, G. Rousse, V. Seznec, J.-M. Tarascon, M.R. Palacín, *Chem. Mater.* 23 (2011) 4109.
- [17] A. Rudola, K. Saravanan, C.W. Mason, P. Balaya, *J. Mater. Chem. A* 1 (2013) 2653.
- [18] Y. Sun, L. Zhao, H. Pan, X. Lu, L. Gu, Y.-S. Hu, H. Li, M. Armand, Y. Ikuhara, L. Chen, X. Huang, *Nat. Commun.* 4 (2013) 1870.
- [19] V. Aravindan, W.C. Ling, S. Hartung, N. Bucher, S. Madhavi, *Chem. Asian J.* 9 (2014) 878.
- [20] L. Wu, F. Pei, R. Mao, F. Wu, Y. Wu, J. Qian, Y. Cao, X. Ai, H. Yang, *Electrochim. Acta* 87 (2013) 41.
- [21] L. Xiao, Y. Cao, J. Xiao, W. Wang, L. Kovarik, Z. Nie, J. Liu, *Chem. Commun.* 48 (2012) 3321.
- [22] S.-M. Oh, S.-T. Myung, M.-W. Jang, B. Scrosati, J. Hassoun, Y.-K. Sun, *Phys. Chem. Chem. Phys.* 15 (2013) 3827.
- [23] J. Qian, Y. Chen, L. Wu, Y. Cao, X. Ai, H. Yang, *Chem. Commun.* 48 (2012) 7070.
- [24] D.A. Stevens, J.R. Dahn, *J. Electrochem. Soc.* 148 (2001) A803.
- [25] L. Zhao, J. Zhao, Y.-S. Hu, H. Li, Z. Zhou, M. Armand, L. Chen, *Adv. Energy Mater.* 2 (2012) 962.
- [26] Y. Park, D.-S. Shin, S.H. Woo, N.S. Choi, K.H. Shin, S.M. Oh, K.T. Lee, S.Y. Hong, *Adv. Mater.* 24 (2012) 3562.
- [27] Y.-F. Song, R. Tsunashima, *Chem. Soc. Rev.* 41 (2012) 7384.
- [28] A. Proust, B. Matt, R. Villanneau, G. Guillemot, P. Gouzerh, G. Izet, *Chem. Soc. Rev.* 41 (2012) 7605.
- [29] H. Lv, Y.V. Geletii, C. Zhao, J.W. Vickers, G. Zhu, Z. Luo, J. Song, T. Lian, D.G. Musaev, C.L. Hill, *Chem. Soc. Rev.* 41 (2012) 7572.
- [30] U. Kortz, *Eur. J. Inorg. Chem.* 2009 (2009) 5055.
- [31] M.T. Pope, U. Kortz, *Polyoxometalates*, in: *Encyclopedia of Inorganic and Bioinorganic Chemistry*, John Wiley, 2012.
- [32] A. Sartorel, M. Bonchio, S. Campagna, F. Scandola, *Chem. Soc. Rev.* 42 (2013) 2262.
- [33] S. Uematsu, Z. Quan, Y. Sugauma, N. Sonoyama, *J. Power Sources* 217 (2012) 13.
- [34] H. Wang, N. Kawasaki, T. Yokoyama, H. Yoshikawa, K. Awaga, *Dalt. Trans.* 41 (2012) 9863.
- [35] N. Sonoyama, Y. Sugauma, T. Kume, Z. Quan, *J. Power Sources* 196 (2011) 6822.
- [36] A. Xie, C. Ma, L. Wang, Y. Chu, *Electrochim. Acta* 52 (2007) 2945.
- [37] E. Ni, S. Uematsu, Z. Quan, N. Sonoyama, *J. Nanoparticle Res.* 15 (2013) 1732.
- [38] H. Wang, S. Hamanaka, Y. Nishimoto, S. Irie, T. Yokoyama, H. Yoshikawa, K. Awaga, *J. Am. Chem. Soc.* 134 (2012) 4918.
- [39] P.J. Domaille, *J. Am. Chem. Soc.* 106 (1984) 7677.
- [40] S. Ramos, R.O. Duarte, J.J.G. Moura, M. Aureliano, *Dalt. Trans.* (2009) 7985.
- [41] R.L. Frost, K.L. Erickson, M.L. Weier, O. Carmody, *Spectrochim. Acta. A. Mol. Biomol. Spectrosc.* 61 (2005) 829.
- [42] M.R. Mohammadi, M. Hakimi, E.-J. Chem. 9 (2012) 43.
- [43] A. Ponrouch, E. Marchante, M. Courty, J.-M. Tarascon, M.R. Palacín, *Energy Environ. Sci.* 5 (2012) 8572.
- [44] A. Ponrouch, R. Dedryvère, D. Monti, A.E. Demet, J.M. Ateba Mba, L. Croguennec, C. Masquelier, P. Johansson, M.R. Palacín, *Energy Environ. Sci.* 6 (2013) 2361.
- [45] A. Ponrouch, A.R. Goñi, M.R. Palacín, *Electrochem. Commun.* 27 (2013) 85.
- [46] P. Thomas, D. Billaud, I. Nancy, B.P. Vandoeu, *Electrochim. Acta* 47 (2002) 3303.
- [47] A. Naji, P. Thomas, J. Ghanbaja, D. Billaud, *Micron* 31 (2000) 401.
- [48] S. Li, J. Qiu, C. Lai, M. Ling, H. Zhao, S. Zhang, *Nano Energy* 12 (2015) 224.
- [49] O. Redlich, A.T. Kister, *Ind. Eng. Chem.* 40 (1948) 345.
- [50] D.K. Karthikeyan, G. Sikha, R.E. White, *J. Power Sources* 185 (2008) 1398.
- [51] N. Bucher, S. Hartung, A. Nagasubramanian, Y.L. Cheah, H.E. Hoster, S. Madhavi, *ACS Appl. Mater. Interfaces* 6 (2014) 8059.

5.5 A novel ionic liquid for Li ion batteries – uniting the advantages of guanidinium and piperidinium cations

The study presented in this chapter, “A novel ionic liquid for Li ion batteries – uniting the advantages of guanidinium and piperidinium cations” (RSC Advances 2014, 4, 1996) describes the work on a new electrolyte for NIBs and LIBs. This work was jointly performed by N. Bucher, S. Hartung and M. Arkhipova. N. Bucher focussed on the electrochemical characterisation and battery testing. S. Hartung was leading the physicochemical characterization and drafted the manuscript. M. Arkhipova synthesised and identified the IL.

Electrolytes play a crucial role for both NIBs and LIBs. Conventional carbonate-based electrolytes possess some inherent safety risks, particularly as a consequence of their volatility and therefore flammability. Room temperature ILs, which are defined as salts with a melting point below 100 °C, have received considerable interest recently as electrochemically and thermally stable electrolytes. Not only do they promise improved safety characteristics, they are also considered to increase the voltage window of batteries and reduce electrolyte decomposition, which would contribute to higher cycling stabilities. Inherent disadvantages, however, are high viscosity and ionic conductivity. The approach presented in this work is based on the combination of advantageous structural properties from two different classes of ionic liquids to form a new cation. The rationale behind choosing the guanidinium structure as one component is to utilise both the option to tailor this structure to specific needs due to its six substituents and its low viscosity. The piperidinium structure was chosen due to its large electrochemical window, high cathodic stability vs. Li-metal and thermal stability. The physico-chemical characteristics of the new *N,N,N',N'*-tetramethyl-*N'',N''*-pentamethyleneguanidinium bis(trifluoromethylsulfonyl)imide (PipGuan-TFSI), *i.e.* thermal stability as measured by TGA, viscosity as measured by rheometry, and Li⁺-conductivity as measured by coin cell tests with a 1M solution of LiTFSI in PipGuan-TFSI as electrolyte, are intermediary between the parent structures.

Electrochemical stability has been investigated both in a two-electrode coin cell set-up with Li-metal as a counter and reference electrode and in a three-electrode set-up with the redox couple Ag|Ag⁺ as a reference. Lithium-transport in the system was investigated by cyclic voltammetry in a coin cell set-up with stainless steel and lithium metal as the two electrodes. These electrochemical measurements showed that the IL-based electrolyte, *i.e.* a 1M solution of LiTFSI in PipGuan-TFSI, has a sufficiently large electrochemical window to be employed as battery electrolyte. To deduce information on the stability of the electrolyte vs. Li-metal, and on the formation of a solid-electrolyte interphase, which plays a crucial role during battery cycling, impedance spectroscopy was employed. Charge-transfer resistance was shown to increase during the initial twelve hours, which suggests the formation of a protective layer on the electrodes consisting of partially decomposed electrolyte. Afterwards, charge-transfer-resistance is constant, which indicates the decomposition processes cease and the system is stable. Finally, in order to verify

this IL's suitability as battery electrolyte, it was tested in a LIB half-cell with LiFePO_4 as the positive electrode, and Li-metal as the negative electrode. Resulting capacities match well with half-cells which were built with conventional carbonate-based electrolytes at very slow C-rates and at a temperature of 55 °C. At higher C-rates, capacity declines, which is attributed to reduced Li^+ -transport in the system. With regard to discharge capacities, PipGuan-TFSI does not lie between the two parent structures, but is superior to both. Thus, the novel IL presented in this publication, PipGuan-TFSI, was shown to be an intermediary between its two 'parent structures' and exceeds both with regard to battery performance, which makes it a suitable candidate for IL based electrolytes.

In addition to the results described in this publication, initial tests^[133] in NIBs with the electrode material described above, $\text{Na}_{2+x}\text{V}_6\text{O}_{16}$, were performed. First results indicate that cycling stability could not be improved when employing PipGuan-TFSI with NaTFSI as the conducting salt instead of conventional propylene carbonate-based electrolytes. However, further studies are necessary to substantiate this.

A novel ionic liquid for Li ion batteries – uniting the advantages of guanidinium and piperidinium cations

Nicolas Bucher, Steffen Hartung, Maria Arkhipova, Denis Yu, Philipp Kratzer, Gerhard Maas, Madhavi Srinivasan, Harry E. Hoster

Reproduced from RSC Advances, Volume 4, Issue 4, 2014, Pages 1996-2003 with permission from The Royal Society of Chemistry.

The publication can be found under the following weblink:

<http://dx.doi.org/10.1039/C3RA46118A>

A novel ionic liquid for Li ion batteries – uniting the advantages of guanidinium and piperidinium cations

 Cite this: *RSC Adv.*, 2014, 4, 1996

 Nicolas Bucher,^{†ab} Steffen Hartung,^{†ab} Maria Arkhipova,^{†e} Denis Yu,^{ad} Philipp Kratzer,^e Gerhard Maas,^e Madhavi Srinivasan^{ac} and Harry E. Hoster^{*abd}

We report on the synthesis and the properties of *N,N,N',N'*-pentamethyleneguanidinium bis(trifluoromethylsulfonyl)imide (PipGuan-TFSI). The cation of this novel ionic liquid combines guanidinium and piperidinium structural elements. We tested it for its viscosity, ion conductivity, and also for its thermal and electrochemical stability. Furthermore, a 0.5 M solution of lithium TFSI in PipGuan-TFSI was tested as an electrolyte for Li-ion batteries. These experiments included cycles of Li deposition/dissolution on stainless steel and (de)intercalation into/from LiFePO₄ electrodes. The tests involving LiFePO₄ cathodes were performed at various C-rates and temperatures for a better quantitative comparison to other electrolyte systems. We discuss in how far PipGuan-TFSI successfully combines the advantages of guanidinium and piperidinium ionic liquids for battery electrolyte applications.

 Received 31st July 2013
 Accepted 5th November 2013

DOI: 10.1039/c3ra46118a

www.rsc.org/advances

Introduction

Ionic liquids (ILs) are salts with a melting point below 100 °C. Room temperature ionic liquids, which is a subgroup defined by a melting point below room temperature, have attracted great interest in recent years as tunable “designer solvents”. ILs are electrochemically and thermally stable, have a negligible volatility, and thus a low flammability.^{1,2} Those properties make them suitable not only for (sustainable) chemical synthesis³ or carbon capture^{4,5} but also for energy storage applications⁶ such as super capacitors, batteries, fuel cells and solar cells.^{2,7–12} The gain in safety due to the low volatility of ILs comes with a higher viscosity and concomitantly lower ion conductivity¹³ as compared to traditional, molecular solvents. Furthermore, any IL to be used in electrochemical energy storage devices must exhibit a suitable stability window. Both the ion conductivity and the potential window are tackled by the design of new ionic liquids.^{14–16}

IL based electrolytes in Li ion batteries (LIBs) are usually ternary mixtures containing Li⁺ ions and the anions and cations of the respective IL. The Li salt and the IL thus share the same

anion. Therefore, the IL cation becomes the subject of target oriented optimization. Common basic structures are pyridinium,¹⁷ imidazolium,^{18–21} ammonium,^{20–23} sulfonium, pyrrolidinium,^{20,21,24–26} guanidinium,^{27–33} or piperidinium.^{19–21,34,35} The infinite number of possible structural variations in combination with the substantial synthesis efforts calls for a systematic strategy. Parallel to computational studies that are on the way in many research groups,^{14–16} there is an obvious demand for systematic synthesis variations in combination with a set of electrochemical benchmark tests. For substances whose properties are already close to the desired optimum, variations can be incremental, *e.g.*, modifying moieties of existing cation structures. For substances with more room for improvement, however, more substantial yet still systematic variations may speed up the progress – in analogy to Nature’s principles of genetic crossing that was successfully transferred to the field of multi-parameter optimization problems.

In this paper, we will demonstrate how the advantages of two different structural elements can be combined towards a new cation with better key properties than the parent structures. The two original structural elements are guanidinium and piperidinium. Guanidinium cations can be modified at six different sides and the resulting ILs have low viscosities. The main drawback of guanidinium cations, however, is their lack of electrochemical stability at the negative potential limit.^{23,27,29,30} Piperidinium based ILs, on the other hand, were reported to have electrochemical windows exceeding 5 V and high cathodic stability *versus* lithium metal. Moreover, piperidinium ILs have a high thermal stability, which is crucial with regard to safety.^{34,36} In the first part of this paper we will describe the

^aTUM CREATE, Singapore 138602, Singapore. E-mail: harry.hoster@tum-create.edu.sg; Tel: +65 9455 3973

^bTechnische Universität München, 85748 Garching, Germany

^cSchool of Materials Science and Engineering, Nanyang Technological University, Singapore 639798, Singapore

^dEnergy Research Institute @ NTU, 1 CleanTech Loop, #06-04 CleanTech One, Singapore 637141, Singapore

^eInstitute of Organic Chemistry I, University of Ulm, Albert-Einstein-Allee 11, 89081 Ulm, Germany

[†] Authors contributed equally to this manuscript.

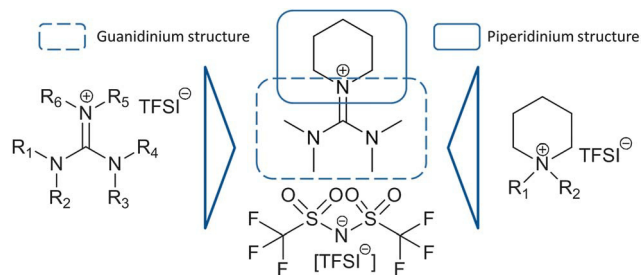


Fig. 1 *N,N,N',N'*-Tetramethyl-*N'',N''*-pentamethyleneguanidinium bis(trifluoromethylsulfonyl)imide (PipGuan-TFSI).

synthesis of a new cation in which one side arm of a guanidinium cation was substituted with a piperidinium ring (PipGuan, see Fig. 1). Being initially synthesised as PipGuan chloride, an anion exchange towards PipGuan bis(trifluoromethylsulfonyl)imide (TFSI) yields a new IL, PipGuan-TFSI.

We will then elucidate the physical and electrochemical properties of this IL. Those characterisations include nuclear magnetic resonance (NMR) and infrared (IR) spectrometry, thermogravimetric analysis supported by mass spectroscopy (TGA-MS), differential scanning calorimetry (DSC), and viscosity and conductivity measurements. The electrochemical properties were tested by cyclic voltammetry (CV) and electrochemical impedance spectroscopy (EIS). Finally, we tested a solution of LiTFSI in PipGuan-TFSI as an electrolyte for a LiFePO₄ battery half-cell and compared the results at two different temperatures to the behaviour of the same cell using a commercial electrolyte. We will discuss in which respect the properties of the new cation structure reflect a compromise between the two parent structures and where the product of the crossing is superior to either of them.

Materials and methods

Synthesis

The novel guanidinium-based ionic liquid *N,N,N',N'*-tetramethyl-*N'',N''*-pentamethyleneguanidinium bis(trifluoromethylsulfonyl)imide was synthesised from tetramethylurea by partially modifying reported procedures (Fig. 2).^{28,31} Rigorously dried organic solvents were used. All amines were dried with KOH pellets and stored under an argon atmosphere. ¹H NMR spectra were referenced to the residual proton signal of the solvent [$\delta(\text{CDCl}_3) = 7.26$ ppm]. ¹³C spectra were referenced to the solvent signal

[$\delta(\text{CDCl}_3) = 77.00$ ppm], and ¹⁹F spectra to external C₆F₆ [$\delta(\text{C}_6\text{F}_6) = -162.9$ ppm].

As a first step, *N,N,N',N'*-tetramethylchloroformamidinium chloride was obtained by a dropwise addition of tetramethylurea (20 mL, 167 mmol) to freshly distilled oxalyl chloride (15.7 mL, 183 mmol) dissolved in 20 mL of dry dichloromethane at room temperature. The solution was stirred overnight and the solvent was removed under vacuum. The remaining precipitate was washed several times with dry diethyl ether until the washing ether was colourless. The solid *N,N,N',N'*-tetramethylchloroformamidinium chloride was dried for three hours at 20 °C/0.05 mbar to yield 27.09 g (95%) as a white moisture sensitive powder.

N,N,N',N'-Tetramethyl-*N'',N''*-pentamethyleneguanidinium chloride was prepared by dropwise addition of a solution of piperidine (2.5 mL, 25 mmol) and triethylamine (3.5 mL, 25 mmol) in 20 mL of dry diethyl ether to a solution of *N,N,N',N'*-tetramethylchloroformamidinium chloride (4.3 g, 25 mmol) in 40 mL of dry acetonitrile at 0 °C. The mixture was stirred overnight at room temperature. The precipitated triethylammonium chloride was filtered off, and the solvents were distilled on the rotary evaporator. A 0.1 M NaOH solution was added to the residual oil, until the pH was slightly alkaline. To remove the coloured impurities, the aqueous solution was washed several times with diethyl ether. Volatile components were distilled on the rotary evaporator (40 °C/70 mbar) and the solid residue was subsequently dried at 50 °C/0.05 mbar. Afterwards, it was dissolved in dry acetonitrile/diethyl ether (2 : 1 v/v, 10 mL) and the solid was filtered off. The organic solvents were removed and the product was dried for 8 h at 80 °C/0.05 mbar. Crystallisation from ethyl acetate/dimethyl formamide (2 : 1) gave 4.2 g of *N,N,N',N'*-tetramethyl-*N'',N''*-pentamethyleneguanidinium chloride (77% yield) as a white hygroscopic powder.

N,N,N',N'-Tetramethyl-*N'',N''*-pentamethyleneguanidinium bis(trifluoromethylsulfonyl)imide (PipGuan-TFSI) was synthesised by anion exchange. Lithium bis(trifluoromethylsulfonyl)imide (2.9 g, 10 mmol) and *N,N,N',N'*-tetramethyl-*N'',N''*-pentamethyleneguanidinium chloride (2.2 g, 10 mmol) were dissolved in 30 and 10 mL, respectively, of deionised water. The solutions were combined resulting in two phases. After stirring the mixture at 70 °C for 30 min, it was cooled to room temperature, and dichloromethane (30 mL) was added. The organic phase was separated and washed with several portions of deionised water until chloride could not be detected any more in the rinsing water using AgNO₃. The organic phase was

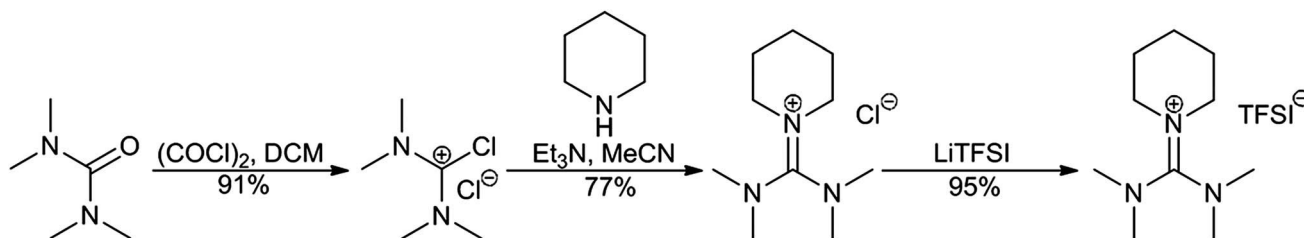


Fig. 2 Synthesis route to PipGuan-TFSI.

dried with Na₂SO₄, stirred over charcoal for 15 min, and filtered. The solvent was removed on a rotary evaporator, and the product was dried for 8 h at 120 °C/0.05 mbar. *N,N,N',N'*-Tetramethyl-*N'',N''*-pentamethyleneguanidinium bis(trifluoromethylsulfonyl)imide was obtained as a slightly yellowish oil (4.4 g, 95% yield).

Physical and electrochemical characterisation

NMR spectra were recorded on a Bruker DRX 400 spectrometer (¹H: 400.13 MHz; ¹³C: 100.61 MHz; ¹⁹F: 376.46 MHz). IR spectra were recorded with a Bruker Vector 22 FTIR spectrometer. Thermal stability was determined by TGA (Mettler Toledo STARE TGA/DSC1; Mettler-Toledo TGA/SDTA 851 for *N,N,N',N'*-tetramethyl-*N'',N''*-pentamethyleneguanidinium chloride), the decomposition point was defined as $T_{\text{dec}} \hat{=}$ temperature of highest decomposition gradient at a heating rate of 5 K min⁻¹. The decomposition products were detected by mass spectrometry (Pfeiffer Vacuum Thermostar GSD320). Differential scanning calorimetry was performed with a Perkin Elmer DSC 7 instrument. Microanalyses were obtained with an Elementar vario MICRO cube instrument. Lithium bis(trifluoromethylsulfonyl)imide for synthesis was received from Acros Organics or IoLiTec GmbH with a purity of 99%. Viscosity was measured using a Rheometer (Anton Paar GmbH, Rheometer MCR 501), conductivity was measured using a conductivity meter (Eutech Instruments, CyberScan 600 Series). The electrochemical window was measured by linear sweep voltammetry (scan rate: 10 mV s⁻¹) in two different cells: (i) a two-electrode 2016 coin cell with stainless steel as the working electrode and lithium as the counter and reference electrode and (ii) a three-electrode beaker cell with glassy carbon as the working, Ag|AgNO₃ as the reference, and platinum as the counter electrode. For the reference electrode, a Ag wire was immersed in a solution of 0.01 M AgNO₃ in acetonitrile, with 0.1 M N(octyl)₄BF₄ as conducting salt. A junction with the compartment containing the IL was realized with a vycor glass frit. For both set-ups, the electrochemical windows were calculated for the cut-off current densities 0.1 mA cm⁻² and 0.5 mA cm⁻². EIS was performed in a symmetric lithium coin cell set-up (Li|electrolyte|Li). Plating/stripping experiments were conducted using a 2016 coin cell set-up with lithium metal and stainless steel electrodes. For both measurements, a Biologic VMP3 potentiostat was used. Battery tests were performed with an electrolyte consisting of the synthesised PipGuan-TFSI and 0.5 M lithium bis(trifluoromethylsulfonyl)imide (LiTFSI, SOLVAY, 99.99%). Note that the maximum concentration attainable at 300 K was 0.8 M. Commercial lithium iron phosphate (LFP, ENAX) was used as cathode material. The composite cathodes were prepared by mixing LFP, acetylene black (Alfa Aesar, > 99%), and polyvinylidene fluoride (PVdF, Arkema, Kynar HSV 900) binder in the weight ratio of 80 : 10 : 10, with *N*-methyl-2-pyrrolidone (NMP, Sigma Aldrich, ≥99%), to form a slurry. The well-mixed, homogenous mixture was coated on an Al foil using a doctor blade, and dried at 80 °C in air to remove the solvent. Circular pieces with 16 mm diameter were punched out of the coated Al foil and roll-pressed between twin rollers

to improve adherence of the coating to the Al foil. After drying the electrodes for 4 h under vacuum at 110 °C, the electrodes were assembled in a half-cell configuration in 2016 coin cells, using 16 mm circular lithium metal pieces as the anode, separated by a glass fibre separator (Whatman) swollen with the aforementioned electrolyte. Charge/discharge experiments were carried out with an Arbin battery tester. All measurements were performed with the purified and dry ionic liquid. Magnetic resonance techniques (¹H-NMR, ¹³C-NMR, ¹⁹F-NMR), infrared spectroscopy, mass spectrometry, Karl-Fischer analysis and elemental analysis did not indicate the presence of any impurities other than small traces of water (according to Karl-Fischer: <50 ppm).

Results and discussion

Analytical data

***N,N,N',N'*-Tetramethylchloroformamidinium chloride.** ¹H NMR (CDCl₃): δ = 3.55 (s, 12H, NCH₃) ppm.

***N,N,N',N'*-Tetramethyl-*N'',N''*-pentamethyleneguanidinium chloride.** Melting point = 158–159 °C, $T_{\text{dec}} = 330$ °C, ¹H NMR (CDCl₃): δ = 1.25–1.50 (m, 6H, CH₂(CH₂)₃CH₂, pip), 2.77 (s, 12H, NCH₃), 2.97–3.13 (m, 4H, NCH₂, pip) ppm. ¹³C NMR (CDCl₃): δ = 22.6 (N(CH₂)₂CH₂, pip), 24.5 (NCH₂CH₂CH₂, pip), 40.05 and 40.09 (NCH₃), 49.3 (NCH₂CH₂CH₂, pip), 161.9 (CN₃) ppm. IR (ATR): ν = 2930 (m), 2856 (m), 1564 (s), 1435 (m), 1407 (s), 1277 (m), 1253 (m) cm⁻¹. MS (CI): $m/z = 184$ (100%, [cation]⁺). Anal. calcd. for C₁₀H₂₂ClN₃*0.75H₂O: C 51.49, H 10.15, N 18.01; found: C 51.48, H 10.27, N 17.94%.

***N,N,N',N'*-Tetramethyl-*N'',N''*-pentamethyleneguanidinium bis(trifluoromethylsulfonyl)imide (PipGuan-TFSI).** Melting point = 3 °C, $T_{\text{dec}} = 463$ °C, ¹H NMR (CDCl₃): δ = 1.65–1.80 (m, 6H, CH₂(CH₂)₃CH₂, pip), 2.98 and 2.99 (2 s, 6H each, NCH₃), 3.20–3.35 (m, 4H, NCH₂, pip) ppm. ¹³C NMR (CDCl₃): δ = 23.4 (N(CH₂)₂CH₂, pip), 25.1 (NCH₂CH₂CH₂, pip), 40.32 and 40.35 (NCH₃), 49.9 (NCH₂CH₂CH₂, pip), 162.8 (CN₃) ppm. ¹⁹F NMR (CDCl₃): δ = -75.3 ppm. IR (NaCl): ν = 2951 (m), 2864 (m), 1569 (s), 1411 (m), 1347 (s), 1330 (s), 1176 (s), 1134 (s), 1053 (s) cm⁻¹. MS (CI): $m/z = 184$ (100%, [cation]⁺). Anal. calcd. for C₁₂H₂₂F₆N₄O₄S₂ (464.44): C 31.03, H 4.77, N 12.06; found: C 31.03, H 4.68, N 12.25%.

Thermal properties of PipGuan-TFSI

DSC revealed a melting point of 3 °C as measured by DSC. It is lower than the one of *N,N*-diethyl-*N',N'',N''*-tetramethyl- or *N,N,N',N'*-tetramethyl-*N'',N''*-dipropylguanidinium-TFSI (9.9 and 12.9 °C, respectively) but slightly higher than the one of *N,N,N',N'*-tetramethyl-*N''*-ethyl-*N''*-propylguanidinium-TFSI (-1.6 °C).^{29,30} In general, the melting point of ionic liquids increases for more symmetrical cations, because symmetry facilitates a closer packing of the ions. Leaving the methyl groups at *N* and *N'* constant, the melting point tends to decrease with increasing chain length of the alkyl chain at *N''*, up to a critical molar mass.³⁰ Considering that the piperidinium contains five carbon atoms, the relative position of the melting point of PipGuan-TFSI is within the expected range.

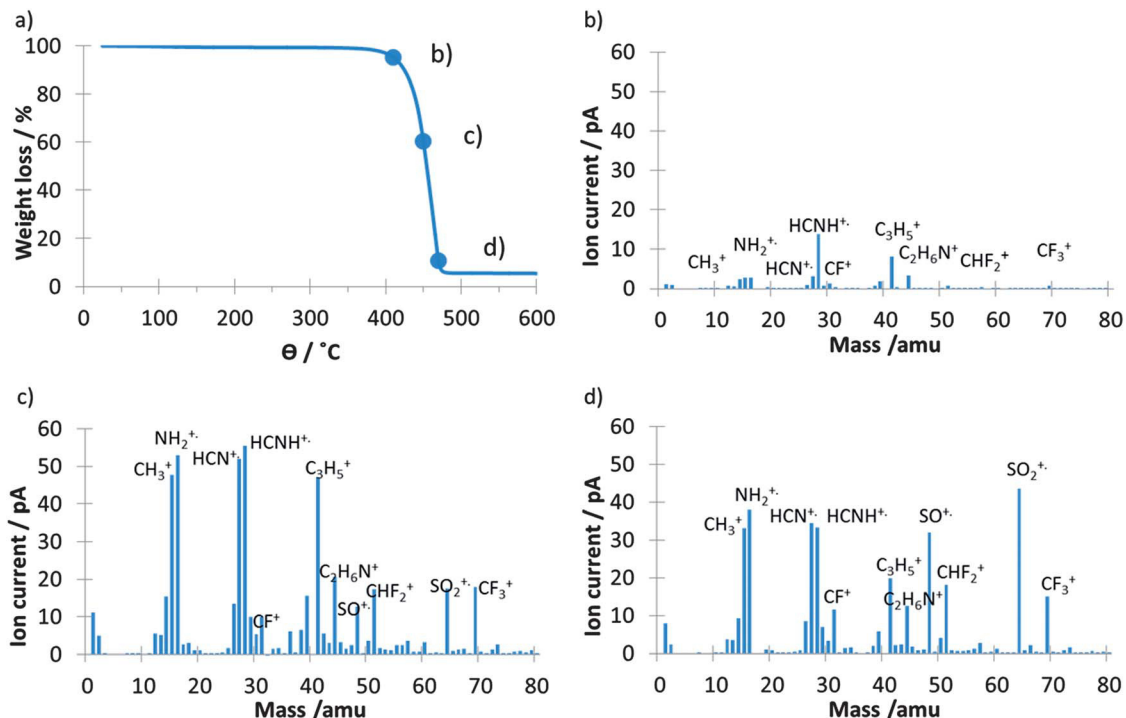


Fig. 3 (a) TGA of PipGuan-TFSI (5 K min⁻¹), (b) MS of PipGuan-TFSI at 410 °C, (c) MS of PipGuan-TFSI at 450 °C, (d) MS of PipGuan-TFSI at 470 °C.

TGA showed that PipGuan-TFSI is stable up to 415 °C (5% of mass loss). The temperature of highest decomposition gradient is at 463 °C. The mass spectra of the decomposition products were analysed at the onset, in the middle, and at the end of the decomposition (Fig. 3). In the beginning, the fragments seem to indicate the decomposition mainly of the cation (Fig. 3a), whereas at the end, the fragments are predominantly decomposition products of the anion (Fig. 3b). In the middle of decomposition, fragments from both cation and anion are present (Fig. 3c). Thus, it can be assumed that the cation is the limiting ion for thermal stability. Comparing this data with other ILs, PipGuan-TFSI is thermally more stable than other guanidinium ILs, but less stable than piperidinium based ILs.^{30,34}

Viscosity and conductivity

Viscosities and conductivities were measured for pure PipGuan-TFSI and for a solution of 0.5 M LiTFSI, a potential LIB electrolyte. As found in similar systems,^{9,27} the viscosity of the Li⁺ containing solution is higher than that of the pure IL for all temperatures. For both samples, the viscosity decreases with increasing temperature (Fig. 4) according to a Vogel–Tammann–Fulcher relationship (eqn (1)),^{37,38} for the fitted parameters see Table 1.

$$\eta = \eta_0 \exp\left(\frac{B}{T - T_0}\right) \quad (1)$$

The values are comparable to those reported for hexaalkyl guanidinium-based ionic liquids with TFSI as the anion.³⁰

Room temperature viscosities of previously reported hexaalkyl guanidinium³⁰ and piperidinium³⁴ based ILs are in the range of 58–113 mPa s and 190–370 mPa s, respectively. For

PipGuan-TFSI, our measurements reveal 108 mPa s at 25 °C. As expected, this value lies between those for guanidinium and piperidinium. The viscosity of the 0.5 M LiTFSI electrolyte was found to be 164 mPa s at room temperature.

Conductivities were measured in an Ar filled glovebox at 28 °C. The measurements revealed 1.46 mS cm⁻¹ and 0.74 mS cm⁻¹ for pure PipGuan TFSI and the 0.5 M LiTFSI electrolyte, respectively. Again, the conductivity of the pure IL lies between the value ranges reported for *N,N,N',N'*-tetramethyl-*N''*-alkyl¹-*N''*-alkyl² guanidinium-TFSI (alkyl^{1/2} = methyl, ethyl, propyl and butyl), *i.e.*, 1.02–2.86 mS cm⁻¹ (at 25 °C),³⁰ and for *N*-alkyl¹-*N*-alkyl² piperidinium-TFSI (alkyl^{1/2} = methyl, ethyl, propyl, butyl, pentyl, hexyl, or heptyl), which are 2.1 · 10⁻⁵–0.92 mS cm⁻¹ (at 20 °C),³⁴ respectively.

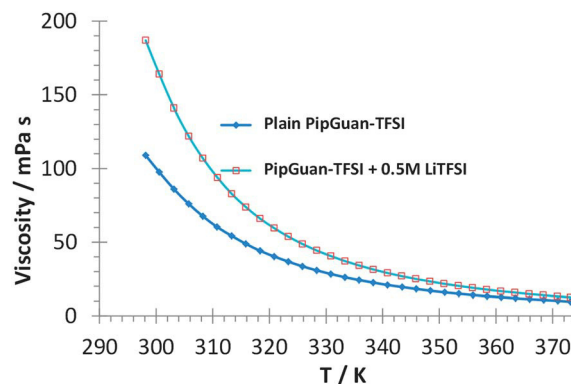


Fig. 4 Temperature dependence of viscosity for PipGuan-TFSI and 0.5 M solution of LiTFSI in PipGuan-TFSI.

Table 1 Parameters for the Vogel–Tammann–Fulcher equation for PipGuan-TFSI and the electrolyte (0.5 M solution of LiTFSI in PipGuan-TFSI)

	$\eta_0/\text{mPa s}$	B/K	T_0/K	R^2
PipGuan-TFSI	$0.26 \pm 7\%$	$705 \pm 2\%$	$190 \pm 1\%$	>0.9999
Electrolyte	$0.17 \pm 9\%$	$797 \pm 3\%$	$174 \pm 1\%$	>0.9999

Electrochemical measurements

Fig. 5a and b show the electrochemical window of PipGuan-TFSI measured in two different ways. Fig. 5a was measured with a three-electrode set-up, with glassy-carbon as the working, Ag|AgNO₃ as the reference, and platinum as the counter electrode. The three-electrode set-up shows an electrochemical window of 4.40 V between -2.55 V and 1.85 V vs. Ag|Ag⁺, all for a cut-off current density of 0.5 mA cm^{-2} . For a cut-off at 0.1 mA cm^{-2} , the window narrows to 4.16 V with -2.50 V and 1.66 V vs. Ag|Ag⁺ as cathodic and anodic limits, respectively (see Table 2). Fig. 5b shows the measurement in a coin cell to simulate working conditions in a LIB. The two-electrode set-up with stainless steel as a working and Li metal as a counter electrode showed an electrochemical window of 5.11 V (0.2 V ... 5.31 V) for a cut-off current density of 0.5 mA cm^{-2} , and of 4.44 V (0.44 V ... 4.88 V) for a cut-off at 0.1 mA cm^{-2} .

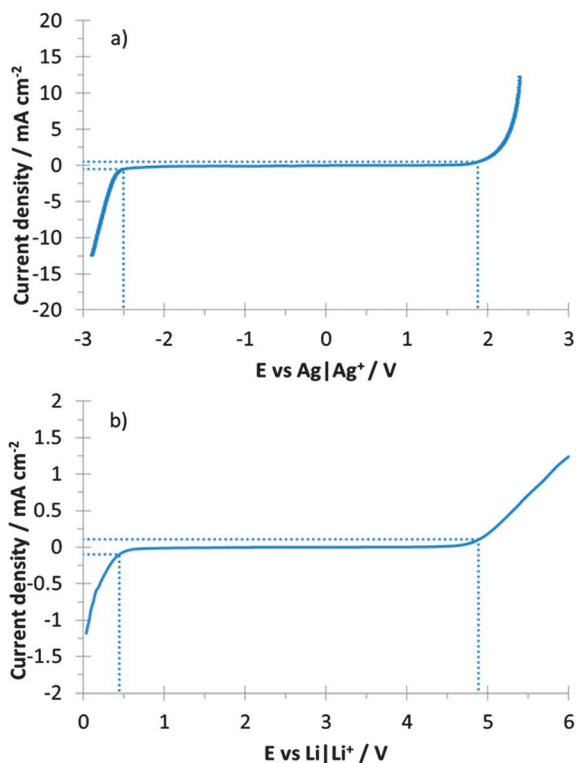


Fig. 5 (a) Electrochemical window of PipGuan-TFSI using a 3-electrode set-up with Ag|AgNO₃ as reference, glassy carbon as working and Pt as counter electrode, (b) electrochemical window of PipGuan-TFSI using a coin cell set-up with Li as combined counter&reference and stainless steel as a working electrode; the dotted lines represent a cut-off current density of 0.5 mA cm^{-2} for (a), and 0.1 mA cm^{-2} for (b).

Table 2 Electrochemical stability limits and electrochemical window for PipGuan-TFSI

	2 Electrodes, vs. Li Li ⁺		3 Electrodes, vs. Ag Ag ⁺	
	0.1	0.5	0.1	0.5
Cut-off current density/ mA cm^{-2}				
Anodic limit/V	4.88	5.31	1.66	1.85
Cathodic limit/V	0.44	0.20	-2.50	-2.55
Electrochem. window/V	4.44	5.11	4.16	4.40

It should be pointed out that the Li reference potential obtained in these cells is not well-defined because there is no controlled Li⁺ content in the Li-TFSI solution as required for a true Li|Li⁺ system.³⁹ Nevertheless, the upper potential limit indicates that PipGuan-TFSI could be suitable for high-voltage battery cells.

For an application of PipGuan-TFSI in Li-ion batteries the electrochemical properties of the Li⁺ containing electrolyte (PipGuan-TFSI + 0.5 M LiTFSI) are more important than those of the plain IL. Fig. 6 shows the first and second cycle of a freshly mounted coin cell with stainless steel as working and lithium as combined counter&reference electrode, respectively. Starting at 2 V, the first CV cycle shows broad cathodic features starting at 1.5 V in the negative going scan. Those presumably reflect electrolyte decomposition, in analogy to previous observations for other ILs.^{24,27,40,41}

The fact that these features are only observed in the first negative going scan indicates that the product is a passivating layer (sometimes referred to as solid electrolyte interphase, SEI). In following cycles, no major features are visible until -0.08 V. Integration of oxidation and reduction charges shows that for the scan from -0.08 V to -0.25 V and back, the total cathodic charge adds up to about twice the total anodic charge that is regained above -0.08 V. The anodic charge is assigned to the stripping of Li layers that were plated onto the stainless steel

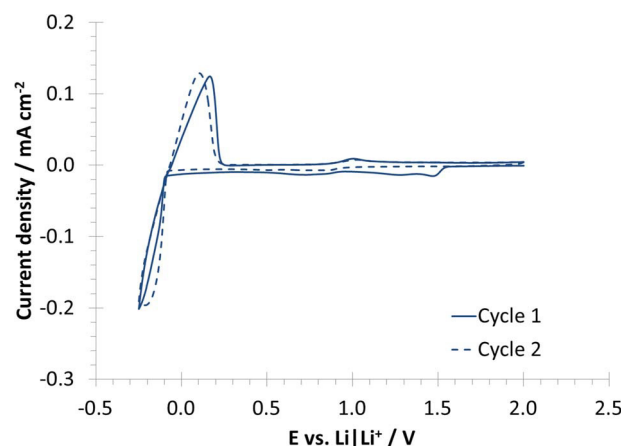


Fig. 6 Cyclic voltammogram for 0.5 M LiTFSI in PipGuan-TFSI in a coin cell set-up with stainless steel as a working and Li as a combined counter&reference electrode, respectively, with a scan rate of 0.3 mV s^{-1} .

electrode at $E < -0.08$ V. The cathodic charge thus splits into contributions from Li plating and electrolyte decomposition in coarsely equal shares. Scans to lower E revealed a more pronounced increase of the negative as compared to the positive charge in the anodic counter-peak, indicating that electrolyte decomposition becomes dominating at more negative potentials. Comparing the CV in Fig. 6 with the linear sweep scan of the plain IL in Fig. 5b, the onset of electrolyte decomposition seems to be shifted to more negative potentials in the presence of Li^+ ions in the solution.

It was speculated previously that the addition of LiTFSI enables the formation of a passivating layer that widens the potential window.^{40,41} In-depth studies on the composition of this layer have been conducted earlier by other groups.^{42–44}

As highlighted above, however, the Li based reference potentials in the plain and in the LiTFSI containing IL should not be directly compared: if the potential determining equilibrium reaction is $\text{Li}_{\text{solid}} \leftrightarrow \text{Li}^+ + \text{e}^-$, the Li^+ concentration in the neat IL is undefined and can easily be several orders of magnitude below the one in the electrolyte with 0.5 M LiTFSI.³⁹ According to the Nernst equation the pseudo-reference potential in the neat IL can thus be several multiples of 59 mV more negative than the $\text{Li}|\text{Li}^+$ potential in the electrolyte. Such a shift could be the main reason for the different onset potentials for cathodic IL decomposition without (Fig. 5b) and with (Fig. 6) LiTFSI in the solution. IUPAC recommends the utilization of

dissolved redox couples (*e.g.*, ferrocene/ferrocenium) as internal references in such systems.^{39,45–47} Using this method, we seek to clarify the actual effect of LiTFSI on the width of the potential stability window in upcoming experiments. As to the potential scale in Fig. 6, one should also emphasise that Li deposition and dissolution is setting in at -0.08 V in the negative and positive going scan, respectively, and not at 0 V as one should expect. This means that the $\text{Li}|\text{Li}^+$ potential is more negative for the freshly deposited Li film than for the Li foil used as combined counter&reference electrode. We tentatively assign this potential difference to a chemical modification of the surface of the Li foil due to (electro-)chemical side reactions as they will be discussed in more detail below. Apart from the open questions related to the electrochemical equilibrium potentials, however, the Li plating/stripping behaviour in Fig. 6 confirms transport of Li^+ between the two electrodes and thus the suitability of PipGuan-TFSI as electrolyte solvent for Li-ion batteries.

Apart from the Li^+ transport properties and the potential dependent electrochemical stability of PipGuan-TFSI we also studied its interaction with metallic Li. Specifically, we used EIS to analyse the charge transfer properties of the interface between metallic Li and PipGuan-TFSI + 0.5 M LiTFSI. Fig. 7 shows the evolution of the impedance response of a cell that was stored at room temperature under open circuit conditions, just interrupted by the EIS measurements. The intercept of the

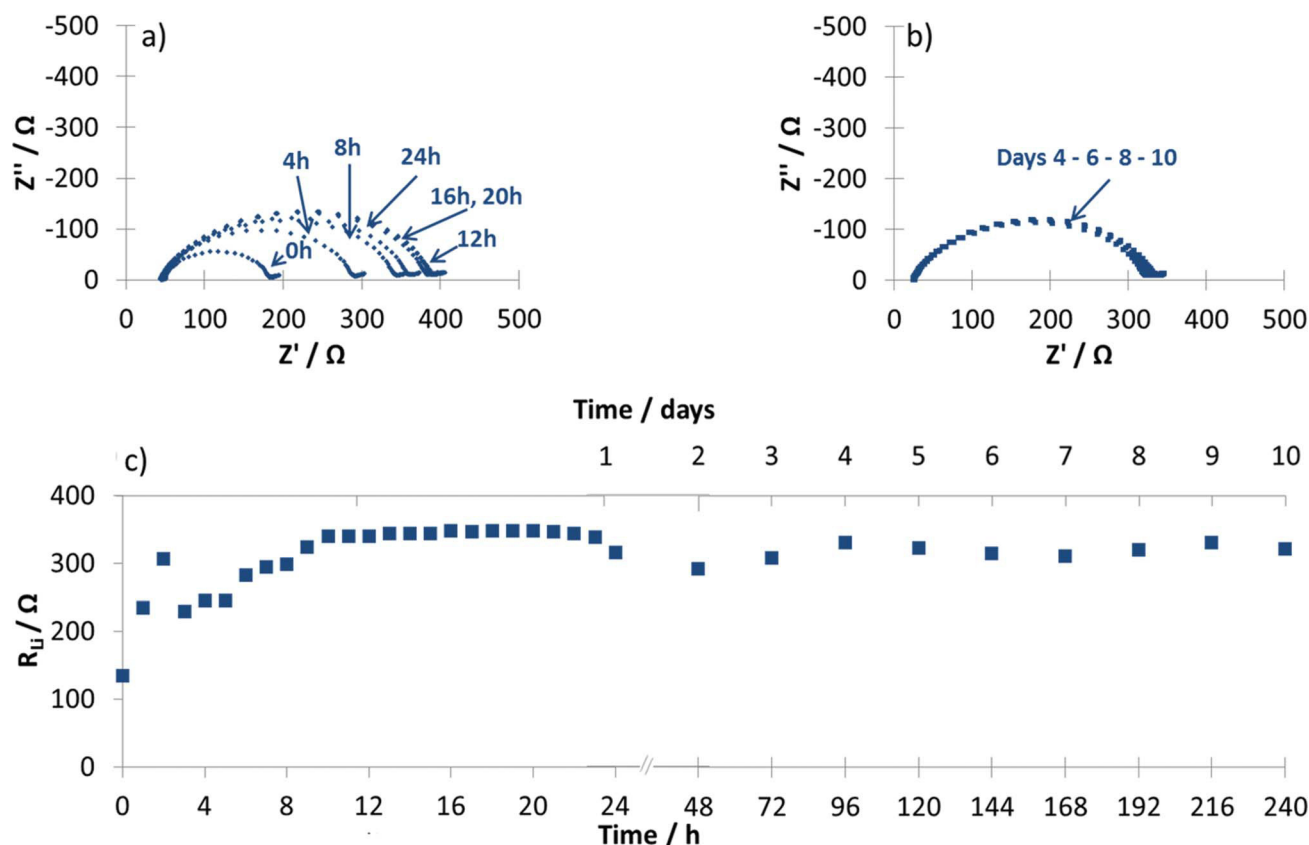


Fig. 7 Impedance response of a symmetrical Li|0.5 M LiTFSI in PipGuan-TFSI|Li cell stored at room temperature during the first (a) 12 hours, (b) 10 days, (c) time evolution of R_{Li} .

semicircles at high frequencies (left side) was associated with the bulk resistance. The difference between the two intercepts with the real axis was interpreted as the electrode-electrolyte resistance (R_{Li}), combining both the charge transfer and the passivating layer resistance. Of these two components, R_{Li} is probably dominated by the resistance of the passivating layer.^{17,48,49} As can be seen from Fig. 7a, resistance stabilised after 12 hours. Fig. 7b shows the long-term impedance test over 10 days, which shows only little change in the R_{Li} resistance. This indicates that a passivating layer is forming at the lithium electrode during the first 12 hours, and that it stays stable afterwards. Due to the open circuit conditions, this formation must be a chemical or a corrosion type of reaction.

To complete the picture of PipGuan-TFSI as a suitable electrolyte solvent for Li-ion batteries we examined the charge/discharge behaviour of LiFePO₄ half cells at different C-rates and two different temperatures (24 and 55 °C). Coin cells were tested by running four cycles at every C-rate before increasing the C-rate. The presented capacities correspond to the fourth cycle for every C-rate. Fig. 8a shows a discharge capacity of 154 mA h g⁻¹ for charge/discharge at 0.025 C. The same capacity was found in a test experiment with the same electrodes and commercial electrolyte (EC:DMC, 1 M LiPF₆) at 0.2 C. For 0.05 C and 0.1 C, the discharge capacities attained with the PipGuan-TFSI based electrolyte reduce to 143 mA h g⁻¹ and 101 mA h g⁻¹, respectively. Such a negative correlation of C-rate and capacity is commonly observed and attributed to the high viscosity of ionic liquids.^{9,19,50} This assignment fits

to the observed charge/discharge behaviour at 55 °C (Fig. 8b), where a capacity of 148 mA h g⁻¹ is reached at 0.2 C. This capacity is almost 150% of the value obtained at 0.1 C and 24 °C. Furthermore, it is about the same capacity as we could reach for an identical half cell with standard electrolyte (1 M LiPF₆ in EC/DMC) at the same C-rate and at 24 °C (curve not shown here). In summary, the data in Fig. 8 indicate that the main disadvantage of PipGuan-TFSI as an electrolyte solvent for Li-ion batteries is a poor Li⁺ conductivity due to a high viscosity. Increasing the temperature to 55 °C lowers the viscosity by about a factor of four, which must be the reason for the improved half-cell performance at that temperature.²⁹ Furthermore, the achieved discharge capacities for PipGuan-TFSI based electrolyte (143 mA h g⁻¹ at 0.05 C, 101 mA h g⁻¹ at 0.1 C at 24 °C) lay above the values of 93 mA h g⁻¹ (0.05 C) and 80 mA h g⁻¹ (0.1 C) that were reported for *N*-butyl-*N*-methylpiperidinium-TFSI¹⁹ and *N*-butyl-*N,N',N'',N'''*-pentamethylguanidinium-TFSI,³² respectively. In this respect, the performance of the PipGuan-TFSI based electrolyte does not lie between the two classes of material but is better than the respective individual performances.

Conclusions

A new ionic liquid that combines the structures of piperidinium and guanidinium based ionic liquids, PipGuan-TFSI, has been synthesised. The physical properties, *i.e.*, thermal stability, viscosity and conductivity of this new material lie between these two different classes of ionic liquids. PipGuan-TFSI has a large electrochemical window and is able to reversibly plate and strip lithium. Thus, it is promising as a new electrolyte in lithium ion batteries. Its performance in a half cell equals that of commercial electrolytes at low C-rates or at elevated temperatures. As PipGuan-TFSI outperforms other common guanidinium and piperidinium based ionic liquids with regard to achieved capacities of LiFePO₄ half cells, the synthesis goal has been exceeded. The approach of target oriented “genetic crossing” of structural elements in IL molecules is a promising complement to computational screening and incremental modification of existing ILs. We expect this approach to trigger further improvements in the development of advanced electrolytes in the near future.

Acknowledgements

The authors would like to thank Mr Jan Geder for helping with the TGA-MS measurements, Ms. Shubha Nageswaran for fruitful and interesting discussions regarding the work described in this article, and Mr Xiaohan Wu for his help in conducting the experiments. The authors would also like to thank SOLVAY SA for providing the LiTFSI-salt. Maria Arkhipova thanks the State of Baden-Wuerttemberg for a graduate fellowship. This work was financially supported by the Singapore National Research Foundation under its Campus for Research Excellence and Technological Enterprise (CREATE) programme.

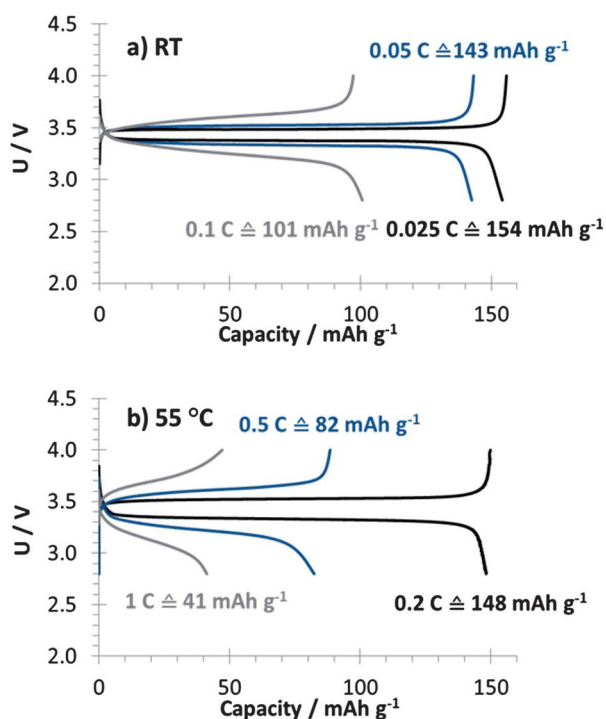


Fig. 8 Charge/discharge behaviour of 0.5 M LiTFSI in PipGuan-TFSI in a coin cell with lithium iron phosphate and lithium electrodes; (a) 24 °C, (b) 55 °C.

Notes and references

- 1 A.-O. Diallo, A. B. Morgan, C. Len and G. Marlair, *Energy Environ. Sci.*, 2013, **6**, 699.
- 2 H. Ohno, *Electrochemical Aspects of Ionic Liquids*, John Wiley & Sons, Inc., Hoboken, NJ, USA, 2005.
- 3 P. Wasserscheid and T. Welton, *Ionic Liquids in Synthesis*, Wiley-VCH Verlag GmbH & Co. KGaA, Weinheim, Germany, 2007.
- 4 N. MacDowell, N. Florin, A. Buchard, J. Hallett, A. Galindo, G. Jackson, C. S. Adjiman, C. K. Williams, N. Shah and P. Fennell, *Energy Environ. Sci.*, 2010, **3**, 1645.
- 5 X. Zhang, X. Zhang, H. Dong, Z. Zhao, S. Zhang and Y. Huang, *Energy Environ. Sci.*, 2012, **5**, 6668.
- 6 J. F. Wishart, *Energy Environ. Sci.*, 2009, **2**, 956.
- 7 M. Galiński, A. Lewandowski and I. Stępniański, *Electrochim. Acta*, 2006, **51**, 5567–5580.
- 8 M. Armand, F. Endres, D. R. MacFarlane, H. Ohno and B. Scrosati, *Nat. Mater.*, 2009, **8**, 621–629.
- 9 A. Lewandowski and A. Świdarska-Mocek, *J. Power Sources*, 2009, **194**, 601–609.
- 10 H. Sakaebe, H. Matsumoto and K. Tatsumi, *Electrochim. Acta*, 2007, **53**, 1048–1054.
- 11 F. Endres, *Phys. Chem. Chem. Phys.*, 2012, **14**, 5008–5009.
- 12 S. Passerini and W. A. Henderson, in *Encyclopedia of Electrochemical Power Sources*, ed. J. Garche, Elsevier B.V., 2009, vol. 5, pp. 85–91.
- 13 C. H. Hamann, A. Hamnett and W. Vielstich, *Electrochemistry*, Wiley VCH, Weinheim, 2007, vol. 2.
- 14 E. I. Izgorodina, *Phys. Chem. Chem. Phys.*, 2011, **13**, 4189–4207.
- 15 J. Scheers, P. Johansson and P. Jacobsson, *J. Electrochem. Soc.*, 2008, **155**, A628.
- 16 P. Johansson, L. E. Fast, A. Matic, G. B. Appetecchi and S. Passerini, *J. Power Sources*, 2010, **195**, 2074–2076.
- 17 A. Farnicola, F. Croce, B. Scrosati, T. Watanabe and H. Ohno, *J. Power Sources*, 2007, **174**, 342–348.
- 18 S. Seki, Y. Ohno, Y. Kobayashi, H. Miyashiro, A. Usami, Y. Mita, H. Tokuda, M. Watanabe, K. Hayamizu, S. Tsuzuki, M. Hattori and N. Terada, *J. Electrochem. Soc.*, 2007, **154**, A173–A177.
- 19 J. Jin, H. H. Li, J. P. Wei, X. K. Bian, Z. Zhou and J. Yan, *Electrochem. Commun.*, 2009, **11**, 1500–1503.
- 20 V. Borgel, E. Markevich, D. Aurbach, G. Semrau and M. Schmidt, *J. Power Sources*, 2009, **189**, 331–336.
- 21 M. Montanino, F. Alessandrini, S. Passerini and G. B. Appetecchi, *Electrochim. Acta*, 2013, **96**, 124–133.
- 22 M. Egashira, S. Okada, J. Yamaki, D. A. Dri, F. Bonadies and B. Scrosati, *J. Power Sources*, 2004, **138**, 240–244.
- 23 J. Sun, M. Forsyth and D. R. MacFarlane, *J. Phys. Chem. B*, 1998, **102**, 8858–8864.
- 24 S. Fang, Z. Zhang, Y. Jin, L. Yang, S. Hirano, K. Tachibana and S. Katayama, *J. Power Sources*, 2011, **196**, 5637–5644.
- 25 A. P. Lewandowski, A. F. Hollenkamp, S. W. Donne and A. S. Best, *J. Power Sources*, 2010, **195**, 2029–2035.
- 26 T. Waldmann, H.-H. Huang, H. E. Hoster, O. Höfft, F. Endres and R. J. Behm, *ChemPhysChem*, 2011, **12**, 2565–2567.
- 27 S. Fang, L. Yang, J. Wang, H. Zhang, K. Tachibana and K. Kamijima, *J. Power Sources*, 2009, **191**, 619–622.
- 28 W. Kantlehner, E. Haug, W. W. Mergen, P. Speh, T. Maier, J. J. Kapassakalidis, H.-J. Braeuner and H. Hagen, *Liebigs Ann. Chem.*, 1984, 108–126.
- 29 Y. Jin, S. Fang, L. Yang, S. Hirano and K. Tachibana, *J. Power Sources*, 2011, **196**, 10658–10666.
- 30 S. Fang, L. Yang, C. Wei, C. Jiang, K. Tachibana and K. Kamijima, *Electrochim. Acta*, 2009, **54**, 1752–1756.
- 31 M. Gnahn, C. Berger, M. Arhipova, H. Kunkel, T. Pajkossy, G. Maas and D. M. Kolb, *Phys. Chem. Chem. Phys.*, 2012, **14**, 10647–10652.
- 32 X. Zhang, S. Fang, Z. Zhang and L. Yang, *Chin. Sci. Bull.*, 2011, **56**, 2906–2910.
- 33 H. Kunkel and G. Maas, *Eur. J. Org. Chem.*, 2007, 3746–3757.
- 34 M. Montanino, M. Carewska, F. Alessandrini, S. Passerini and G. B. Appetecchi, *Electrochim. Acta*, 2011, **57**, 153–159.
- 35 J. Reiter, M. Nádherná and R. Dominko, *J. Power Sources*, 2012, **205**, 402–407.
- 36 K. Liu, Y.-X. Zhou, H.-B. Han, S.-S. Zhou, W.-F. Feng, J. Nie, H. Li, X.-J. Huang, M. Armand and Z.-B. Zhou, *Electrochim. Acta*, 2010, **55**, 7145–7151.
- 37 O. O. Okoturo and T. J. VanderNoot, *J. Electroanal. Chem.*, 2004, **568**, 167–181.
- 38 M. L. F. Nascimento and C. Aparicio, *Phys. B*, 2007, **398**, 71–77.
- 39 A. a. J. Torriero, J. Sunarso and P. C. Howlett, *Electrochim. Acta*, 2012, **82**, 60–68.
- 40 P. Reale, A. Farnicola and B. Scrosati, *J. Power Sources*, 2009, **194**, 182–189.
- 41 J. Hassoun, A. Farnicola, M. A. Navarra, S. Panero and B. Scrosati, *J. Power Sources*, 2010, **195**, 574–579.
- 42 P. C. Howlett, N. Brack, A. F. Hollenkamp, M. Forsyth and D. R. MacFarlane, *J. Electrochem. Soc.*, 2006, **153**, A595.
- 43 P. C. Howlett, D. R. MacFarlane and A. F. Hollenkamp, *Electrochem. Solid-State Lett.*, 2004, **7**, A97.
- 44 L. Suo, Y.-S. Hu, H. Li, M. Armand and L. Chen, *Nat. Commun.*, 2013, **4**, 1481.
- 45 P. De Vreese, K. Haerens, E. Matthijs and K. Binnemans, *Electrochim. Acta*, 2012, **76**, 242–248.
- 46 A. Lewandowski, L. Waligora and M. Galinski, *Electroanalysis*, 2009, **21**, 2221–2227.
- 47 D. Weingarh, a. Foelske-Schmitz, a. Wokaun and R. Kötz, *Electrochem. Commun.*, 2012, **18**, 116–118.
- 48 J. Thevenin, *J. Power Sources*, 1985, **14**, 45–52.
- 49 S. Seki, Y. Ohno, H. Miyashiro, Y. Kobayashi, A. Usami, Y. Mita, N. Terada, K. Hayamizu, S. Tsuzuki and M. Watanabe, *J. Electrochem. Soc.*, 2008, **155**, A421.
- 50 H. Matsumoto, H. Sakaebe, K. Tatsumi, M. Kikuta, E. Ishiko and M. Kono, *J. Power Sources*, 2006, **160**, 1308–1313.

6 Conclusion

Sodium-ion batteries (NIBs) hold promise as an alternative to the currently dominant lithium-ion battery (LIB) technology. Apart from advantages in terms of resource availability and cost, kinetic factors have also been shown^[39–43] to be favourable for Na-insertion as compared to Li-insertion. However, understanding of NIBs lags behind knowledge of LIBs, as interest in this technology has been modest until recently. Therefore, to establish NIBs as a viable commercial option, further research into this promising technology is essential, both in terms of searching for suitable materials and improving fundamental understanding of the processes occurring during the insertion and extraction of Na-ions.

This work describes investigations on vanadium-based electrode materials for NIBs. For the vanadates NVO ($\text{Na}_{2+x}\text{V}_6\text{O}_{16}$), LVO ($\text{Li}_{2+x}\text{V}_6\text{O}_{16}$) and KVO ($\text{K}_{2+x}\text{V}_6\text{O}_{16}$), cycling in different potential regions in half-cells vs. $\text{Na}|\text{Na}^+$ leads to significantly different results in terms of both capacity and cycling stability. In a narrow potential region between 4.0 V - 1.6 V, capacity increases during initial cycling. After 15 cycles, the respective capacities are 71 mA h g⁻¹ for NVO and KVO, and 97 mA h g⁻¹ for LVO. These capacities fall short of other materials reported for NIB cathodes. For example, the well-researched material class of layered transition metal oxides $\text{Na}_x\text{MeO}_{2+z}$ (Me: Mn, Co, Fe, Ni, etc.) delivers capacities of more than 140 mA h g⁻¹.^[134] However, in contrast to this material class, cycling stability is excellent for the vanadates in this potential region. No considerable capacity loss was observed in the first 100 cycles for NVO. Capacities for LVO and KVO drop slightly (capacity retention of ~ 85% after 100 cycles), even though LVO is still the analogue with the highest capacity after 100 cycles. Reports on which of those vanadates shows the highest capacity in LIB have been inconsistent.^[135–137] Capacity can be tremendously increased by extending the potential region to 4.0 V – 1.0 V. The obtained capacities of ~ 196 mA h g⁻¹ for NVO and ~ 231 mA h g⁻¹ for LVO are among the highest reported for NIB cathodes. However, this was achieved to the detriment of cycling stability. All materials exhibit significant capacity fading over the course of cycling (NVO: 196 mA h g⁻¹ in the 1st/58 mA h g⁻¹ in the 100th cycle; LVO: 231 mA h g⁻¹/100 mA h g⁻¹; KVO: 144 mA h g⁻¹/50 mA h g⁻¹). The data shows that the alkali ion clearly has an influence on capacity retention of alkali metal vanadates in NIBs. Recent research has started focussing on synthetic approaches to achieve a better trade-off between capacity and cycling stability for NVO.^[95,97,98] For example, optimising the morphology of this material appears to be quite promising.^[95] However, in order to develop successful strategies to combine good cycling stability and high capacities, a better understanding of the underlying factors is required.

Thorough understanding of structural processes during cycling enhances the mechanistic understanding of insertion processes and can also serve as a basis to derive strategies for further optimisation. For example, even though LVO is isostructural to NVO, there are certain structural differences, such as a shorter distance between the VO_x -layers for LVO. The effect of the alkali ion in the initial

structure was studied previously for LIBs^[135,138], but no studies had been published for the case of NIB cathodes. However, identification of the causes of observable trends, such as the development of capacity over the course of cycling, helps to deduce promising routes for improvements.

Therefore, electrochemical *in operando* XRD measurements were targeted and a new set up for XRD measurements during cycling using laboratory-scale instruments in reflection mode was developed. The commonly used Kapton or Beryllium windows were replaced with a very thin (6 μm) Al-foil. Kapton contributes broad reflections to the XRD pattern in 2θ region in which the vanadates also have reflections, while Be causes concerns with regard to toxicity and cost. In addition, electrochemical *in operando* synchrotron XRD measurements were conducted. Unlike diffraction measurements in reflection mode, synchrotron measurements were conducted in transmission mode. Thus, information on processes occurring in the bulk of the electrode, rather than only within some μm close to the surface of the electrode, could be deduced.

Based on this data, a mechanism for the insertion of Na^+ into the host structure was derived. These results also provide the basis for explaining the electrochemical behaviour of vanadates as NIB electrode materials. The $\text{A}_2\text{V}_6\text{O}_{16}$ unit cell has four lattice sites that take part in reversible extraction and insertion of Na-ions during charge/discharge in the narrow potential region (4.0 V – 1.6 V). Structural stress as a consequence of these processes is low, as indicated by changes of the unit cell vectors and volume. This structural reversibility is mirrored in the reversibility of the electrochemistry, *i.e.* high cycling stability. Upon insertion of further Na-ions at lower potentials (4.0 V – 1.0 V), Na^+ is forced into interstices in the layer of VO_x -polyhedra. Thus, the structure is forced apart. This development cannot be reversed during the subsequent extraction of Na^+ . Repeated insertion of Na-ions into the interstices leads to an irreversible expansion of the unit cell which, over the course of cycling, results in a loss of long range order and concomitant capacity decrease.

Interestingly, LVO undergoes structural changes already in the electrochemically stable range as a result of ion exchange. This process is different from the opposite situation, *i.e.* cycling NVO in a LIB, for which no ion exchange occurs.^[136] In NIBs, however, Li^+ in the LVO structure is gradually replaced by Na^+ . A small minority of Li^+ ($\sim 10\%$) remains in the structure. Previous research for alkali metal oxides in LIBs showed that the cycling stability of NVO in LIBs can be increased by chemical insertion of lithium into the structure, *i.e.* pre-lithiating the material, before cycling.^[137] The suggested causes of this increased stability were mainly structural, particular a stabilisation of the host structure. A similar effect is suggested here: the retained Li^+ in the initial LVO structure results in an increase of structural stability during cycling. One disadvantage, though, is that the diffusion coefficient for Na^+ in LVO is slightly lower than for NVO in the reversible potential range (4.0 – 1.6 V), which is in agreement with literature for LIBs^[136]. This is attributed to the smaller interlayer spacing between the VO_x -layers for LVO. However, in contrast to the (chemically) lithiated NVO, the electrochemically sodiated LVO shows a higher capacity than the pristine material. Thus, (partially)

replacing Na^+ with a smaller, harder cation appears to be a promising strategy to enhance both capacity and stability.

Another strategy presented here to avoid capacity fading as a result of structural degradation is to replace the very process that is detrimental to structural integrity, *i.e.* avoid insertion of charge carriers into a given crystal structure, with a different mechanism for charge storage. One approach that was demonstrated is to replace materials with a defined long-range order with a different class of materials such as POMs. Even though POMs have been shown to work in LIBs^[139–144], they had not been employed in NIBs before. POMs consist of polyanionic clusters with cavities between the respective compounds. These cavities are similar to voids in carbon-based materials, which are often used for battery anodes, even though the underlying chemistry and structure differs. Insertion of Na^+ into these pores is known to result in low volume changes for carbon,^[84,145] which alleviates structural stress within the material. The POM investigated in this work is $\text{Na}_6[\text{V}_{10}\text{O}_{28}]$. Na^+ can insert into the voids between the individual clusters, induced by a reduction of the vanadium ions in the polyanionic clusters. Using this material, charge is stored in an anodic potential region. Both its high capacity ($> 200 \text{ mA h g}^{-1}$ at 50 mA g^{-1}) and excellent stability, which constitutes a significant improvement over the aforementioned vanadates, indicate that this material class holds promise as electrode material for NIBs. Further mechanistic studies on the Na^+ -insertion mechanism might prove helpful in further elucidating advantageous characteristics of POMs, and thus optimise their properties as Na^+ -hosts.

In general, the ‘library’ of materials that is suitable for Na^+ -insertion is expanding quickly and understanding of the fundamental processes in NIBs progresses rapidly. However, additional efforts are necessary to develop systems that can compete with current commercial batteries. The work presented in this thesis adds to these efforts by investigating the performance of vanadates in NIBs and revealing the interplay between structural and electrochemical reversibility. The positive effects on cycling performance of incorporating small ions, such as Li^+ , in the vanadate structure as well as employing POMs as NIB electrode materials have been demonstrated. These strategies pave the way for further improvement of the cyclability of NIB electrode materials.

References

- [1] B. Scrosati, *Renew. Energy* **1994**, *5*, 285.
- [2] B. Scrosati, *J. Solid State Electrochem.* **2011**, *15*, 1623.
- [3] P. O. Eggen, L. Kvittingen, A. Lykknes, R. Wittje, *Sci. Educ.* **2012**, *21*, 179.
- [4] K.-D. Kreuer, Ed., *Fuel Cells*, Springer New York, New York, NY, **2013**.
- [5] M. L. Perry, T. F. Fuller, *J. Electrochem. Soc.* **2002**, *149*, S59.
- [6] K. B. Hueso, M. Armand, T. Rojo, *Energy Environ. Sci.* **2013**, *6*, 734.
- [7] M. S. Whittingham, *Prog. Solid State Chem.* **1978**, *12*, 41.
- [8] K. M. Abraham, *Solid State Ionics* **1982**, *7*, 199.
- [9] W. Rüdorff, *Angew. Chemie* **1959**, *71*, 487.
- [10] W. Rüdorff, H. H. Sick, *Angew. Chemie* **1959**, *71*, 127.
- [11] C. Delmas, J. J. Braconnier, C. Fouassier, P. Hagenmuller, *Solid State Ionics* **1981**, *3-4*, 165.
- [12] J. J. Braconnier, C. Delmas, P. Hagenmuller, *Mater. Res. Bull.* **1982**, *17*, 993.
- [13] Z. Yang, J. Zhang, M. C. W. Kintner-Meyer, X. Lu, D. Choi, J. P. Lemmon, J. Liu, *Chem. Rev.* **2011**, *111*, 3577.
- [14] S. Koohi-Kamali, V. V. Tyagi, N. A. Rahim, N. L. Panwar, H. Mokhlis, *Renew. Sustain. Energy Rev.* **2013**, *25*, 135.
- [15] A. Collinson, J. N. Baker, *Power Eng. J.* **1999**, *13*, 107.
- [16] S. Srinivasan, *Fuel Cells. [electronic Resource]: From Fundamentals to Applications*, Springer Science+Business Media, LLC, Boston, MA, **2006**.
- [17] P. Simon, Y. Gogotsi, *Nat. Mater.* **2008**, *7*, 845.

- [18] R. Kötz, M. Carlen, *Electrochim. Acta* **2000**, *45*, 2483.
- [19] M. Ehsani, Y. Gao, A. Emadi, *Modern Electric, Hybrid Electric, and Fuel Cell Vehicles: Fundamentals, Theory, and Design*, CRC Press, **2009**.
- [20] J. Nelson Weker, M. F. Toney, *Adv. Funct. Mater.* **2015**, *25*, 1622.
- [21] M. R. Palacín, *Chem. Soc. Rev.* **2009**, *38*, 2565.
- [22] S. Hartung, N. Bucher, H.-Y. Chen, R. Al-Oweini, S. Sreejith, P. Borah, Z. Yanli, U. Kortz, U. Stimming, H. E. Hoster, M. Srinivasan, *J. Power Sources* **2015**, *288*, 270.
- [23] S. Hartung, N. Bucher, V. S. Nair, Y. L. Cheah, Y. Wang, H. E. Hoster, M. Srinivasan, *Chemphyschem* **2014**, *15*, 2121.
- [24] D. Larcher, S. Beattie, M. Morcrette, K. Edström, J.-C. Jumas, J.-M. Tarascon, *J. Mater. Chem.* **2007**, *17*, 3759.
- [25] N. Yabuuchi, K. Kubota, M. Dahbi, S. Komaba, *Chem. Rev.* **2014**, *114*, 11636.
- [26] M. M. Doeff, Y. Ma, S. J. Visco, L. C. De Jonghe, *J. Electrochem. Soc.* **1993**, *140*, 169.
- [27] Y. Ma, M. M. Doeff, S. J. Visco, L. C. De Jonghe, *J. Electrochem. Soc.* **1993**, *140*, 2726.
- [28] D. A. Stevens, J. R. Dahn, *J. Electrochem. Soc.* **2000**, *147*, 1271.
- [29] D. A. Stevens, J. R. Dahn, *J. Electrochem. Soc.* **2001**, *148*, A803.
- [30] N. Yabuuchi, K. Kubota, M. Dahbi, S. Komaba, *Chem. Rev.* **2014**, *114*, 11636.
- [31] S. Komaba, W. Murata, T. Ishikawa, N. Yabuuchi, T. Ozeki, T. Nakayama, A. Ogata, K. Gotoh, K. Fujiwara, *Adv. Funct. Mater.* **2011**, *21*, 3859.
- [32] N. Yabuuchi, M. Kajiyama, J. Iwatate, H. Nishikawa, S. Hitomi, R. Okuyama, R. Usui, Y. Yamada, S. Komaba, *Nat. Mater.* **2012**, *11*, 512.

- [33] S. Komaba, T. Ishikawa, N. Yabuuchi, W. Murata, A. Ito, Y. Ohsawa, *ACS Appl. Mater. Interfaces* **2011**, *3*, 4165.
- [34] D. Kundu, E. Talaie, V. Duffort, L. F. Nazar, *Angew. Chemie Int. Ed.* **2015**, *54*, 3431.
- [35] Y. Hamon, T. Brousse, F. Jousse, P. Topart, P. Buvat, D. M. Schleich, *J. Power Sources* **2001**, *97-98*, 185.
- [36] M. Dollé, S. Patoux, M. M. Doeff, *Chem. Mater.* **2005**, *17*, 1036.
- [37] S. Patoux, M. Dollé, M. M. Doeff, *Chem. Mater.* **2005**, *17*, 1044.
- [38] C. Masquelier, L. Croguennec, *Chem. Rev.* **2013**, *113*, 6552.
- [39] M. Okoshi, Y. Yamada, A. Yamada, H. Nakai, *J. Electrochem. Soc.* **2013**, *160*, A2160.
- [40] Y. Yamada, Y. Koyama, T. Abe, Z. Ogumi, *J. Phys. Chem. C* **2009**, *113*, 8948.
- [41] Y. Yamada, Y. Iriyama, T. Abe, Z. Ogumi, *Langmuir* **2009**, *25*, 12766.
- [42] K. Kuratani, N. Uemura, H. Senoh, H. T. Takeshita, T. Kiyobayashi, *J. Power Sources* **2013**, *223*, 175.
- [43] S. P. Ong, V. L. Chevrier, G. Hautier, A. Jain, C. Moore, S. Kim, X. Ma, G. Ceder, *Energy Environ. Sci.* **2011**, *4*, 3680.
- [44] N. Bucher, S. Hartung, A. Nagasubramanian, Y. L. Cheah, H. E. Hoster, S. Madhavi, *ACS Appl. Mater. Interfaces* **2014**, *6*, 8059.
- [45] V. Palomares, P. Serras, I. Villaluenga, K. B. Hueso, J. Carretero-González, T. Rojo, *Energy Environ. Sci.* **2012**, *5*, 5884.
- [46] V. Palomares, M. Casas-Cabanas, E. Castillo-Martínez, M. H. Han, T. Rojo, *Energy Environ. Sci.* **2013**, *6*, 2312.
- [47] B. L. Ellis, L. F. Nazar, *Curr. Opin. Solid State Mater. Sci.* **2012**, *16*, 168.
- [48] H. Pan, Y.-S. Hu, L. Chen, *Energy Environ. Sci.* **2013**, *6*, 2338.

- [49] L. P. Wang, L. Yu, X. Wang, M. Srinivasan, Z. J. Xu, *J. Mater. Chem. A* **2015**, 3, 9353.
- [50] C. Delmas, C. Fouassier, P. Hagenmuller, *Phys. B+C* **1980**, 99, 81.
- [51] D. Buchholz, C. Vaalma, L. G. Chagas, S. Passerini, *J. Power Sources* **2015**, 282, 581.
- [52] J. Billaud, G. Singh, A. R. Armstrong, E. Gonzalo, V. Roddatis, M. Armand, T. Rojo, P. G. Bruce, *Energy Environ. Sci.* **2014**, 7, 1387.
- [53] N. Sharma, N. Tapia-Ruiz, G. Singh, A. R. Armstrong, J. C. Pramudita, H. E. A. Brand, J. Billaud, P. G. Bruce, T. Rojo, *Chem. Mater.* **2015**, 27, 6976.
- [54] P. Moreau, D. Guyomard, J. Gaubicher, F. Boucher, *Chem. Mater.* **2010**, 22, 4126.
- [55] P. P. Prosini, C. Cento, A. Masci, M. Carewska, *Solid State Ionics* **2014**, 263, 1.
- [56] K. Zaghib, J. Trottier, P. Hovington, F. Brochu, A. Guerfi, A. Mauger, C. M. Julien, *J. Power Sources* **2011**, 196, 9612.
- [57] S.-M. Oh, S.-T. Myung, J. Hassoun, B. Scrosati, Y.-K. Sun, *Electrochem. Commun.* **2012**, 22, 149.
- [58] K. Saravanan, C. W. Mason, A. Rudola, K. H. Wong, P. Balaya, *Adv. Energy Mater.* **2013**, 3, 444.
- [59] G. Li, D. Jiang, H. Wang, X. Lan, H. Zhong, Y. Jiang, *J. Power Sources* **2014**, 265, 325.
- [60] Z. Jian, L. Zhao, H. Pan, Y. S. Hu, H. Li, W. Chen, L. Chen, *Electrochem. Commun.* **2012**, 14, 86.
- [61] A. K. Padhi, K. S. Nanjundaswamy, C. Masquelier, S. Okada, J. B. Goodenough, *J. Electrochem. Soc.* **1997**, 144, 1609.
- [62] R. A. Shakoor, D.-H. Seo, H. Kim, Y.-U. Park, J. Kim, S.-W. Kim, H. Gwon, S. Lee, K. Kang, *J. Mater. Chem.* **2012**, 22, 20535.
- [63] P. Barpanda, G. Oyama, S. Nishimura, S.-C. Chung, A. Yamada, *Nat. Commun.* **2014**, 5, 4358.

- [64] Y. Lu, L. Wang, J. Cheng, J. B. Goodenough, *Chem. Commun.* **2012**, *48*, 6544.
- [65] L. Wang, Y. Lu, J. Liu, M. Xu, J. Cheng, D. Zhang, J. B. Goodenough, *Angew. Chemie Int. Ed.* **2013**, *52*, 1964.
- [66] X. Wu, W. Deng, J. Qian, Y. Cao, X. Ai, H. Yang, *J. Mater. Chem. A* **2013**, *1*, 10130.
- [67] H.-W. Lee, R. Y. Wang, M. Pasta, S. W. Lee, N. Liu, Y. Cui, *Nat. Commun.* **2014**, *5*, 5280.
- [68] X. Xiang, K. Zhang, J. Chen, *Adv. Mater.* **2015**, *27*, 5343.
- [69] R. Zhao, L. Zhu, Y. Cao, X. Ai, H. X. Yang, *Electrochem. Commun.* **2012**, *21*, 36.
- [70] C. Guo, K. Zhang, Q. Zhao, L. Pei, J. Chen, *Chem. Commun.* **2015**, *51*, 10244.
- [71] K. Sakaushi, E. Hosono, G. Nickerl, T. Gemming, H. Zhou, S. Kaskel, J. Eckert, *Nat. Commun.* **2013**, *4*, 1485.
- [72] P. Ge, M. Fouletier, *Solid State Ionics* **1988**, *28-30*, 1172.
- [73] D. P. DiVincenzo, E. J. Mele, *Phys. Rev. B* **1985**, *32*, 2538.
- [74] S. Y. Hong, Y. Kim, Y. Park, A. Choi, N.-S. Choi, K. T. Lee, *Energy Environ. Sci.* **2013**, *6*, 2067.
- [75] Y. Cao, L. Xiao, M. L. Sushko, W. Wang, B. Schwenzer, J. Xiao, Z. Nie, L. V Saraf, Z. Yang, J. Liu, *Nano Lett.* **2012**, *12*, 3783.
- [76] H.-G. Wang, Z. Wu, F.-L. Meng, D. Ma, X.-L. Huang, L.-M. Wang, X.-B. Zhang, *ChemSusChem* **2013**, *6*, 56.
- [77] Y. Wen, K. He, Y. Zhu, F. Han, Y. Xu, I. Matsuda, Y. Ishii, J. Cumings, C. Wang, *Nat. Commun.* **2014**, *5*, 4033.
- [78] C. Delmas, A. Nadiri, J. L. Soubeyroux, *Solid State Ionics* **1988**, *28-30*, 419.
- [79] P. Senguttuvan, G. Rouse, M. E. Arroyo Y De Dompablo, H. Vezin, J. M. Tarascon, M. R. Palacín, *J. Am. Chem. Soc.* **2013**, *135*, 3897.

- [80] P. Senguttuvan, G. Rousse, V. Seznec, J.-M. Tarascon, M. R. Palacín, *Chem. Mater.* **2011**, *23*, 4109.
- [81] Y. Xu, E. M. Lotfabad, H. Wang, B. Farbod, Z. Xu, A. Kohandehghan, D. Mitlin, *Chem. Commun.* **2013**, *49*, 8973.
- [82] J. P. Huang, D. D. Yuan, H. Z. Zhang, Y. L. Cao, G. R. Li, H. X. Yang, X. P. Gao, *RSC Adv.* **2013**, *3*, 12593.
- [83] Y. Wang, X. Yu, S. Xu, J. Bai, R. Xiao, Y.-S. Hu, H. Li, X.-Q. Yang, L. Chen, X. Huang, *Nat. Commun.* **2013**, *4*, 2365.
- [84] V. L. Chevrier, G. Ceder, *J. Electrochem. Soc.* **2011**, *158*, A1011.
- [85] L. Baggetto, P. Ganesh, R. P. Meisner, R. R. Unocic, J.-C. Jumas, C. A. Bridges, G. M. Veith, *J. Power Sources* **2013**, *234*, 48.
- [86] L. D. Ellis, T. D. Hatchard, M. N. Obrovac, *J. Electrochem. Soc.* **2012**, *159*, A1801.
- [87] J. Qian, Y. Chen, L. Wu, Y. Cao, X. Ai, H. Yang, *Chem. Commun.* **2012**, *48*, 7070.
- [88] A. Darwiche, C. Marino, M. T. Sougrati, B. Fraisse, L. Stievano, L. Monconduit, *J. Am. Chem. Soc.* **2012**, *134*, 20805.
- [89] S. Komaba, Y. Matsuura, T. Ishikawa, N. Yabuuchi, W. Murata, S. Kuze, *Electrochem. Commun.* **2012**, *21*, 65.
- [90] K. West, B. Zachau-Christiansen, T. Jacobsen, S. Skaarup, *J. Power Sources* **1989**, *26*, 341.
- [91] K. West, B. Zachau-Christiansen, T. Jacobsen, S. Skaarup, *Solid State Ionics* **1988**, *28-30*, 1128.
- [92] S. Tepavcevic, H. Xiong, V. R. Stamenkovic, X. Zuo, M. Balasubramanian, V. B. Prakapenka, C. S. Johnson, T. Rajh, *ACS Nano* **2012**, *6*, 530.
- [93] K. West, B. Zachau-Christiansen, T. Jacobsen, S. Skaarup, *Solid State Ionics* **1990**, *40/41*, 585.
- [94] G. Wang, G. Pistoia, *J. Electroanal. Chem.* **1991**, *302*, 275.

- [95] Y. Dong, S. Li, K. Zhao, C. Han, W. Chen, B. Wang, L. Wang, B. Xu, Q. Wei, L. Zhang, X. Xu, L. Mai, *Energy Environ. Sci.* **2015**, *8*, 1267.
- [96] H. Liu, H. Zhou, L. Chen, Z. Tang, W. Yang, *J. Power Sources* **2011**, *196*, 814.
- [97] H. He, G. Jin, H. Wang, X. Huang, Z. Chen, D. Sun, Y. Tang, *J. Mater. Chem. A* **2014**, *2*, 3563.
- [98] D. Nguyen, J. Gim, V. Mathew, J. Song, S. Kim, D. Ahn, J. Kim, *ECS Electrochem. Lett.* **2014**, *3*, A69.
- [99] R. F. Egerton, *Physical Principles of Electron Microscopy - An Introduction to TEM, SEM, and AEM*, Springer US, Boston, MA, **2005**.
- [100] R. Marassi, F. Nobili, *Encycl. Electrochem. Power Sources* **2009**, 769.
- [101] R. Marassi, F. Nobili, *Encycl. Electrochem. Power Sources* **2009**, 758.
- [102] D. C. Bell, N. Erdman, *Low Voltage Electron Microscopy: Principles and Applications*, John Wiley & Sons, Ltd, Chichester, **2013**.
- [103] Y. Leng, *Materials Characterisation: Introduction to Microscopic and Spectroscopic Methods*, JohnWiley & Sons (Asia), Singapore, **2008**.
- [104] E. Margui, R. Van Grieken, *X-Ray Fluorescence Spectrometry and Related Techniques: An Introduction*, Momentum Press, New York, NY, **2013**.
- [105] R. Jenkins, *X-Ray Fluorescence Spectrometry*, John Wiley & Sons, Ltd, New York, NY, **1999**.
- [106] R. H. Geiss, in *Encycl. Mater. Charact.* (Eds.: R.C. Brundle, C.A.J. Evans, S. Wilson), Elsevier, Greenwich, CT, **1992**, pp. 120–134.
- [107] D. Tonti, I. De Ciencia, D. M. De Madrid, *Encycl. Electrochem. Power Sources* **2009**, 673.
- [108] C. Suryanarayana, M. G. Norton, *X-Ray Diffraction: A Practical Approach*, Springer US, Boston, MA, **1998**.
- [109] Y. Waseda, E. Matsubara, K. Shinoda, *X-Ray Diffraction Crystallography*, Springer, Berlin, Heidelberg, **2011**.

- [110] C. Hammond, *The Basics of Crystallography and Diffraction*, Oxford University Press, Oxford, UK, **2015**.
- [111] H. Wiedemann, *Synchrotron Radiation*, Springer, Berlin, Heidelberg, **2003**.
- [112] N. Yagi, in *Compr. Biomed. Phys.* (Ed.: A. Brahme), Elsevier B.V., **2014**, p. 4056.
- [113] M. F. Toney, in *Encycl. Mater. Charact.* (Eds.: C. Evans, S. Wilson, R. Brundle), Boston: Butterworth-Heinemann ; Greenwich, CT: Manning, **1992**, pp. 198–213.
- [114] H. Dittrich, A. Bieniok, *Encycl. Electrochem. Power Sources* **2009**, 718.
- [115] J.-P. Itie, F. Baudalet, V. Briois, E. Elkaim, A. Nadji, D. Thiaudiere, in *X-Rays Mater.* (Eds.: G. Philippe, R. Guinebretière), London : Iste ; Hoboken, NJ : Wiley, 2012, **2012**, pp. 1–48.
- [116] G. Currell, *Analytical Instrumentation: Performance, Characteristics and Quality*, John Wiley & Sons, Ltd, Chichester, **2000**.
- [117] J. M. Mermet, *Encycl. Anal. Sci.* **2005**, 210.
- [118] C. Daniel, J. O. Besenhard, *Handbook of Battery Materials*, Wiley Online Library, Weinheim, Germany, **2011**.
- [119] J. Park, *Principles and Applications of Lithium Secondary Batteries*, Wiley-VCH Verlag GmbH & Co. KGaA, Weinheim, Germany, **2012**.
- [120] A. J. Bard, L. R. Faulkner, *Electrochemical Methods : Fundamentals and Applications*, John Wiley & Sons, Ltd, New York, NY, **2001**.
- [121] C. H. Hamann, A. Hamnett, W. Vielstich, *Electrochemistry*, Wiley Online Library, Weinheim, Germany, **2007**.
- [122] M. Schmid, *Studies on Cathode Materials Based on α -Na 0.7 MnO₂ for Sodium Ion Batteries (Internship Report)*, **2015**.
- [123] D. W. Dees, S. Kawauchi, D. P. Abraham, J. Prakash, *J. Power Sources* **2009**, 189, 263.
- [124] W. Weppner, R. A. Huggins, *J. Electrochem. Soc.* **1977**, 124, 1569.

- [125] K. M. Shaju, G. V. Subba Rao, B. V. R. Chowdari, *Electrochim. Acta* **2004**, *49*, 1565.
- [126] E. Markevich, M. D. Levi, D. Aurbach, *J. Electroanal. Chem.* **2005**, *580*, 231.
- [127] J. Wang, *Analytical Electrochemistry*, Wiley VCH, Hoboken, NJ, **2006**.
- [128] G. Bontempelli, R. Toniolo, *Encycl. Electrochem. Power Sources* **2009**, 643.
- [129] Z. B. Stoyanov, D. E. Vladikova, *Encycl. Electrochem. Power Sources* **2009**, 632.
- [130] R. Bottom, in *Princ. Appl. Therm. Anal.* (Ed.: P. Gabbott), Blackwell Publishing Ltd, Oxford, UK, **2008**, pp. 87–118.
- [131] M. Wagner, *Thermal Analysis in Practice*, Mettler Toledo, **2009**.
- [132] B. M. Mckenna, J. G. Lyng, in *Instrum. Assess. Food Sens. Qual.* (Ed.: D. Kilkast), Woodhead Publishing Limited, Cambridge, UK, **2013**, pp. 129–162.
- [133] X. Tian, *Ionic Liquids in Sodium Ion Batteries* (Master's Thesis), Ulm University, **2015**.
- [134] K. Kubota, N. Yabuuchi, H. Yoshida, M. Dahbi, S. Komaba, *MRS Bull.* **2014**, *39*, 416.
- [135] J. Kawakita, T. Miura, T. Kishi, *Solid State Ionics* **1999**, *124*, 21.
- [136] M. Pasquali, G. Pistoia, *Electrochim. Acta* **1991**, *36*, 1549.
- [137] M. E. Spahr, P. Novák, W. Scheifele, O. Haas, R. Nesper, *J. Electrochem. Soc.* **1998**, *145*, 421.
- [138] G. Pistoia, G. Wang, D. Zane, *Solid State Ionics* **1995**, *76*, 285.
- [139] E. Ni, S. Uematsu, Z. Quan, N. Sonoyama, *J. Nanoparticle Res.* **2013**, *15*, 1732/1.
- [140] H. Wang, N. Kawasaki, T. Yokoyama, H. Yoshikawa, K. Awaga, *Dalt. Trans.* **2012**, *41*, 9863.
- [141] N. Sonoyama, Y. Suganuma, T. Kume, Z. Quan, *J. Power Sources* **2011**, *196*, 6822.

- [142] A. Xie, C.-A. Ma, L. Wang, Y. Chu, *Electrochim. Acta* **2007**, *52*, 2945.
- [143] H. Wang, S. Hamanaka, Y. Nishimoto, S. Irle, T. Yokoyama, H. Yoshikawa, K. Awaga, *J. Am. Chem. Soc.* **2012**, *134*, 4918.
- [144] S. Uematsu, Z. Quan, Y. Suganuma, N. Sonoyama, *J. Power Sources* **2012**, *217*, 13.
- [145] S. Li, J. Qiu, C. Lai, M. Ling, H. Zhao, S. Zhang, *Nano Energy* **2015**, *12*, 224.

List of Figures

Figure 1. Development of the number of publications on the topic sodium-ion battery as found by Web of Science, search term: "sodium-ion batter*"; #: year to date; date of search Oct 26, 2015.....	9
Figure 2. Schematic of a sodium-ion battery (anode: $\text{Na}_6[\text{V}_{10}\text{O}_{28}]^{[22]}$, cathode: $\text{Na}_{2.5}\text{V}_6\text{O}_{16}^{[23]}$).....	14
Figure 3. a) Secondary electrons, b) backscattered electrons.....	26
Figure 4. Generation of contrast due to differences in thickness and atomic masses.....	27
Figure 5. X-ray fluorescence.....	28
Figure 6. Photoelectric effect employed in X-ray photoelectron spectroscopy.....	29
Figure 7. Electronic transitions during X-ray generation.....	31
Figure 8. Geometry of the interaction of incident X-rays with crystallographic planes.....	32
Figure 9. Set-up for coin cell measurements (adapted from ^[122]).....	35
Figure 10. Schematic circuit of a a) 2-electrode and b) 3-electrode set-up (CE: Counter Electrode, WE: Working Electrode, RE: Reference Electrode).....	35
Figure 11. Schematic profile of CV measurements: a) Potential vs. time; b) current vs. potential.....	39
Figure 12. Electrical circuit scheme equivalent for interfacial electrochemical reactions.....	41
Figure 13. (Figure 1 in the publication). Setup of the electrochemical <i>in operando</i> XRD cell.....	59

List of Publications and Conference Contributions

- March 2016 Steffen Hartung, Nicolas Bucher, Joseph B. Franklin, Anna M. Wise, Linda Y. Lim, Han-Yi Chen, Johanna Nelson Weker, Maria-E. Michel-Beyerle, Michael F. Toney, Madhavi Srinivasan "Mechanism of Na⁺ Insertion in Alkali Vanadates and Its Influence on Battery Performance" *Adv. Energy Mater.* **2016**, 1502336, doi:10.1002/aenm.201502336
- Mar 2016 Nicolas Bucher, Steffen Hartung, Joseph B. Franklin, Anna M. Wise, Linda Y. Lim, Han-Yi Chen, Johanna Nelson Weker, Michael F. Toney, Madhavi Srinivasan "P2-Na_xCo_yMn_{1-y}O₂ (y = 0, 0.1) as Cathode Materials in Sodium-Ion Batteries – Effects of Doping and Morphology To Enhance Cycling Stability" *Chem. Mater.* **2016**, doi:10.1021/acs.chemmater.5b04557
- Aug 2015 Steffen Hartung, Nicolas Bucher, Ramona Bucher, Madhavi Srinivasan "Electrochemical cell for *in operando* X-ray diffraction measurements on a conventional X-ray diffractometer" *Rev. Sci. Instrum.* **2015**, 86, 086102/1-086102/3
- Aug 2015 Steffen Hartung, Nicolas Bucher, Han-Yi Chen, Rami Al-Oweini, Sivaramapanicker Sreejith, Parijat Borah, Zhao Yanli, Ulrich Kortz, Ulrich Stimming, Harry E. Hoster, Madhavi Srinivasan "Vanadium-based polyoxometalate as new material for sodium-ion battery anodes" *J. Power Sources* **2015**, 288, 270 - 277
- May 2014 Steffen Hartung, Nicolas Bucher, Vivek Sahadevan Nair, Cheah Yan Ling, Yuxi Wang, Harry E Hoster, Madhavi Srinivasan "Sodium Vanadium Oxide: A New Material for High-Performance Symmetric Sodium Ion Batteries" *ChemPhysChem.* **2014**, 15, 2121-2128
- May 2014 Nicolas Bucher, Steffen Hartung, Arun Nagasubramanian, Yan Ling Cheah, Harry E. Hoster, Srinivasan Madhavi "Layered Na_xMnO_{2+z} in Sodium Ion Batteries – Influence of Morphology on Cycle Performance" *ACS Appl. Mater. Interfaces* **2014**, 6, 8059-8065
- Apr 2014 Vivek Sahadevan Nair, Sivaramapanicker Sreejith, Parijat Borah, Steffen Hartung, Nicolas Bucher, Yanli Zhao, Srinivasan Madhavi "Crystalline Li₃V₆O₁₆ rods as high-capacity anode materials for aqueous rechargeable lithium batteries (ARLB)" *RSC Adv.* **2014**, 4, 28601-28605

- Mar 2014 Dr. Vanchiappan Aravindan, Dr. Wong Chui Ling, Steffen Hartung, Nicolas Bucher, Prof. Srinivasan Madhavi "Carbon-Coated $\text{LiTi}_2(\text{PO}_4)_3$: An Ideal Insertion Host for Lithium-Ion and Sodium-Ion Batteries" *Chem. Asian J.* **2014**, *9*, 878-882
- Feb 2014 Steffen Hartung, Nicolas Bucher, Arun Nagasubramanian, Yan Ling Cheah, Harry E. Hoster, Madhavi Srinivasan "Spherical $\text{Na}_x\text{MnO}_{2+z}$ as Cathode in Sodium-ion Batteries – Increasing Performance by Optimizing Morphology" oral presentation: 'Singapore Battery Meeting', **2014**, Singapur
- Nov 2013 Steffen Hartung, Nicolas Bucher, Vivek Sahadevan Nair, Yan Ling Cheah, Harry E. Hoster, Madhavi Srinivasan "Sodium Vanadium Oxide – A New Material for High-Performance Sodium Ion Batteries" oral presentation: 'The 7th Asian Conference on Electrochemical Power Sources', **2013**, Osaka, Japan
- Okt 2013 Steffen Hartung, Madhavi Srinivasan "New Materials for Better Energy Storage Devices – Selected Examples" oral presentation: 'Singapore International Energy Week', **2013**, Singapur
- Jul 2013 Nicolas Bucher, Steffen Hartung, Maria Arkhipova, Denis Yu, Philipp Kratzer, Gerhard Maas, Madhavi Srinivasan, Harry E. Hoster "A novel ionic liquid for Li ion batteries – uniting the advantages of guanidinium and piperidinium cations" *RSC Adv.* **2014**, *4*, 1996-2003
- Apr 2013 Steffen Hartung, Nicolas Bucher, Irina Gocheva, Harry E. Hoster, Madhavi Srinivasan "Effect of Doping and Electrolyte on the Performance of Sodium Manganese Oxides in Sodium Ion Batteries" oral presentation: '13th Topical Meeting of the International Society of Electrochemistry', **2013**, Pretoria, South Africa
- Jan 2013 Nicolas Bucher, Steffen Hartung, Irina Gocheva, Yan L. Cheah, Madhavi Srinivasan, Harry E. Hoster "Combustion-synthesized sodium manganese (cobalt) oxides as cathodes for sodium ion batteries" *J. Solid State Electrochem.* **2013**, *17*, 1923-1929